UNIVERSITY OF SOUTHAMPTON

FACULTY OF ENGINEERING AND THE ENVIRONMENT

Civil, Maritime and Environmental Engineering and Science

Fluid Structure Interaction group

Vortex- and Wake- Induced Vibrations in an array of cylinders

by

Linh Nguyen The Tuan

Thesis for the degree of Doctor of Philosophy

October 2015

UNIVERSITY OF SOUTHAMPTON

ABSTRACT

FACULTY OF ENGINEERING AND THE ENVIRONMENT

Civil, Maritime and Environmental Engineering and Science

Thesis for the degree of Doctor of Philosophy

Vortex- and Wake- Induced Vibrations in an array of cylinders

Linh Tuan The Nguyen

Flow-induced vibration (FIV) is an important phenomenon, by which the flow around bluff bodies creates forces that excite vibration. When marine risers are designed in a tandem arrangement, two aspects of FIV including Vortex Induced Vibration (VIV) and Wake-Induced Vibration (WIV) are very important, resulting in strong vibrations and fatigue damage. In this thesis, the simultaneous effects of VIV and WIV are studied for the case of circular cylinders by means of Computational Fluid Dynamics (CFD) software ANSYS Fluent. An Arbitrary Lagrangian-Eulerian (ALE) formulation is applied on a deformable mesh needed for modelling a free vibrating cylinder. The response dynamics and wake interactions are addressed. Major aspects considered in the thesis include: the Reynolds number (Re), the mass-damping parameter, the degrees of freedom of a single cylinder and of a downstream cylinder and the combined effect of VIV and WIV.

The current predictions focus on sub-critical Re flow so that turbulence models are applied using two-dimensional Reynolds Averaged Navier-Stokes (RANS) equations. Force coefficients are analysed based on pressure distribution and Strouhal number. The VIV and WIV response is analysed by considering oscillating amplitude, frequencies and motion trajectories.

The work concentrates on FIV vibration in three main cases: a single circular cylinder, and a downstream cylinder in tandem and staggered arrangements. The cylinder was elastically mounted on a mass-spring-damper system, with 1 degree of freedom (dof), 1+1dof, 2 dof or 4 dof. The study results showed the cylinder's vibration is strongly affected by the mass-damping ratio and reduced velocity. The coupling between inline and crossflow vibrations could increase the amplitude of motion dramatically compared to crossflow vibration only. The amplitude of vibration changes the wake pattern as well as the trajectory of the cylinder. The vibration in the inline direction on the downstream cylinder in the wake of the upstream one is remarkably high compared to the crossflow direction.

With a 2 dof system, the simultaneous effects of VIV and WIV give rise to vibration in each direction with two natural frequencies. WIV can be observed in the low-frequency response of the cylinder, which is considerably larger than the high-frequency VIV response. The combination of these two components can result in vibrations of the cylinder with higher amplitudes compared to any single form of excitation. The trajectories of the cylinder with a 4 dof system are very chaotic.

Table of Contents

List of Tables

List of Figures

DECLARATION OF AUTHORSHIP

I, Linh Tuan The Nguyen declare that this thesis and the work presented in it are my own and has been generated by me as the result of my own original research.

Vortex and wake induced vibration in an array of cylinders

I confirm that:

1. This work was done wholly or mainly while in candidature for a research degree at this University;
2. Where any part of this thesis has previously been submitted for a degree or any other qualification at this University or any other institution, this has been clearly stated;
3. Where I have consulted the published work of others, this is always clearly attributed;
4. Where I have quoted from the work of others, the source is always given. With the exception of such quotations, this thesis is entirely my own work;
5. I have acknowledged all main sources of help;
6. Where the thesis is based on work done by myself jointly with others, I have made clear exactly what was done by others and what I have contributed myself;
7. Parts of this work have been published as:

    - Linh, T.T.N., Temarel, P., Chaplin, J.R. 2015. Flow around two circular cylinders in tandem with 2D RANS: Fixed and free oscillation, *7th International Conference on Hydroelasticity in marine technology, Split, Croatia*
    - Linh, T.T.N., Temarel, P. 2014. Numerical simulation of an oscillating cylinder in cross-flow at a Reynolds number of 10,000: forced and free oscillations. In: *OMAE2014-23394. Proc. 33rd Int. Conf. on Offshore Mechanics and Arctic Engineering. San Francisco, USA*.
    - Linh, T.T.N., Temarel, P., Chaplin, J.R. 2013. Flow around fixed cylinder in tandem, *16th Numerical towing tank symposium, Mulheim, Germany*.

    - Linh, T.T.N. 2013. Application of CFD on Vortex induced vibration around marine riser. *Proc. Int. Conf. on Petroleum Technology, Vietnam Petroleum Institute, Ha Noi, Vietnam.*

    - Linh, T.T.N., Temarel, P., Chaplin, J.R. 2013. Vortex and wake induced vibration in an array of riser, *4th UK Marine Technology Postgraduate Conference, University College London, UK*

Signed: ....

Date: ....

Acknowledgements

I would like to extend thanks to the many people, who so generously contributed to the work presented in this thesis.

Special mention goes to my enthusiastic supervisor, Professor Pandeli Temarel. My Ph.D. has been an amazing experience and I thank Penny wholeheartedly, not only for his tremendous academic guidance but also for the time, funding and advice. His enthusiasm and the high level of responsibility is the excellent example for me to pursuit academic careers. Similar, profound gratitude goes to Professor John Chaplin, who has been a truly dedicated supervisor. I am particularly indebted to John for his constant supports and suggestions for the educative correspondences I received about aspects of Vortex-Induced Vibration, the data support and the valuable experiences by attending his VIV experiences that were very beneficial for my research.

I am very thankful to the Faculty of Engineering and the Environment, the University of Southampton, Vietnam Ministry of Education and Training, Petro Vietnam Oil and Gas Group for their financial support and the travel funds that I was awarded. Without them, I could not have a chance to start and complete this Ph.D. I would like to thank my current employer in Vietnam (PetroVietnam University) for arranging my study-leave.

I am also hugely appreciative to Professor Grant Hearn for his valuable suggestions and correction during my 9-month-report and transfer report, Associate Professor Le Thi Minh Nghia, for sharing her fluid dynamics expertise so willingly from the first day I start my Ph.D.

I appreciate the kind technical support from Saurabh Prabhakar, Saravana Kumar from ANSYS Corporation to develop a UDF that is very importance for my thesis. Thanks to my colleagues at Fluid Structure Interaction Group, Fanfan Sun, Pareecha Rattanasiri, Greg Melling, Charles Badoe, Arun Krishnan, Zahir Ramli for their useful discussion on CFD and turbulence model. Special mention goes to my friends Nguyen Thanh An, Nguyen Viet Hung, Truong Ngoc Cuong, Nguyen Huu Hoa, Nguyen Duc Kien, for going far beyond the call of duty. They always give me the useful advices, not only in my research, but also in the social life problems.

Finally, but by no means least, thanks go to my mother, my wife and my daughter for their wholehearted encouragement and companionship throughout the years I spent in Southampton. Thanks my parents and my grandfather who always teach me about importance of learning and the value of knowledge. They are the most important people in my world and I dedicate this thesis to them. Thanks to all who have brought great joy to my life and have managed to live through the demands on my career. It would not have been without you, thank you all so much.

Nomenclature

A	Amplitude of motion/Area of cylinder
A^*	Non-dimensional amplitude
c	Damping constant
C_a	Added mass coefficient
C_μ	Constant (0.09)
C	Courant number
C_d	Drag coefficient
C_l	Lift Coefficient
C_p	Pressure coefficient
D	Cylinder Diameter
f^*	frequency ratio
f_{ex}	excitation frequency
f_i	external forces
f_n	natural frequency of a structure
$f_{n,air}$	natural frequency in air
$f_{n,water}$	natural frequency in water
f_o	oscillation frequency
f_s	shedding frequency
f_{St}	Strouhal frequency
F_d	Drag Force
F_l	Lift Force
$F_{fluid,y}$	Fluid force in y direction

g	Gravitational acceleration
I	Turbulent intensity
k	Turbulent kinetic energy
K	Spring constant
l	Turbulent length scale
L	Characteristic length/ Spacing between cylinder
m^*	Mass ratio
M	Mass of oscillating system
p	Free stream static pressure
p_c	Cylinder surface pressure
P	Pair
Re	Reynolds number
S	Single
S_t	Strouhal number
$\bar{S}_{ij}$	Strain rate tensor
t	time
$\boldsymbol{T}$	stress tensor
T_e	excitation period
T_y	vortex shedding period
u	fluid velocity
$\bar{u}$	mean velocity
u'	fluctuating velocity
Ur	Reduced velocity

U_τ	friction velocity
$\boldsymbol{V}$	Velocity vector
y^+	dimensionless first cell height
y_1	distance of first layer to the wall
β	Turbulent viscous ratio
Δ	First cell size
Δt	Time step size
ε	rate of dissipation
ζ	Damping coefficient
λ, λ^*	Wave length, wave length
μ	Dynamic viscosity
μ_t	Eddy viscosity
ρ	fluid density
τ_{ij}	Reynolds stress tensor
τ_ω	wall shear stress
ν	Fluid kinematic viscosity
ν_t	Turbulent viscosity
ω	Specific dissipation rate

Abbreviations

2D	2 Dimensional
3D	3 Dimensional
CFD	Computational Fluid Dynamics
DC	Downstream cylinder
DES	Detached Eddy Simulation
DNS	Direct numerical simulation
DOF	Degree of freedom
EWF	Enhanced wall function
EWT	Enhanced wall treatment
FIV	Flow induced vibration
FSM	Fractional Step Method
FVM	Finite Volume method
ITTC	International Towing Tank Conference
LES	Large Eddy Simulation
ITA/NITA	(Non) Iterative Time Advancement
MDM	Moving Dynamic Mesh
MDOF	Multidegree of freedom
PDE	Partial Differential Equation

PISO	Pressure-Implicit with Splitting of Operators
PVN	Petro Vietnam Group
RANS	Reynolds Averaged Navier Stokes
RKE	Realizable $k - \varepsilon$ model
SAS	Scale Adaptive Simulation
SDOF	Single Degree of Freedom
SGS	Subgrid Scale
SIMPLE	Semi-Implicit Method for Pressure Linked Equation
SIMPLEC	SIMPLE Consistent
SKW	Standard k omega model
SPA	Spalart Allmaras
SST	Shear Stress Transport
SST KW	Shear Stress Transport K Omega Model
TrBL	Boundary layer transition
TrW	Wake transition
TrSL	Shear layer transition
UC	Upstream cylinder
UDF	User Defined Function

URANS	Unsteady Reynolds Averaged Navier Stokes
VIV	Vortex Induced Vibration
VMS LES	Variational Multiscale Large Eddy Simulation
WBL	Wall boundary layer
WIV	Wake Induced Vibration

Chapter 1 : Introduction

This thesis describes a series of computational investigations of Flow-Induced Vibration (FIV) phenomena, which are associated with the responses of structures placed in fluid flow. More specifically, the concept cover cases in which the interaction develops between fluid dynamic forces and inertia, damping and elastic forces of the structures. The study of these phenomena not only relate to fluid dynamics but also structural mechanics and mechanical vibrations.

Fluid flow, its characteristics and its effects on structures receive the attention of scientific and industrial communities. For example, researching in FIV started in ancient Greeks times, where Aeolian harps were designed to create musical sound from wind-induced vibration. Leonardo da Vinci discovered that audible sounds were created by wake eddy and vortex induced air pressure fluctuations produced as airflow around cylindrical obstacles. However, systematic studies did not take place until a century ago when Strouhal established the relationship between vortex shedding frequency and flow velocity for a given cylinder diameter (Blevins, 2001). FIV has been experienced in numerous fields including aerospace industry, power generation (turbine blade, heat exchanger), civil engineering (bridges, skyscrapers), and offshore technology. With continuously developing technologies, FIV can be used to obtain energy from the sea and ocean currents; however, FIV is often responsible for the destruction of buildings and artefacts such as the collapse of the Tacoma Bridge Narrows, USA, in 1940. Ocean currents are responsible for damaging offshore platforms and marine risers due to unexpectedly high vibration amplitude and fixing such problems is very costly.

The phenomena associated with FIV are wide-ranging concepts, including Vortex-induced vibration(VIV), galloping, wake galloping, flutter, buffeting response, fluid elastic instability, etc. Each of these vibrations arises from distinct fluid dynamic phenomena that can be classified by the nature of the flow and the structure, as shown in Figure 1.1 (Blevins, 2001).

In FIV, non-linear interactions occur between the flow field and the structure that encounters the flow. This interaction happens in the flows when the fluid experiences a large pressure gradient when encountering the structure. For a bluff body structure with no streamline shape, flow separation occurs on its surface generating forces which result in an excitation energy. This is known as “Fluid-Structure Interaction (FSI)”

The focus of this thesis is mainly on flows across cylindrical structures in general. However, due to time limitations, only two main aspects of FIV that are crucial for cylindrical structures are investigated: Vortex-Induced Vibration (VIV) which is caused primarily by the process of vortex shedding, and Wake-Induced vibration (WIV), due to the wake galloping behind the body.

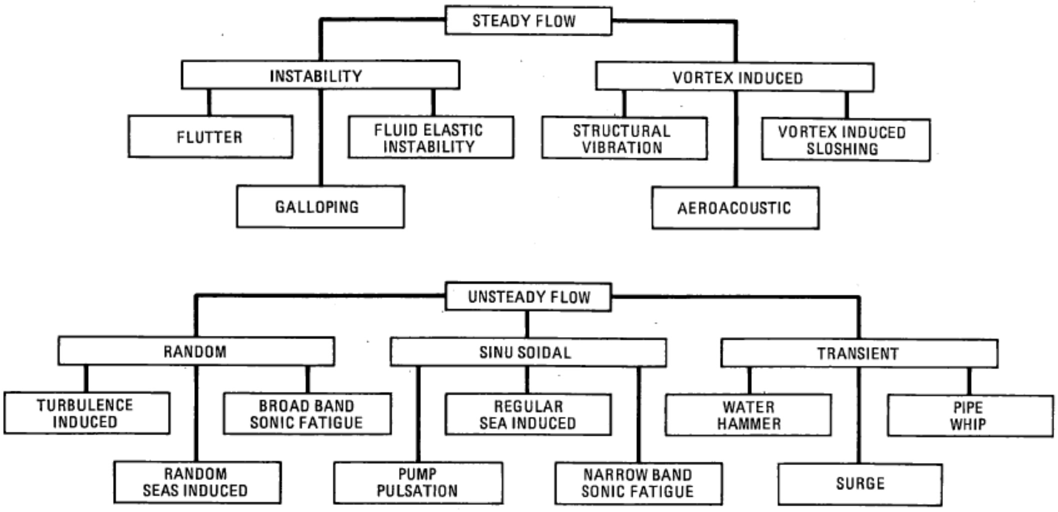

Figure 1.1 Classification of flow induced vibration (Blevins 2001)

1.1. Motivation

FIV is widely recognised as a major concern in the designs of modern mechanical artefacts, among which marine risers and crossflow heat exchangers receive major attention. Along with the development of technology, FIV became more and more important in recent years as constructions become lighter, more flexible and prone to vibrate. The collapse of Tacoma Bridge Narrow in 1940 demonstrated that FIV can be extremely hazardous and cannot be ignored when designing and constructing any structure.

In the last two decades, the offshore oil exploration industry has witnessed a significant transformation. As the result of onshore oil fields becoming depleted, oil exploration is reaching the deeper subsea areas where it’s impossible in the past. As the result, VIV in offshore structures has become a major factor affecting all stages of development of offshore structures including conceptualization, design, analysis, construction and monitoring and governs the arrangement of risers, from fabrication to method of installation, instrumentation and operation. Advances to deeper waters in search of hydrocarbon resources have resulted in multi-billion dollar offshore projects around the world, for example: Chynne (2747), Independence Hub (2414), Atlantics (2145), Nakika (2000) to name a few, shown in Figure 1.2, with the world record drilling of 3051 m (GRID-Arendal, 2014). In such water depths, long flexible cylindrical structures are increasingly required (e.g. umbilics, risers, conductor tubes, pipeline spans) and prediction of VIV responses has become increasingly important as even weak interactions may produce large deflections as well as cause issues such as clashing, failure by fatigue, etc. A recent estimation by British Petroleum puts the estimated cost of countering VIV to approximately 10% of the project cost itself (Byrd et al., 2014).

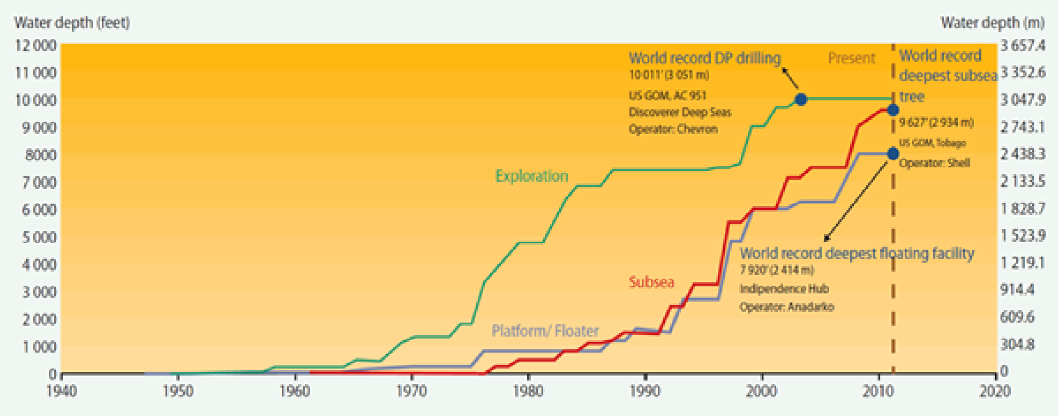

Figure 1.2: Worldwide progression of water deep capabilities for offshore drilling and production (GRID-Arendal, 2014)

In addition, the demand of offshore industry to increase productivity led to the development of complex multi-tube riser systems, which form an important link between the floating structure and the subsea system. The production riser has to be flexible in order to resist the hydrodynamic load. It consists of a cluster of pipes, typically, an export riser and a number of flowline and auxiliary risers interconnected along their length by spacers (spreader bars) suspended in a main structural system on a number of cables (the distance between the spacers is designed to meet operational requirements for installation and maintenance). The deep-water riser is additionally provided with buoyancy devices to reduce tensile stresses. The flowline riser conveys the crude oil from the wells to the production platform on the surface. The export riser conducts the processed crude to the pipeline on the ocean floor. The auxiliary risers, used for various purposes, include gas lift pipes and maintenance pipes for guiding tools. Typically, the cross-sectional configuration of the multi-tube riser systems can be, as shown in Figure 1.3, in the form of a circular array (a central export pipe is surrounded by one or two arrays of smaller satellite pipes), a linear array or a dense rectangular array (highly regular square or staggered, appearing solid when viewed from any direction other than along a row or column). When the risers are formed in an array, in addition to VIV, a cylindrical structure situated downstream also undergoes WIV possibly caused by the unsteadiness or non-uniformity of the incident flow it experiences. Wake-induced vibrations are not very well understood in the literature (Chaplin and Batten, 2014). They are linked to various concepts, including wake-induced galloping (associated with the non-uniformity of the force coefficients of one cylinder in the wake of another), buffeting (due to the incidence of vortices and turbulence shed from the upstream cylinder) and proximity interference (a fluid-elastic instability that occurs when the gap between two cylinders is less than about 2 diameters). Previous investigations showed that high amplitude VIV occurs in the crossflow direction in the range of reduced velocity (Ur) from 4 to 12 with the amplitude smaller than 1.6D, where D denotes cylinder diameter. On the other hand, WIV occurs over a wider range of Ur and generates higher amplitude in both inline and crossflow direction due to the appearance of vortices from body upstream. The amplitude of WIV appears to increase with increasing Ur without any limit in some situations (Chaplin and Batten, 2014). When designing marine risers systems, VIV and WIV should be considered as the most influential factors, which are strongly affected by the mass ratio (structural mass divided by displaced mass) as well as reduced velocities.

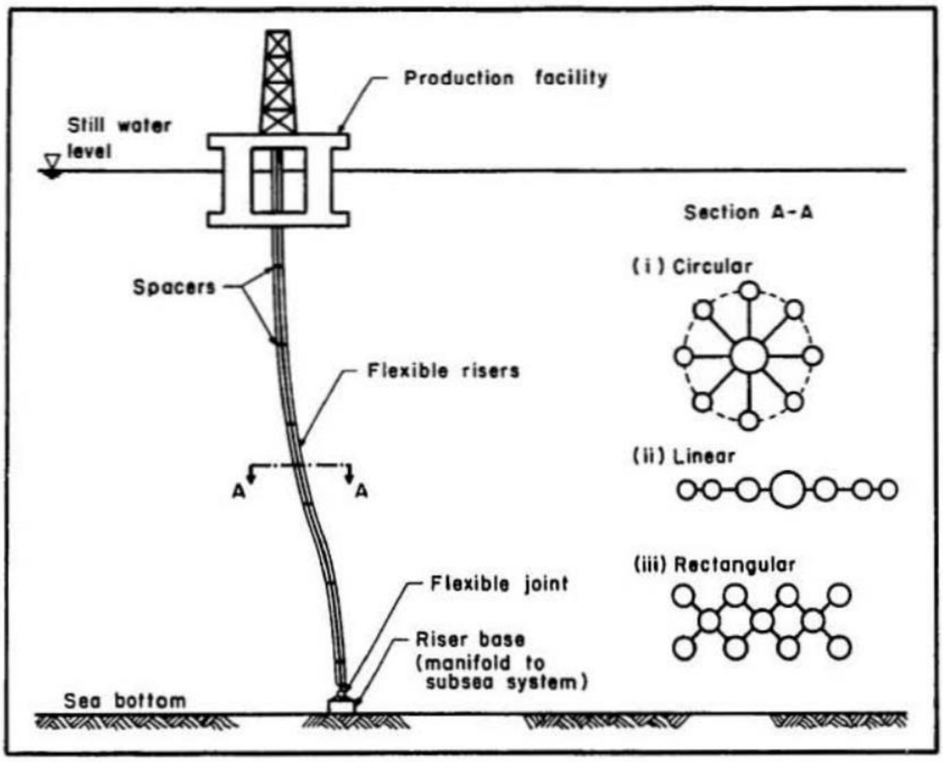

Figure 1.3. Schematic representation of multi-tube production riser (Rzentkowski, 1990)

In operation, marine risers are subjected to flow conditions corresponding to a wide range of Reynolds number (Re), typically from 10^3 to 10^7, depending on diameter and free-flow velocity. These conditions are difficult and expensive to simulate in an experimental setup. Thus using Computational Fluid Dynamics (CFD) tools to study/predict the response of the riser undergoing VIV is an attractive alternative. Unfortunately, well-established numerical modelling procedures for CFD (e.g., finite elements, finite difference, and control volumes) are not robust for high Re flows. As the Re increases, these methods are prone to developing spurious node-to-node oscillations – which eventually cause the numerical solution procedure to break down (Chen et al., 2006). These oscillations can be suppressed by refining the mesh, but the necessary degree of refinement and running for a large number of vortex shedding occurrences can be extremely costly in term of computation.

The interest of this research lies on the South China Sea area where Vietnam Petroleum Group (PVN), the main sponsor of this project, is producing oil and gas offshore. In the past, most oil fields of PVN were either onshore or in very shallow water areas, e.g. White Tiger, Dragon and Rang Dong oil fields. At a water depth less than 100m, the FSI and vibration of risers was not a big concern. However, within, the last 8 years, with the discovery of some new oil fields in deep water block in Phu Khanh and Tu Chinh – Vung May Basin, such as Dai Hung 1 and Dai Hung 2, PVN had started to focus more on FSI problem as the risers required are much longer, more than 1000m. In PVN's deep water oil fields, typically, risers are often designed in tandem (i.e. linear, according to Figure 1.3) or in square arrangement. In addition, the South China Sea condition is rather calm and peaceful, different from North Sea where the sea condition is very rough. Furthermore, the risers are fairly small, with the diameter lying in a range of 3.5 - 21 inches, with resultant typical Reynolds number smaller than 300,000.

For these reasons, whilst investigating behaviour in range of Reynolds numbers and different types of riser arrangements, the focus will be on two main aspects:

- VIV of single cylinder at subcritical Reynolds number,
- Behaviour of cylinders in tandem and staggered arrangement, also at subcritical Reynolds number.

In fact, the investigation of this thesis focuses on VIV of a single cylinder and the simultaneous effect of VIV and WIV of a downstream cylinder, to enhance understanding of FSI in marine risers systems. To this end, the circular cylinder will be used, as it is a common geometry used in many applications as well as being the most studied bluff body in term of VIV. Available design guides provided by standard agencies and practitioners, the author review of current state of knowledge reveals that there are still gaps of knowledge on the single cylinder VIV and, especially, WIV on a downstream cylinder. The following include several research directions that are suggested for the present:

- Downstream cylinder oscillation: The majority of VIV studies concentrated on the response of the bluff body on its own (Blevins, 2001). In addition to the response amplitude, wake downstream of the cylinder was studied by analysing the fluid force exciting the downstream body, e.g. drag and lift forces. For the wake, the shedding pattern and frequency are areas of interest in numerical and measurement studies. For a fixed circular cylinder, detailed studies have been carried out; however, for the downstream cylinder, operating in the vortex shedding regime of the upstream cylinder, only a few investigation were undertaken, as reported in Govardhan and Wiliamson (2000). Furthermore, in the literature, for cylinders operating downstream, most experiments and simulations are only limited in one direction (crossflow), the interaction between inline and crossflow directions is still very limited.
- Multidegree of freedom vibration:

In the majority of previous experimental and numerical simulation investigation into VIV and WIV, measurements were obtained with an elastically mounted (spring-mass-damper) system with 1 degree of freedom (dof) in each direction, e.g. Guilmineau and Queutey (2004), Pan et al. (2007), Navrose and Mittal (2013). However, in these tests with risers, and in the field, WIV and VIV excite different modes simultaneously. Wake-induced vibrations can be large amplitude motions in the lowest modes, whilst at a higher frequency vortex shedding causes self-limited vibrations in higher modes. These mechanisms interact; hence, restricting the support system to 1 dof in each direction may be inappropriate. Thus, one important aim of this research is to study combined vortex- and wake-induced vibrations in simpler, two-dimensional conditions that for the first time will allow a bi-modal response in each direction. The current studies carry out numerical simulations for novel systems proposed by Chaplin and Batten (2014) including 2 dof system in 1 direction or 4 dof system in 2 direction (2 dof in each direction), to investigate the simultaneous wake- and vortex-induced vibration via numerical simulation.

- Computational fluid dynamics: With the continuing development of computational capacity, numerical solutions could provide data difficult to obtain experimentally. When experimental facilities are not adequate to deal with or measure certain flow parameters, use of numerical methods have significant advantages. According to Govardhan and Williamson (2006), the reason for VIV experiments being limited to relatively low Re is due to laboratory constraints. Moreover, the use of CFD is becoming a cost-effective solution for the industry, with reasonably good predictions. High-quality CFD studies are on the increase, e.g. Dong and Karniadakis (2005) used Direct Numerical Simulation (DNS) obtaining very good agreement with measurements. However, the computational resources currently available at the University of Southampton do not permit adequate resolution for fully 3D VIV with a large number of time steps e.g greater than 80 vortex-shedding cycles, while current simulations could require more than 100. For example, Large Eddy Simulation (LES) for a single cylinder required 108 processors for 120 hours of wall time for 20 vortex shedding cycles for one simulation (Kim et al., 2014) while DNS even requires more. Hence, in this research, 2D Reynolds Average Navier-Stokes (RANS) simulation methods will be used to study VIV and WIV on circular cylinders

1.2. Research objectives

In this research, the main aim is to investigate the dynamic behaviour of cylinders in an array, with particular reference to amplitude of vibration and possibility of clashing/collision of cylinder due to wake and vortex shedding using numerical simulation. The following approach is adopted to achieve the main aim:

- To study of the flow around a stationary circular cylinder and the flow around two stationary cylinders in a tandem arrangement. All investigations are carried out with unsteady, viscous and incompressible flow conditions.
- To select appropriate CFD solvers and examine the influence of turbulence modelling on this FSI problem.
- To understand influence of VIV on the dynamic motion of the cylinder. Investigations were carried out using a single degree of freedom (crossflow) and 1+1(2) dof (1 dof crossflow and 1 dof inline) systems.
- To simulate the behaviour of the downstream cylinder responding to WIV due to lack of understanding in the behaviour of a cylinder in the wake of an upstream cylinder, e.g. Zdravkovich (1987), Chaplin and Batten (2014). The downstream cylinder here is set to oscillate with 1 dof (crossflow), 1+1 dof (1 dof crossflow and 1 dof inline), 2 dof (crossflow only) and 4 dof (2 dof crossflow and 2 dof inline) as aforementioned.
- To investigate the behaviour of the downstream cylinder in staggered arrangement with multi-degree of freedom elastic mounted systems.
- The numerical predictions, for aforementioned cases, using 2D simulations are validated through comparisons with other numerical predictions and experimental results.
- Finally, the accuracy of CFD simulation and their contributions in enhancing the understanding of flow-induced vibrations are discussed.

1.3. Methodologies

To achieve the aforementioned objectives, the current work is split into various stages. Initially, the fixed cylinder, including single cylinder and two cylinders in tandem arrangement within range of Reynolds number (3900, 10000 and 20000) is carried out using various turbulence models. This is done as a pilot study for further application of CFD computations of more complex cases using advanced CFD techniques at the later stage of the work.

The next stage is simulating the single cylinder in VIV using unsteady model and moving dynamic mesh methods on the flow around a circular cylinder in (i) crossflow direction and (ii) both inline and crossflow directions. The good agreement with benchmarks results will provide confidence on the model and VIV methodologies. This is an important step towards the investigation of VIV and WIV when a stationary cylinder is placed upstream. Thus, at this stage, the turbulence models ($k -$

ω), moving dynamic mesh strategy and coupling method through user define function (UDF) are validated through comparison with other experimental results for Reynolds number up to 22000.

Based on the findings of the study of cylinder(s) in VIV, the adopted numerical simulation technique is applied to the flow around cylinder in tandem, with the downstream cylinder elastically mounted forming 1 dof and 1+1 dof systems. Initially, the 1 dof downstream cylinder in crossflow is validated against experimental data. Then, the interaction of 1+1 dof vibration (in both inline and crossflow direction) will be carried out when the downstream cylinder is exposed on the upstream cylinder's wake.

The system in the previous investigations will be further enhanced to research the motion of a downstream cylinder in more than 1 dof in each direction. In this particular case, the cylinder is elastically mounted with 2 dof in each direction, where another mass-spring-damping system was attached to the previous system. The system with two natural frequencies with an initial separation of 5 diameter (D) with Ur more than 130, based on low frequencies will be investigated. The study of combined vortex- and wake-induced vibrations, albeit in simpler two-dimensional flow conditions, allows for the first time the investigation of a bi-modal response in each direction.

Turbulence is the most challenging aspect of flow model and is treated numerically using RANS methods base on $k-\omega$ and $k-\varepsilon$ models. For the moving cylinder, the FIV phenomenon is solving by coupling the flow solution with the cylinder body motion. For the stationary and free oscillating cylinder, the following data are obtained:

- Flow variables: these includes flow force (lift and drag), their frequencies, time-averaged and fluctuating values. In addition, vortex shedding frequency, pressure distribution on cylinder surface and separation angle are reported.
- Reponses characteristics: These include amplitude of vibration, frequency ratio and frequency spectrum of the displacement and force signals for the cylinder in VIV. In addition, the trajectories motion of the downstream cylinder in VIV and WIV are also reported.

1.4. Structure of the thesis

This thesis is divided into ten chapters with contents as follows:

- Chapter 1 introduces the research project and provides an overview of the thesis. The objectives, research methodologies and structure of the report are also presented.
- Chapter 2 contains a comprehensive literature review including computational fluid dynamics and experimentation related to flow around a single cylinder, cylinders in

tandem, vibrations of a forced and free oscillating cylinder and studies on VIV and WIV of a downstream cylinder

- Chapter 3 describes the computational method, used to solve the FIV problems, namely ANSYS Fluent (ANSYS, 2011). The basic governing equations, turbulence modelling, numerical scheme for selected software, equations of motion used, grid requirements and mesh strategy for CFD modelling will be addressed.
- Chapter 4 contains investigations of flow around a stationary circular cylinder and two stationary cylinders in a tandem arrangement using RANS code. Reynolds numbers of 3,900, 10,000 for single cylinder and 22,000 for tandem arrangement cases are used. Comparisons between numerical and experimental results is used to validate the numerical methods. Turbulence model and boundary conditions setups are suggested for the next steps.
- Chapter 5 investigates the flow around a forced oscillating cylinder using $k - \omega$ and $k - \varepsilon$ turbulence model at Reynolds number 10,000. The study focuses on the discussion of the influence of the cylinder oscillation on the physical flow quantities, and the comparison between simulation results, current and others in literature, and experimental results at the same Reynolds numbers is undertaken.
- Chapter 6 investigates the VIV using a $k - \omega$ turbulence model. A single circular cylinder is simulated using 1 dof (crossflow) and 2 dof (inline + crossflow) elastically mounted system. CFD simulations were carried out on a single cylinder, treated as a rigid body, and results are validated with available benchmark data. The Reynolds number was kept the same, 10,000 and Ur ranges from 3 to 15. The focus is on the cylinder responses, the effect of mass-damping ratio on vibration characteristics and the influence of 2 dof representation compared with 1 dof system.
- Chapter 7 studies Vortex- and Wake- Induced Vibration in the downstream cylinder when there is a tandem arrangement. Similar to the previous chapter, the downstream cylinder is elastically mounted using in 1 dof (crossflow) and 1+1 dof (inline and crossflow). Ur varies from 2 to 14. The effect of 1+1 dof on the downstream cylinder and WIV, due to the vortices shed by the upstream cylinder, is discussed including drag, lift, amplitude of motion and motion trajectories.
- Chapter 8 investigates the behaviour of multi-degree of freedom system representation for the downstream cylinder. A range of Ur similar to chapter 7, are used. Initially, simulations with 2 dof (crossflow only) are undertaken. Subsequently, a 4 dof system (2 dof inline + 2 dof crossflow) is used and provides a discussion on the influences of 4 dof motion in the cylinder.

- Chapter 9 studies the case with a staggered arrangement. The study focuses on the dynamics responses of the downstream cylinder and comparison between 2 dof and 4 dof vibration, between a staggered and tandem arrangement.
- Chapter 10 provides the main findings and contributions from the current work as well as suggestions for future research.

Chapter 2 : Literature review

Research on flow-induced vibration is cross-disciplinary. Firstly, flow physics for a stationary bluff body (in this particular case, a circular cylinder) needs to be understood. In addition, bluff body dynamics and its vibration response have to be analysed with the flow around it. This chapter provides a brief overview on selected fundamentals, including VIV and WIV of a downstream cylinder in a tandem arrangement. The chapter will start with stationary cylinder's flow physics including a single cylinder and cylinder in tandem and then moves on FIV aspects.

2.1. Basic concept

2.1.1. Regime of flow

One of the key dimensionless parameters associated with the flow around a smooth circular cylinder is the Reynolds numbers (Re). Vortex shedding from a smooth, circular cylinder in a steady subsonic flow is a function of Reynolds number which is defined as:

$$Re = \frac{UD}{\nu} \tag{2.1}$$

where U is the flow velocity, D is cylinder diameter and ν is the kinematic viscosity of fluid defined as

$$\nu = \frac{\mu}{\rho} \tag{2.2}$$

where μ is dynamic viscosity, ρ is fluid density

The characteristics of the flow around a smooth cylinder change with Reynolds number. Zdravkovich (1997) described a succession of transitions from laminar to turbulent in various regions include: wake transition (TrW), shear layer transition (TrSL) and boundary layer transition (TrBL). At very low Reynolds number ($Re < 5$), no separation occurs. Larger values of Reynolds number creates separation and a wake, which can be called as vortices. From approximately a Reynolds number of 40, alternating vortices are shed as fluid layers separate at two opposite sides of the cylinder. As the Re increases, the transition first occurs in the wake region and turbulence develops along the wake downstream of the cylinder. This occurs when Re is between 180 – 400. The next transition occurs in the shear layer. The transition region moves forward towards the separation point as Re increases. The TrSL regime occurs in Re ranges from 350 up 2x10^5. The next transitional region is the boundary layer, which gains most of the attention in present day research. In this regime, the Re effect on the boundary layer can be classified into three categories. When the Reynolds number is smaller than 2×10^5, it is called the subcritical range. In this range of Reynolds numbers, the attached boundary layer is laminar, the separated layers are in the early stages of transition, and the wake is fully turbulent. The Reynolds number range from 2×10^5 to 3.5×10^6 is called the critical range. In this range, the boundary layer starts as laminar and gradually separates with turbulent reattachment, a separation bubble, and finally turbulent boundary layer separation. When the Reynolds number is greater than 3.5×10^6, it is called the supercritical region (Blevins, 2001). The boundary layer starts as laminar, then transitions to turbulent before the separation point. The regimes of fluid flow across a circular cylinder and its transition with Reynolds number is summarised in Figure 2.1 (Lienhard, 1966).

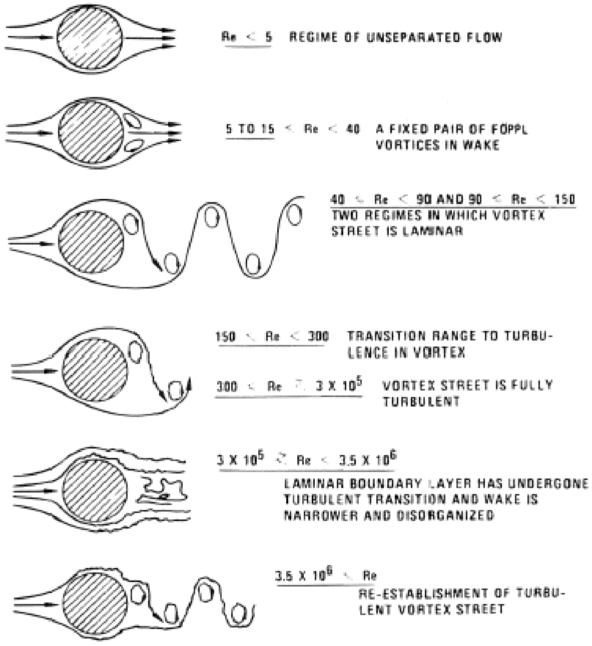

Figure 2.1. Regimes of fluid flow across smooth circular cylinders (Lienhard, 1966)

2.1.2. Vortex shedding

Vortex shedding is a phenomenon which is created when a fluid such as air or water past a bluff body at certain velocities, depending on the size and shape of the body (Scanlan and Billah, 1991). In this flow, vortices are created downstream and detach periodically from either side of the body. The dimensionless number *Strouhal number*, St, is commonly used as a measure of the predominant shedding frequency, f_s and is defined as

$$St = \frac{f_s D}{U} \tag{2.3}$$

where f_s is vortex shedding frequency, U is free stream velocity and D is cylinder diameter. It depends mainly on the Re number and shows small dependence on surface roughness, except the transition region ($3x10^5 < Re < 3x10^6$), as seen in Figure 2.2.

Vortex shedding also occurs from multiple cylinders and from a cylinder near a surface as shown in studies by Vickery (1962), Bearman (1978) and Kiya (1980) .When the flow is past a cylinder in an array, the crossflow vibration has a large effect on vortex shedding. The large amplitude cylinder vibration can change the vortex shedding frequency by ±40% from the stationary cylinder shedding frequency (Feng 1968).

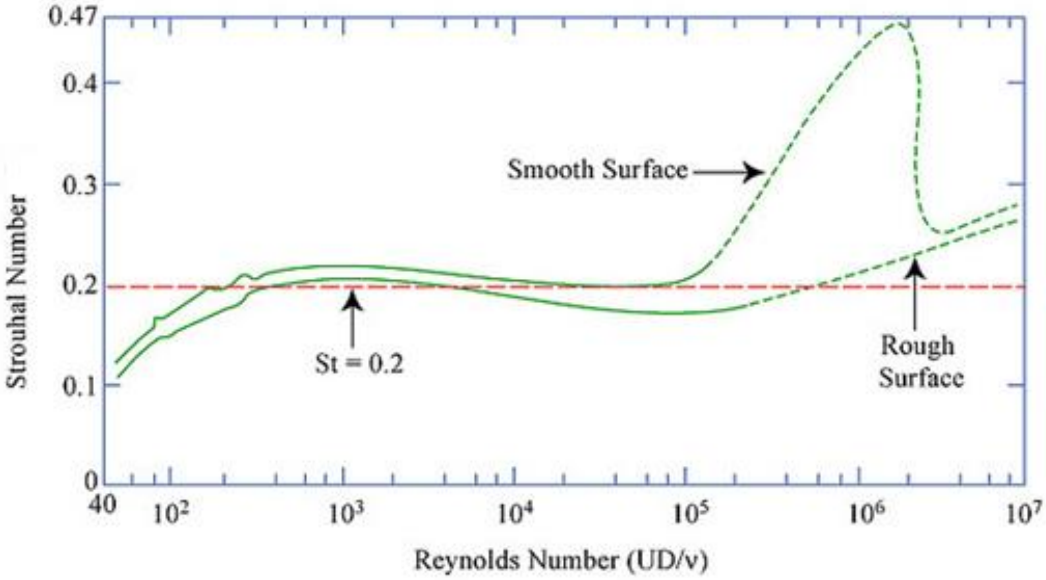

Figure 2.2. Relationship between Strouhal number and Reynolds number for circular cylinder (Techet, 2005). Data from Lienhard (1966), Achenbach and Heinecke (1981), Roshko (1955)

2.1.3. Drag, lift and pressure coefficients

When considering the vibration of a body, force coefficients are very important in investigating, the drag, lift and pressure distribution coefficient. The drag force on the cylinder acts in the same direction as the flow acting on the cylinder, whist lift force on the cylinder is at right angles to the flow (Figure 2.3). Drag and lift coefficient depend on shape and orientation of a body as well as the Reynold numbers.

Drag coefficient, C_d is defined as:

$$C_d = \frac{F_d}{0.5\rho U^2 A} \tag{2.4}$$

Lift coefficient, C_l is similarly defined as:

$$C_l = \frac{F_l}{0.5\rho U^2 A} \qquad (2.5)$$

where, A is the projected area in the flow direction, F_d is drag force, F_l is lift force per unit length

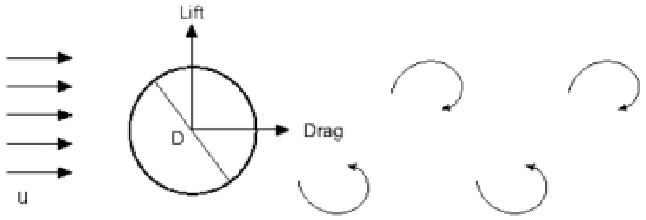

Figure 2.3. Forces acting around circular cylinder

Theoretically, the drag force is oscillating about a mean at twice the frequency of the lift force for the flow past a circular cylinder. If these forces are decomposed into mean and oscillatory components, it can be seen that, for flow with laminar boundary layer (Re < 10^5), the mean drag coefficient, $\overline{C_d}$, has a value around 1, while the mean lift coefficient is zero. In contrast, the fluctuating lift coefficient, C_l', is greater than the oscillating drag coefficient. So that, the cross-flow vibration is more significant than the in-line vibration in a single cylinder VIV. When simulating the flow past a cylinder, it is important that turbulence models simulate force coefficients correctly.

Apart from forces, the pressure coefficient, C_p is important to consider and is defined as:

$$C_p = \frac{p_c - p}{\frac{1}{2}\rho U^2} \qquad (2.6)$$

where p_c is pressure at the cylinder surface and p is free stream static pressure and $\rho U^2/2$ is the stagnation pressure. In numerical simulation, accurate prediction of C_p distribution around a cylinder and separation is a good test of the turbulence modelling.

2.2. Vortex induced vibration

In fluid dynamics, VIV can be defined as a motion induced on body in a crossflow by periodical oscillation of the wake (Bearman, 1984). VIV is commonly excited by three-dimensional separated flow and influenced by a large number of system parameters including lift, drag, mass ratio, structure stiffness, and damping coefficient. The body of literature related to VIV is massive and covers: experimental and numerical investigation methods; single degree or multi-degree of freedom motion; flexible or rigid body motion; and in air, water or other fluids.

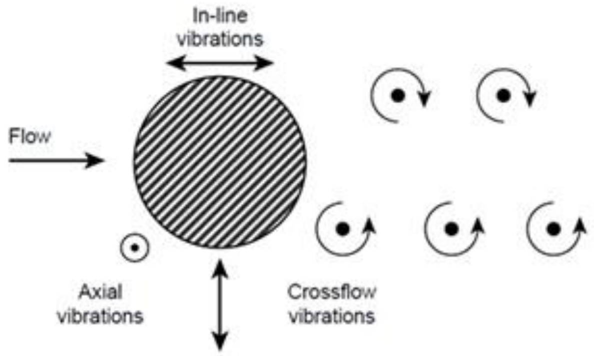

Figure 2.4. Vibration of a cylinder submitted to vortex shedding (Khalak and Williamson, 1997)

The vibration in VIV can be classified as inline vibrations and crossflow vibrations (or transverse vibrations), as shown in Figure 2.4. Studies of Naudascher (1987) and Vandiver (1987) show that an inline vibration is an order of magnitude smaller than crossflow vibrations.

2.2.1. Reduced velocity and mass ratio

The structural parameters are also important in VIV. The simplest case of a rigid cylinder mounted on an elastic base with a negligible structure damping can be modelled as a mass-spring system. Two most influential factors are mass ratio determined from

$$m^* = \frac{4M}{\rho \pi D^2 L} \qquad (2.7)$$

where M is the total mass of the oscillating system and L is the submerged length of the cylinder; and reduced velocity, Ur as

$$Ur = \frac{U}{f_n D} \qquad (2.8)$$

where f_n is natural frequency of the structure.

Mass ratio and reduced velocity are often used as the standard criteria for almost VIV experiments and numerical simulations to determine the dynamic behaviour of a structure in VIV, in addition to system properties, e.g. stiffness, damping ratio. The amplitude ratio from Feng (1968) and Khalak and Williamson (1997) are compared in Figure 2.5 with the effects of mass ratio. Feng (1968) conducted the experiments in air with high mass ratio, m^* = 248. The amplitude curve shows initial and lower branches with a mode change in between two branches. The experiments carried out by Khalak and Williamson (1997) are with much lower mass ratio m^* = 2.4. There are three different branches in amplitude curve including initial, upper and lower branches. In Figure 2.5 and 2.6, the upper branch is present and has an amplitude value that is about 40% greater than the maximum amplitude measured by Feng. In high mass ratio, VIV can be observed in limited range of reduced velocity from 4 <Ur < 8, while in low mass ratio, the range is wider, from 3< Ur <13.

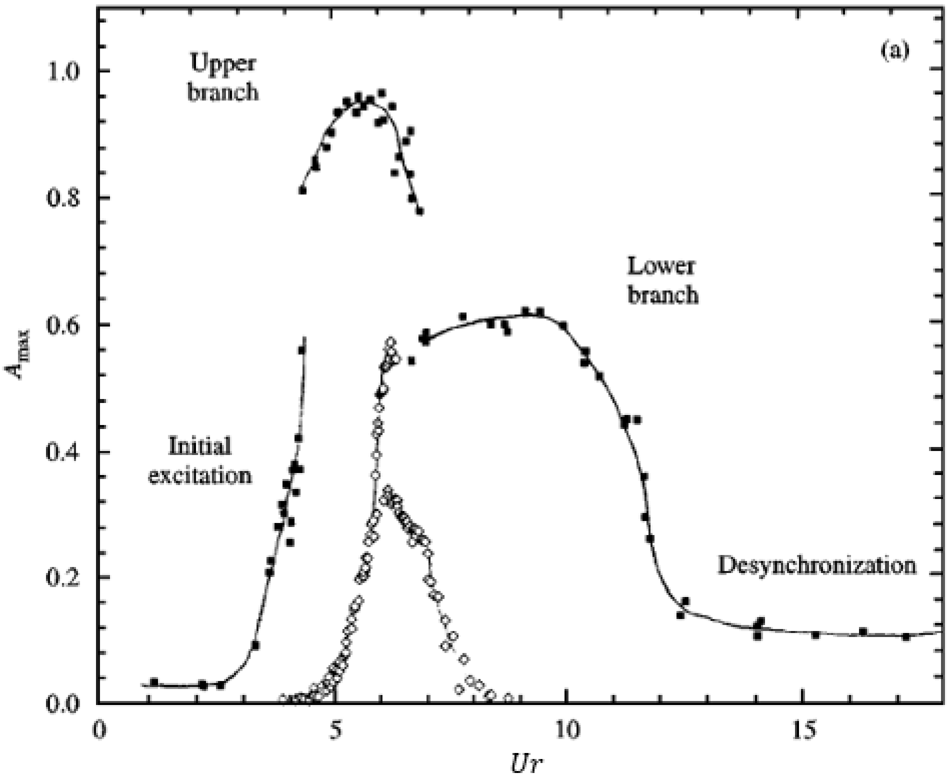

Figure 2.5. Response amplitude and frequency for low mass and damping. Compare the amplitude response between the low mass ratio $m*$ = 2.4 (■)(Khalak and Williamson, 1997), with of Feng (◇) (1968) $m*$ = 248

2.2.2. Frequencies

The frequency is an another important factor in VIV. In Figure 2.6, Govardhan and Williamson (2000) present the frequency ratio as a function of reduced velocity for three different mass ratios. For a mass ratio of 10.3, it is shown that within this same reduced velocity range, the cylinder response frequency (f_o) is close to the natural frequency of the structure (f_n), where frequency ratio $f^* = f_o/f_n$ is close to one. Measurements of the velocity at arbitrary points in the wake showed that the vortices are shed with the frequency of oscillation of the cylinder, not with the frequency they would be shed if the cylinder was fixed. Therefore, it is said that, in this reduced velocity range, the vortex shedding is locked to or synchronised with the cylinder vibration, so we refer to this range as “locked-in” or “synchronisation” range. The existence of a well-defined synchronisation range at which the cylinder vibrates with the highest amplitudes indicates that VIV is a type of resonant response.

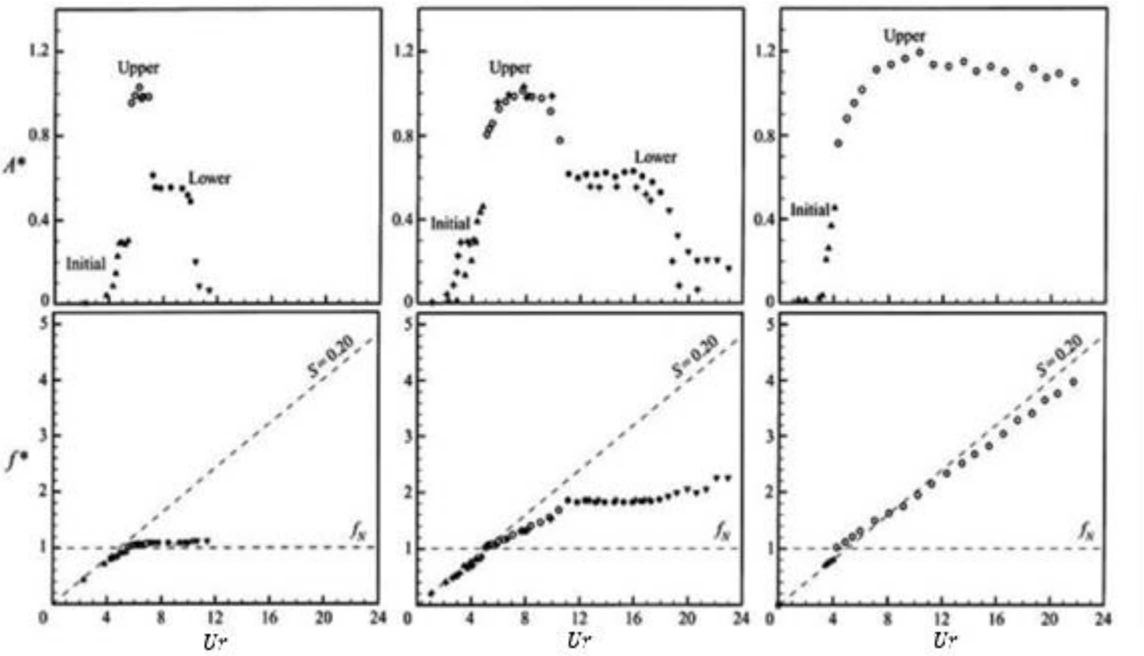

Figure 2.6. Amplitude and frequency ratio dependency on mass ratio (Reproduced from Govardhan and Williamson, 2000)

The effects of mass ratio on the oscillation frequency are summarised by Govardhan and Williamson (2000), as seen in Figure 2.7. Changes in mass ratio effect the frequency ratio. When the mass ratio >>1, locked-in occur when f^* = 1 or is very close to. However, in very low mass ratio case, e.g $m^* \leq 1.2$, the locked in region occurs with higher frequency ratio. And with m^* < 0.54, only upper batch could be recognized without recognition of the desynchronisation area.

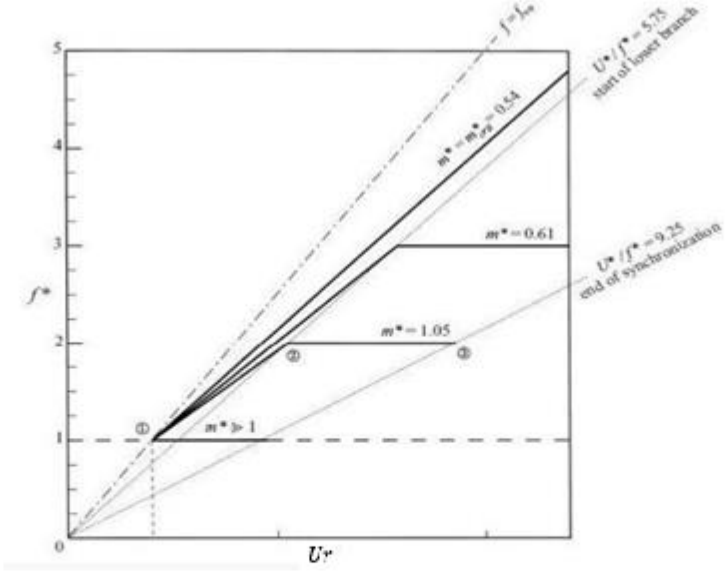

Figure 2.7. Schematic plot of frequency dependence on mass ratio (Reproduced from Govardhan and Williamson 2000)

2.2.3. Vortex patterns

Vortex pattern is an important aspect of VIV. The periodic vortex wake pattern for a cylinder comprise single vortices (S) and vortex pair (P) giving pattern such as S, P, 2S, 2P, S+P and 2P+2S model. The types of vortex patterns depend on the non-dimensional amplitude (A* = A/D) and wave length ratio $\lambda^* = \lambda$ (/D) or reduced velocity, as seen in Figure 2.8a. Williamson and Jauvtis (2004) discovered a new triplet vortices being formed in each half cycle, defined as 2T when A* is greater than 1.5. Different vortex patterns have different impacts in the structure, contribute to amplitude of motion of cylinder in VIV. More detailed representation of each vortex-wake pattern is shown in Figure 2.8(b). The transition from one mode of vortex formation to another happens at the critical curve.

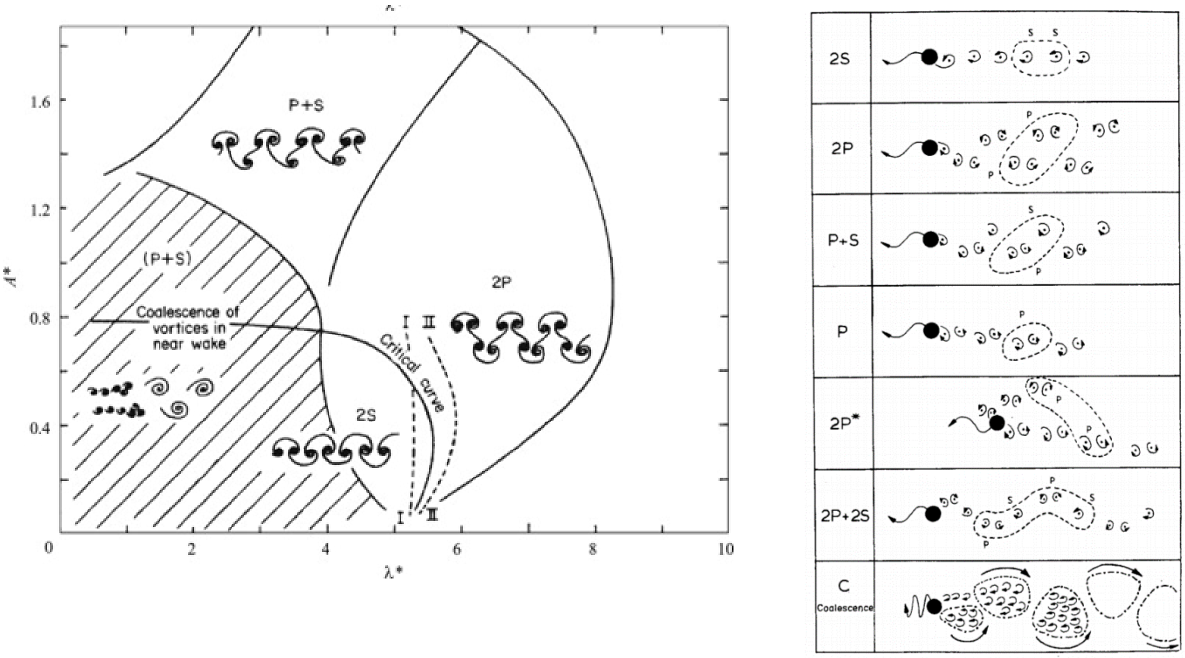

Figure 2.8. (a) Map of vortex synchronization patterns, (b) details of vortex wake patterns (Williamson and Roshko, 1988)

2.3. Cylinder flows

One of the main targets of this research is flow around cylinders. A good understanding the flow around cylinders is important to research FIV. Although the geometry of the body is simple, the resulting flow is one of the most challenging problems that is encountered in many different engineering fields.

2.3.1. Flow around a single cylinder

One of the most challenging for cylinder flow is Reynolds number. Most numerical simulations are implemented at low subcritical Reynolds number range because at this range the attached boundary layer is laminar and relatively thick and can be resolved by the grids. For example, in the high subcritical or supercritical Reynolds number, the attached turbulent boundary layer becomes much thinner than in the low Reynolds number cases, nearly six times thinner for Re=1.4×10^5 than Re=3.9×10^3 (Shih Chieh Lo et al., 2005). Therefore, the computer resources and simulation time requirement is inversely proportional to the Reynolds number. As far as the present research concerned, studies for static and FIV cylinder flow are undertaken for fully turbulent wake in sub-critical regime.

Accurate prediction of the transition point and the turbulent wake decides the accuracy of the simulation. To solve this problem, some valid approach of turbulent treatment is needed such as Direct Numerical Simulation (DNS), Large Eddy Simulation (LES) or RANS. The simulation using DNS (Dong and Karniadakis, 2005) at Reynolds number 10,000 and LES (Stephen et al, 2011) at Reynolds number 3900, 10,000 and 20,000, Catalano et al. (2003) at high Reynolds number > $5x10^5$ show very good agreement in terms of lift, drag, pressure distribution with experiment. While DNS is ideally designed to resolve the entire turbulence spectrum, LES is also designed to solve large flow scales down to a cut (set up by grid filter), beyond which flow scales are modelled. Achieving a satisfactory simulation of the flow using these methods is very expensive in term of computational cost, as noted in Versteeg and Malalasekera (1995) and Pope (2000).

Although cheaper in term of computational code, the RANS method requires a special transition model with empirical relations for onset and length of the transition zone. A common practice when using RANS for a Re above the subcritical regime is to assume a fully turbulent condition. The position of the transition point and the flow status in the boundary layer can have a large influence on the lift and drag coefficient. When CFD is used to simulate the turbulence with models based on transport equations, at least three different strategies can be used to predict or account for boundary layer transition (Shur et al., 2005). Some methods use specific boundary conditions or initial conditions to achieve this, while some of the others need to modify the model. As the flow develops over the body, it will be effectively laminar where the eddy viscosity is zero, and effectively turbulent and determined by the governing turbulence equations in the regions where it is nonzero. The appropriate initial inputs will decide the accuracy of the output results. Numerical simulations around a circular cylinder at critical Reynolds number was carried out by (Catalano et al., 2003) using RANS solvers. The eddy viscosity is obtained using standard $k-\varepsilon$ turbulent model in RANS code. The pressure distribution and skin friction was compared with established experimental data at three Reynolds numbers: 0.5x10^6, 10^6 and 2x10^6. The mean pressure distribution and drag coefficient are predicted well at Re = 0.5x10^6 and 10^6. However all models give inaccurate results at higher Reynolds number. Zhao et al. (2007), Elmiligui et al. (2010) show a good agreement using RANS turbulent model in subcritical Reynolds number. Baranyi et al. (2009) compared the simulation result using ANSYS Fluent for heat and unheated cylinders in terms of $St - Re$ relationship at low Re regime to validate his experiemental result. A reasonably good agreement can be observed between experimental and numerical results.

In general, different numerical methods had been used for flow around fixed cylinders. All RANS, LES or DNS prediction showed good agreement with experiments. Although less accurate when compared with LES or DNS, RANS is still a popular method as it is economical in terms of computation cost, robustness and reasonable accuracy.

2.3.2. An elastically mounted single cylinder.

An important approach for understanding of VIV involves testing a cylinder undergoing forced or controlled sinusoidal oscillation in free stream. Sarpkaya (1978), Gopalkrishnan (1993), Carberry et al. (2005) amongst others, measured the forces on cylinders undergoing harmonic motion for a range of frequencies. The cylinder was oscillated with fixed amplitude ratio A/D from 0.3 to 1.2 (where A is amplitude of displacement) with different frequencies. A general trend can be observed with the change from low to high frequency with a change in the force coefficients and the mode of vortex formation. A “jump” can be detected during this transition.

Numerical simulations have been carried out for a forced oscillating cylinder in both 2D and 3D simulation used different methods. Dong and Karniadakis (2005) used 3D DNS at Re 10,000 to investigate flow around a fixed and forced oscillating cylinder. The numerical simulation captured the lift, drag coefficient and lift phase angle reasonably well. However, the simulation was limited to only 4 frequencies and low -, high – frequencies data were ignored. Placzek et al. (2009) carried out numerical simulation in a cross-flow at low Re = 100 in both forced and free oscillation using a 2D RANS code. Changes in force coefficients and vortex shedding mode were captured very well for this low Reynolds number. Tutar and Holdo (2000) conducted a LES (2D and 3D) investigation of flow past a forced oscillating cylinder at Re = 24000 using a Smagorinsky model and a damping term within a cylindrical boundary layer. While the Strouhal number is in fair agreement with experimental data, a large disagreement in pressure coefficient is observed. Although, 3D simulations show some advantages compare with 2D in low Re, however, a 2D RANS simulation provides some good results when applied to high Reynolds number.

Sarpkaya (2004), Williamson and Govardhan (2004) provide a comprehensive overview of the field of VIV and discuss the status quo, current progress and unresolved problems. Many investigators focused on the flow. The amplitude ratio, frequency ratio, mass ratio and wake modes are typical characteristic parameters for the free vibration of a cylinder. Feng (1968) conducted free oscillating cylinder motion in the transverse direction with a mass damping ratio of 248. The peak amplitude of motion was A/D 0.6 when a reduced velocity is approximately 6 (Figure 2.5). The relatively lighter body from experiments of Khalak and Williamson (1997), Govardhan and Wiliamson (2000) show a much higher peak amplitude. The low mass ratio type of response is characterized not only in initial branch and lower branch, but also by the new appearance of a much higher “upper response branch” (Figure 2.6). The three branches of response are associated with different mode of vortex shedding. The 2S mode of vortex shedding is observed on the initial branch, 2P mode at lower branch and modified 2S mode is observed on the upper branch, one of vortices is weaker than the other in the vortex pair in this mode (Navrose and Mittal, 2013).

Many numerical studies had been carried out for the free oscillating cylinder case. Most of the computational studies investigated free vibration in low Reynolds number and low mass-ratio. A lot of studies with different mathematical models, including RANS (Guilmineau and Queutey, 2004), (Placzek et al., 2009), Large Eddy Simulation (Tutar and Holdo, 2000), (Al-Jamal and Dalton, 2004), Direct Numerical Simulation (Dong and Karniadakis, 2005) or DES (Saltara et al., 2011) can be found in literature for a large range of Reynolds number. To reproduce experiments with a low mass damping system is an important objective for this current study.

2.3.3. Interference between two-fixed cylinders.

Numerous researches using experiments have been performed by Bearman and Wadcock (1973), King and Johns (1976), Igarashi (1984), Zhang and Melbourne (1992), Sun et al. (1992). Numerical investigation for circular cylinders in tandem and side by side have been also reported. According to Zdravkovich (1987), the interference depends strongly on orientation, spacing and number of cylinders in the cluster. Two vortex streets are formed in the downstream of two cylinders when the distance between cylinder L/D > 3.8. Due to the spacing between cylinders, for L/D < 6, three flow regimes can be defined. For 1 < L/D < 1.2-1.8, the free shears layers separating from the upstream cylinder do not reattach on the downstream cylinder and the vortex street behind the latter is formed by the shear layer from the former. When 1.2-1.8 < L/D < 3.4-3.8, the separated flow from the upstream cylinder reattaches on the downstream cylinder and the vortex stream is formed behind the downstream cylinder. For 3.4 - 3.8 < L/D < 6.0, the separated shear layer from the upstream cylinder form up and create the vortices in front of the downstream cylinder. The spacing this occurs at is called critical spacing (Zdravkovich and Pridden, 1977). The upper boundary at L/D was proposed by Ohya et al. (1988). For L/D > 6.0, the new vortex street is formed behind the downstream cylinder and independently shed from the downstream cylinder with a lower vortex shedding frequency than that for the upstream cylinder, see Ohya et al. (1988) and Okajima and Sugitani (1984). Ljungkrona et al. (1991) investigated the flow around subcritical Reynolds number Re = 2.0 x 10^4, at three difference turbulent intensities of the approach cross-flow (0.1, 1.4 and 3.2%). The spacing of the cylinders was in the range 1.25 < L/D < 5.0. The results indicated that the effect of increased free-stream turbulent intensity on the distance of the tube spacing. The critical spacing between the cylinders was found to decrease as the turbulent intensity was increased. An overall increase in root mean square (rms) lift coefficient was also found as the turbulence intensity was increased.

Numerical simulations have been carried out on flow past two fixed cylinders in tandem at the subcritical from 1000 to 22,000. The 3D simulation using LES was carried out by Kitagawa and Ohta (2008) and 2D using different RANS $k - \varepsilon$ models (Dehkordi et al., 2011). The gaps between the cylinders were changed from 2D to 4D and the interference effect and vortex interaction between two cylinders was analysed. The results showed good agreement with experimental data at the same Reynolds number in term of force coefficients. Two dimensional FEM also used to simulate tandem and side by side arrangement at Re 100, 200 and 1000 by Meneghini et al. (2001), Jester and Kallinderis (2003). The numerical studies of flow past two side-by-side circulars cylinder at the distance 1 < B/D < 5, Re = 5800 (Shao and Zhang, 2007) using commercial code ANSYS Fluent with LES turbulence model. Both flow field and temperature field are investigated and the calculated results showed very good agreement with the experimental results.

In additional to two cylinders in tandem and side by side, the effect of interference between circular cylinders in cross flow was classified with four categorization of cluster arrangement: two pipes, three-pipe clusters, regular square multiple cluster and irregular and triangular multi-pipe clusters (Figure 2.9). The interference depends strongly on orientation, spacing and number of pipes in the cluster. Flow around two cylinders in tandem arrangement is the most complete which was researched in various arrangements. However, research mostly focuses on behaviour of cylinder in subcritical state of flow and Zdravkovich stated that: “A particularly limited data base is available for supercritical and post critical states of flow”. Bearman (1984) also supported the Zdravkovich’s statement about lack of data at higher Reynolds number.

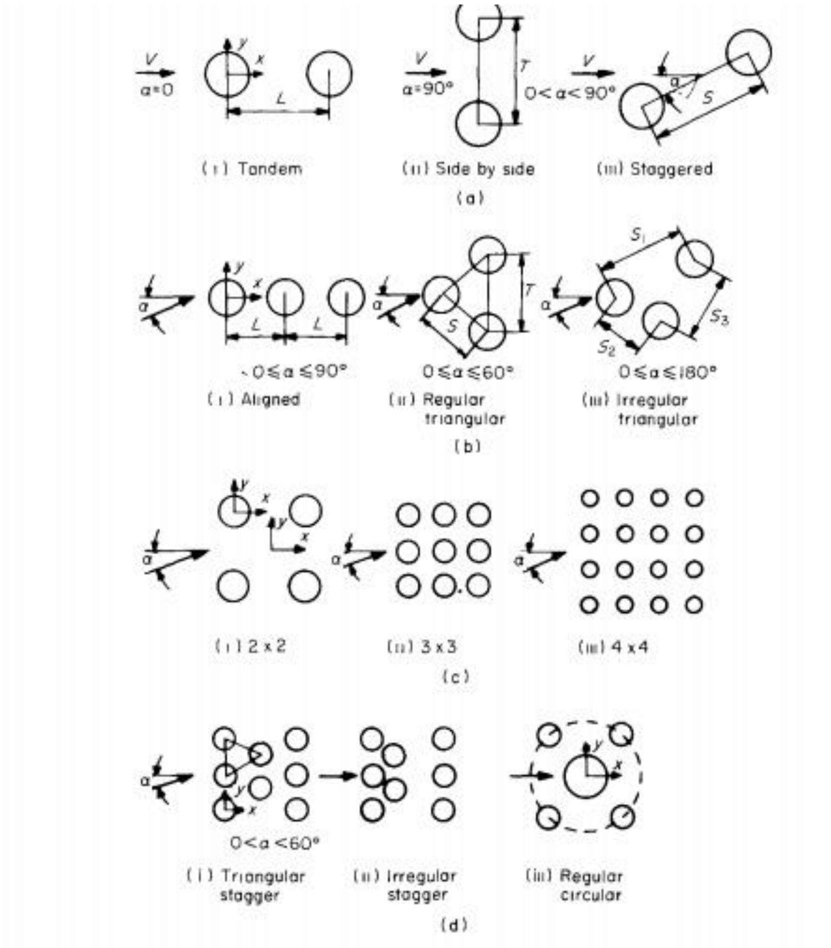

Figure 2.9. Classification of pipe clusters: (a) for two pipes; (b) for three-pipe clusters; (c) for regular square multi-pipe clusters; (d) for irregular and triangular multi-pipe clusters. (Zdravkovich, 1987)

2.3.4. Elastic mounted cylinders in a tandem arrangement

In case of one cylinder vibrating in the wake of a fixed one, the interaction between vortex and wake induced vibration had also been researched in experimental and numerical investigations.

Research of VIV of elastically mounted rigid cylinders in a tandem arrangement, which focus on cylinders free to respond in the in-line and crossflow directions and the resulting interference between two cylinders was reviewed by Moriya et al. (1983). Experiment of Zdravkovich (1985) found a strong relationship between location of two cylinder and VIV. In VIV, the range of locked-in regime limited at reduced velocity of 15 when WIV appears at much higher reduced velocity with higher amplitude of motion Zdravkovich and Medeiros (1991), Assi et al. (2010), Chaplin and Batten (2014). Experiments of Huera-Huarte and Gharib (2011a) on two cylinders in side by side and a tandem arrangement showed the interference is very weak if gap-to-gap exceeded 3.5 times the cylinder diameter. At the gap greater than 4D, there is very minor influence to the upstream cylinder while the appearance of vortices between two cylinders increases the amplitude of motion of the downstream one. Germain et al. (2006) carried out experiments with dual riser interaction in uniform and steady current to predict the dynamic of downstream cylinder. The applied Re number range was from $5.5x10^3$ to $5.5x10^4$. Both in-line and cross-flow responses were studied and observations demonstrated that wake effects can be relatively strong. When risers end up in close proximity due to wake induced oscillations, collisions between cylinders can be observed at reduced velocity greater than 21 and initial spacing between cylinder equal to 5D.

The numerical study by Mittal and Kurma (2004) on VIV and WIV of two cylinders in a tandem arrangement showed the upstream cylinder is acting like a single cylinder while the downstream cylinder motion is really complicated. The influence of freestream turbulence for two cylinders in side by side arrangement was investigated by Wang et al. (2008). The results showed that the freestream turbulence increase vortex induced force, that causing the higher amplitude of motion of the cylinder. Zhao and Cheng (2012) studied VIV and WIV of four circular cylinders in square configuration in steady flow numerically. It was found that the angle of incidence affected not only the vibration amplitude but also the locked-in region. Derakhshandeh et al. (2014) investigated flow charateristics and VIV respones of downstream cylinder using Scale Adaptive Simulation (SAS) and Shear Stress Transport (SST) $k-\omega$ turbulent model. The results indicated that, SAS were more accurate compared to SST although both model show reasonably good agreement. The $k-\omega$ models also used by (Cui et al., 2014) Vortex-induced vibration (VIV) of two elastically coupled circular cylinders in side-by-side arrangement where two similar cylinder allow to vibrate in crossflow direction is 2 dof system. The data showed that, the response frequencies of both cylinders increased with an increase in the reduced velocity until they are close to the sum of the two natural frequencies.

2.3.5. Laboratory measurements and full-scale measurement for VIV on risers.

In VIV research on risers, both numerical methods and laboratory measurements can be used. In general, empirical models were more successful at predicting cross-flow displacements and curvature than current coded-base on CFD. Overall ratio between predictions and measurement of cross-flow displacements were around 95% and 75% respectively (Chaplin et al., 2005)

Chaplin et al. (2005) carried out blind predictions of the laboratory measurement of VIV of a model riser subject to a stepped current, based on 11 different numerical models, which including CFD-based codes and empirical models based on an empirical understanding of VIV in a two dimensional condition. The prediction of cross-flow displacements from empirically based codes (VIVA, VIVANA, VIcoMo, SHEAR7 and ABVIV) and Wake oscillator codes were very close to measurement (all between 85% and 105% of corresponding measurement). However, results of CFD-based codes

(Norsk Hydro, USP, DeepFlow and VIVIC) were of smaller cross-flow displacements, with ratios of predictions to measurements in range 65-90% and in-line dynamics displacements have ratios between 135% to 175% compared with measurement.

Fujarra (2007) investigated Vortex induced oscillations on a vertical inclined (0-45^0) cylinder which was free to oscillate in the cross-flow direction. The results for amplitude, drag and lift are compatible with decomposition of the flow into the directional normal to the axis of the cylinder. However, only vertical cylinders are in agreement with other measurements. (Lee et al. (2006)) provided VIV test results for two faired flexible cylinder in tandem for three lateral spacing (5, 10, and 20 cylinder diameters), which were subjected to uniform flows. The VIV responses and motions of both cylinders are presented with conclusion that fairing is effective approach to reduce the influences of VIV.

In addition to laboratory experiments, to supply comparative data for numerical methods, researchers all over the word, despite its high expenses and difficulties have carried out a number of full-scale measurements. Srivilairit and Manuel (2007) analysed full scale field measurement of riser acceleration and current velocity from the riser, located in 1000m of water depth and used a numerical technique known as Proper Orthogonal Decomposition (POD) to identify energetic current profiles and VIV response of the riser for in line and cross flow motions.

Vandiver et al. (2005) carried out the field testing of a long, flexible, model riser at high mode number and using sensor to capture the high vibration modes and to predict VIV for a lake Seneca condition profile. Four factors affecting the location of the power-in region were identified: angle of pipe relative to vertical, the current profile, the current direction gradient and the end effects at high mode number. An experiment on the VIV response of a long cylinder with strakes was carried out by Jaiswal and Vandiver (2007) in which the current profile varying from near uniform to highly shear. The results were used to compare with modelling result using mode superposition and an appropriate Green function.

2.4. Reduction of Vortex induced vibration

Due to the harmful structural effects of VIV, reducing VIV is an important question in engineering and research. The amplitude of resonant VIV and the associated magnification of steady drag can be remarkably reduced by the following methods.

1. Avoid resonance

Keep reduced velocity, $\frac{\mathrm{U}}{f_n D} < 1$, so that in line and crossflow resonances are avoided. This method is achieved by stiffening the structure, which is often used for small structure (Blevins 2001).

2. Streamline cross section

   This method is applied to reduce the separation from the structure, so the vortex shedding is minimised and drag will be reduced. Streamlining the downstream side of a structure can reduce the effect of VIV around cylinder (see Figure 2.10d).

3. Add a vortex suppression device

   The vortex induced vibration can greatly reduce by adding a vortex suppression device. Some devices with proven effectiveness are showing in Figure 2.10

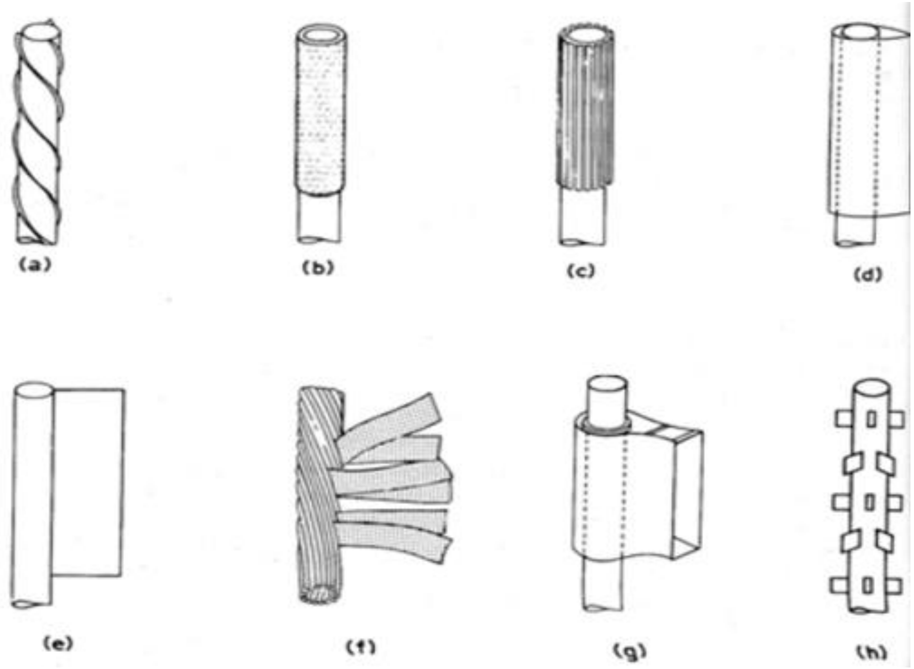

Figure 2.10: Add-on devices for suppression of VIV of cylinder: (a) helical strake; (b) shroud; (c) axial slats; (d) streamlined fairing; (e) splitter; (f) ribboned cable; (g)pivoted guiding vane; (h) spoiler plates (Blevins, 2001)

These devices were developed through ad hoc experiments; they act by disrupting or preventing the formation of an organized 2D vortex street. The cylinder with strakes is the most popular solution for VIV control which is widely applied in reducing the effect of VIV to marine risers, according to Wilson and Tinsley (1989), Pinto et al. (2006).

2.5. How current work fits

In the literature, many aspects of FIV had been carried out for a single cylinder and a downstream cylinder. The subcritical Re range was focused on due to a limitation with the computational resources. So that, in the current research due to the availability of validation data, the study will focus on the subcritical Re range, smaller than 35,000.

For a single cylinder, the literature review showed that the method for numerical prediction with 2 dof could be enhanced. So that, the present research, the numerical method using 2D RANS was developed to simulate the dynamics responses of a single cylinder with 2 dof to compare with experimental results. The Reynolds number was focused in the subcritical range to explore some more understanding the behaviour of risers in Vietnam sea operating condition.

For a downstream cylinder, there is still a gap of knowledge on the numerical simulation for a free vibrating downstream cylinder. Although there are some experimental data for a downstream cylinder which allow to move in 2 directions, however, numerical simulation method to predict this problem is still missing. So in this thesis, a free vibrating downstream cylinder is simulated to enhance the capability of applying numerical analysis to predict cylinder VIV at the subcritical Reynolds number 22,000.

In addition, in most cases, the cylinder is restricted to elastic support with 1 dof (crossflow) or 2 dof (crossflow and inline). However, Wake induced motion can have large amplitudes of motion in the lowest modes while vortex shedding frequency is at higher mode, so to restrict support system to one or two degree of freedom may be not appropriate (Chaplin and Batten, 2014). In this study, a 2 dof elastic system in crossflow direction will be created in steady flow. The flow is simulated using Reynolds-Averaged Navier-Stokes (RANS) equation using finite volume methods. The displacements of the cylinder are calculated using equation of motion of the system for a wide range of reduced velocities. The response frequency, amplitude of motion and flow characteristics will be considered.

Chapter 3 : Computational methods

This chapter introduces the background theories of CFD and existing numerical techniques available for solving fluid flow problems for the intended FIV research. It includes fundamental equations used in CFD, available mathematical models, and their applications.

The application of CFD began in the 1960's, when the aerospace industry integrated CFD techniques into the design, R&D and manufacturing of aircraft and jet engines (Fergizer and Peric, 1997). CFD codes are being accepted as design tools by many industrial users. Today, many industries, for example, ship industry, power plant, machinery, chemical process, environmental engineering, and so on, use CFD code as one of the crucial design tools. CFD offers no capacity limit, no scale limit and cost efficiency. Nowadays, CFD can be used to model experiments in a towing tank with up to 3.2 billion computational cells (Nishikawa et al., 2013).

3.1. Governing equations

In obtaining the basic equations of fluid flow, it is necessary to choose the appropriate fundamental laws of physics (Anderson, 1995) such as:

a. Mass conservation,
b. Newton's second law (F = ma),
c. Energy conservation.

These concepts are applied to provide a suitable model of the fluid flow and to formulate the mathematical equations which embody these physical principles. Applying the fundamental laws result in the governing equations. In Computational Fluid Dynamics, these mathematical equations are outlined in the following sections.

3.1.1. Continuity equation

In fluid dynamics, the continuity equation states that, in any steady state process, the rate at which mass enters a system is equal to the rate at which mass leaves the system. Consider the flow as an array of infinitesimally small fluid elements. The differential form of the continuity equation can be expressed as:

$$\frac{\partial \rho}{\partial t} + div(\rho \mathbf{V}) = 0 \tag{3.1}$$

where ρ is fluid density, t is time and $\mathbf{V} = (u, v, w)$ is the velocity vector express in Cartesian coordinates. If the fluid is incompressible, ρ = constant, so that, $\frac{\partial \rho}{\partial t} = 0$. Then, the continuity equation simplifies to $div\boldsymbol{V} = 0$, which in Cartesian coordinates is

$$\frac{\partial u}{\partial x} + \frac{\partial v}{\partial y} + \frac{\partial w}{\partial z} = 0 \tag{3.2}$$

3.1.2. The Momentum equation

In this section, we apply fundamental physical principles to model the flow, namely: $F = ma$ (Newton's second law). We apply Newton's second law to a moving fluid element, the net force on fluid element equals its mass multiplied by the acceleration of the element, where net forces are equal to body forces and surface forces. For incompressible flow, the conservation of momentum equations are written using tensor notation as:

Momentum x:

$$\frac{\partial(\rho u)}{\partial t} + \nabla.(\rho u\mathbf{V}) = -\frac{\partial p}{\partial x} + \frac{\partial \tau_{xx}}{\partial x} + \frac{\partial \tau_{yx}}{\partial y} + \frac{\partial \tau_{zx}}{\partial z} + \rho g_x \tag{3.3a}$$

Momentum y:

$$\frac{\partial(\rho v)}{\partial t} + \nabla.(\rho u\mathbf{V}) = -\frac{\partial p}{\partial y} + \frac{\partial \tau_{xy}}{\partial x} + \frac{\partial \tau_{yy}}{\partial y} + \frac{\partial \tau_{zy}}{\partial z} + \rho g_y \tag{3.3b}$$

Momentum z:

$$\frac{\partial(\rho w)}{\partial t} + \nabla.(\rho u\mathbf{V}) = -\frac{\partial p}{\partial z} + \frac{\partial \tau_{xz}}{\partial x} + \frac{\partial \tau_{yz}}{\partial y} + \frac{\partial \tau_{zz}}{\partial z} + \rho g_z \tag{3.3c}$$

Or with viscous friction:

Momentum x:

$$\frac{\partial(\rho u)}{\partial t} + \nabla.(\rho u\mathbf{V}) = -\frac{\partial p}{\partial x} + \mu\left(\frac{\partial^2 u}{\partial x^2} + \frac{\partial^2 u}{\partial y^2} + \frac{\partial^2 u}{\partial z^2}\right) + \rho g_x \tag{3.4a}$$

Momentum y:

$$\frac{\partial(\rho v)}{\partial t} + \nabla.(\rho u\mathbf{V}) = -\frac{\partial p}{\partial y} + \mu\left(\frac{\partial^2 v}{\partial x^2} + \frac{\partial^2 v}{\partial y^2} + \frac{\partial^2 v}{\partial z^2}\right) + \rho g_y \tag{3.4b}$$

Momentum z:

$$\frac{\partial(\rho w)}{\partial t} + \nabla.(\rho u\mathbf{V}) = -\frac{\partial p}{\partial z} + \mu\left(\frac{\partial^2 w}{\partial x^2} + \frac{\partial^2 w}{\partial y^2} + \frac{\partial^2 w}{\partial z^2}\right) + \rho g_z \tag{3.4c}$$

Or, in compact notion:

$$\frac{\partial(\rho\mathbf{V})}{\partial t} + \nabla.(\rho u\mathbf{V}) = -\nabla p + \mu\Delta^2\mathbf{V} + \rho\boldsymbol{g} \tag{3.5}$$

where ρ is fluid density, μ is dynamic viscosity, τ_{ij} denotes the stress in the j^{th} direction exerted on a plane perpendicular to the i axis and g_i denotes body acceleration in i direction. These momentum equations 3.3a - 3.3c are called the Navier-Stokes equations in conservation form, in honour of two men – the Frenchman Claude-Louis Navier and the Englishman George Gabriel Stokes (Anderson, 1995).

The continuity and momentum equations along with energy conservation equations form a set of coupled, non-linear differential equations. It is not possible to solve these equations analytically for engineering problems, but they can provide approximate solutions. These equations are fundamental for Computational Fluid Dynamics.

3.2. Computational Fluid Dynamics

The study of the fluid flow can be carried out in three ways as mentioned in the previous chapter (numerical methods, full-scale and laboratory experiments), and the one of popular approach is call Computational Fluid Dynamics. Due to the expense and the difficulties involved in large scale or full-scale experiments, numerical methods have become the preferred method to modelling fluid flow. Computational fluid dynamics (CFD) has become a well-known method to study fluid flow, which is economic, less time consuming and provide reasonably good results in the fluid dynamics. CFD solves the Navier-Stokes Equations numerically. There are three main processes for using CFD: Pre-processing, solver and post-processor.

- In pre-processing, the flow problem is set up in the computational domain, in which geometry and grid generation can be built. The region of fluid called the computational domain is made up of a number of discrete elements called the mesh. The users need to define the properties of the fluid, meshing strategies and boundary regions. Software packages that can be used are Workbench Geometry, Meshing tool, ANSYS ICEM CFD, Gambit, etc.
- In the solver: the physical properties of the fluid will be modelled and detailed boundary conditions setup in the computer domain and governing equations are solved. This is usually done iteratively by computing flow parameters of the fluid in the time domain. The

choice of mathematical flow model include RANS, LES, DES, DNS, etc. Software packages that can be used are: ANSYS Fluent, ANSYS CFX, OpenFOAM, etc.

- In post-processing, the main purpose is to visualise and quantitatively process the result from the solver, e.g. plot in graphs, contours or vector form. After a solution is obtained, validation of results is necessary to test for convergence, such as grid convergence, time step effect, etc. The results are compared with experimental results or other published numerical results to give confidence for the case set up and its solution. Figure 3.1 presents processes in CFD and CFD software structure.

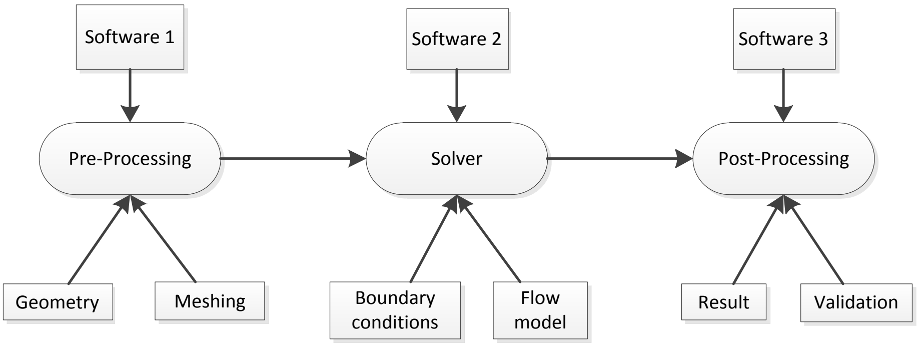

Figure 3.1. CFD software structure chart (Anderson, 1995)

3.3. Turbulence models

Currently, the CFD method is applied as a tool to carry out expensive, difficult, or even impossible experiments. The availability of powerful super computers has given the opportunity for performing accurate simulations when modelling problems of fluid dynamics. In addition, many numerical methods and flow models have been developed for different types of flow, some of which are summarised below.

3.3.1. Large eddy simulation

Large Eddy Simulation (LES) is a numerical method used to simulate turbulent flows based on the concept that the large scale motions of the flow are calculated explicitly, while the effect of the smaller universal scales are modelled using a sub-grid scale (SGS) model. Navier-Stokes equations are spatially filtered to obtain the LES governing equation. LES is applied to capture a large turbulent flow structure far away from a wall (Figure 3.2), used for flow over a bluff-body or flow at low Reynolds number (Germano et al., 1991). However, one deficiency of LES is that a very fine mesh must be used around the body wall. As a result, it increases significantly computational cost. Even though it is proven to achieve good simulation results, it is too expensive and a really time consuming method, hence it is not applied widely in industry and is not used in the current research.

3.3.2. Direct Numerical Simulation

Direct Numerical Simulation (DNS) is a simulation in which the Navier-Stokes equation are solved without any turbulence model or time averaging, to capture the fastest fluctuation or turbulent flow (Orszag, 1970). Dong and Karniadakis (2005) applied DNS to cylinder flow at Re of 10,000 by employing a multilevel-type parallel algorithm in dealing with high computational requirements and the results are in good agreement with measurements. However, this method requires a really small time step with huge memory storage requirements, and is even more expensive computationally than LES, even for very low Reynolds number. Therefore, DNS is not feasible for the current research.

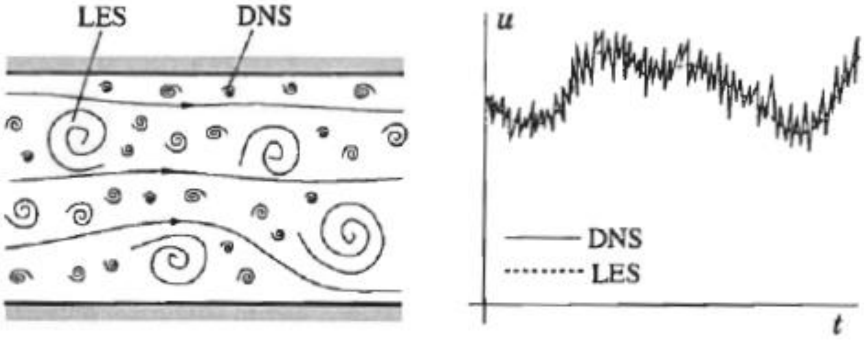

Figure 3.2. Schematic representation of turbulent motion and time dependent velocity component (Ferizger and Peric, 1997)

3.3.3. Reynolds Average Navier-Stokes

Reynolds Average Navier-Stokes (RANS) are time-averaged equations of motion for fluid flow. RANS equations govern the mean velocity and pressure. RANS code is known as a very useful mathematical model to solve turbulence flows. Historically, the RANS method was initially developed to predict turbulent flow with spectral equilibrium, where turbulence is characterized by a single time-scale dictated by the large scales of motion (Tennekes and Lumley, 1972). Furthermore, the flow is assumed to be time independent. However, such assumption is invalid when turbulent flows are unsteady, as it is the case with the cylinder’s turbulent wake. Therefore, time dependent formulations of RANS, unsteady RANS (uRANS) are necessary to describe such flow.

In comparison with LES methods, RANS results show the same trends with tolerable accuracy. LES gives better agreement than RANS (Catalano et al., 2003), however, as far as lift, drag and Strouhal number are concerned, the difference between these two methods make RANS a promising candidate in simulating cylinder flow. In motor and aero-industry, RANS is widely used, because of its reasonably good results with much cheaper computational cost. However, prediction for transition in the boundary layer is still a challenging task for RANS (Catalano et al., 2003, Stephen et al., 2011).

The concept behind the equations is Reynolds decomposition, where an instantaneous quantity is decomposed into its time-averaged and fluctuating quantities. In the Reynolds averaged approach to turbulence, practically all of the unsteadiness is modelled and slow variations in mean flow are solved explicitly. The RANS equations are a development of Navier Stokes equations of motion for incompressible Newtonian fluid: Type equation here.

$$\frac{\partial u_i}{\partial t} + u_j \frac{\partial u_i}{\partial x_j} = f_i - \frac{\nabla p}{\rho} + \nu \frac{\partial^2 u_i}{\partial x_j \partial x_j} \qquad (3.6)$$

where the decomposition quantities are:

$$u_i = \overline{u_i} + u_i' \ , p = \bar{p} + \acute{p}. \qquad (3.7)$$

Substituting decomposition terms into the Navier-Stokes equation, the RANS equation are obtained, namely:

$$\rho \frac{\partial u_i}{\partial t} + \rho \frac{\partial \overline{u_i}\,\overline{u_j}}{\partial x_j} = \rho f_i + \frac{\partial}{\partial x_j}\left[-\bar{p}\delta_{ij} + 2\mu \bar{S}_{ij} - \rho \overline{\acute{u}_i}\,\overline{\acute{u}_j}\right], \qquad (3.8)$$

where $\bar{S}_{ij}$ is the mean rate of strain tensor,

$$\bar{S}_{ij} = \frac{1}{2}\left(\frac{\partial \overline{u_i}}{\partial x_j} + \frac{\partial \overline{u_j}}{\partial x_i}\right), \qquad (3.9)$$

$u, \bar{u}, \acute{u}$ represent instantaneous, mean and fluctuating velocity terms, respectively, ν is kinematic viscosity and f_i is a vector representing external forces.

In order to solve the RANS equations for mean-flow properties of turbulent flow, we need to define the value of the Reynolds stress tensor $\rho\overline{\acute{u}_i}\,\overline{\acute{u}_j}$ or τ_{ij}. This is a second order symmetric tensor with 6 independent components. For general three-dimensional flows, we have four unknown mean flow properties, namely, three velocity components and pressure. All together, the six independent components of the Reynolds Stress tensor and the four mean flow quantities result in ten unknowns. The conversion of mass and the three components of the conservation of momentum equations provide only four equations to determine ten unknowns. Therefore, more equations or assumptions are needed to solve the problem.

The most widely used assumption which applies in RANS is the Boussinesq eddy viscosity assumption (Schmitt, 2007). It is the basis for all two-equation models and postulates that the Reynolds stress tensor, τ_{ij}, is proportional to the mean strain rate tensor S_{ij}

$$\tau_{ij} = 2\mu_t S_{ij} - \frac{2}{3}\rho k \delta_{ij} \tag{3.10}$$

where μ_t is a scalar property called the eddy viscosity which is normally computed from two transport variables and the last term is included for modelling incompressible flow and, thus to ensure that the definition of turbulence kinetic energy is obeyed, k satisfies:

$$k = \frac{\overline{\acute{u}_\iota}\overline{\acute{u}_J}}{2} \tag{3.11}$$

The Boussinesq assumption is a crucial application for the two-equation turbulence model. This assumption is a huge simplification, which allows one to think of the effect of turbulence on the mean flow in the same way as molecular viscosity affects a laminar flow. The assumption also makes it possible to introduce intuitive scalar turbulence variables such as the “turbulent energy” and “dissipation” and to relate these variables to even more intuitive variables like “turbulence intensity” and “turbulence length scale” (Bredberg, 2000).

3.3.3.1. The Spalart Allmaras (SPA)

SPA is a one-equation model which provides good predictions for some related aerospace simulations (Karim et al., 2008). It solves a transport equation for the viscosity-like variable $\tilde{v}$ (ANSYS, 2011)

$$\frac{D\tilde{v}}{Dt} = G_v \left\{ \frac{\partial}{\partial x}\left[(\mu + \rho\tilde{v})\frac{\partial \tilde{v}}{\partial x_j}\right] + C_{b2}\rho\left(\frac{\partial \tilde{v}}{\partial x_j}\right)^2 \right\} - Y_v + S_{\tilde{v}} \tag{3.12}$$

Eddy viscosity is obtained from $\mu_t = \rho\tilde{v}f_{v1}$ where $f_{v1} = \frac{(\tilde{v}/\,v)^3}{(\tilde{v}/v)^3 + C_{v1}^3}$ where G_v is the production of turbulent viscosity, Y_v is destruction of turbulent viscosity, $S_{\tilde{v}}$ is user defined source term and C_{b2}, C_{v1} are constants.

The model is mainly applied for applications with mild separation, such as supersonic/transonic flow over aerofoil, but does not give good agreement with experimental results compared with other models, e.g DNS (Constantinides and Oakley, 2006).

3.3.3.2. The $k - \varepsilon$ model

The $k - \varepsilon$ model is a two-equation model in which the transport equations are solved through the turbulent kinematic energy, k, and the rate of dissipation, ε. The eddy viscosity in this case is defined by:

$$\mu_t = C_\mu \rho \frac{k^2}{\varepsilon} \tag{3.13}$$

where C_μ is an empirical constant. Furthermore, an advanced near wall treatment modifies the values of turbulent viscosity and dissipation rate near the cylinder surface to account for laminar viscosity dominated effects.

Transport equations for k and ε:

$$\frac{D}{Dt}(\rho k) = \frac{\partial}{\partial x_j}\left[\left(\mu + \frac{\mu_t}{\sigma_\varepsilon}\right)\frac{\partial k}{\partial x_j}\right] + G_k - \rho\varepsilon \tag{3.14}$$

$$\frac{D}{Dt}(\rho\varepsilon) = \frac{\partial}{\partial x_j}\left[\left(\mu + \frac{\mu_t}{\sigma_\varepsilon}\right)\frac{\partial \varepsilon}{\partial x_j}\right] + C_{\varepsilon 1}\frac{\varepsilon}{k}\, G_k - \rho C_{\varepsilon 2}\frac{\varepsilon^2}{k} \tag{3.15}$$

In which $C_\mu = 0.09, C_{\varepsilon 1} = 1.44,$ $C_{\varepsilon 2} = 1.92$, $\sigma_k = 1.0$, $\sigma_\varepsilon = 1.3$ and G_k represent the generation of turbulence kinetic energy due to mean velocity gradients (ANSYS, 2011)

This model is widely used for industrial application due to its robustness, computational economy and reasonable accuracy. Pinto et al. (2006), Elmiligui et al. (2010) obtained very good agreement in terms of lift, drag and Strouhal number using this model for flow around a stationary cylinder. Near the wall area, $k - \varepsilon$ makes use of an empirical formula, known as the wall function, to predict the flow in order to save computational power. However, although wall function reduces computational cost, it is not sufficient for representing a complex flow accurately.

In Fluent, the $k - \varepsilon$ model contains three main versions (ANSYS, 2011)

- Standard $k - \varepsilon$ model: This is widely used despite its known limitations as it is robust. Performs poorly for complex flows, involving severe pressure gradient, separation and strong streamline curvature. It is suitable for initial iterations, initial screening of alternative designs, and parametric studies.
- Renormalization group (RNG) $k - \varepsilon$ model: This is suitable for complex shear flows involving rapid strain, moderate swirl, vortices, and locally transitional flows e.g. boundary layer separation, massive separation, and vortex shedding behind bluff bodies, stalling wide-angle diffusers and room ventilation.
- Realizable $k - \varepsilon$ model: It offers largely the same benefits and has similar applications to RNG. Possibly more accurate and easier to converge than RNG.

3.3.3.3. The $k - \omega$ model

Within RANS models, $k - \omega$ is a two-equation model in which the transport equations are solved through the turbulent kinetic energy, $k = \frac{\overline{\acute{u_i}\acute{u_j}}}{2}$ and the specific dissipation rate $\omega = \frac{\varepsilon}{k}$ This model was used to achieve good prediction of force near a wall (Wilcox, 1988).

The turbulent kinetic energy, k, and the specific dissipation rate, ω, are obtained from the following transport equations:

$$\frac{\partial}{\partial t}(\rho k) + \frac{\partial}{\partial x_i}(\rho k u_i) = \frac{\partial}{\partial x_j}\left(\tau_k \frac{\partial k}{\partial x_j}\right) + G_k - Y_k + S_k \quad (3.16)$$

$$\frac{\partial}{\partial t}(\rho \omega) + \frac{\partial}{\partial x_i}(\rho \omega u_i) = \frac{\partial}{\partial x_j}\left(\tau_\omega \frac{\partial \omega}{\partial x_j}\right) + G_\omega - Y_\omega + S_\omega \quad (3.17)$$

where G_k represents the generation of turbulent kinetic energy due to mean velocity gradient, G_ω represents the generation of ω, S_k and S_ω are user defined source terms, Y_k and Y_ω represent the dissipation, τ_k and τ_ω represent the effective diffusivity of k and ω due to turbulence given by:

$$\tau_k = \mu + \frac{\mu_t}{\sigma_k} \quad (3.18a)$$

$$\tau_\omega = \mu + \frac{\mu_t}{\sigma_\omega} \quad (3.18b)$$

where σ_k and σ_ω are turbulent Prandtl numbers for k and ω, and μ_t is turbulence viscosity. The $k - \omega$ model allows better treatment of flow near a wall. The boundary layer is affected by the nature of the flow, thus a fine mesh is required near a wall. However, one deficiency of this model is its sensitivity to free stream values.

3.3.3.4. SST $k - \omega$ model

The Shear Stress Transport (SST) $k - \omega$ is another two-equation based model which was developed by Menter (1994). It combines the robustness and accuracy of $k - \omega$ model in the near-wall region with the free-stream independence of the $k - \varepsilon$ model in the farfield. To achieve this, $k - \varepsilon$ is converted into the $k - \omega$ model. The SST model also accounts for the transport of the turbulent shear stress inside boundary layers by modifying the turbulent eddy-viscosity function. The aim is to improve the accuracy of prediction for flows with strong adverse pressure gradient, as well as flows with pressure-induced boundary layer separation.

3.3.3.5. SST model

The transition SST model is a four-equation model based on the coupling of the SST $k-\omega$ transport equations with two other transport equations, one for the “intermittency” and one for the “transition onset criteria”, in terms of momentum thickness Reynolds number. The model was proved to be effective for simulating the interaction of a current with a circular cylinder (Kirkgoz et al., 2009).

3.3.4. Detached Eddy Simulation

Although the two-equation models provide a good compromise between complexity and accuracy among RANS models, their application is restricted to steady flow. Thus, a solution is sought achieving both computational efficiency and the capability of predicting the chaotic nature of flows such as vortex shedding. This leads to a hybrid based on the LES and RANS models, known as the Detached Eddy Simulation (DES). DES combines the best aspects of RANS and LES in a single solution strategy (Spalart, 1997). In this method, the model switches to a subgrid scale formulation in regions fine enough for LES calculations. Grid generation is more complicated than for a simple RANS or LES case due to the RANS-LES switch. However, DES requires a larger computational cost compared to RANS by using 3D simulation in ANSYS Fluent and is not really appropriate to apply in this project due to limited computational resources.

3.4. Numerical Schemes

3.4.1. Selection of solver

There is a wide range of solvers for CFD available at the University of Southampton such as ANSYS Fluent, ANSYS CFX and OpenFOAM. The super-computers (IRIDIS 3 and 4) are provided for dealing with computationally intensive problems.

For applications to the flow around circular cylinder and marine risers, Pinto et al (2006), Shao and Zhang (2007), Baranyi et al. (2009) performed simulations using Fluent. In addition, China Ship Scientific Research Centre, Seoul national University, Samsung Ship Model Basin (Korea) also use Fluent solver to investigate VIV around a circular cylinder. Baranyi et al. (2010), Fang and Han (2011) used another ANSYS fluid flow solver - CFX to simulate flow hydrodynamics around a circular cylinder. Although CFX has been applied in recent years for research, its application in research and industry is still minor compared with Fluent. The opensource code OpenFOAM requires the user to be familiar with the Linux code system. The text command used in OpenFOAM appears to be less user-friendly for CFD users compared with commercial software.

For the author’s investigation, ANSYS Fluent was chosen for the following reasons:

- Fluent is a well-known CFD software, which has been widely used before;
- The Window interface of ANSYS Fluent is easier to use.
- The whole package is integrated in ANSYS Workbench including geometry, meshing, solver and post-processing, thus carrying out CFD simulation easier than other solvers.
- Some advanced solver technologies in Fluent provide fast, accurate CFD results, flexible moving and deforming meshes which is very important for the current research.
- The application of ANSYS is widely accepted in industry, and ANSYS results are regarded as reliable by industry.

For these reason, ANSYS Fluent is used in this research.

3.4.2. Equation discretisation

In this study, flow simulation is performed using commercial software ANSY Fluent. The partial differential equations (PDE) that govern the conservation of momentum, mass (Chapter 3.1), transportation equations of turbulence and approximated equations (Chapter 3.3) need to be solved. Equation discretisation is the scheme to transform the governing equations into a numerical analogue that can be solved by the computer. There are three methods commonly used in CFD, namely: Finite difference (FDM), Finite element (FEM) and Finite volume (FVM)

The finite difference method is the oldest of the three employing the concept of Taylor expansion to solve the second order PDE governing fluid flow (Richardson, 1911). This method is straightforward, with the derivatives in the PDE expressed as discrete quantities of variables resulting in simultaneous algebraic equations with unknowns defined at the nodes of the mesh. FDM is easy to implement and to obtain higher order of accuracy; however, it is restricted to simple grids and does not conserve momentum, energy and mass on coarse grids.

The finite element method was first used by Courant (1943) for solving torsion problems. FEM analysis of fluid flow was developed in the mid to late 70‘s. In FEM, the computational domain is subdivided into a finite number of elements. The simulation with 3D FEM for steep waves and their interaction with vertical cylinders showed very good agreement to experimental results with very modest computational cost (Ma and Patel, 2001). Although it has the highest accuracy with coarse grids and is excellent for viscous flows and free surface problems, FEM is slow for large problems and not suitable for turbulent flow (Zienkiewicz et al., 2014)

The finite volume method separates the computational domain into a finite number of control volumes. FVM procedure is used to transform PDE variables into a set of algebraic equations that describe the discrete or numerical solution of the governing equations. The discretisation process results in a set of algebraic equations that resolve the variables at a specified finite number of points within the control volumes using an integration method. Through integration on the control volumes, the flow throughout the domain can be fully modelled. FVM can be used both for structured and unstructured meshes, and can be applied for high speed flow and turbulent flows (Bakker, 2012). Hence, FVM is more common in recent CFD applications compared to FEM and FDM. In this simulation, the CFD simulation packages, ANSYS Fluent is developed based on FVM.

ANSYS Fluent uses a control volume based technique to convert a general scalar transport equation to an algebraic equation that can be solved numerically. A discretised equation of a given control volume can be written as:

$$\frac{\partial \rho \varphi}{\partial t} V + \sum_{f}^{N_{face}} \rho_f \vec{v}_f \, \varphi_f \cdot \vec{A}_f = \sum_{f}^{N_{face}} \tau_f \nabla \varphi_f \cdot \vec{A}_f + S_{\varphi} V \tag{3.19}$$

where velocities $\vec{v}_f$ and diffusion coefficient φ_f are integrated over the number of faces enclosing cells, N_{face}. The vector product $\rho_f \vec{v}_f \cdot \vec{A}_f$ is mass flux through the face of area $\vec{A}_f$. φ is scalar of control volume V and S_{φ} is source term of scalar φ

3.3.3. Spatial discretisation schemes

Spatial discretisation divides the computational domain into small sub-domain making up the mesh. The face values from Equation 3.19 are required for the convection term and must be interpolated from cell centre values. In this current simulation, the upwind scheme, is used, that the face value of φ_f is derived from quantities of cells upstream, relative to the direction of the normal velocity v_n in Equation 3.19.

As far as the present work is concerned, a second order-upwind is used. In the second order upwind scheme, quantities at cell faces are calculated based on the multidimensional linear reconstruction approach (Barth and Jespersen, 1989). A second order accuracy is achieved at the cell faces through a Taylor series expansion of cell-centred solution about the cell centroid. Thus, the face value φ_f is computed using the following expression:

$$\varphi_f = \varphi + \nabla \varphi \cdot \vec{r} \tag{3.20}$$

where φ and $\nabla\varphi$ are the cell-centred value and its gradient in the upstream cell and $\vec{r}$ is the displacement vector from the upstream cell centroid to the face centroid (ANSYS, 2011). This scheme is used for turbulence scalars (kinetic energy, dissipation rate or specific dissipation rate) for all RANS simulations.

3.3.4. Temporal Discretization

All simulations in the current work are time dependent using transient simulation; thus the governing equations are not only discretised in space but also in time. Therefore, in addition to spatial discretisation, a temporal discretisation scheme is required for governing equations, in which, the differential equation will be integrated over time step Δt. The integration of a transient term can be shown in a generic expression for the time evolution of φ

$$\frac{\partial\varphi}{\partial t} = F(\varphi) \tag{3.21}$$

where F incorporates any spatial discretization. If the time derivative is discretized using backward differences, the first order accurate temporal discretization is given by

$$\frac{\varphi^{n+1} - \varphi^{n}}{\partial t} = F(\varphi) \tag{3.22}$$

and the second-order accurate form is

$$\frac{3\varphi^{n+1} - 4\varphi^{n} + \varphi^{n-1}}{2\partial t} = F(\varphi) \tag{3.23}$$

where, n+1, n and n-1 indicate values at time steps $t + \Delta t$, t and $t - \Delta t$ respectively

When a moving dynamic mesh undergoes high distortion, the second-order implicit scheme could lead to instability of the mesh, and is not recommend by ANSYS Fluent. Therefore, all moving dynamics mesh case in this thesis are run in first order implicit formulation where the quantity φ can be written:

$$\varphi^{n+1} = F(\varphi)\partial t + \varphi^{n} \tag{3.24}$$

In addition, to ensure stability of the numerical calculations and obtain accurate CFD results, the Courant number is kept around 1. The Courant number is defined as:

$$CFL = \max\left(\frac{u\Delta t}{\Delta x}, \frac{v\Delta t}{\Delta y}, \frac{w\Delta t}{\Delta z}\right) \tag{3.25}$$

where, u, v, w present velocity in x, y, z directions.

3.3.5. Pressure velocity coupling scheme

ANSYS Fluent provides four segregated types of algorithms: SIMPLE, SIMPLEC, PISO, COUPLED and for time-dependent flows using the **Non-Iterative Time Advancement** option (NITA) Fractional Step (FSM). These schemes are referred to as the pressure-based segregated algorithm.

Typically, for an iterative time advancement (ITA) scheme shown in Figure 3.3a, steady-state calculations will generally use SIMPLE or SIMPLEC, while PISO is recommended for transient calculations. According to ANSYS (2011) the PISO algorithm with "neighbour correction" (momentum correction) is highly recommended for all transient flow calculations, especially when a large time step is applied. PISO can maintain a stable calculation with a larger time step and an under-relaxation factor of 1.0 for both momentum and pressure. For steady-state problems, PISO with neighbour correction does not provide any noticeable advantage over SIMPLE or SIMPLEC with optimal under-relaxation factors. PISO with "skewness correction" is recommended for both steady-state and transient calculations on meshes with a high degree of distortion. For most problems, it is not necessary to disable the default coupling between neighbour and skewness corrections. For highly distorted meshes, however, disabling the default coupling between neighbour and skewness corrections is recommended.

One deficiency of the ITA scheme is a considerable amount of computational effort required due to the large number of outer iterations performed for each time-step. The NITA scheme is developed to improve this problem. Instead of reducing the splitting error to zero, it only needs to be of the same order as the truncation error. The NITA scheme, shown in Figure 3.3b does not need the outer iterations, performing only a single outer iteration per time step, which significantly speeds up transient simulations. In addition, the NITA scheme still allows for an inner iteration to solve the individual set of equations which specially developed for time dependent flow. For this benefit, NITA FSM scheme is used for simulated unsteady flow simulation.

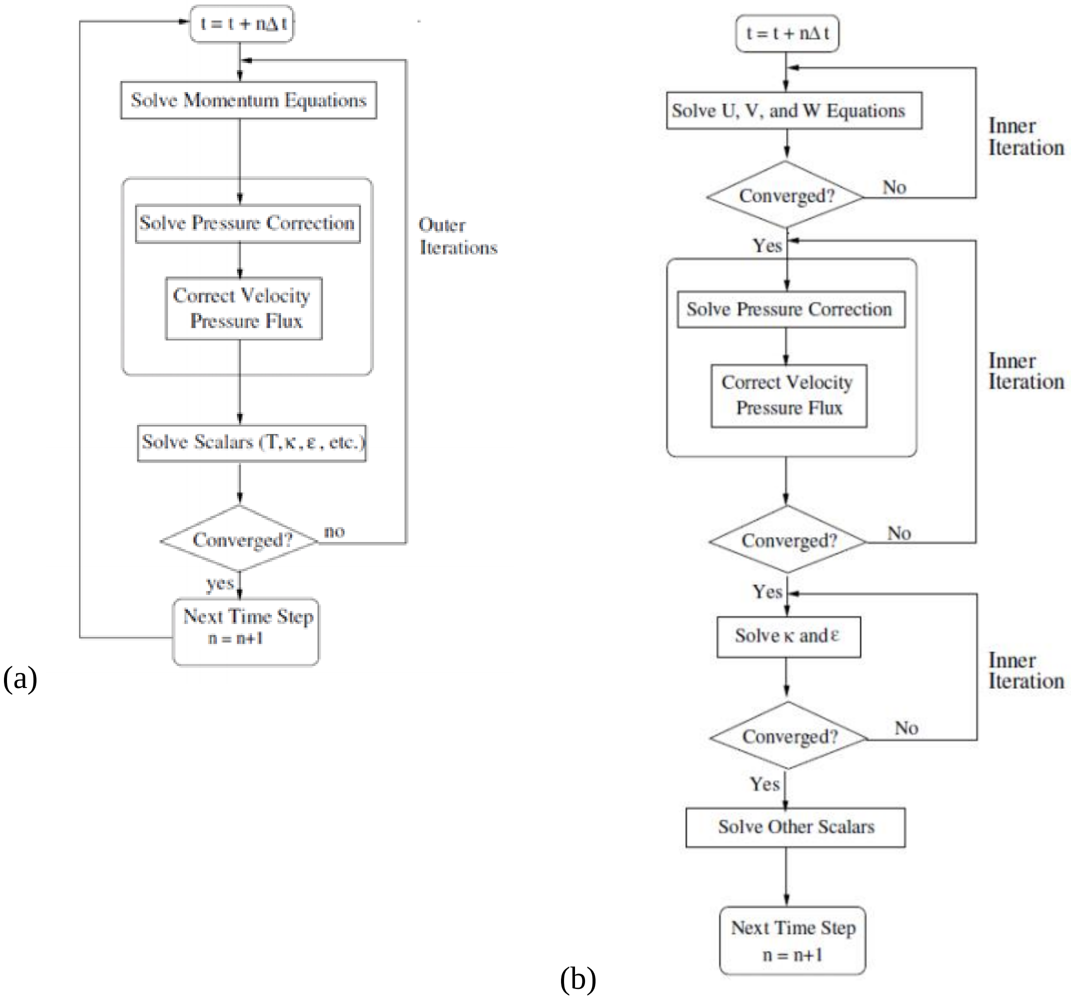

Figure 3.3: Overview of (a) Iterative time advancement solution, (b) NITA solver (ANSYS, 2011)

3.3.6. Solution criteria

Numerical solutions are a product of an iterative process, where the set of linearized equations are simultaneously solved. For each conservation equation, a repetitive iterative process achieves “convergence”. Due to the inherent approximations in discretization and due to the finite memory of the computing machine (round off), convergence is judged based on the residuals of each conservation equation.

To minimize effect of the round off error, a double precision solver is used (ANSYS, 2011). For all simulations taken in this thesis, the maximum relative errors were less than 10^{-5} for all variables, e.g. velocities, turbulences parameters, etc.

3.5. Equations of motion

To obtain the flow field prediction with the moving boundary of a forced oscillating cylinder or elastically mounted cylinder, a User Defined Function (UDF) has to be written in C language to communicate with Fluent.

For the forced oscillating cylinder case, the simple harmonic motion of the cylinder in crossflow is expressed by

$$y(t) = A\sin(2\pi f_o t). \tag{3.26}$$

where y is the cylinder displacement, A is cylinder displacement amplitude and f_o is the cylinder oscillation frequency.

A free oscillating cylinder with 1 dof system can be modelled as a cylinder with mass m, supported by the spring with spring constant K and a damper with damping constant c. The equation of motion in crossflow direction for this mass-spring-damper system can be expressed as:

$$m\ddot{y} + c\dot{y} + Ky = F_{fluid,y} \tag{3.27}$$

where $F_{fluid,y}$ is fluid force acting on the body in the y direction and obtained from pressure and viscous forces on the body.

In a manner similar to a 1 dof system, the equations of motion in crossflow direction of a viscous damped multi-degree of freedom system can be expressed as:

$$[m]\ddot{\vec{y}} + [c]\dot{\vec{y}} + [k]\vec{y} = \vec{F} \tag{3.28}$$

where $[m] = \begin{bmatrix} m_1 & 0 \\ 0 & m_2 \end{bmatrix}$, $[c] = \begin{bmatrix} c_1 + c_2 & -c_2 \\ -c_2 & c_2 \end{bmatrix}$, $[k] = \begin{bmatrix} k_1 + k_2 & -k_2 \\ -k_2 & k_2 \end{bmatrix}$ are the mass, damping and stiffness matrices, $\vec{y} = \begin{pmatrix} y_1 \\ y_2 \end{pmatrix}$ and $\vec{F} = \begin{pmatrix} F_1 \\ F_2 \end{pmatrix}$ are displacement and force vector and where $F_1 = 0, F_2 = F_{fluid,y}$ and y_1, y_2 are the crossflow displacements of m_1, m_2.

When the system is oscillating in both inline and crossflow directions, another equation is added in the UDF. In this equation, $F_{fluid,y}$ is substituted by $F_{fluid,x}$ which present total drag force acting on the cylinder. The cylinder is assumed to be a rigid body throughout all simulations undertaken in this thesis.

The inline and crossflow motion is not coupled, however, the displacement in inline and crossflow direction will be updated to the into ANSYS Fluent to calculate the new forces acting on the body in the next time step. The Fluid Structure coupling will be investigated in this way.

3.6. Mesh strategy for CFD modelling

The mesh or grid used is a crucial factor that affects the quality of the results. In this work comprising 2D simulations, the ANSYS meshing tool was used to discretise the domain.

3.6.1. Structure and unstructured mesh

The two mesh formations that can be used are structured and unstructured. A structured mesh is a series of blocks in which there is certain regularity (Anderson, 1995).

Structured meshing is restricted with reference to element choices, namely quadrilateral in two dimensions or hexahedra in three dimensions. The advantage of using a structured mesh is the high quality meshing elements and the user can control the area of interest better. However, to generate a good mesh depends on the skill and experience of the user. For a complicated geometry, it is hard to control the unstructured mesh and the process of creating and modifying a structured mesh is a time consuming one.

An unstructured mesh has no regularity. Thus, for complicated geometries, the unstructured mesh allows maximum flexibility that is available in the software.

A third alternative, namely, the hybrid mesh provides a combination of structured and unstructured meshing within the domain. But in this study, where the 2D grid generation and the shape of the domain is simple, a structured mesh was adopted using the ANSYS Meshing tool in ANSYS 14 (ANSYS, 2011)

For the problems investigated, structured meshing gives the best meshing quality and adapts to the dynamic mesh method.

3.6.2. Boundary layer thickness, y^+ and first layer height of mesh near the wall

In order to obtain accurate flow parameter description around the body, the structured mesh should be fine near the structure surface (e.g using inflation layers). The mesh has to be good both in terms of mesh quality (e.g. orthogonal mesh, skewness) and cell distribution, especially first mesh height in the vicinity of the body surface must be controlled.

One challenge in obtaining accurate CFD predictions is the wall shear stress at the interface layer between fluid and structure. In order to obtain the wall shear stress, the concept of placing the first computational node as near the wall as possible and assuming that the velocity profile near the wall is known is applied. Estimation of the value for the dimensionless first cell height is given by the formula

$$y^+ = \frac{y_1 U_\tau}{\nu} \tag{3.29}$$

where y_1 is the distance for the first layer to the wall, ν is kinematic viscosity and $U_\tau = \sqrt{\tau_\omega/\rho}$ is the friction velocity where τ_ω is wall shear stress. Figure 3.4 illustrate the velocity profile in the boundary layer.

The dimensionless velocity is defined as

$$u^+ = \frac{U}{U_\tau} \tag{3.30}$$

where U is velocity parallel to the wall. To capture the fluid phenomena of interest many assumptions concerning the y^+ value have been suggested and depend on the problem modelled and the type of flow as illustrated in Figure 3.4.

- Within the viscous sublayer $u^+ = y^+$ where $y^+ < 5$
- Within the buffer layer or blending region, namely the zone in which the laminar wall law blends to the turbulent wall law, typically it is known as $5 < y^+ < 15$
- In the logarithmic law region; $u^+ = A\, lny^+ + B$, where A and B are constants estimated from experiment, here typically $15 < \ y^+ < 600$
- The wake region is, usually, extended from the logarithmic region

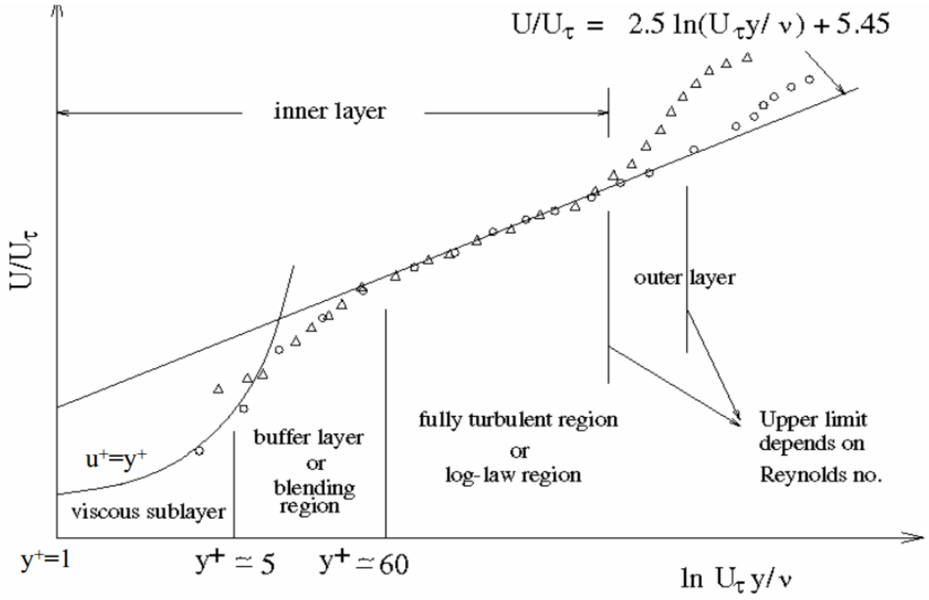

Figure 3.4. Velocity profile in boundary layer of the flat plate (Anderson, 1995).

There are two common approaches for obtaining accurate results near the wall modelling

- Application of wall function is widely used in industry. The difficult near-wall region is not explicitly resolved within the numerical model but is bridged using the wall function. The wall function is often used in $k - \varepsilon$ models and the meshing should be arranged with the value of y^+ is in the range of 30 to 100 (in the logarithmic region). The wall function is often used in case of high Reynolds number; however, predicted forces on the body are not as good as the near wall resolution.
- The near wall resolution is a method that fully resolves the flow structure around the wall, where flow separation and forces on the body can be predicted accurately. The near wall resolution approach requires a very fined mesh in a very narrow region adjacent to the wall in other to capture accurately the variation of the flow variables. Near wall resolution is often used in $k - \omega$ turbulence model and requires y^+ value at the first node adjacent to the wall in viscous sublayer to be y^+ <5, and ideally, close to 1 (Consultants, 2006).

The current simulation focuses on calculating forces around the cylinder in subcritical Re. Hence, it is possible to control y^+ value around 1 with reasonable computational cost. Hence, the near wall resolution is used.

To achieve the expected y^+, Equations 3.29 and 3.30 are used with wall shear stress τ_w given

$$\tau_w = C_f . \frac{1}{2} \rho U_{freestream}^2 \tag{3.31}$$

where the skin friction coefficient C_f according to the using Schlichting skin-friction correlation (Schlichting and Kestin, 1979):

$$C_f = [2 \log_{10}(Re) - 0.65]^{-2.3} \tag{3.32}$$

3.6.3. Dynamic mesh implementation

Different numerical techniques are applied in literature to simulate fluid-structure iteration problems where the structure is not fixed. There are two main approaches which can be adopted: (i) those where the structure is allowed to move freely in a static mesh (often refer to offset mesh) and (ii) those where the fluid mesh deforms to match the location of the structure’s boundary (referred as deformed mesh). Using static mesh prevents the problem of complex mesh deformation, however due to independence of the structure boundary location, obtaining predictions of boundary layer scalar, velocities, stresses is difficult and less accurate. In the second category, where the mesh is deforming/moving to match displacement of the structure, Arbitrary Lagrangian-Eulerian (ALE) formulation is used (Lesoinne and Farhat, 1996)

In ANSYS Fluent the dynamic mesh capability is used to simulate problems with boundary motion adopting the ALE method. The motion of the structure, in this case, a circular cylinder, is obtained from the integrated forces and stress exported from Fluent Solver, via the use of a User Defined Function (UDF). The UDF calculates the new position of the cylinder and exports back to the solver and a new iteration start. Thus, there is two way coupling in FSI.

There are three dynamic mesh schemes in ANSYS Fluent, namely, smoothing, layering, and remeshing. A combination of these three schemes can be used to tackle the most challenging dynamic mesh problems.

- Layering enables the dynamic layering method which can be used to add or remove layers of cells adjacent to a moving boundary based on the height of the layer adjacent to the moving surface in prismatic mesh zones. Layering can maintain very good mesh quality and the meshing near the wall can be easily preserved. However, one constraint of layering is sliding interfaces to transition between adjacent cell zones, resulting in limiting movement in one direction. Thus, for freely oscillating bodies, this method is not applicable.
- Remeshing enables local or zonal remeshing methods, often used adjacent with smoothing. In local remeshing, the cells that violate skewness or size criteria are agglomerated and locally remeshed. In zonal remeshing, the complete cell zone, including the boundary zones, is remeshed (ANSYS, 2011). Remeshing can solve large displacement problems, where the cells can become degenerate because of high skewness. However, for the moving cylinder case, the large number of oscillations will result in deteriorating the quality of the whole domain after many times of remeshing. So this method is not appropriate for VIV simulation.
- Smoothing enables the spring-based or diffusion-based smoothing method. In spring-based smoothing, edges between any two mesh nodes are idealized as a network of interconnected springs. In diffusion-based smoothing, the interior mesh motion is governed by the solution to a diffusion problem. Computationally, diffusion is more costly than spring-based smoothing, but it produces better quality mesh and allows cylinder oscillations of high amplitude without any limitation on the direction of motion. The node positions are updated based on

$$\vec{x}_{new} = \vec{x}_{old} + \vec{u}\Delta t \tag{3.33}$$

  where, $\vec{x}$ and $\vec{u}$ are displacement and velocity vector at time step Δt. Diffusion-based smoothing method is used in the current investigation due to its efficiency.

To control the dynamic mesh zone, two distinct Define Macros available in FLUENT Macros are used. They are:

- DEFINE_CG_MOTION used to specify the motion of particular dynamics zone with linear and angular velocities at every time step. ANSYS FLUENT uses these velocities to update the node positions on the dynamic zone based in solid-body motion.
- DEFINE_SDOF_PROPERTIES used to specify custom properties of moving objects for the six-degrees of freedom (SDOF) solver in ANSYS FLUENT. These include mass, moment and products of inertia, and external forces and moments. The properties of an object, which can comprise of multiple zones, can change in time, if desired.

These two Defined Macros are used in the developed UDF, and applied to the moving body, attaining coupling between the cylinder's motion and the flow field. The following steps clarify how the coupling between fluid and structure works:

- To begin with, the cylinder is stationary. Fluid forces on the cylinder are calculated by the Fluent Solver.
- The forces are transferred to the UDF, where the cylinder's equation of motion is solved and the velocity of its centre of gravity is updated in the solver.
- The cylinder's boundary is updated and followed by the mesh deformation. The motion of the cylinder is solved by (a) Finite difference method (FDM) (b) Six degree of freedom macros (SDOF), depending on the problem solved, see Table 3.1.

Table 3.1. Applied mesh deformation scheme

1 dof (crossflow)	FDM, SDOF
2 dof(1 dof crossflow + 1 dof inline)	FDM
2 dof(2 dof crossflow only)	FDM
4 dof(2 dof crossflow + 2 dof inline	FDM

- The force on the cylinder at the new position is calculated and the iterative process continues until the end of simulations.
- The forces, motions of the cylinder saved file for post-processing

With the dynamic mesh models, one of the challenges for the current research is big displacements of the cylinder that may lead to large distortion in the adjacent meshing area around the cylinder and even break down. In addition, the meshes around the cylinder need to be preserved. If the mesh quality around the cylinder decreases, the solver will not provide the correct results.

To control the stability of the cylinder, the area around the cylinder is separated as an independent part from the fluid domain (Figure 3.5). The separated area is the dynamic mesh zone while the other areas are stationary. The dimension of the separated area is up to 15D x 15D, hence, the cylinder is able to move up to 6D in each direction with the MDM smoothing-diffusion scheme (Figure 3.6).

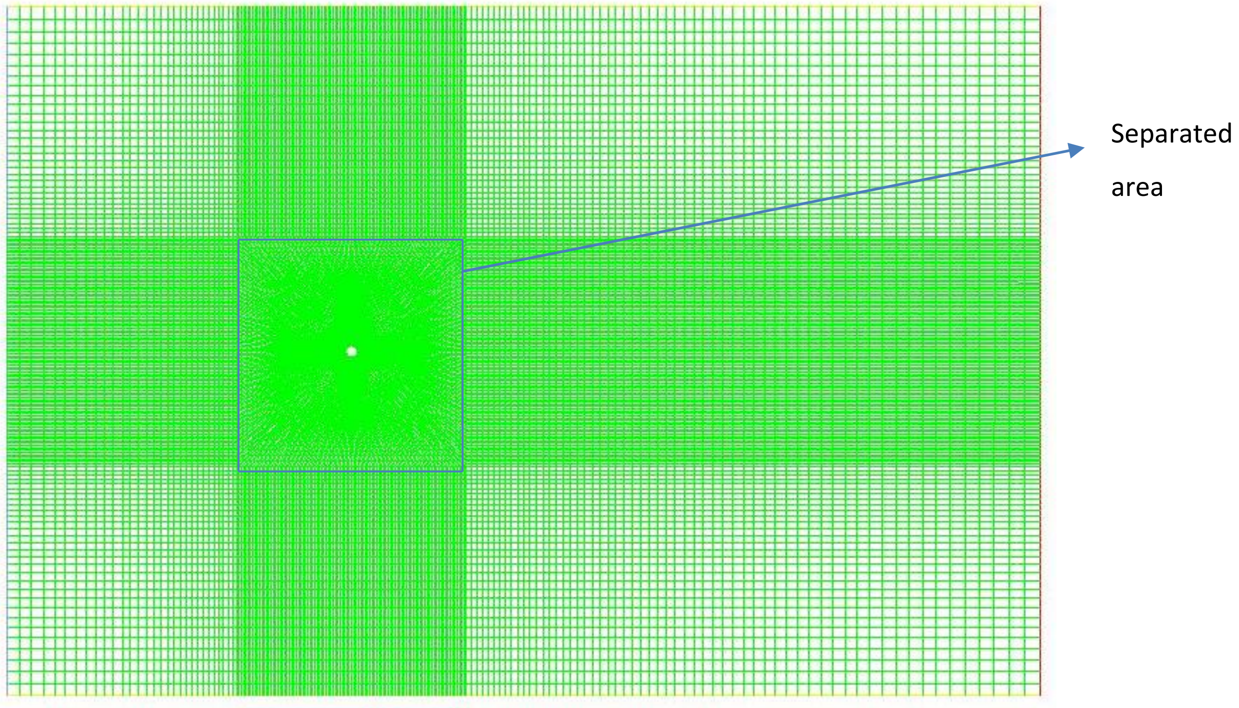

Figure 3.5. Dynamic mesh implementation for the free-oscillating cylinder domain.

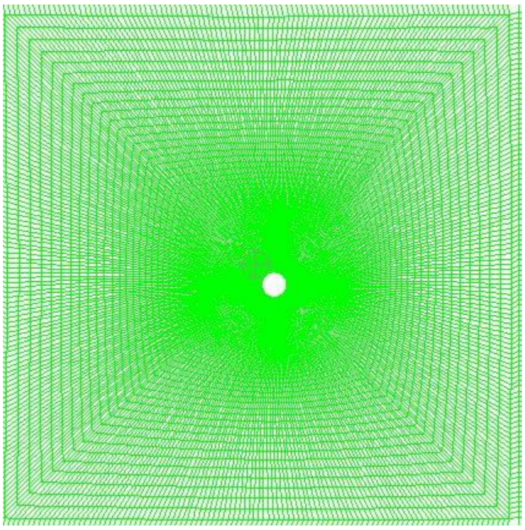

Figure 3.6. Moving mesh in the separated area.

During the simulations, the mesh quality around the cylinder is controlled by a diffusion parameter being assigned a value in the interval [0,2]. In the simulation, the diffusion parameter is assigned the value of 1 in the case of high distortion. Consequently, the mesh around the cylinder, up to 1.5D changes very slightly. This ensures y^+ always maintains its expected value and ensures that the force on the cylinder is calculated accurately. Hence, the dynamic mesh process does not influence y^+.

In some high distortion cases, the relaxation factors are changed to maintain the numerical stability. In this case, the pressure component was reduced to 0.9 or 0.8 from the default value of 1. This adjustment may increase the residual error, but it will help to maintain the stability of the process throughout the simulation.

Chapter 4 : Stationary cylinders

The aim of this chapter is to provide, as a first step, validation of the computational approach. Due to wide application of CFD in industry and research, the notion of validation (modelling accuracy) and verification (numerical schemes' accuracy) have become increasingly important. Any CFD code would have its own uncertainties related to code assumptions, boundary conditions, numerical schemes or turbulence models. Since numerical models are approximations of the real problem, it is important to find an appropriate model which provides the best agreement with measurements, i.e. the physical problems.

In this chapter, two cases involving stationary cylinders are investigated (i) a single stationary cylinder in crossflow and (ii) two cylinders in a tandem arrangement in crossflow.

In the first part of this chapter, results from numerical simulations of flow around a single stationary cylinder are summarised. The numerical method is based on solving 2D RANS equations and employs a two-equation turbulence model. The simulations are conducted for Reynolds number range from 10 to $2x10^4$, which are in the subcritical regime. The choice of two particular Re values, that of 3900 and 10000, is due to experimental data being available for validation. After setting up the model to investigate the flow around a circular cylinder, calculations will be made by ANSYS Fluent 14.5. Wall resolving grids are used for this smooth cylinder case. Different grids are used in order to assess convergence and find the appropriate grid. Various turbulence models are used to assess their suitability.

In the second part of this chapter, the flow around stationary circular cylinders in a tandem arrangement is investigated numerically. Simulations are presented for the subcritical Reynolds number 22,000, with cylinder separations L/D in the range 2 to 5, where L is the centre-to-centre distance and D the diameter. The simulations are carried out using different $k-\varepsilon$ and $k-\omega$ turbulence models with different flow parameters, such as the incident turbulence intensity I and the turbulent-to-laminar viscosity ratio β.

The following aspects are investigated:

- Selection of the appropriate numerical schemes and turbulence models for future FIV research.
- Comparison of drag, lift coefficients, pressure coefficient and Strouhal number with experimental measurements and other numerical results.

4.1. Turbulence parameters

When using a turbulence model, accurate boundary conditions are important to predict flow accurately, especially for high Reynolds number. In Fluent, with RANS model, turbulence variables like k, ε and ω influence the accurate of the simulation. They are defined as follows:

For standard $k - \varepsilon$ model and its variations (RNG, Realizable):

Turbulent kinetic energy

$$k = \frac{3}{2}(UI)^2 \tag{4.1}$$

Turbulent dissipation rate:

$$\varepsilon = c_{\mu}^{\frac{3}{4}} k^{\frac{3}{2}} l^{-1} \tag{4.2a}$$

$$or\ \varepsilon = c_{\mu} \frac{k^2}{\beta \nu} \tag{4.2b}$$

For the $k - \omega$ and Menter SST models

Specific Dissipation Rate:

$$\omega = \frac{0.09k}{\beta \nu} = \frac{\varepsilon}{k} \tag{4.3}$$

where U is the free stream velocity magnitude, l is the turbulence of eddy length scale, β is turbulence viscous ratio, ν is kinematic viscosity and c_{μ} is a $k - \varepsilon$ model parameter whose value is typically given as 0.09.

In CFD, it is very hard to estimate directly turbulence parameters, k, ε and ω, which do not appear on current available data. Therefore, these turbulence parameters are calculated from assignment of turbulence intensity (I) and either turbulence length scale (l) or turbulence viscosity ratio (β).

4.1.1. Turbulence intensity

Turbulence intensity, I, is defined as the ratio of r.m.s of the velocity fluctuation, u', to the mean free stream velocity, $\overline{u}$,

$$I = \frac{u'}{\overline{u}} \tag{4.4}$$

A turbulence intensity of 1% or less is generally considered low. For external flows, the value of turbulence intensity at the freestream can be as low as 0.05%, depending on the flow characteristics of the experiment. A good estimate of the turbulence intensity at the freestream boundary can be obtained from experimentally measured data. Initial turbulence intensity used can be estimated through the Reynolds number (Saxena, 2008) as

$$I = 0.16Re^{-1/8} \tag{4.5}$$

4.1.2. Turbulence viscosity ratio

Turbulence viscosity ratio (β) is the ratio of turbulence ν_t to laminar (molecular) viscosity (ν_l):

$$\beta = \frac{\nu_t}{\nu_l} \tag{4.6}$$

For external flows the free stream turbulence viscosity ratio is fairly small. Typically, this parameter is set so that $1 < \beta < 10$ (Saxena, 2008)

4.1.3. Turbulence length scale

Sometimes, turbulence length scale is used instead of turbulence viscosity ratio. The turbulence length scale l is a physical quantity which represents the size of the large eddies in turbulent flow and can be estimated by

$$l = 0.07L \tag{4.7}$$

where L is a characteristic length or the physical size of the obstruction, in this case is equal to cylinder diameter D. However, for external flows, it is not possible to determine a good characteristic length, hence, selecting the value of β is more applicable for external flows (Saxena, 2008).

In the current simulation, equations 4.1 – 4.3 are used to estimate the turbulence input values.

4.2. Single circular cylinder

The numerical study will start with the simple case of flow around stationary circular cylinder using RANS turbulence model.

4.2.1. Simulation set up

4.2.1.1 Computational domain and boundary condition

The cylinder studied has diameter D. The computational domain consists of an upstream length 10D and the downstream length 30D and width length 10D (Figure 4.1). The wall boundary conditions including the body used in the simulation are those of impermeability and non-slip condition with the inlet velocity defined by a uniform flow in inline (x) direction. The velocity of the flow is changed to reach the expected Reynolds number in the simulation. The flow exit is treated as pressure outlet. The velocity associated with each specified Reynolds number is shown in Appendix A.

A structured quadrilateral mesh is employed in these simulations. The structured mesh is generated using ANSYS Meshing tool from ANSYS Workbench 12.1. The mesh is imported into ANSYS Fluent. There are 400 elements around the cylinder and 80 elements along the side of the adjacent square area. Figure 4.2a shows the mesh in the computational domain and Figure 4.2b & 4.2c show the mesh near the cylinder.

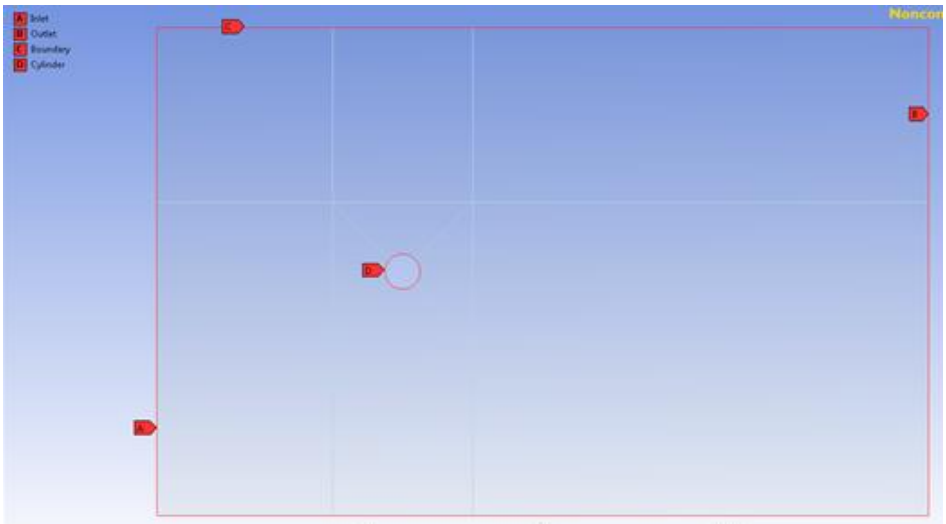

Figure 4.1. Flow domain

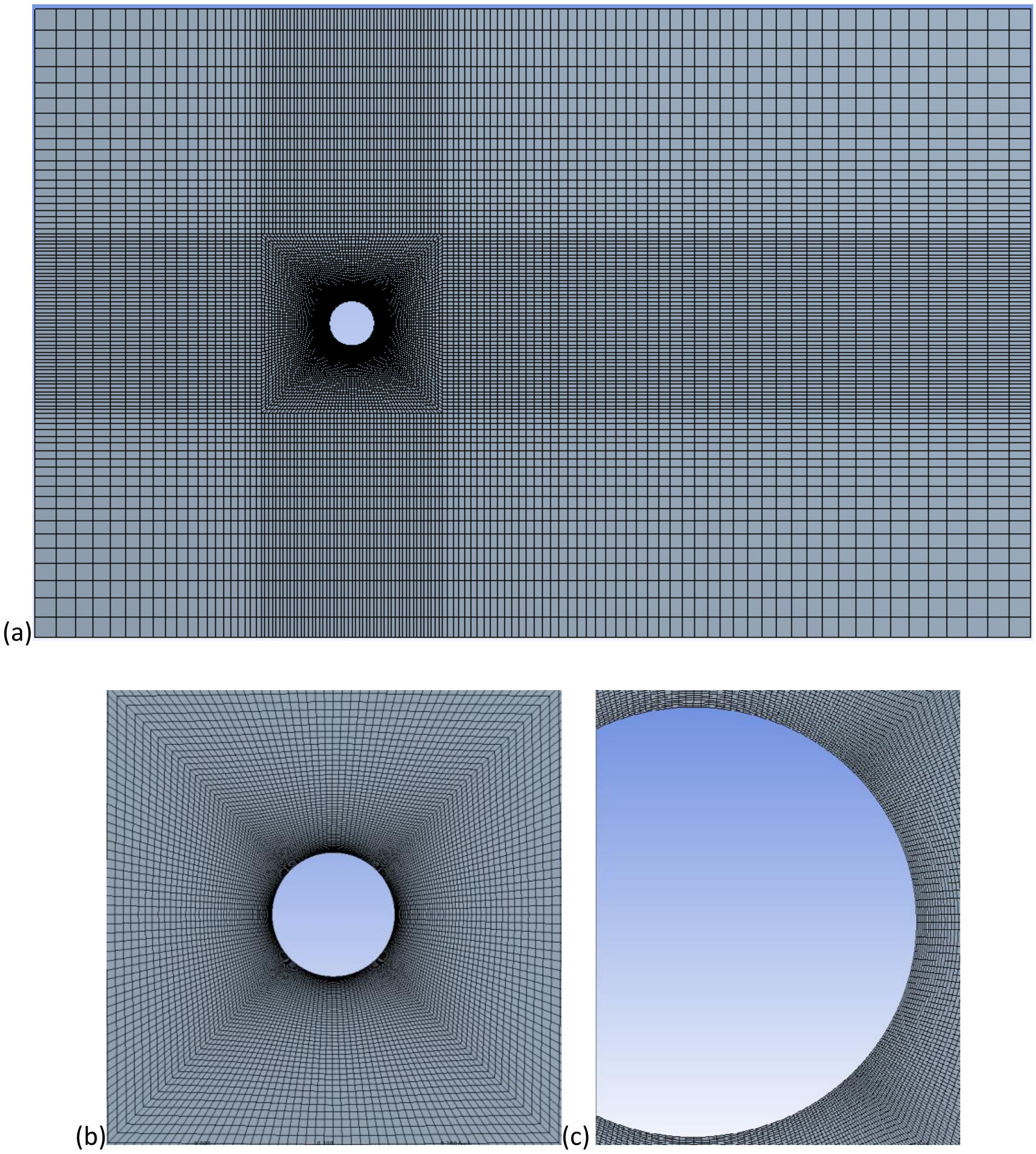

Figure 4.2 Grid generation (a) Computational domain, (b) grid around the cylinder, (c) zoomed view of mesh near cylinder.

In CFD, in order to predict drag coefficients effectively at subcritical Reynolds number, it is necessary to keep the value of $y^+ < 5$ (Section 3.6.2). The first cell height is smaller than 0.0014D to achieve the expected y^+ values. Once the calculations were carried out, the ANSYS report tool is used to re-check the y^+ value. In the current simulation, for Reynolds number of 20,000 the y^+ value is smaller than 1.2 around the circular cylinder (Figure 4.3). For lower Reynolds number (10000), the y^+ around the cylinder is maintained less than 1.

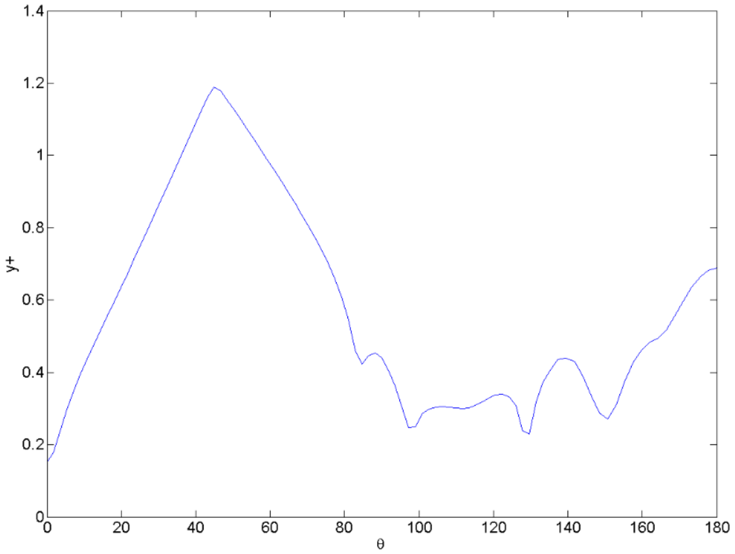

Figure 4.3: Mean y^+ around the cylinder circumference at Re 20000

4.2.1.2. Simulation setting

The numerical solution of this flow is obtained using commercial CFD code: ANSYS Fluent 12.1 and the discretization is based on the finite volume method. In this section, different CFD code setting are summarised as presented in Table 4.1.

Table 4.1 Numerical setting for steady flow, unsteady flow for different Reynolds number

Settings	Re < 47	47 < Re < 1000	1000 < Re < 20000
Simulation type	2D, Steady	2D, Unsteady	2D, Unsteady
Solver	double precision, pressure based	double precision, pressure based	double precision, pressure based
Turbulence model	Laminar	Laminar, $k-\varepsilon$	$k-\varepsilon,\ k-\omega$ and SST model
Pressure	Standard	Standard	Standard
Pressure-velocity coupling	SIMPLE	SIMPLE	SIMPLE
Momentum	2nd order upwind	2nd order upwind	2nd order upwind
Turbulence kinetic energy			2nd order upwind
Turbulence dissipation rate (for $k-\varepsilon$ model)			2nd order upwind
Specific dissipation rate (for $k-\omega$ and SST)			2nd order upwind
Inlet	Velocity inlet	Velocity inlet	Velocity inlet
Outlet	Pressure outlet	Pressure outlet	Pressure outlet
Top wall	Symmetry	Symmetry	Symmetry
Bottom wall	Symmetry	Symmetry	Symmetry
Cylinder	No slip wall	No slip wall	No slip wall

In meshing the solution domain, there are a number of choices designated cell-based gradient method, node-base gradient method and least square cell based or node based gradient method. The accuracy of the least-squares gradient method is comparable to that of the node-based gradient method; both are superior to the cell-based gradient. However, it is less expensive to compute the least-squares gradient than the node-based gradient. Therefore, least square cell-based gradient method has been selected as the default gradient method in the ANSYS FLUENT solver (ANSYS, 2011). In this simulation, convergence occurs when the value of total residual of all afore-mentioned equations becomes smaller than 10^{-5}.

4.2.2. Convergence study

4.2.2.1. Grid convergence study

The first simulation was carried out as a grid convergence study. In order to determine whether the simulation results are independent of the mesh, the convergence of the mesh has to be investigated. Different mesh resolutions from approximately 13,000 to 80,000 elements were tested for the two Reynolds numbers of 3900 and 10000. A structured mesh was used for all grid because of the simplicity of the simulation model. The convergence is checked through changes of mean drag coefficient C_d and r.m.s amplitude of lift coefficient C_l for difference mesh sizes. The summary of the results is shown in Table 4.2. Initially, $k-\varepsilon$ model is used for the convergence test because of its independence from the free stream condition, hence turbulence properties was set with Fluent default values.

Table 4.2. Mesh convergence data of Re = 3900 & 10,000 using realizable $k-\varepsilon$ (RKE)

	Re = 10,000			Re = 3900		
Case	Mesh Size (number of cells)	C_d	C_l	Mesh size (number of cells)	C_d	C_l
A	13300	0.88	0.33	13300	0.97	0.36
B	20300	0.87	0.28	16100	0.98	0.28
C	31200	0.86	0.28	20300	0.94	0.30
D	37800	0.86	0.21	37800	0.92	0.27
E	44800	0.86	0.21	44800	0.92	0.27
F	56010	0.86	0.21	56010	0.92	0.27
G	78000	0.86	0.21	78000	0.92	0.27

Mesh convergence of C_d and C_l for a smooth cylinder for Re equal to 3900 and 10000 are also presented in Figure 4.4. As can be observed from this diagram, the value of C_d and C_l change very slightly or did not change when the number of elements exceeded 37000. The pressure distribution (C_p) around the cylinder as shown in Figure 4.5 also indicated that from mesh C (medium) onwards, there is very little change in the pressure distribution. So, the mesh size of 44800 (medium 2 mesh) will be used to carried out further calculations. Additional results will be presented in the section 4.2.3.

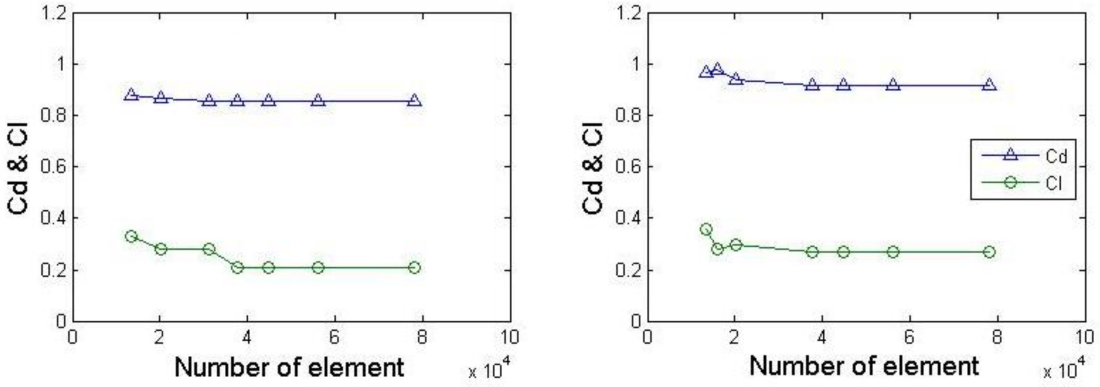

Figure 4.4 Drag and lift coefficients at different grid resolution using realizable $k-\varepsilon$ (a) Re = 10,000, (b) Re = 3900

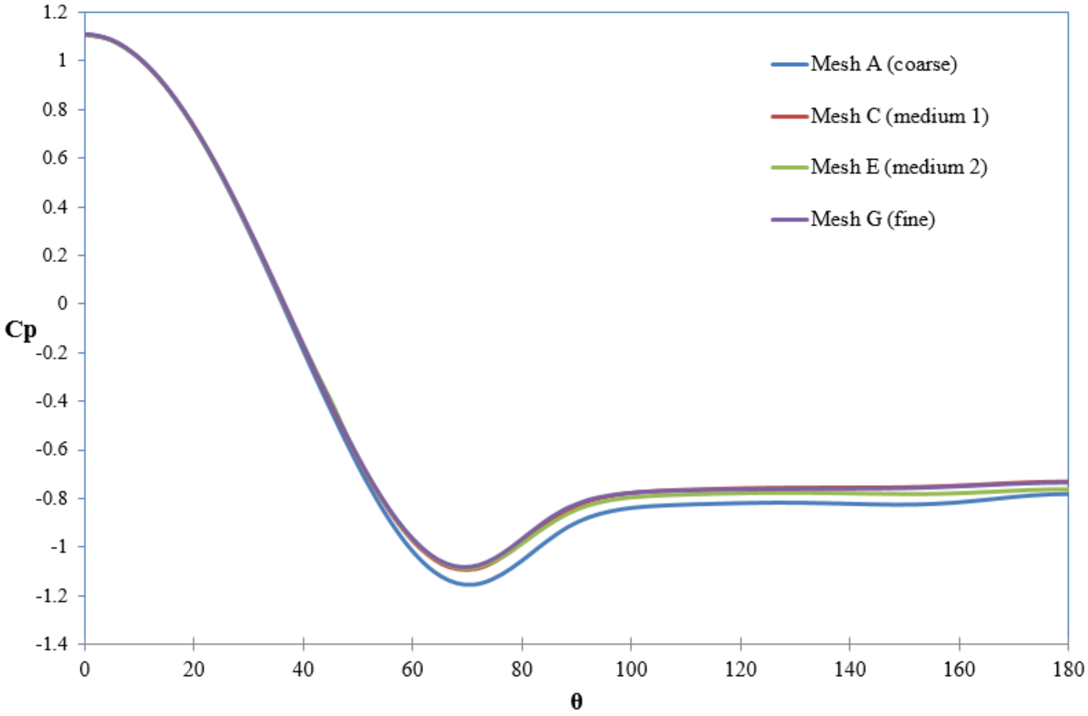

Figure 4.5. Mean pressure distribution around the cylinder at Reynolds number 3900

4.2.2.2. Time step convergence

Courant number is an important quantity to consider for solution convergence and is related to time step, first cell height and velocity selected appropriate, defined by:

$$C = \frac{U\delta t}{\Delta} \tag{4.8}$$

where δt is time step, U is velocity of flow and Δ is first cell height.

Due to Courant – Fredrich - Lewy condition (Courant et al., 1928), the Courant number should be chosen to be $C \leq 1$ to maintain simulation accuracy. Different time steps were tested to validate the model used for Re = 3900 and Re = 10000. The convergence is checked by changes in C_d and C_l for different Courant numbers from 0.5 to 32. The results are shown in Figure 4.6. The values of C_d and C_l change very slightly or did not change when the value of $C \leq 2$, which satisfy Courant – Fredrich - Lewy condition. In this work, simulation will be carried out with time step to keep $C \leq 1$.

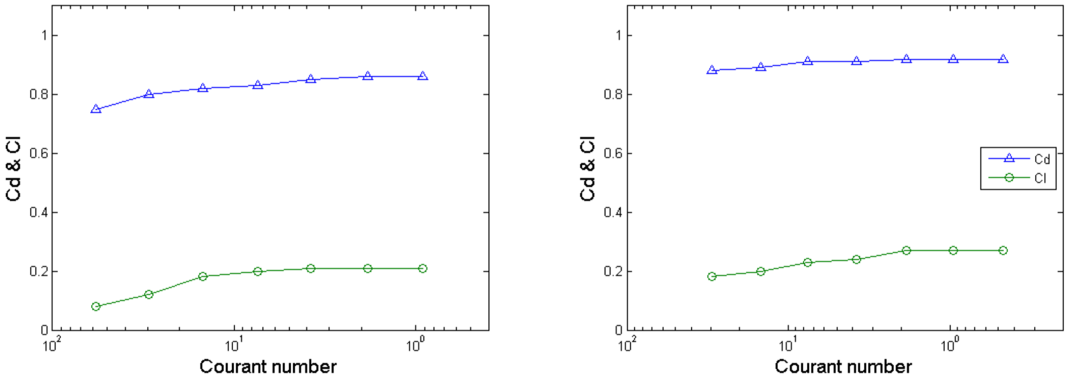

Figure 4.6. Courant number convergence chart at (a) Re = 10,000, (b) 3900 using realizable $k-\varepsilon$ model

4.2.3. Simulation results

4.2.3.1. Drag coefficient for $10 \leq Re \leq 20000$

Drag is an important characteristic to be considered, since drag plays a central role in flow around cylinder research. The drag of a cylinder has been investigated with a wide range of Reynolds number from 10 to 20,000. The laminar model is used up to Re = 189 and the turbulence model is used for higher Reynolds numbers.

Figure 4.7 compares the drag coefficient from ANSYS Fluent with established experimental data from Wieselberger (1921), Schlichting and Kestin (1979) and numerical result by Stephen et al (2011) using 3D LES. Results show very good agreement in terms of drag coefficient with experiment up to Reynolds number equal to 20,000. In general, the results reflect the good agreement in drag for both laminar and subcritical regions. Application of turbulence model shows the accuracy in predicting drag around the circular cylinder in different Re.

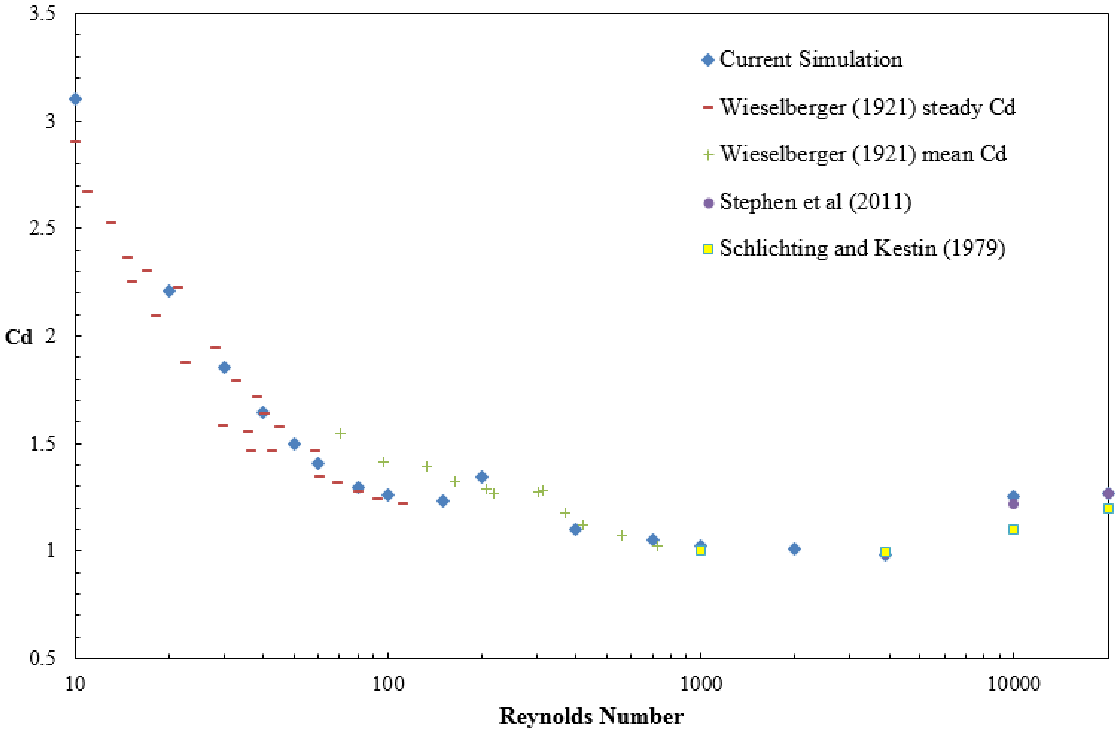

Figure 4.7. Drag coefficients over a range of Reynolds numbers

4.2.3.2. Drag and lift coefficient in turbulence flow (Re = 3,900 and 10,000)

The flow around a circular cylinder is 2D only when $Re < 190$ and for larger Reynolds number, the flow generated is 3D. But in this research project, 3D is really expensive in terms of computational cost. Therefore, the flow around the circular cylinder is carried out using a 2D FVM. For Re = 3900 and 10,000, the two-equation model used include $k-\varepsilon$ and $k-\omega$ formulations. Each formulation offers alternative options i.e. standard $k-\varepsilon$ (SKE) or realizable $k-\varepsilon$ (RKE) and standard $k-\omega$ (SKW) or Shear stress transport (SST) $k-\omega$ (SST KW). Alternatively, there is a more extensive ANSYS four-equation SST model. The calculated drag and lift coefficients (C_d & C_l) based on 2-equation and 4-equation models are compared with available experimental data in Table 4.3 together with associated values of S_t number.

Table 4.3. Summary of drag, lift coefficient and Strouhal number at Re = 3900 and 10000.

Reynolds numbers	3900			10000		
	C_d	C_l	S_t	C_d	C_l	S_t
Laminar	1.6	1.4	0.2	1.7	1.5	0.21
SKE	0.8	0.05	0.2	0.7	0.19	
RKE	0.98	0.4	0.22	0.92	0.4	0.21
SKW	1.2	0.7	0.2	1.25	0.7	0.2
SST KW	1.63	1.5	0.22	0.91	0.2	0.21
SST	1.6	1.6	0.23	1.65	1.75	0.21
VMS – LES (Stephen et al, 2011)	0.99		0.21	1.22		0.2
Experiment (Lourenco and Shih, 1993)*	0.985	-				
Experiment (Breuer 1998)*	1.08					
Experiment (Chen and Ballenge 1971)*	-	0.38		-	0.47	
	-	0.44		-	0.58	
Experiment (Bishop and Hassan 1963)*				-	0.58	
Experiment (Keefe 1961)*				-	0.38	
Experiment (H. Schlichting 1979)*	0.995	-		1.1	-	
* Those data is obtained from Flow induced vibration studies of Blevins (2001)						

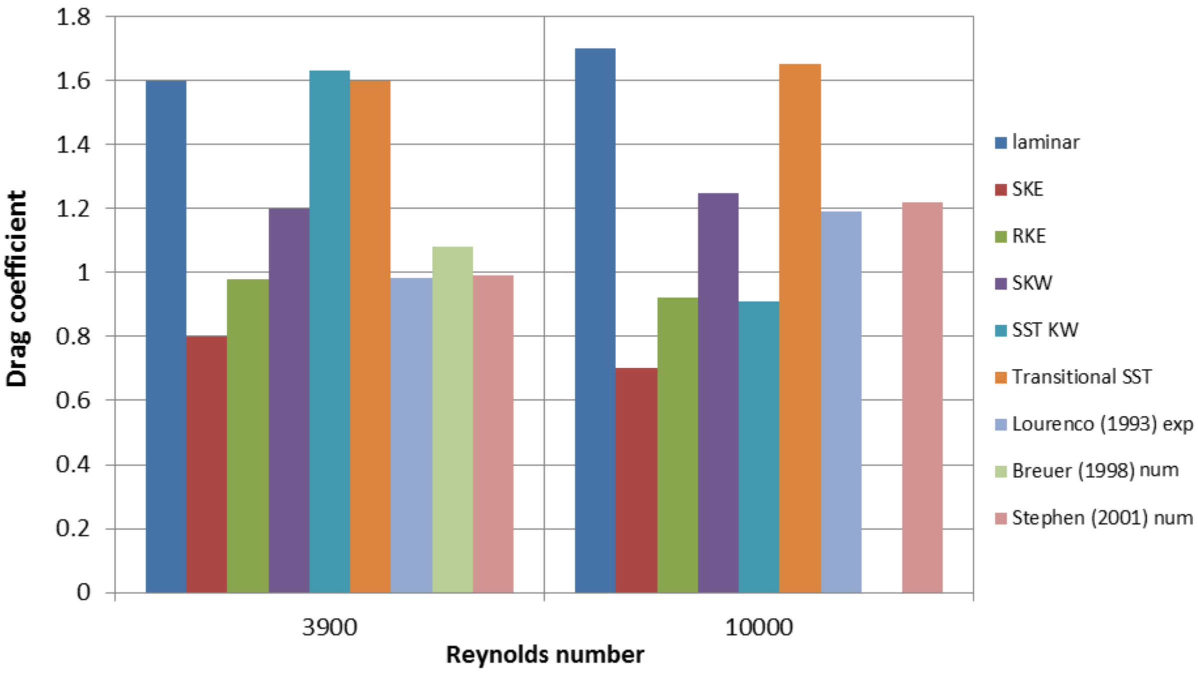

Figure 4.8. Drag coefficient for various turbulence models for Re = 3900 & 10000

Figure 4.8 shows the drag coefficient for different Reynolds numbers. Compared with experimental data carried out by Lourenco and Shih (1993) and numerical simulation by Breuer (1998), Stephen et al (2011) using LES. The drag coefficient given by RKE, and SKW show reasonably good agreement (difference less than 10%) with experimental and numerical data.

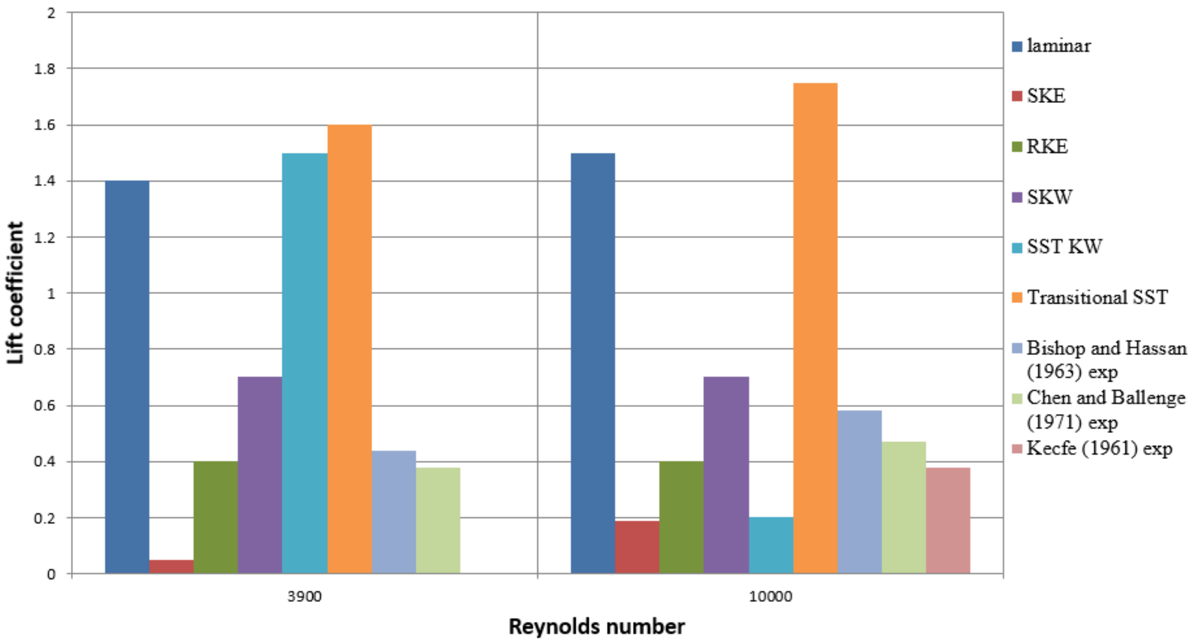

Figure 4.9. Lift coefficient amplitude for various turbulence model for Re = 3900 & 10000

Figure 4.9 compares the lift coefficient amplitude from Fluent with experimental data from Keefe (1961), Bishop and Hassan (1963), Chen and Ballenge (1971) (refer to table 4.3). Results show good agreement for simulations carried out using the RKE method at Reynolds number 3900 for both lift and drag coefficient and SKW for Re 10,000 for drag coefficient. The other turbulence methods show variations in the value of the lift coefficient amplitude, whose magnitude shows sensitivity in the experiment and numerical methods included.

The values of lift and drag coefficient given by the current simulation using a two-equation turbulence model (RKE and SKW) are very close to the experimental results. Those values are also close to the more computationally intensive LES results obtained by Stephen et al (2011). The vortex created by turbulence model SKW can be seen in Figure 4.10. In both Re 3900 and 10,000, the vortex patterns is in 2S forms, that agree well with LES numerical simulation by Stephen et al (2011).

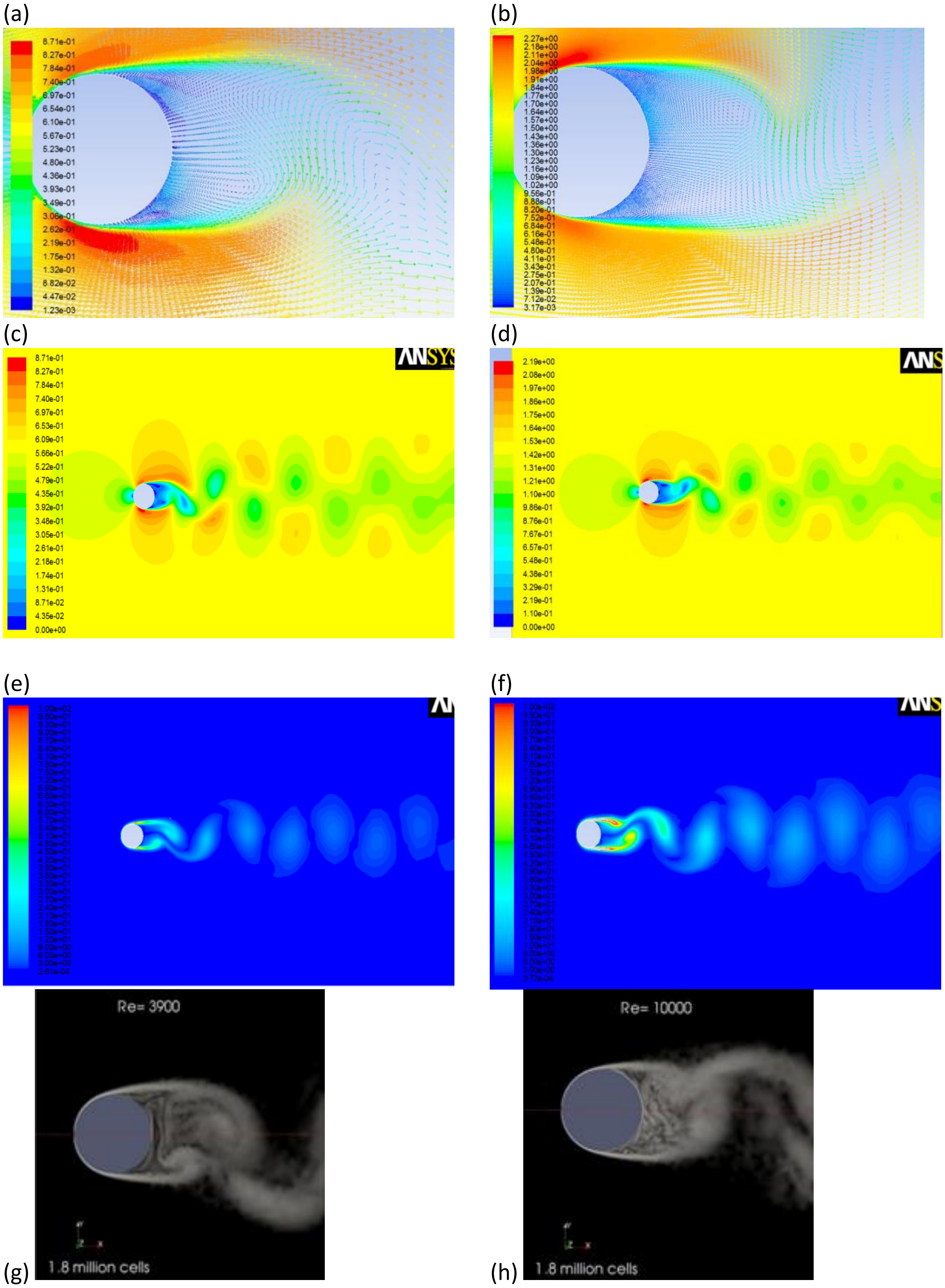

Re = 3900 Re = 10000

Figure 4.10. Vortex shedding at downstream of the cylinder using SKW model (a,b) Velocity vector, (c,d) velocity contour, (e,f) Vorticity magnitude (1/s) at Re = 3900 & 10000, (g,h) snapshot for vorticity modulus (Stephen et al, 2011)

4.2.3.3. Pressure distribution

The pressure distributions around the circular cylinder at Re = 3900 and Re = 10000 have also been calculated using two turbulence models RKE and SKW. Figure 4.11 and 4.12 show the mean pressure coefficient at the cylinder obtained at Re = 3900 and 10000. The overall agreement is good at these two Re numbers and the prediction of C_p at stagnation point is good. However, the prediction is slightly bigger than the experiment results for SKW model results when $\theta > 50^o$. The current simulation results using RKE are shown to be as good as the results obtained by VMS - LES carried out by Stephen et al (2011) and Norberg (2002) at $Re = 8000$.

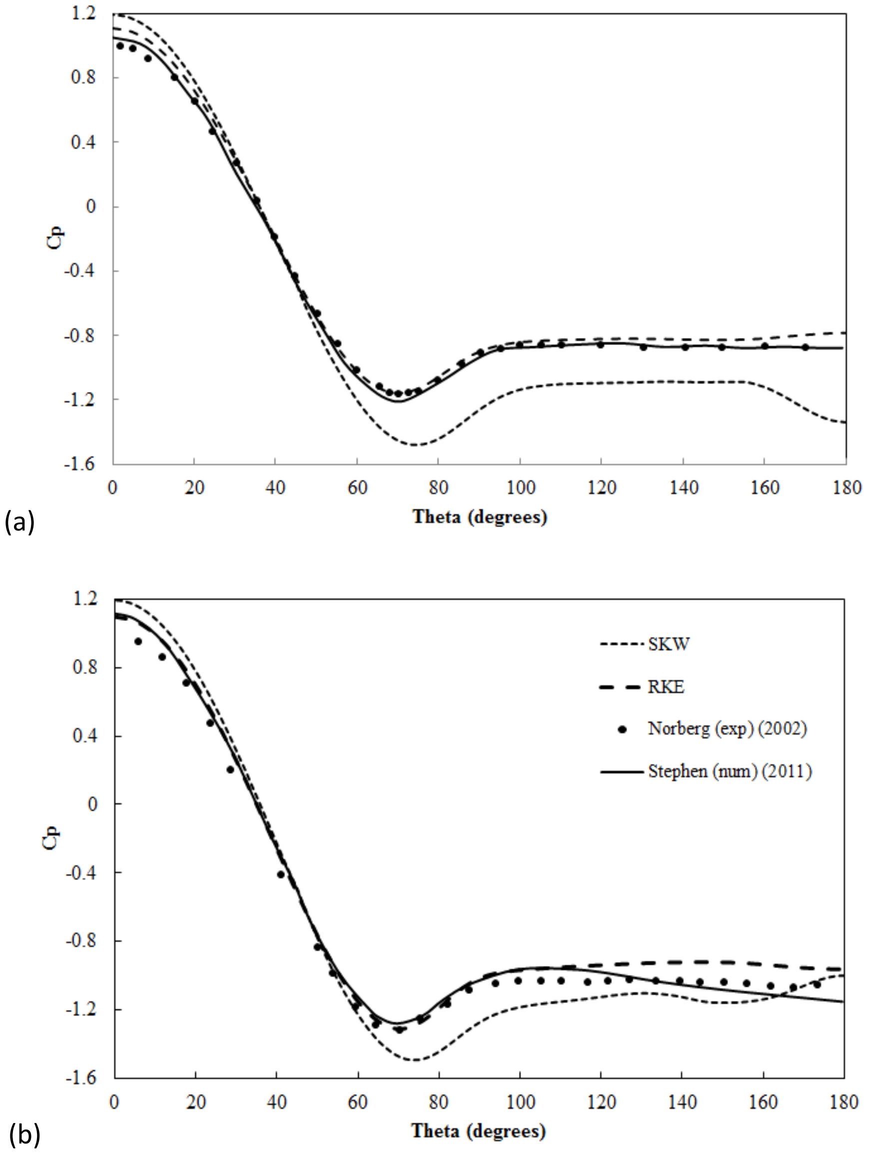

Figure 4.11. Mean pressure coefficient distribution at the cylinder at (a) 3900 and (b) Re = 10000

4.2.4. Conclusion

To begin with, the grid convergence studies showed that a medium size mesh of 44,800 elements is sufficient for accurately describing flow past a stationary cylinder for Re = 3900 & 10,000. Furthermore, the time step convergence studies showed that a Courant number value of 1 or less is sufficient.

The study for Re = 3900 and 10000 using SKE, RKE, SKW, SST KW, and SST turbulence model showed that C_d & C_l are sensitive to turbulence modelling. The RKE model produced good overall results in lift, drag, pressure distribution coefficient and Strouhal number at Reynolds number up to 3900, and SKW showed good agreement for the higher Reynolds number. RKE and SKW models showed the greatest potential for application in VIV in the applied Reynolds number range in subcritical Reynolds number. However, both model show some strengths and weaknesses

The variation of drag coefficient with Reynolds number showed good agreement with experimental results. Furthermore, the predicted drag coefficient is as good as the computationally intensive LES prediction. The 2S vortex-shedding pattern (Section 2.8) was also captured correctly, see Figure 4.10 e,f.

4.3. Flow around two cylinders in a tandem arrangement

In this section, the unsteady viscous flow around two stationary circular cylinders in a tandem arrangement is investigated numerically using a 2D CFD RANS code. Simulations are presented for the subcritical Reynolds number 22,000, with cylinder separations 2 < L/D < 5 due to available validation results e.g. Kitagawa and Ohta (2008). The computed drag and lift coefficients and Strouhal number are compared with experimental measurements and other numerical predictions. The purpose of the research in this section is to choose the appropriate turbulence model that works not only for the single cylinder but also for the tandem case.

4.3.1. Numerical simulation and boundary conditions

4.3.1.1. Computational domain and boundary condition

The geometric size of the computational domain and the boundary condition of all simulations are shown in Figure 4.12. The model philosophy is similar to a single cylinder case.

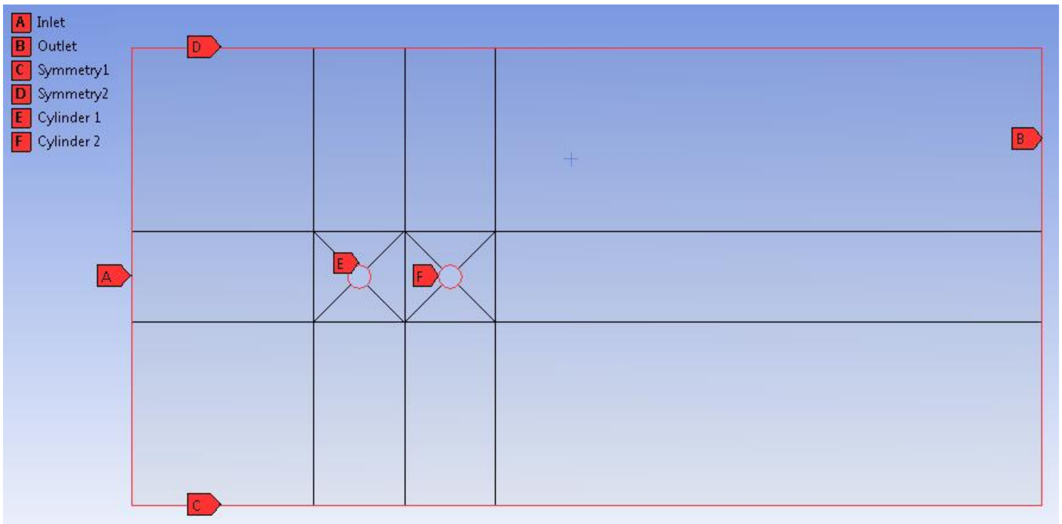

Figure 4.12. The geometric for size of the computational domain for L/D = 4

The two cylinders of equal diameter (D) are placed in 20Dx45D rectangular domain, in which the centre of the upstream cylinder is located at 10D from the inlet boundary and the centre of the downstream cylinder is placed at distances of 30D – 33.5D from the outlet boundary, depending in the separation L. The upper and lower boundaries are both located at 10D from the centre of both cylinders. This domain size has been used by Dehkordi et al. (2011) and showed remarkably good results.

The velocity boundary and initial conditions for all simulations are as follows:

- no-slip conditions on the cylinder surface
- uniform flow at the inlet in x direction ($u = U, v = 0$).
- the upper and lower boundaries were treated as symmetries.
- Free outflow pressure outlet.

4.3.1.2. Grid generation

A structured quadrilateral mesh is also employed in these simulations using ANSYS Meshing tool. Figure 4.13 shows the mesh generation in the computational domain. Value of y^+ around 1 and in the whole domain y^+ < 1.2 for the Reynolds number used on both upstream and downstream cylinders. After the calculations were carried out, ANSYS report tool is used to check the estimates for the y^+ value. The least square cell-based gradient method is also chosen.

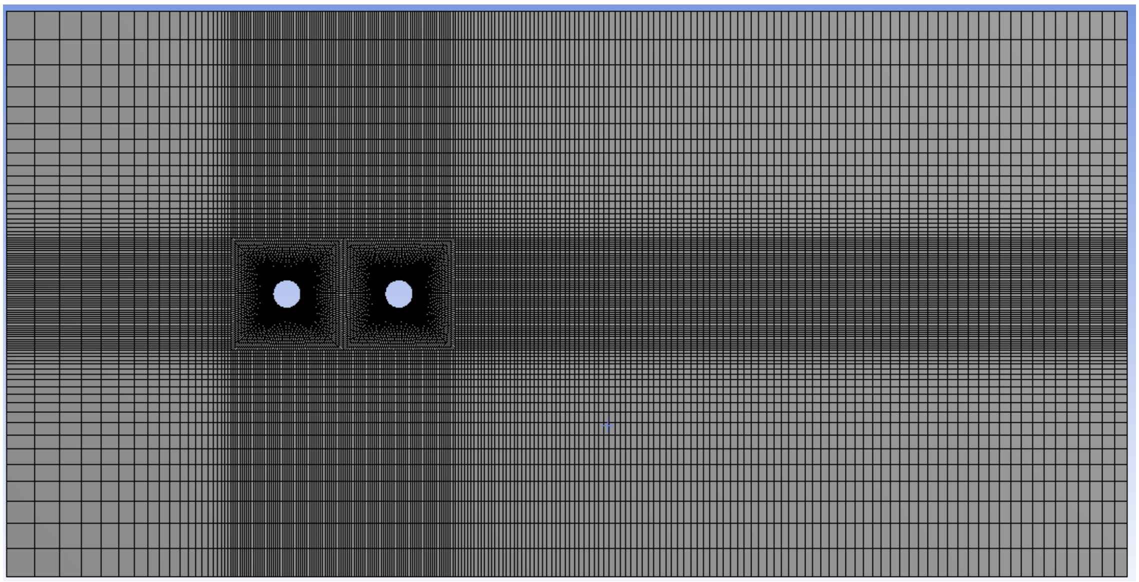

Figure 4.13. Grid system for L/D = 4 with 75000 quadrilateral elements

4.3.2. Grid convergence

To check the convergence of the mesh used, simulations have been run with various grid resolution using SKW model, as shown in Table 4.4.

Table 4.4 Drag coefficient for cylinders in tandem at L/D = 3.5

Case	Grid resolution	C_{d_1} (UC)	C_{d2} (DC)	% different in C_{d_1}	% different in C_{d2}
mesh 0	39309	1.23	0.21	-	-
mesh 1	55700	1.19	0.238	3.36	-11.76
mesh 2	75000	1.165	0.24	2.15	-0.83
mesh 3	108700	1.163	0.238	0.17	0.84
mesh 4	145000	1.162	0.24	0.09	-0.83

The simulation results record very minor changes from mesh 2 onwards (75000 elements), with mesh 3 leading to 0.17% difference relative to mesh 2 in the upstream (UC) drag coefficient and 0.84% change in the downstream (DC) drag coefficient. Hence, mesh 2 is used for this research. The Courant number was controlled to be $C \leq 1$ for all the simulations to achieve converged results (Linh, 2012).

4.3.3. Turbulence parameter sensitivity

For the flow around cylinders, and external flows in particular, it is very important to specify appropriate turbulence quantities at the freestream boundaries. If the values are unphysical it can cause the solution to be unrealistic and can lead to divergence or non-convergence. Turbulence intensity (I) is stated in experimental results, but the turbulence viscosity ratio (β) is not. According to Saxena (2008), in external aerodynamic flows, selecting smaller values of β (0.1 to 1.4) is recommended, whereas in the case of wind-tunnel external flows, larger values of β (1 to 10) are suggested. Using a wide range of turbulence viscosity ratios, the parameter sensitivity setup is carried out to find out its interaction with other turbulence parameters, i.e I, l and β.

4.3.3.1. Effect of turbulence intensity

The effect of turbulence intensity is examined using RANS code, realizable $k-\varepsilon$ turbulence model. The flow around a single cylinder was used to reduce computational cost. The turbulence intensity had very minor effect at low turbulence intensity value ($I < 1.4\%$). When the inlet flow has high turbulence intensity, the lift and drag coefficients for the cylinder are greatly affected with dramatic changes as shown in Figure 4.14. The range of turbulence for I was chosen based on values by Ljungkrona et al. (1991). The other setups and turbulence parameters remained the same.

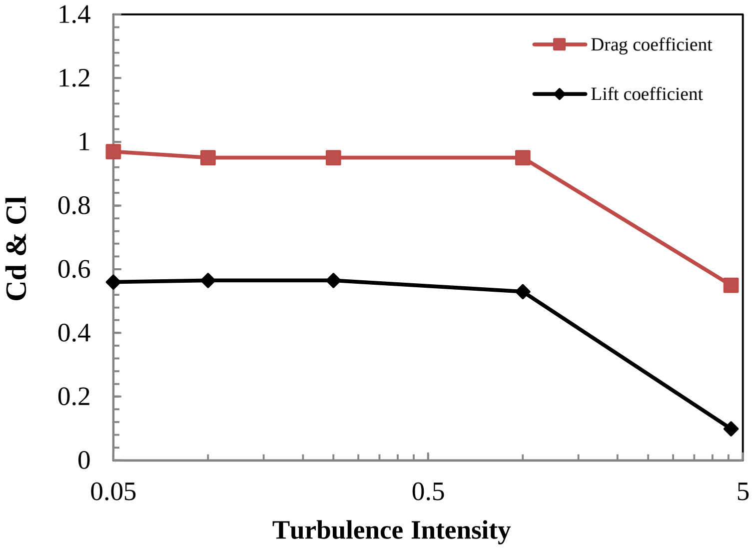

Figure 4.14. C_d & C_l for different turbulence intensity for a single cylinder, Re = 22000.

For freestream inlet condition, the turbulence intensity will be selected to be smaller or equal to 1.4%. At this value, the turbulence intensity shows a negligible effect on the force coefficients around a circular cylinder.

4.3.3.2. Effect of turbulence intensity (*I*) and turbulence viscosity ratio (β)

In Fluent, the turbulence intensity and viscosity ratio are commonly used to estimate the initial inlet flow condition. The appropriate selection of these parameters is essential to achieve accurate results from the simulation. The sensitivity test for the effect of I and β was carried out in standard $k-\omega$ (SKW) and SST $k-\omega$ turbulence models. Variation in drag coefficients for both upstream and downstream cylinder will be observed based on changes in I and β. Turbulence intensity values

(0.1, 1.4, 3.2) for different turbulence viscosity ratios (0.1 to 10) were used. The numerical simulations were carried out for 6 different separations L/D = 2, 2.5, 3, 3.5, 4, 4.5 and 5.

Examining Figure 4.15 for standard k - ω, no discernible trend can be observed, especially for low turbulence intensity. There is no discernible trend for βeither. However, with the higher turbulence intensity, e.g. 1.4 & 3.2 more stable trends are observed. It also demonstrates that an increase in turbulence viscosity ratio will reduce the drag coefficient of the upstream cylinder. Examining Figure 4.16 for SST k - ω, the change in I and β show small changes in drag coefficient for both the upstream and downstream cylinder. The trend is that drag coefficient decreases when β increases.

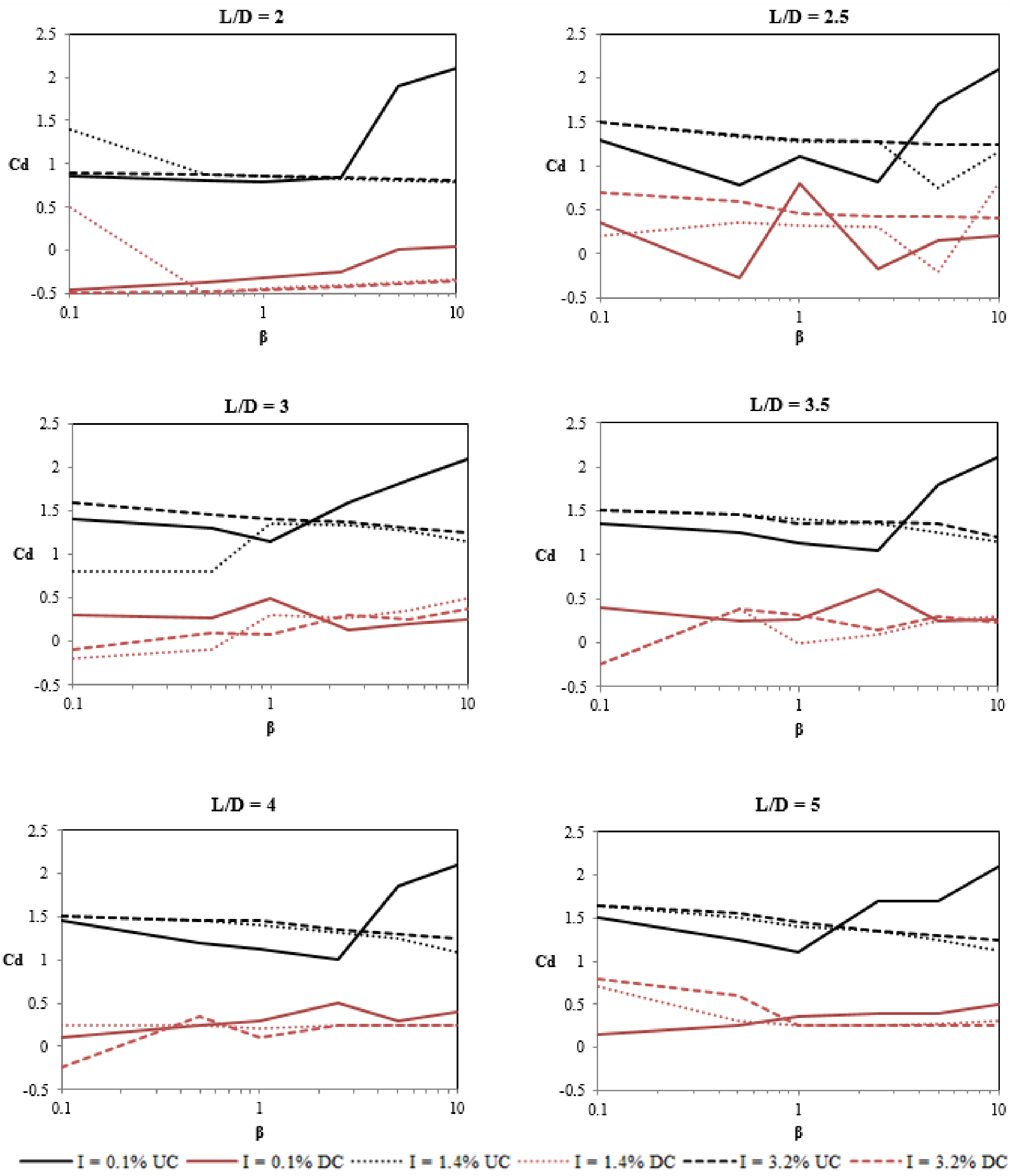

Figure 4.15 Effect of *I* and β on Cd for various cylinder separations L/D, standard k – ω, Re = 22000

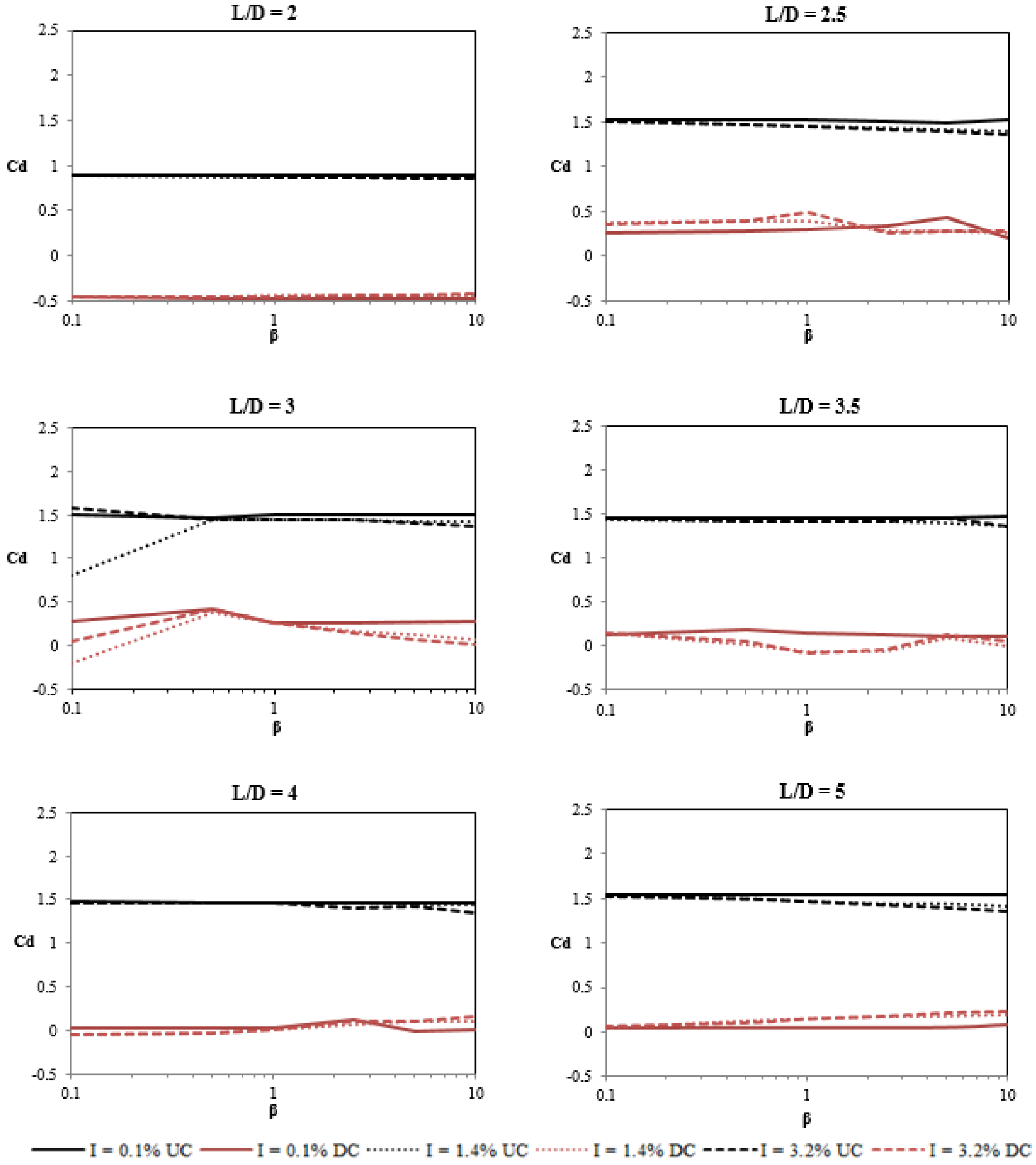

Figure 4.16 Effect of *I* and β on Cd for various cylinders separations, L/D SST k – ω, Re = 22000

Overall, the results indicate that SKW model is sensitive to changes of turbulence intensity and turbulence viscosity ratio while SST $k - \omega$ is least affected. Therefore, standard $k - \omega$ turbulence model is appropriate to investigate the flow in different turbulence intensity condition.

4.3.3.3. Turbulence length scale effect

Ljungkrona et al. (1991) published experimentally measured turbulence length scales and turbulence intensity values. This current work tried to replicate his experiment at L/D = 2.5 using the experimental conditions. The results show that both standard $k - \omega$ and SST $k - \omega$ can meet the experimental results, as shown in Table 4.5 and Figure 4.17.

The numerical results show a lack of agreement with the Ljungkrona experimental results. The standard $k - \omega$ partly agrees with experimental values for the Upstream cylinder Cd while SST $k - \omega$ agrees with the experimental value for the downstream cylinder C_d at I = 1.4 and 3.2% only.

Table 4.5. Drag coefficient at L/D = 2.5

L/D	Turbulence Intensity I (%)	Turbulence length scale (l)	Ljungkrona et al		SKW		SST $k - \omega$	
Re			20,000		22,000		22,000	
2.5			UC	DC	UC	DC	UC	DC
	0.1	0.07	0.92	-0.23	0.75	-0.20	1.50	0.40
	1.4	0.6	0.98	0.32	1.25	0.00	1.39	0.40
	3.2	0.5	1.02	0.43	1.10	-0.08	1.30	0.50

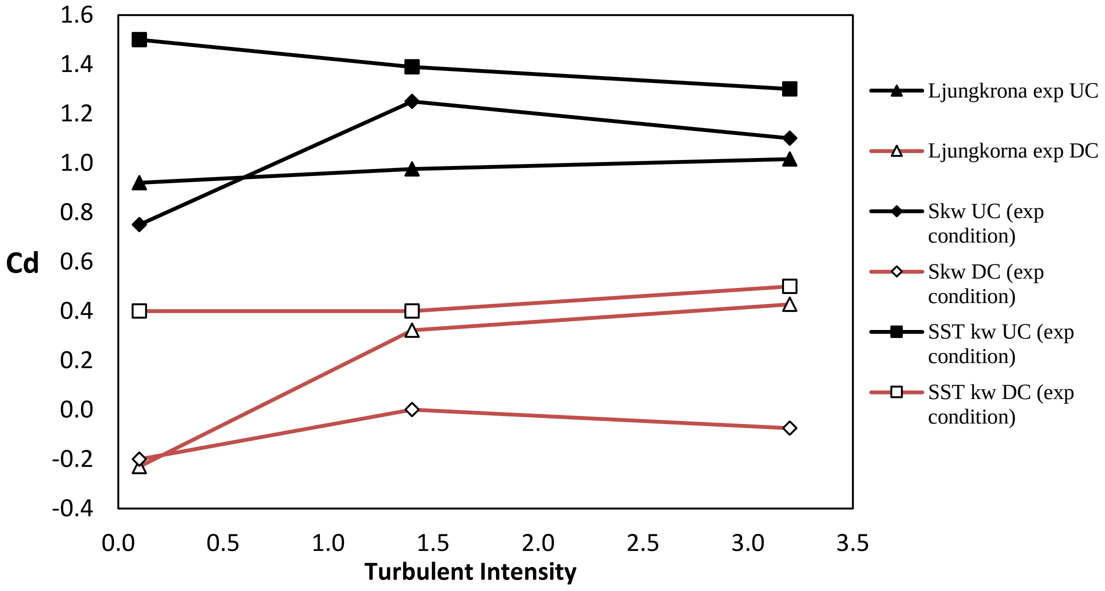

Figure 4.17. Comparison numerical and experimental results at L/D = 2.5

As the application of turbulence length scale showed the disagreement with experimental results, so that, l is not used as an input value for the current simulations.

4.3.4. Summary of results

4.3.4.1. Drag & lift coefficient and Strouhal number

All simulations have been performed at Re = 22,000 in sub-critical regime in order to compare with the experimental study of Ljungkrona et al. (1991) and the numerical study of Kitagawa and Ohta (2008) using LES. Six cylinder separations of L/D = 2, 2.5, 3, 3.5, 4, 5 are selected for the numerical study. The time step size is set to 0.016s and the Courant number is kept smaller than 1 (typically

0.5). Based on the studies of sections 4.3.3, Figure 4.15 & 4.16 support the decision to use $I = 0.1$ and β = 0.5.

Table 4.6. Summary of turbulence models applied

Re	Turbulence model	Comments
2.2×10^4	RKE	Low turbulence inlet condition, ($I \leq$ 1.4%, $\beta \leq 10$)
2.2×10^4	SKW	
2.2×10^4	SST KW	

RKE, realizable $k - \varepsilon$; SKW, Standard $k - \omega$; SST KW, SST $k - \omega$.

The previous research showed that RKE is the most appropriate method for the flow around a single cylinder with the Reynolds number under 10,000. However, it had been shown that the drag coefficient was underestimated and SKW models provide better results in terms of drag coefficient (Linh, 2012).

Initially, RKE was used for researching flow around two cylinders in tandem. The RKE, as shown in Figure 4.18 predicts the general trend of the model, but the drag in both upstream and downstream cylinder is underestimated. This is similar to that observed with the single cylinder. In the flow around two cylinders, the RKE method continues to underestimate drag coefficients on the upstream cylinder, but for the downstream cylinder, the results show a better agreement with Ljungkorna's study. The "jump" is recorded at the critical region of L/D = 3.

The SKW is used in the next with low turbulence intensity ($I \leq$ 1.4%). Drag coefficients for both upstream and downstream cylinders agree with the experimental results by Ljungkrona et al. (1991). The current results show better drag coefficient prediction for the downstream cylinder compared with the LES methods by Kitagawa and Ohta (2008).

The SST k-w turbulence model shows the worst agreement, compared with the other two turbulence models, as seen in Figure 4.18 and Table 4.7. The SST k-w model over predicts the drag coefficient for the upstream cylinder and cannot show a trend similar to other numerical or experimental results for both UC and DC (see Table 4.7).

Table 4.7. Summary of turbulence models results.

Turbulence model		RKE		SKW		SST KW		Ljungkrona, et al. (Exp)	
Re		22,000		22,000		22,000		20,000	
	L/D	C_d (UC)	C_d (DC)	C_d (UC)	C_d (DC)	C_d (UC)	C_d (DC)	C_d (UC)	C_d (DC)
22000	2.00	0.70	-0.26	0.865	-0.453	0.89	-0.46	0.94	-0.40
	2.50	0.65	-0.20	0.78	-0.27	1.50	0.29	0.92	-0.23
	3.00	0.62	0.03	0.8	-0.2	1.50	0.27	0.86	-0.08
	3.50	0.70	0.35	1.125	0.27	1.45	0.20	1.19	0.43
	4.00	0.70	0.25	1.13	0.3	1.47	0.13	1.21	0.42
	5.00	0.70	0.25	1.1	0.35	1.55	0.04	1.19	0.40

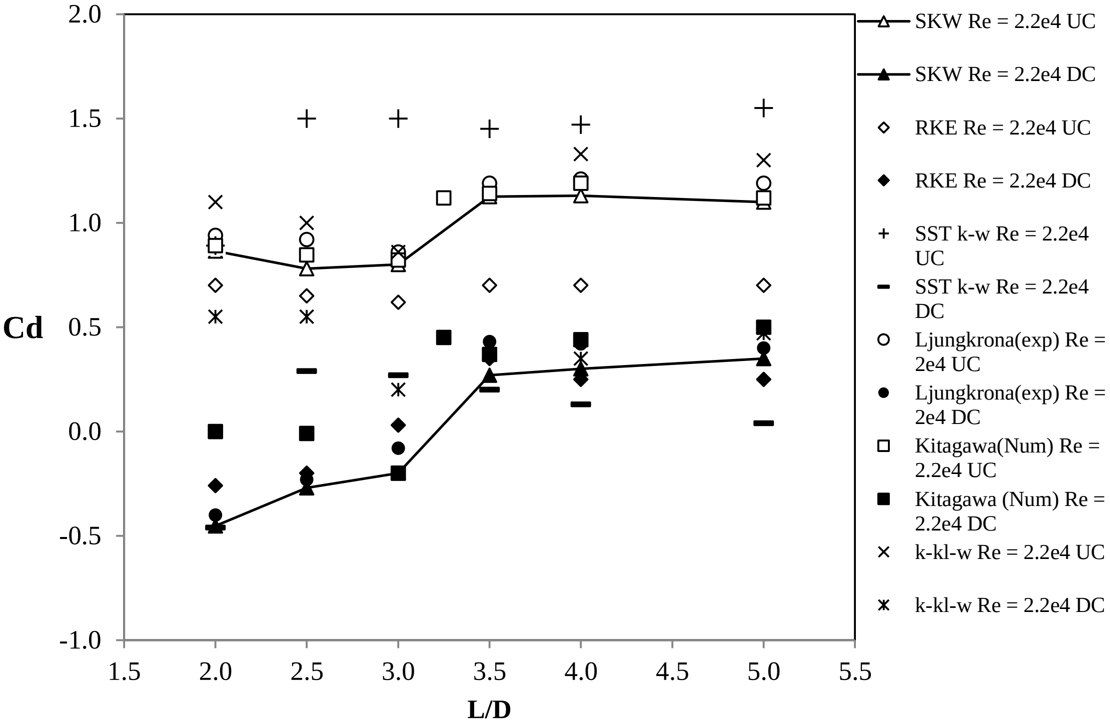

Figure 4.18. Variation of drag coefficient with cylinder spacing, L/D, at Re 20,000 & 22,000

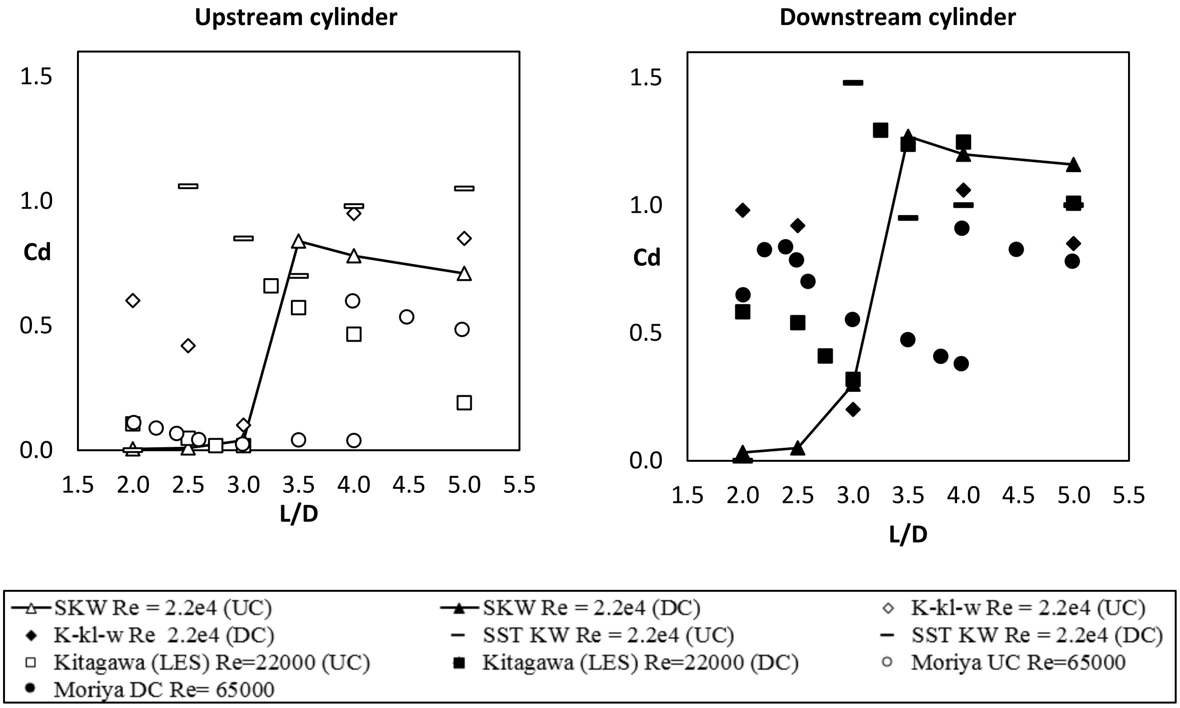

Figure 4.19. Variation of lift coefficient with cylinder separations, L/D, for Re = 22,000 & 65,000

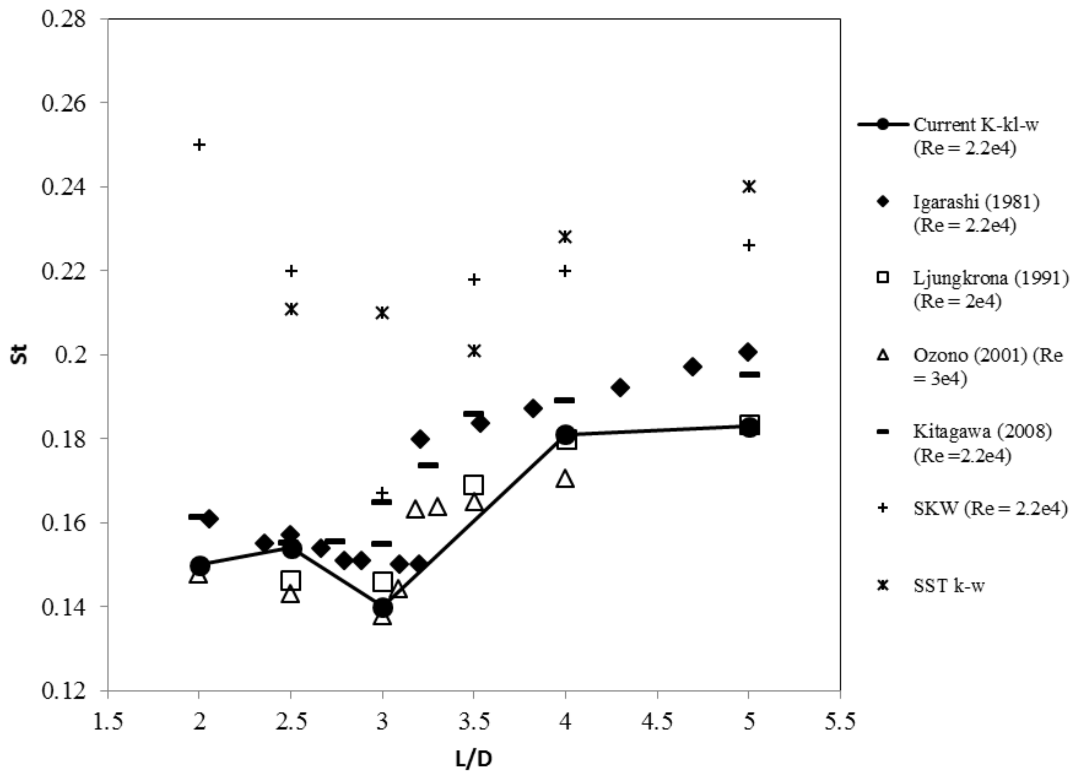

Figure 4.20. Variation of Strouhal number with cylinder separation, Re = 20,000, 22,000 & 30,000

The lift coefficient, shown in Figure 4.19, agrees with the LES numerical simulation by Kitagawa and Ohta (2008) for the downstream cylinder and over-predicts for the upstream cylinder. It is worth noticing that the results by Moriya et al. (1983) for Re = 65000 showed that the critical L/D value, where the jump occurs, increases with increasing Re. The Strouhal, St was obtained from the lift coefficient time history and Figure 4.20, shows the relationship between L/D and St number. The alternative $k-\omega$ base model, $k-kl-\omega$ showed the best agreement with the experiment results by Ljungkrona et al. (1991), Ozono et al. (2001) and other. For L/D <3, the St value decreases gradually as L/D value increases. At L/D = 3, as shown in Figure 4.20, the St was 0.14. The value of St jumps to 0.181 at L/D = 4. However, SKW and SST KW are unable to match experimental results.

4.3.4.2. Pressure distribution

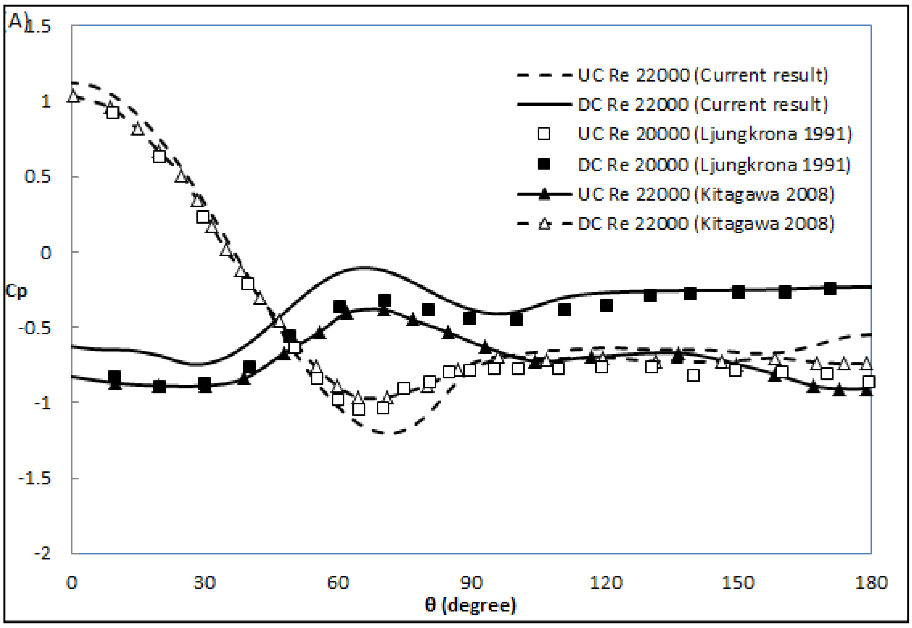

Figure 4.21. Comparison of C_p around both cylinders at L/D = 2 at Re 22,000 & 22,000

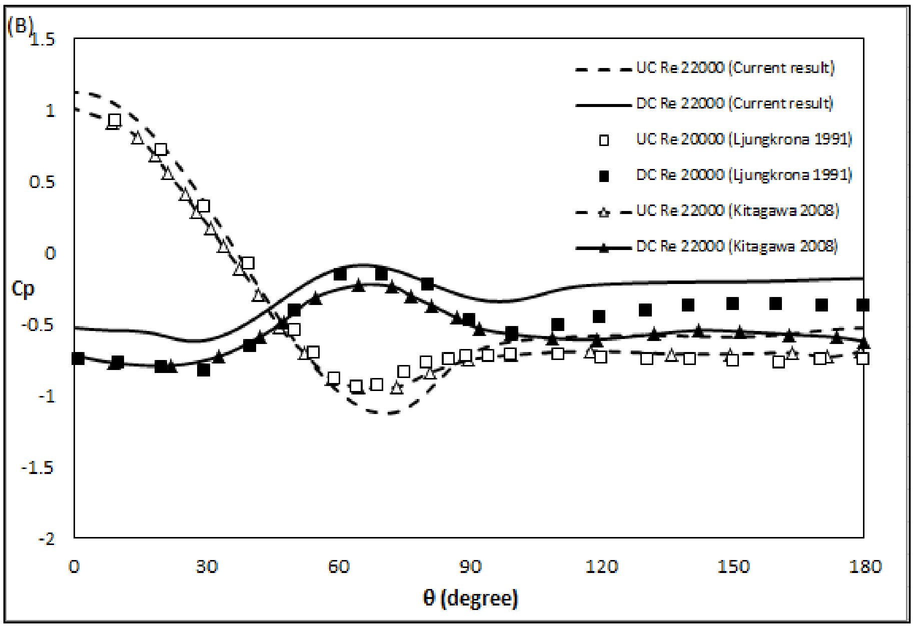

Figure 4.22. Comparison of C_p around both cylinders at L/D = 2.5 at Re 20,000 & 22,000

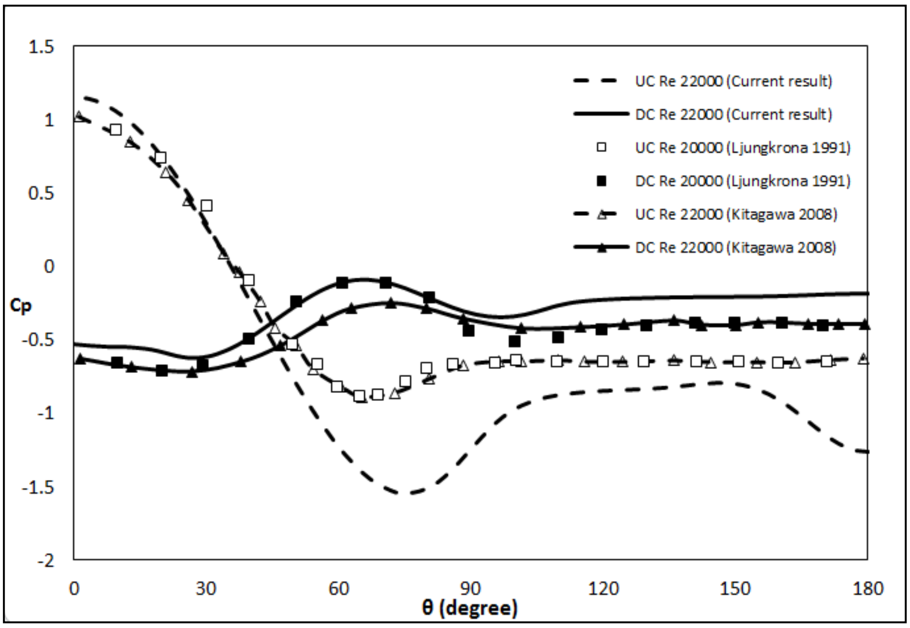

Figure 4.23. Comparison of C_p around both cylinders at L/D = 3 at Re 20,000 & 22,000

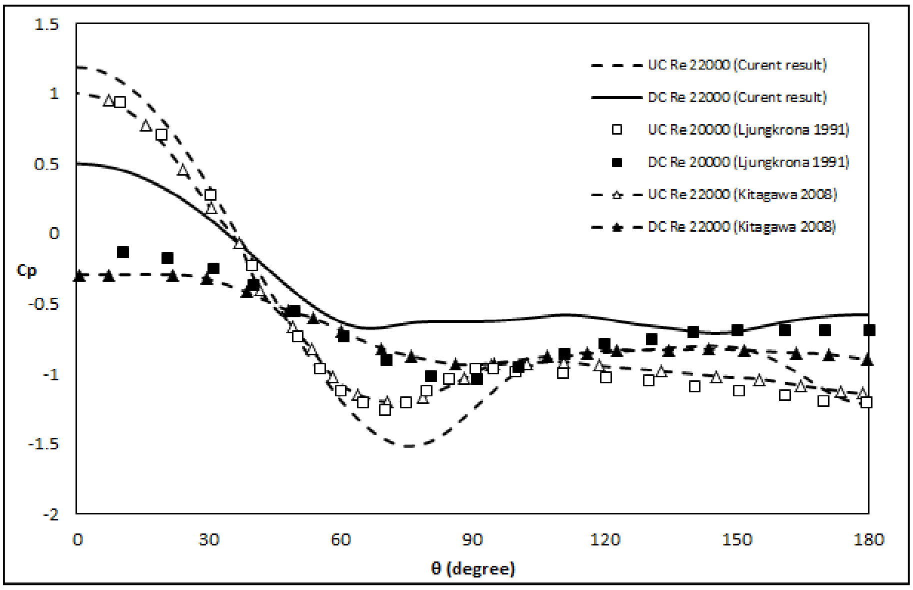

Figure 4.24. Comparison of C_p around both cylinders at L/D = 4 at Re 20,000 & 22,000

The pressure distributions on the surface of both cylinders at L/D = 2, 2.5, 3, 4 are shown in Figure. 4.21 – 4.24, respectively, using SKW turbulence model. The dashed lines represents the pressure coefficients of the upstream cylinder and the solid lines are for the downstream cylinder. The results are compared with experimental data by Ljungkrona et al. (1991) and numerical results by Kitagawa and Ohta (2008) at the exact or approximate Re number which is shown in the figure. Figure 4.21 shows C_p distribution at L/D =2 and the results agree reasonably well with the experimental results of Ljungkrona for the upstream cylinder. Similarly, for the case of L/D =2.5, shown in Figure 4.22, the simulation is quite good when compared with the experimental results, although there is a slight over estimation in downstream cylinder.

However, the pressure distribution is not well predicted at L/D = 3 for the upstream cylinder. The downstream cylinder shows good agreement, but again, C_p is overpredicted $for\ \theta > 120^{o}$. At L/D=4, again, the pressure distribution is over-estimated and large difference can be seen in Figure 4.24.

4.3.4.3. Effects of turbulence intensity

The SKW method is sensitive to the boundary turbulence intensity. Therefore, further investigations were carried out to examine the effects of turbulence intensity. The values of turbulence viscosity were selected in accordance with Saxena (2008), and ANSYS (2011) suggested a range of value 0.1 < I < 1. The higher turbulence intensity can change the critical L/D region (Ljungkrona et al., 1991). The numerical studies included the aforementioned cases with separation $2 \leq L/D \leq 5$ for three different level of turbulence intensity (0.1, 1.4, and 3.2). The turbulence viscous ratio, β is set with value 10. The effect of turbulence intensity is reflected in C_d in both upstream and downstream cylinders.

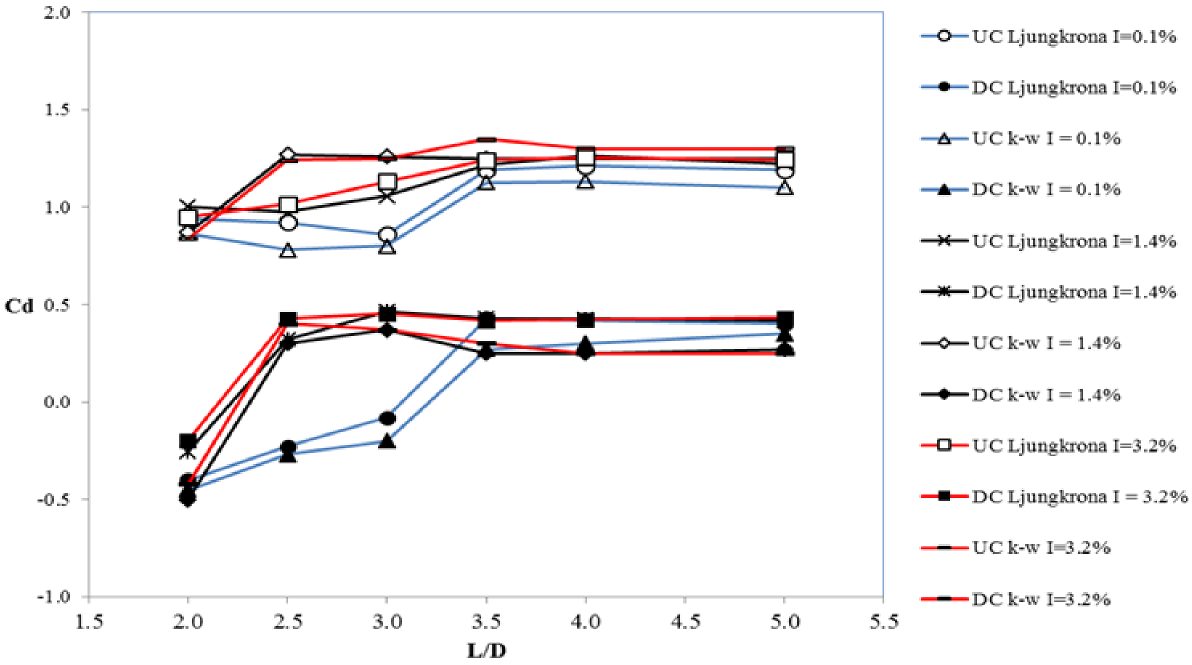

Figure 4.25. Variation of drag coefficient for various turbulence intensity 0.1%, 1.4% and 3.2% at Re = 22000, comparison with Ljungkrona et al (1991)'s experiments at Re = 20000.

For the downstream cylinder, C_d shows the common trends, observed by Ljungkrona et al. (1991) in their experiments. The critical region is affected by increase in turbulence intensity. The "jump" appears at L/D = 2.5 for with I = 1.4% and 3.2 % instead of L/D = 3 for I = 0.1 %. The drag coefficient for L/D > 3 is under-predicted compared with experimental measurements.

For the upstream cylinder, the similarity between prediction and experimental trends can also be recognised. However, drag coefficients are over-predicted in the area L/D = 2.5, 3 and I = 1.4 and

3.2%. The drag coefficient for the upstream cylinder show good agreement when L/D > 3.5 (Figure 4.25).

In general, I = 0.1% showed reasonably good agreement in both UC and DC. At higher turbulence intensity I = 1.4 and 3.2%, there is acceptable agreement in the DC trend, but not in the UC trend. However, at L/D > 4, $I = 1.4\%$ and $\beta = 10$ also shows very good agreement in both UC and DC cylinder, even better than I = 0.1%, as shown in Figure 4.25.

4.3.4.4 Vortex shedding

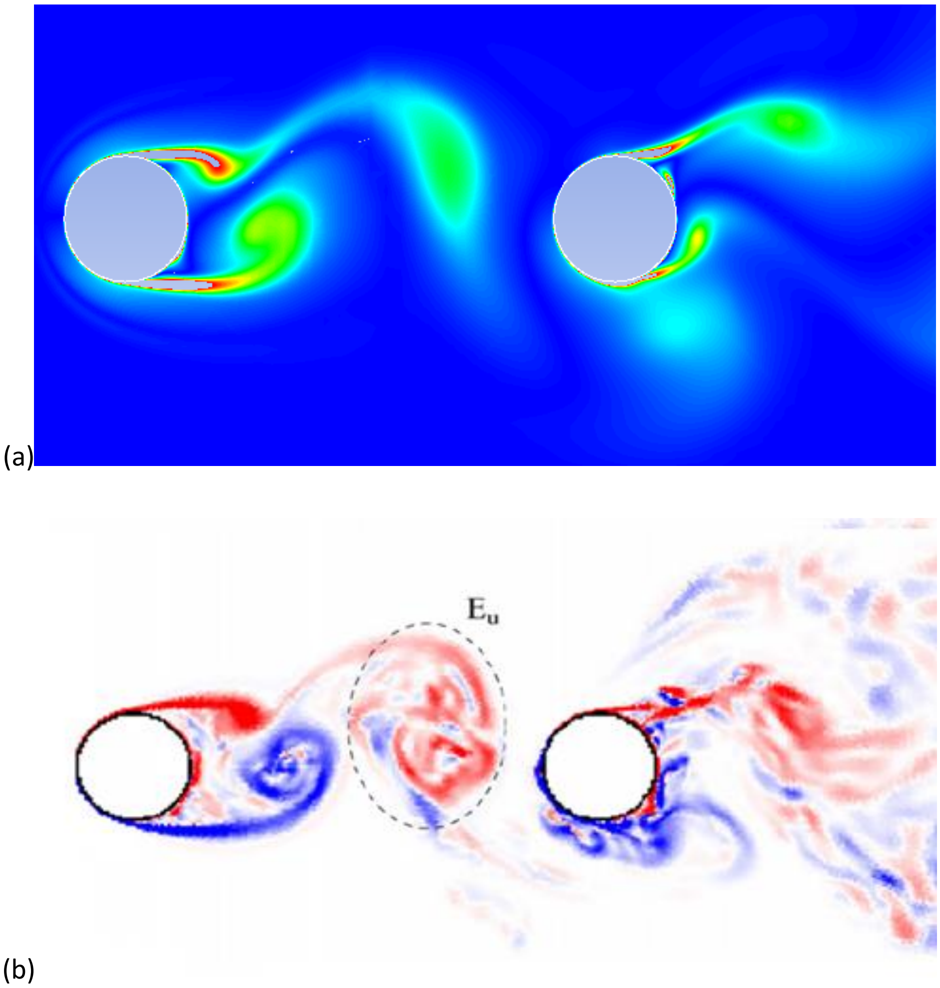

Figure 4.26. Snapshot for vortex shedding from upstream cylinder at L/D = 4 (a) current results (b)Kitagawa et al (2008) at L/D = 4 (Eu: upstream cylinder shedding)

Figure 4.26 provides a snapshot of Vorticity distribution downstream of the cylinders and the results are compared with Kitagawa's numerical results. The plots show that the pattern is quite similar and the vortex shedding by the upstream cylinder appears to reach the downstream cylinder.

4.3.4 Discussion and some explanations

Based on this current research study, some models did not show good results, e.g SST $k-\omega$ and $k-\varepsilon$ model. A review of theory can provide some explanation for these problems with aforementioned turbulence models.

4.3.4.1. $\boldsymbol{k-\varepsilon}$ turbulence model

This is a two-equation model, in which the transport equations are solved for turbulence kinetic energy, k, and the rate of dissipation, ε. This model is famous for its robustness, economy and reasonable accuracy for a wide range of flows. However, the drawback of the k - ε models is their insensitivity to adverse pressure gradient and boundary layer (BL) separation. They typically predict a delayed and reduced separation relative to observation. This can result in overly optimistic design evaluation for flows which separate from smooth surfaces. The $k-\varepsilon$ model is, therefore, not widely used in external aerodynamics (ANSYS, 2011). In ANSYS Fluent, for cases where the flow separates under adverse pressure gradients from smooth surfaces, the $k-\varepsilon$ model is not generally recommended.

In addition, $k-\varepsilon$ does not work well for low Reynolds number (Re < 10,000) and needs the wall function to work. In the current case of medium Reynolds number 20,000 and y^+ is around 1, theoretically only the near wall treatment (Enhanced wall treatment (EWT)) is applicable for the simulation. However, the current numerical study also shows the lack of accuracy in determining the drag coefficient. The numerical results for a single cylinder showed that the Standard Wall function (SWF) provided better agreement compared to EWT in term of C_d, C_l and C_p around a cylinder (Linh, 2012).

According to Fluent, for Reynolds number 22000, in order to have accurate results, a boundary layer accurate turbulence model should be used. For flows which are not fully turbulent, there is a need to use a turbulence model that can approximate the transition with some accuracy and all $k-\varepsilon$ models such as SKE, RNG-KE or RKE, are not applicable. All $k-\varepsilon$ models are not good at detecting transition and are thus only valid for fully turbulent flows.

4.3.4.2. $\boldsymbol{k-\omega}$ and SST $\boldsymbol{k-\omega}$

The ω equation model has some advantages relative to the ε equation. The more prominent advantage is that the equation can be integrated without an additional term through the viscous sublayer. This makes the formulation of robust y^+ EWT relatively straightforward. Furthermore, $k-\omega$ models are typically better in predicting adverse pressure gradient BL flow and separation. However, the downside of SKW is relatively strong sensitivity of the solution to the freestream values of k and ω outside the shearlayer. SKW or SST $k-\omega$ (transitional flow option activated) are naturally low Re models. Low Re omega based Reynolds Stress model (RSM) at least in theory provide better results than SST $k-\omega$, due to high flow streamline curvature and the strong adverse pressure gradient present.

The SST $k-\omega$ model is designed to avoid the freestream sensitivity of the SKW model, by combining elements of the ω- equation and ε- equation. The SST model has been calibrated to accurately compute flow separation from smooth surfaces, which used widely for aerodynamic flows and is more accurate in predicting the details of the wall boundary layer (WBL) characteristics than the Spalart Allmaras (SA) model. The SST uses Enhanced Wall Function (EWF) as the default. (ANSYS, 2011)

The current study results have shown the inlet turbulence intensity dependence of SKW. Thus, SKW is used to calculate the effect of turbulence in flow around cylinders in tandem arrangement with different turbulence intensities. The results show some agreement with the experimental results of Ljungkrona et al (1991) for the downstream cylinder. SST KW avoids freestream turbulence sensitivity, which had been mentioned in ANSYS manual (Figure 4.17). However, SST KW model over-predicted the drag coefficient in the entire L/D range and, surprisingly, shows the worst results.

4.3.4.3. K – kl – w

For k - ω models, low Re terms were proposed by Wilcox (1988) and the model is available in Fluent as an option. It is important to point out that these terms are not required for integrating the equations through the viscous sublayer. The main influence lies in mimicking the laminar-turbulence transition process. However, this function is not widely calibrated for Wall Boundary Layer (WBL) transition. Nevertheless, the combination for the SST model with transition SST model or k-kl transition model is more reliable, (ANSYS, 2011).

Two models for transition prediction available in ANSYS Fluent are SST-transition model and *k* - *kl* - ω Transition model. For many test cases, both models produce similar results (ANSYS 2011). Due to its combination with the SST model, the SST-transition model is favoured. It is important to point out that only laminar-turbulence transition of wall boundary layer can be simulated with any of these two models.

In *k* – *kl* - ω model, proper mesh refinement and specification of inlet turbulence level is crucial for accurate transition prediction. In general, some additional effort is required during the mesh generation phase because of low-Re mesh with sufficient streamwise resolution is needed to accurately resolve the transition region. In the region where laminar separation occurs, additional mesh refinement is necessary in order to properly capture the rapid transition due to separation bubble.

Simulations carried out with $k - kl$ - ω turbulence model show correct trends, as can be seen in Figure 4.18, 4.19 for the upstream cylinder, which shows a dramatics jump at L/D = 3. However, the downstream drag coefficients do not follow the same trends. This turbulence model was over-predicted the drag coefficient both the cylinders at L/D < 2.5. (Figure 4.18)

4.4.4. Conclusion

In this two stationary cylinder section, different RANS based turbulence models have been used to simulate the flow around two fixed cylinders in tandem. Different separations were used in order to investigate the effects of various turbulence parameters (I, l and β) and the hydrodynamic forces acting on the body. The most importance conclusions can be summarized as follows:

- The standard $k - \omega$ shows sensitivity with turbulence parameters (I, β) and can be used to predicting force coefficients with inlet flow by varying turbulence intensity and viscosity ratio. The numerical results showed that SKW can capture the general trends, especially, at the critical drag area, with reasonably good values for both upstream and downstream cylinders.
- k – ε turbulence model can capture the variation of drag coefficient with separation using the highly recommend by ANSYS, realizable $k - \varepsilon$. However, in general, this model under predicts the drag coefficient of the upstream cylinder.
- SST $k - \omega$ provided the worst predictions for this Reynolds number in this numerical study. In general, SST k - ω over predicted drag coefficient for both upstream and downstream cylinders. However, due to its inlet turbulence parameter independence, this model can be applied when the experimental data are not available.
- The new numerical method k – $kl - \omega$ combination of $k - \omega$ with other transition equation and highly recommended by ANSYS also over-predicts drag coefficient at small separations (L/D < 3). However, predictions are close to experimental results for L/D > 3.5. This method shows its reliability in predicting Strouhal number, and showed the best agreement with experimental results.

Finally, although none of these methods provide total agreement with experimental measurement, some models showed its advantages in predicting hydrodynamics parameters around cylinders. Overall, SKW is suitable for carrying out numerical studies for flows around cylinder at subcritical Reynolds number and will be used for further VIV investigation.

Chapter 5 : Forced oscillating cylinder

In this chapter, the turbulent flow past a circular cylinder undergoing forced oscillations in the cross-flow direction at Re = 10000 is numerically examined to study the changes on the forces around the body. Following the results achieved in the previous chapter, Standard $k-\omega$ is chosen for this simulation with the appropriate turbulence intensity and turbulence viscosity ratio (See 5.2.1). Emphasis is placed on the discussion of the influence of the cylinder oscillation on the lift, drag and vortex shedding, and the comparison between simulation results and the experimental results at the same Reynolds numbers. From this point, the cylinder is no longer stationary. The moving dynamic mesh (MDM) is applied and the mesh change due to the motion of the cylinder. However, application of a dynamic mesh may lead to some numerical issues. In reality, the cylindrical structure does not only experience free but also forced oscillations in some cases. Hence, in the current research, initially, a simple forced oscillating cylinder test is carried out.

5.1. Modelling domain

The current simulation aim to verify the benchmark experiments by Gopalkrishnan (1993) and DNS numerical investigation by Dong and Karniadakis (2005). The model used is similar to that in for flow around a fixed cylinder in Chapter 4. The computational domain consists of an upstream length 10D and downstream length 30D and width 20D. The cylinder can oscillate in the crossflow direction with a sinusoidal movement as shown in Figure 5.1.

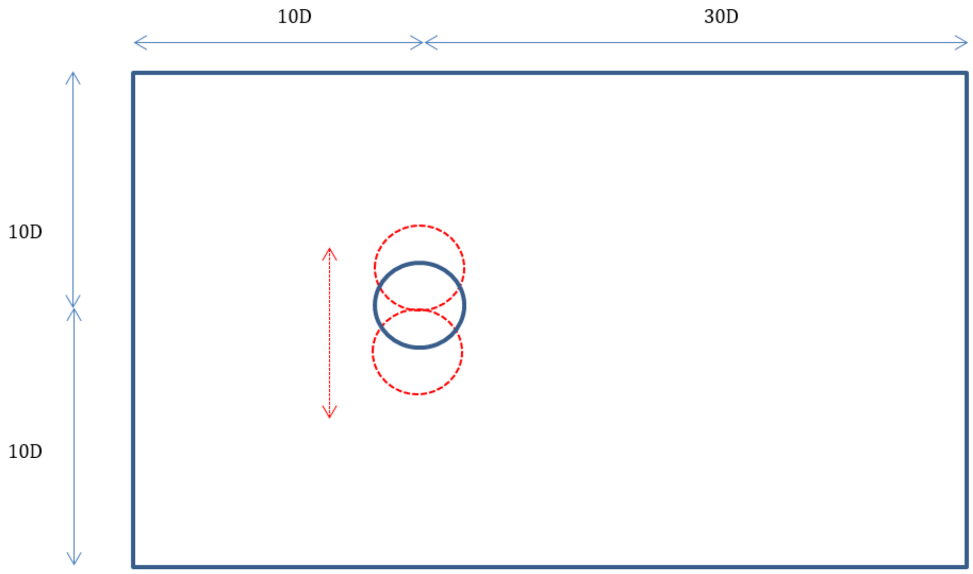

Figure 5.1 Forced oscillating cylinder domain

A structured quadrilateral mesh of 44800 elements is used in this simulation based on the simulation for a single fixed cylinder at a similar Reynolds number in Chapter 4. The $y+$ value was kept around 1 in this study which is satisfactory for the near wall treatment method. Again the first layer height for the cylinder boundary is 0.0014D as before. The Reynolds number 10,000 was chosen because of the availability of data for comparison.

5.2. Simulation setup

5.2.1. Boundary condition

Similar setup for the fixed cylinder at Re = 10,000 case applied, namely, uniform flow at inlet, free outflow condition and symmetry at upper and lower boundaries. However, at the boundary of the cylinder wall, the forced oscillation function is applied to make the cylinder move with pre-defined amplitude. The moving dynamic mesh method is applied on the cylinder wall and the area adjacent to the cylinder boundary for forced oscillation. Of the three dynamics mesh options in ANSYS Fluent, the smoothing – diffusion methods was used. The diffusion parameter is set to 1, to maintain the mesh around the cylinder area, so that the near wall mesh always maintains the expected y^+ value. The preview of mesh motion showed that the near wall mesh was unchanged for 1.5D distance around the cylinder and the outside area deformed like a spring with the movement of the cylinder. The SKW turbulence model was applied for this problem. The initial turbulence intensity and turbulence viscosity ratio was set with the value of $I = 1.4\,\%$ and $\beta = 10$ that showed good agreement for Re = 10,000 for the fixed cylinder case. RKE also used in this simulation with similar turbulence intensity and viscosity ratio.

5.2.2. Equation of motion

For the moving cylinder case, the motion of the cylinder in cross-flow y direction is expressed by the Equation 3.25:

$$y = \mathrm{A}\sin(2\pi f_o t)$$

where y is the cylinder displacement, A is cylinder displacement amplitude , f_o is the cylinder oscillation frequency. All length parameters are normalised with respect to the cylinder diameter D. In this case A = 0.3D was applied. To incorporate the oscillation equation with Fluent, the User Defined Function (Appendix B) is used.

A constant non-dimensional time step $U\delta t/D$ = 0.003 is used to maintain numerical stability. The flow data are gathered at least over 21 vortex shedding cycles to obtain converged flow data. The CPU time generally ranges from 8 – 12 hours on the IRIDIS 3 cluster.

5.3. Numerical simulation results

This simulation aims to generate results consistent with the experiments by Gopalkrishnan (1993) and DNS numerical simulations by Dong and Karniadakis (2005). Gopalkrishnan (1993) demonstrated that the force coefficients show a sharp increase around a certain oscillation frequency (close to Strouhal number between 0.17 and 0.18). In this simulation, we have to consider a range of oscillating frequencies 0.05 $\leq f_o D/U \leq$ 0.35, with moderate displacement A/D=0.3 as shown in Table 5.1. This range covers the frequency which shows the dramatic changes in drag and lift forces observed in Gopalkrisnan's results.

5.3.1. Drag and lift coefficients

The simulation was carried out using SKW for the drag coefficient and lift coefficient amplitude, the results are shown in Figures 5.2 and 5.3 against the non-dimensional frequency. Carberry et al. (2005) clearly showed that the variations of amplitude of lift forces represent the transition from low frequency state to high frequency state with a corresponding change of the near wake structure and the mode of shedding. This "critical area" showing sharp changes in drag and lift coefficients was observed by Gopalkrishnan (1993) when the oscillation frequency is close to the Strouhal frequency. RKE was also applied to check the sensitivity as good agreement for lift coefficient was observed in Chapter 4.

Table 5.1. Summary of cases for flow past an oscillating cylinder

Case	A/D	$f_o D/U_o$
M1	0.3	0.05
M2	0.3	0.1
M2	0.3	0.15
M4	0.3	0.183
M5	0.3	0.21
M6	0.3	0.25
M7	0.3	0.3
M8	0.3	0.35

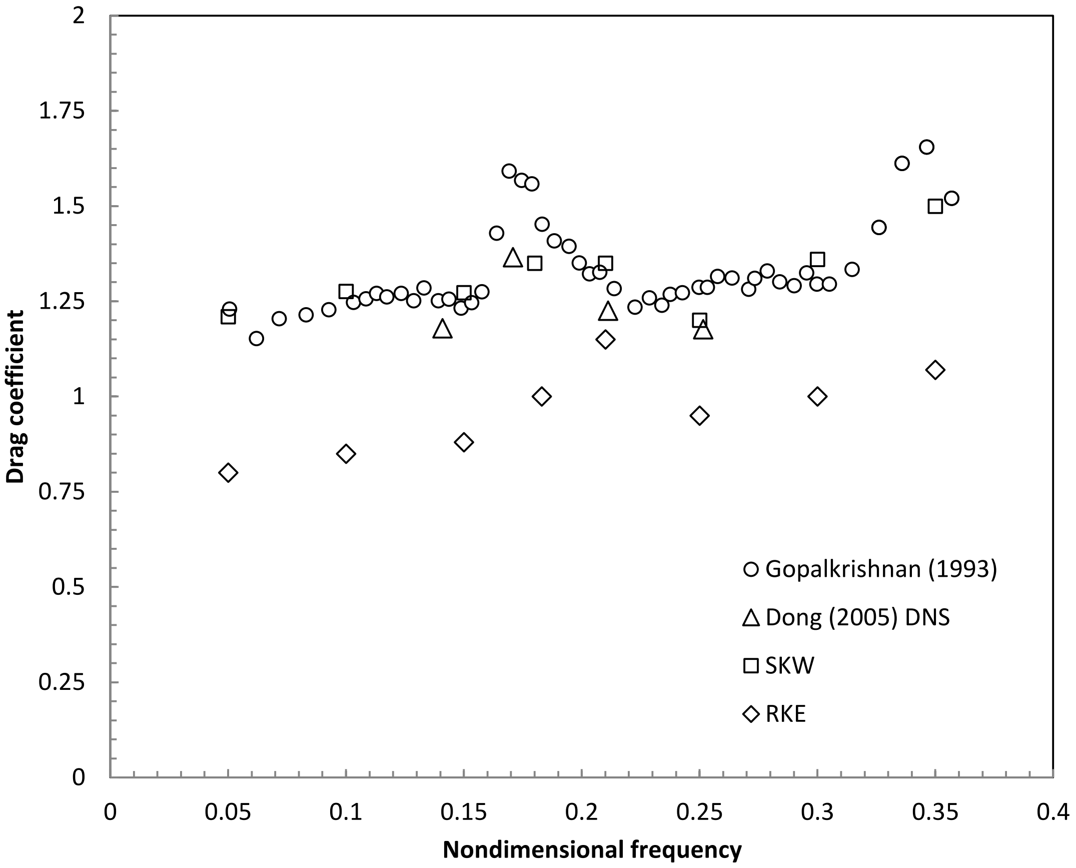

Figure 5.2. Drag coefficient as a function of non-dimensional frequency (A/D = 0.3)

The drag coefficient using SKW in Figure 5.2 follows the trend observed by Gopalkrishnan (1993) and agrees well for the whole non-dimensional frequency range . The simulation correctly captures the sharp rise of the drag coefficient around the critical frequency, when the oscillation frequency is close to the vortex shedding frequency. Changes in drag coefficient are also detected when the frequency increases and there is a sharp rise when the non-dimensional frequency is greater than 0.3. Furthermore, the overall change in drag coefficient is only moderate in the range of non-dimensional frequency from 0.05 to 0.3. The sharp increase appears at the high frequency region, when $f_o D/U$ > 0.3. The RKE model under-predicts the drag coefficient, in general. This is similar to the case with the fixed cylinder simulation. However, a "jump" can be detected when the Strouhal number is approximately 0.2.

Examining Figure 5.3, it can be seen that lift coefficients predicted when using SKW capture the trends well for 0.18 <$f_o D/U$ < 0.35, showing reasonably good agreement with Gopalkrisnan's results. The sharp jump can be observed at the critical frequency region in the vicinity of the vortex shedding frequency. However, the lift is over-predicted at low frequency of oscillation, $f_o D/U$ < 0.15). The lift coefficient magnitude is almost 1, which shows some similarity with the fixed cylinder case. The amplitude of lift increases to as high as 2.5 and 3 at high non-dimensional frequencies, 0.3 and 0.35 respectively. Overall, the lift coefficient shows a large change over the range of oscillation frequencies, compared to the drag coefficient.

The alternative simulation by RKE shows the gradual increment in the lift coefficient, which follows the main trend. However, no jump is exhibited, as in the SKW simulated results.

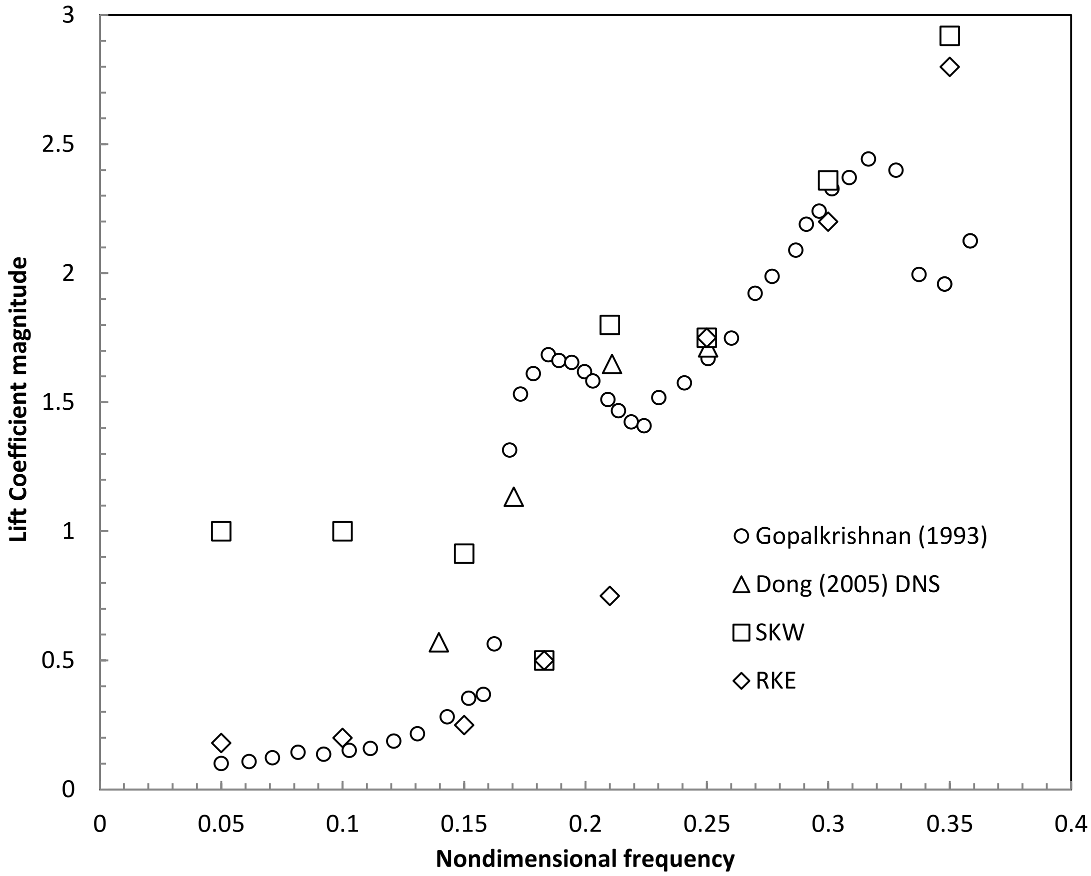

Figure 5.3. Lift coefficient as a function of non-dimensional frequency (A/D = 0.3)

The time history of force coefficients and the cylinder displacement at $f_0 D/U$ = 0.18, 0.21, 0.3 is shown in Figure 5.4. It is observed that as frequency increases, the lift coefficient increases quite dramatically with amplitude values of 0.5, 1.8 and 2.4 respectively.

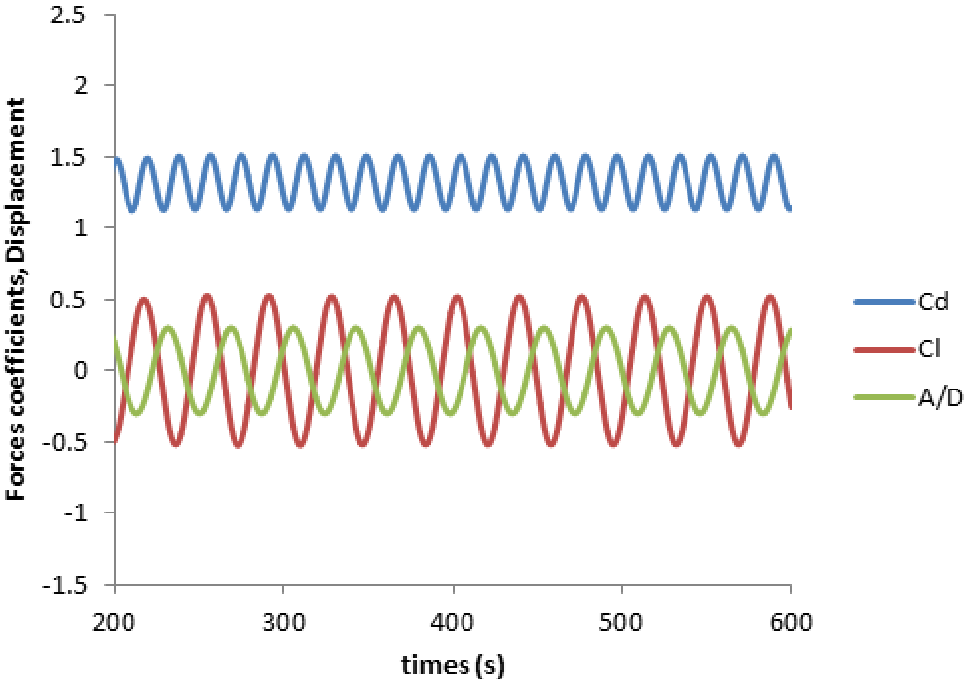

2.5
2
1.5
1
0.5
0
-0.5
-1
-1.5
Forces coefficients, Displacement
200
300
400
500
600
times (s)
Cd
Cl
A/D

(a)

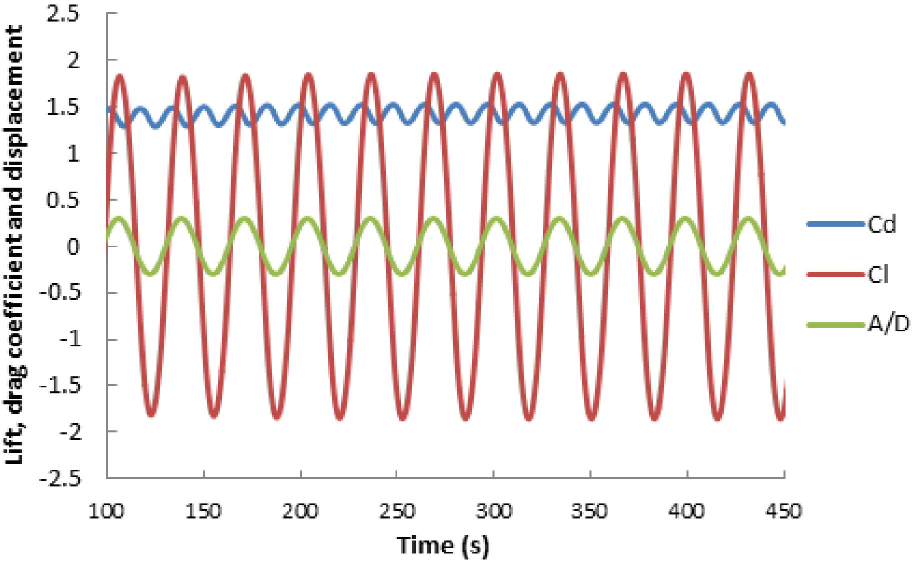

2.5
2
1.5
1
0.5
0
-0.5
-1
-1.5
-2
-2.5
Lift, drag coefficient and displacement
100
150
200
250
300
350
400
450
Time (s)
Cd
Cl
A/D

(b)

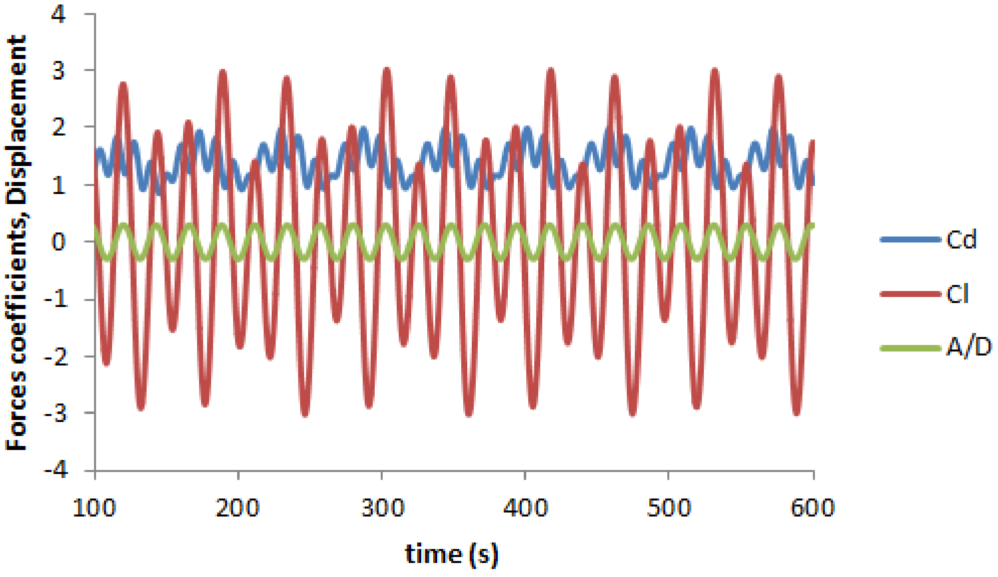

(c)

Figure 5.4. Time history of lift & drag coefficient and cylinder displacement in flow past an oscillating cylinder at Re = 10000, for oscillation frequency $f_o D/U$ set to: (a) 0.18, (b) 0.21, (c) 0.3, with amplitude of A/D = 0.3

5.3.2. Vortex shedding pattern.

The Vorticity field in Figure 5.5 shows the wake structure for two non-dimensional oscillation frequencies $f_o D/U$ equal to 0.21 and 0.3 compared with 2S and 2P modes from Govardhan and Williamson (2000). At low frequency, the vortex structure is formed from the attached shear layer and its length extends across the back of the cylinder. As frequency increases to 0.21 and 0.3, as shown in Figure 5.5(a,b), the elongated vortex structure attached to cylinder moves closer to the cylinder base. At low amplitude of oscillation, the 2S model can be observed (Figure 5.5a, c) and when the frequency is getting larger, the vortex pattern can be observed as the 2P model (Figure 5.5b, d).

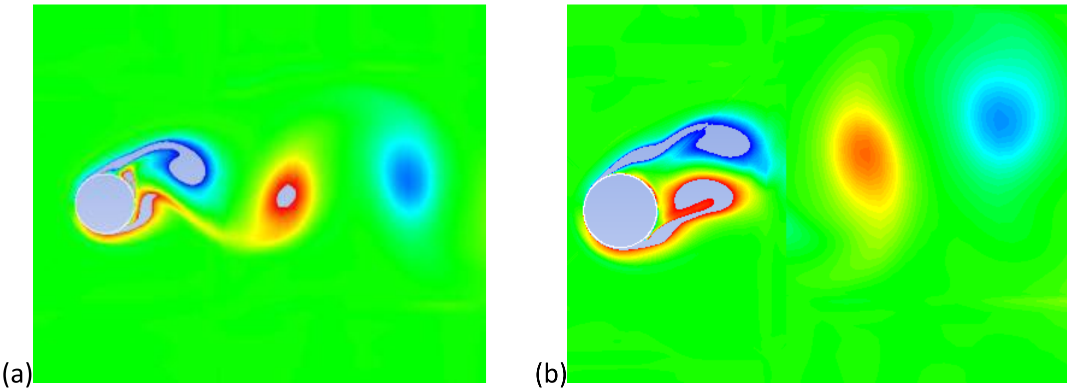

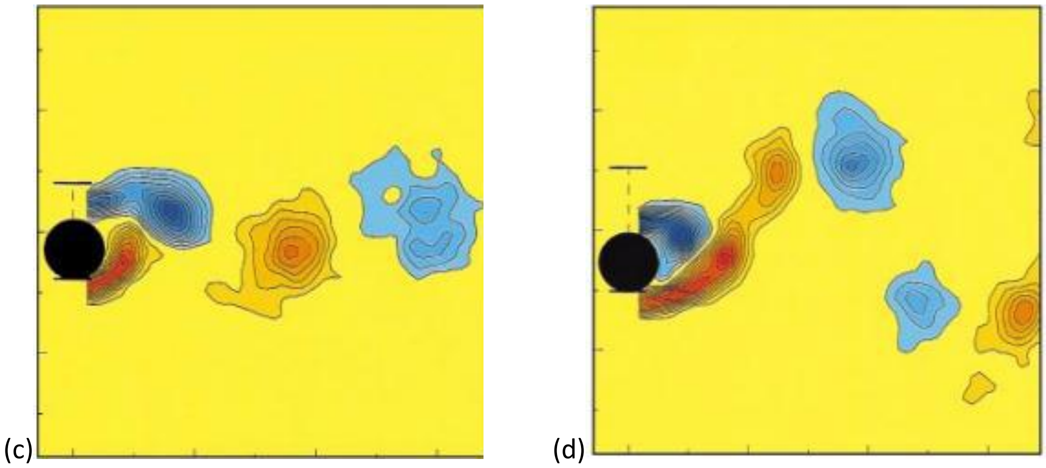

Figure 5.5. Vortex shedding pattern in flow past an oscillating cylinder at Re = 10000, oscillation frequency $f_o D/U_o$ (a) 0.21, (b) 0.3, A/D = 0.3 (c) Snapshot of 2S (d) Snapshot of 2P (Govardhan and Williamson, 2000).

5.3.3. Results for other amplitude ratios

In addition to aforementioned work, high amplitudes of oscillation were tested to examine the application of the dynamic mesh facility. Two additional amplitudes were tested with amplitude of A/D = 0.75 and 1.6 over a similar range of non-dimensional frequency. Results are presented in Figure 5.6 to 5.9.

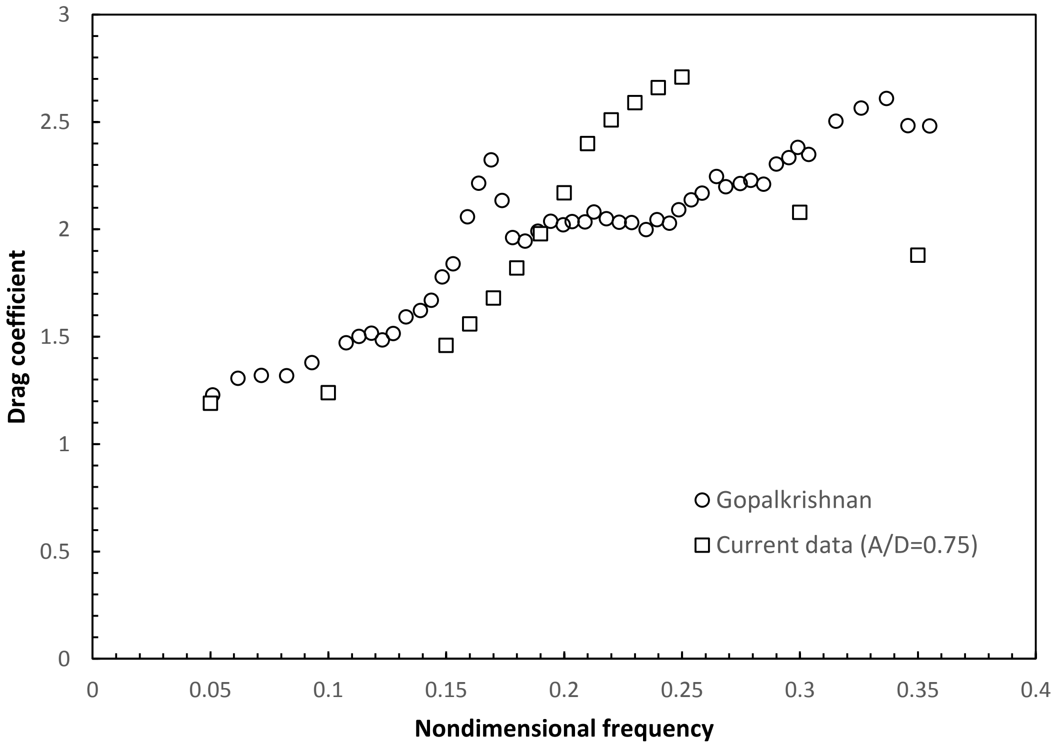

Figure 5.6. Mean drag coefficient as a function of non-dimensional frequency (A/D = 0.75)

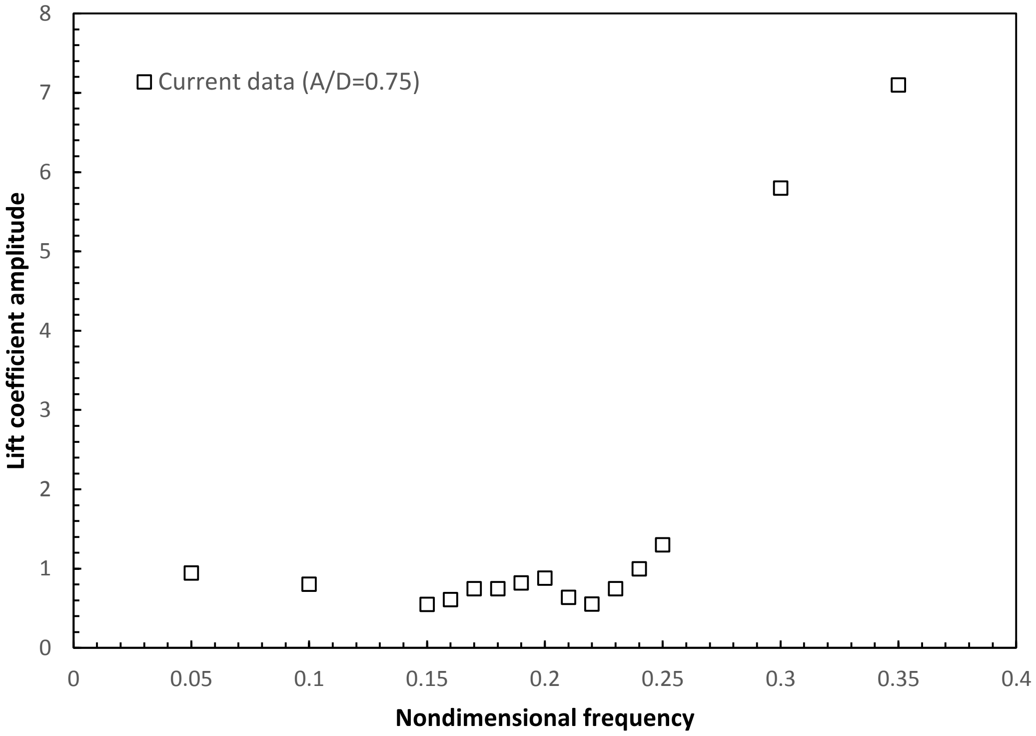

Figure 5.7. Lift coefficient amplitude as a function of non-dimensional frequency (A/D = 0.75)

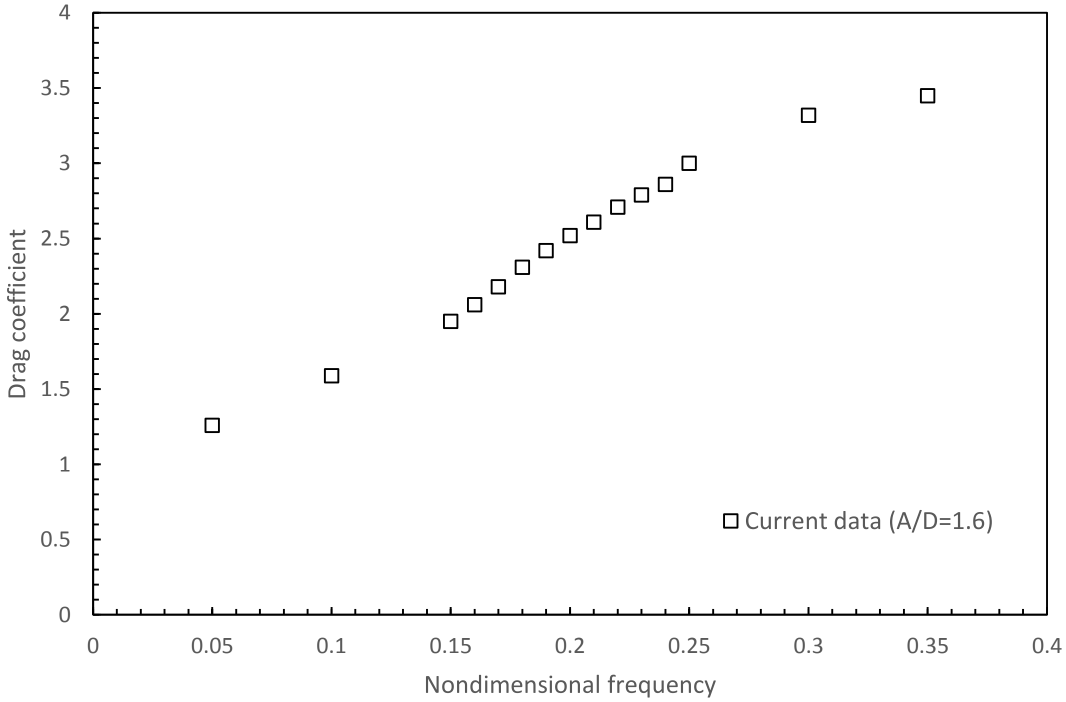

Figure 5.8. Mean drag coefficient as a function of non-dimensional frequency (A/D = 1.6)

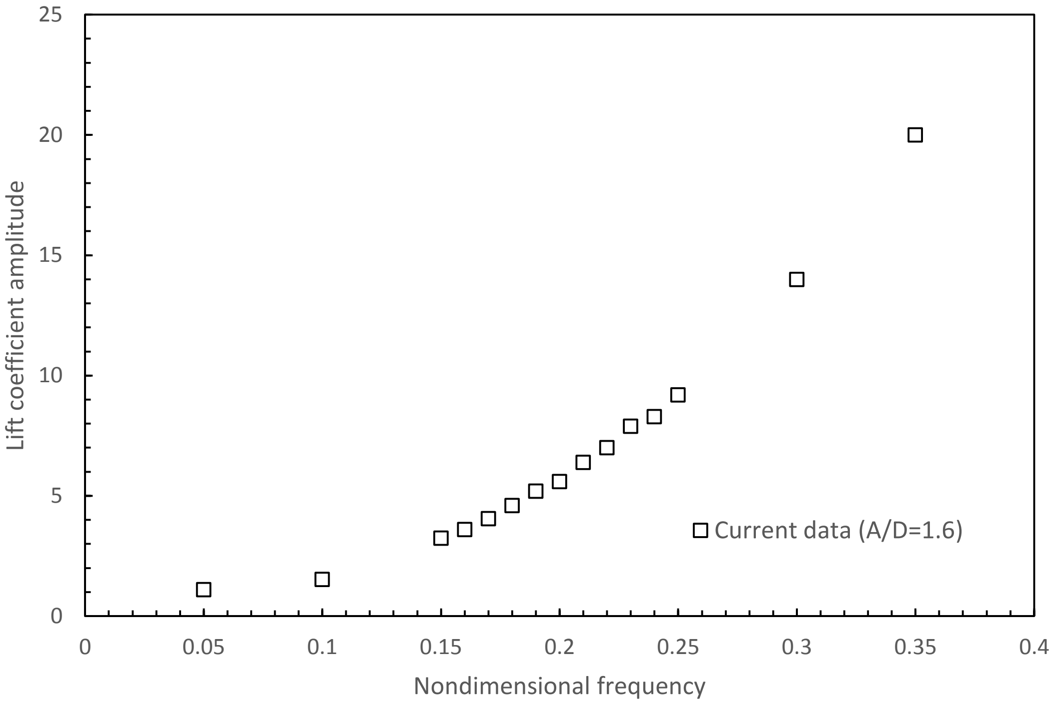

Figure 5.9. Lift coefficient amplitude as a function of non-dimensional frequency (A/D = 1.6)

The increase in the amplitude of forced oscillation increases the mean drag coefficient (Figure 5.6 & 5.8) and the lift coefficient amplitudes (Figure 5.7 & 5.9). The mean drag coefficient reaches 2.8 at A/D = 0.75, while for A/D = 1.6, $C_d \approx 3.5$. The mean drag coefficient at A/D = 0.75 is overestimated compare with Golpakrishnan's results, although the same peak amplitude could be recognised. Compared with the previous simulation results at A/D = 0.3, the peak in the transition areas are almost doubled.

The lift coefficient amplitude are dramatically increased with increasing amplitudes of motion, especially at the high non-dimensional frequency region ($f_o D/U$ = 0.35), where peak $C_l \approx 7$ and 20 at A/D = 0.75 and 1.6 respectively. However, for lower $f_o D/U$ value, with a moderate amplitude of motion A/D = 0.75, the lift coefficients like in the range 0.8 to 1.3, which is very similar to experimental results.

The simulation results of Figure 5.8 and 5.9 with the large value of A/D = 1.6 indicate that the current dynamic mesh method still provide stable results without any error.

5.4. Conclusions

The present study provides numerical results using 2D RANS simulation of the turbulent flow past a forced oscillating cylinder at Re = 10000 for a range of non-dimensional frequency values from 0.05 to 0.35.

At A/D = 0.3, the drag coefficient exhibits very good agreement with experimental measurement and the simulation of Dong and Karniadakis (2005) and captures the expected jump.

However, the lift coefficient is not captured as well at the low frequency end by SKW method. At low frequencies, the lift and drag coefficients are quite similar to those for a stationary cylinder. This is the limitation of the 2D RANS, showing it is hard to capture the right lift at that range. In the higher frequencies, the simulation captures quite well the trend and amplitude of the lift coefficient

The phenomenon of vortex switching can be observed downstream of the cylinder. The vortex shedding pattern switchs from 2S to 2P when the frequency of oscillation increases.

For the higher amplitude of oscillation, the current models are able to produce the results without any mesh constraints. The lift and drag coefficient can be calculated although some over-estimation could be observed. Hence, this study shows that SKW and the dynamic mesh method are suitable for a moving cylinder. It will be applied to the flow around a free oscillating cylinder in the next chapter.

Chapter 6 : Free oscillating cylinder with 1 dof and 2 dof systems.

In this chapter, CFD methods are applied to a rigid cylinder undergoing VIV in (i) crossflow direction (1 dof), and (ii) both crossflow and inline directions (2 dof). The simulation for the forced oscillating cylinder carried out in the previous chapter showed the reliability of MDM in simulating an oscillating cylinder. Following the forced cylinder study, self-excitated vibration study is carried out in this Chapter with the application of the dynamic mesh method to a smooth cylinder at sub-critical Reynolds number of 10,000. The current VIV simulation will be carried out in the range $2 \leq U_r \leq 15$. In both cases, the VIV system simulation has low mass-damping $m^*\zeta$ ratio and the simulation results are validated against benchmark experimental studies. The simulation results will focus on three main aspects:

- Amplitude ratio
- Frequency ratio
- Vortex shedding mode
- Motion Trajectories (for 2 dof motion)

For the 1 dof system, the results are compared with the experiment of Khalak and Williamson (1996) as well as other numerical results by Pan et al. (2007). For the 2 dof system, benchmark experiments by Jauvtis and Williamson (2004) are used. Overall, good agreement between the current numerical studies and experiments and other numerical methods is observed.

6.1. Simulation model

The model of the circular cylinder for 2D flow simulation is shown in Figure 6.1. In literature, cylinders are simulated as a system comprising mass (m), stiffness (K) and damping (c). The model in Figure 6.1a represents the dynamics of a simple structure with vibration mode in the crossflow direction, which is single or one degree of freedom (1 dof) system. The model 6.1b represents a 2(1+1) dof vibration system (Inline + crossflow motion).

Thus, the motion of the cylinder in transverse direction due to the fluid force can be determined by equation 3.27: $m\ddot{y} + c\dot{y} + Ky = F_y$

This equation can also be used for the inline direction with the F_y substituted by the drag force F_x.

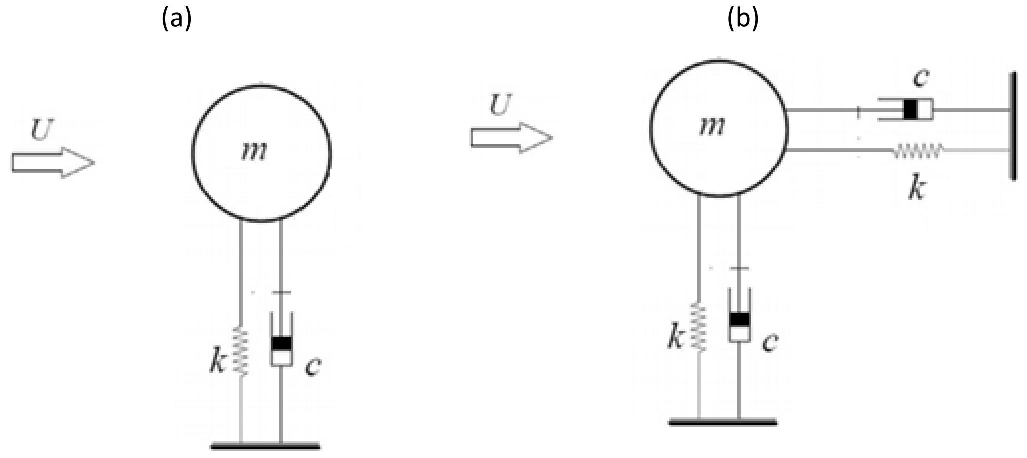

Figure 6.1. Schematic representation of the elastically mounted circular cylinder in cross flow (a) 1 dof system (b) 2 dof system

6.2. Vortex induced vibration for 1 dof system

6.2.1. Numerical method

Initially, a Six degree of freedom method (SDOF), an option in ANSYS Fluent is used to investigate the VIV in crossflow direction. The *DEFINE_SDOF_PROPERTIES Macro* is used to specify relevant properties of moving objects for the six-degrees of freedom solver in ANSYS Fluent. SDOF can be used with only 1 dof by preventing motions in 5 other directions, through a command in the UDF file (Appendix C.1)

The external elastic force is added to solve for the acceleration of the cylinder. The velocity and displacement in the time domain can be calculated accordingly. The governing equation of motion of the centre of gravity is solved from:

$$\dot{v_G} = \frac{1}{m}\sum f_G \tag{6.1}$$

where $\dot{v_G}$ is the rate of change in velocity, m is the mass and f_G represents all forces acting on the body.

When applied into the cylinder system:

$$\ddot{y} = \frac{1}{m}\sum f_G = \frac{F_y - c\dot{y} - ky}{m} \tag{6.2}$$

where $y, \dot{y}, \ddot{y}$ is the displacement, velocity and acceleration of the cylinder at the same time step, F_y is the fluid force and $c\dot{y}$ and ky are elastic force acting on the system. When using SDOF, the velocity is derived and used in the dynamic mesh method to calculate and update the position of the rigid body.

The velocity at each time step is defined by

$$\dot{y}_n = \ddot{y}_{n-1}\Delta t \tag{6.3}$$

The summary of dimensionless and dimensional variables, which is used in this chapter, are presented in Table 6.1. The diameter of the cylinder is chosen as D = 1m. The natural frequency is adjusted to obtain the required reduced velocity values and the mass and damping is defined accordingly. The experiment system properties are summarised in Table 6.1. The current numerical simulation used the same mass-ratio as Khalak and Williamson (1996)'s experiment.

The simulation is conducted with a structured grid of 44,800 elements, which was used in flow around fixed cylinder (Chapter 4). The cylinder body is set free from a neutral position with zero initial velocity. The displacement y is applied to the cylinder boundary. The smoothing-diffusion method applied using the step by step process in 3.6.3.

Table 6.1. Definition of dimensionless and dimensional variables

A^*	A/D	Amplitude ratio
m_d	$\frac{\pi}{4}\rho D^2 L$	The displaced fluid mass
$m_{cylinder}$		Mass of cylinder
m_a	$C_a m_d$	Added mass
m_o	$m_a + m_{cylinder}$	Oscillating system mass
m^*	m_o/m_d	Mass ratio
f_n	$\frac{1}{2\pi}\sqrt{\frac{K}{m_{cylinder}}}$	System natural frequency
f_o		Oscillating frequency of the cylinder
f^*	$\frac{f_o}{f_n}$	Frequency ratio
U_r	$\frac{U}{f_n D}$	Reduced velocity based on natural frequency
c	$4\pi\zeta m f_n$	System damping

Table 6.2. Experimental system properties

Mass ratio	m^*	1.2 - 2.8
Damping ratio	ζ	0.0072
Diameter of the cylinder	D (m)	1
Length of the cylinder	L (m)	1

6.2.2. Influence of Reynolds number

The same Reynolds number of 10,000 used in the previous chapter is selected. However, this is different from Khalak and Williamson's paper. Nevertheless, in VIV experiments, Reynolds number is a lesser influential factor compared with reduced velocity. The change in Reynolds number should not affect the two most effective factors in VIV: the amplitude of motion and the frequency ratio.

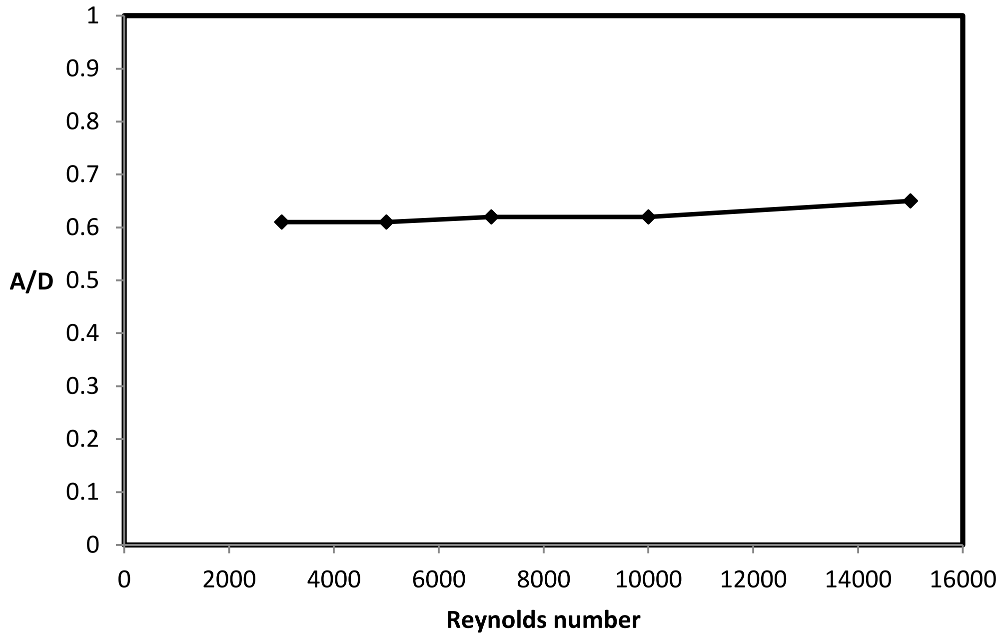

Figure 6.2. Effect of Reynolds number on A/D for reduced velocity Ur = 5.5

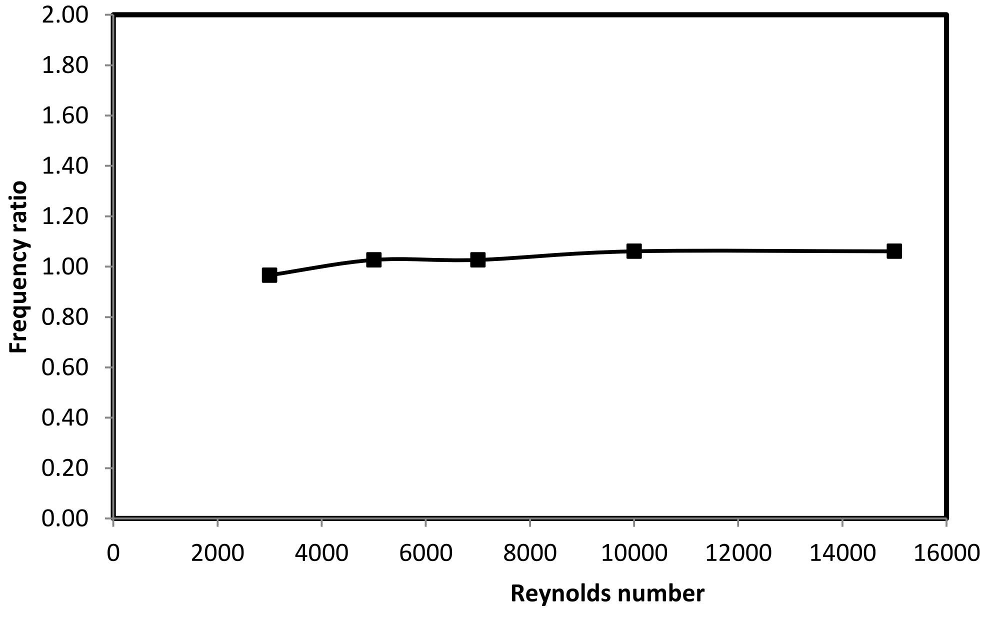

Figure 6.3. Effect of Reynolds number on frequency ratio at reduced velocity 5.5

As indicated in Figure 6.2, when the Reynolds number changes in the range of Reynolds number 3000 to 15000, there is very little change in amplitude of motion due to VIV. The frequency ratio, in Figure 6.3 also shows similar insensitivity. Less than 1% change was observed.

Table 6.3. Run cases summary

Re	Ur	U	D	f_n
10000	1	0.1461	1	0.1461
10000	2	0.1461	1	0.0731
10000	3	0.1461	1	0.0487
10000	4	0.1461	1	0.0365
10000	5	0.1461	1	0.0292
10000	5.5	0.1461	1	0.0266
10000	6	0.1461	1	0.0244
10000	6.5	0.1461	1	0.0225
10000	7	0.1461	1	0.0209
10000	7.5	0.1461	1	0.0195
10000	8	0.1461	1	0.0183
10000	8.5	0.1461	1	0.0172
10000	9	0.1461	1	0.0162
10000	10	0.1461	1	0.0146
10000	11	0.1461	1	0.0133
10000	12	0.1461	1	0.0122
10000	13	0.1461	1	0.0112
10000	14	0.1461	1	0.0104
10000	15	0.1461	1	0.0097

6.2.3 Numerical simulation results

A series of simulations, summarised in Table 6.3 are performed for validating the ability of RANS to predict hydrodynamic loads and responses for a spring-mounted smooth cylinder undergoing vortex-induced vibration. The experiment from Khalak and Williamson (1996) are selected for validation. Two ω based turbulence models SKW and SST KW were used in this simulation. The SKW has shown good agreement for the results of the previous chapter and continues to be used as a preferred method. The SST KW model is also includes as it addressed in the Pan et al. (2007) simulation.

6.2.3.1. Amplitude ratio (A* = A/D)

The variation of the non-dimensional amplitude of vibration A* = A/D as a function of reduced velocity is shown in Figure 6.4 with mass damping ratio $m^*\zeta$ of 0.0108. Comparison with experimental measurements by Khalak and Williamson (1996) are also included. In Khalak and

Williamson (1996) and Pan et al. (2007) with $m^*\zeta$ = 0.013, the Reynolds number increased in proportion with the reduced velocity from 2500 to 13,000.

As can be seen the general trend observed in these experiments is captured by the present data using SKW, including the three different branches: initial, upper and lower branch. The upper branch appears to be missing in the results reported by Pan et al. (2007), based on a 2D RANS simulation method with an SST KW turbulence model. In the present SKW model results, the highest obtained amplitude recorded was A* = 0.8 when Ur = 5, compared with the highest amplitude A* = 1.08 for Ur = 5.8 from the experiment. The big "jump" in amplitude of vibration can be clearly observed, namely an amplitude smaller than 0.03D for Ur = 2, to approximately 0.8D when Ur = 5. In this transition region, the amplitude of the lift force decreases when the drag force jumps up as can be seen in Figure 6.6. At Ur = 10.5, the Reynolds numbers for all three cases plotted in Figure 6.4 coincide, and the results are in close agreement.

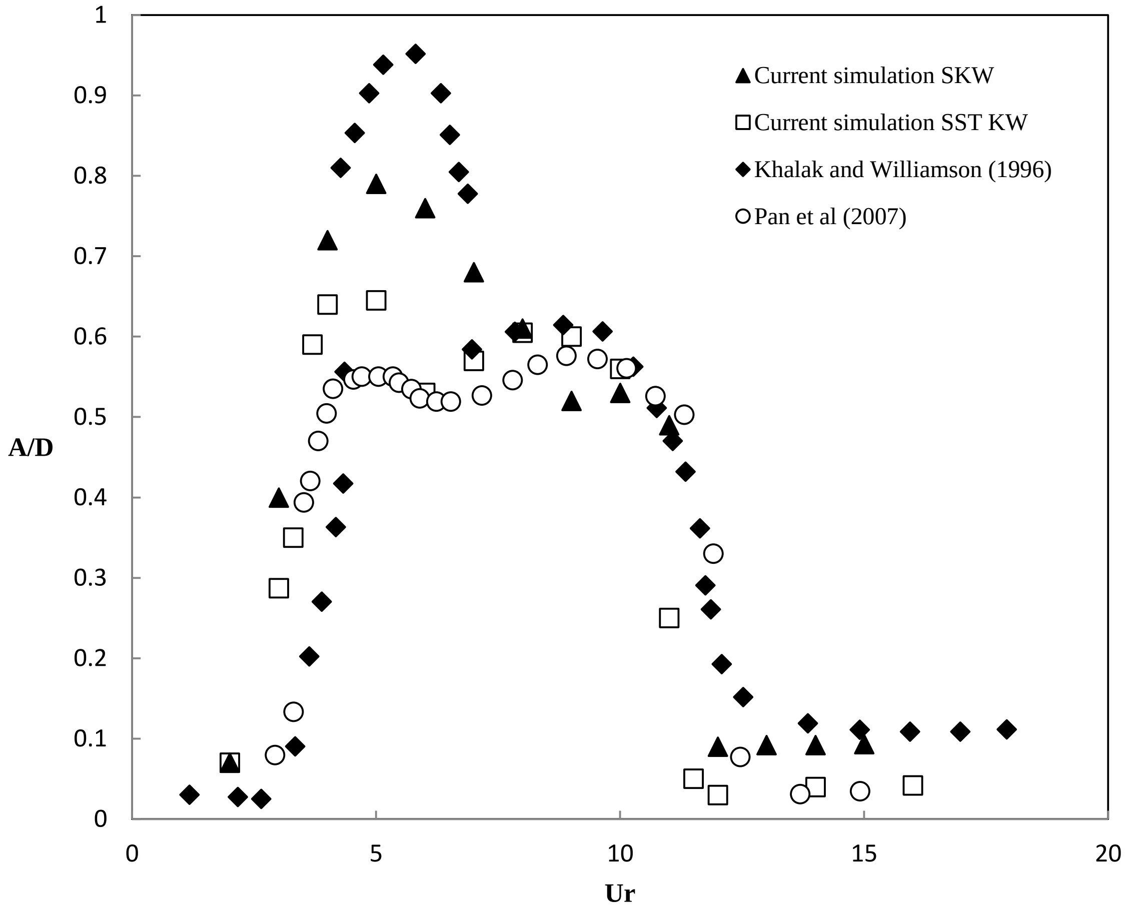

Figure 6.4. Variation of amplitude of motion ratio with reduced velocity.

Over the region 5 < Ur < 9, we can observe the cylinder vibration corresponding to the upper branch and for 9 < Ur <12, that corresponding to the lower branch in the experiment. The displacement of the cylinder is nearly sinusoidal in time, as can be seen in Figure 6.6, and agrees well with experiments using the same mass-damping ratio. When Ur>12, the decrease in amplitude of motion is sudden, to approximately A*= 0.1, and remains at this low value when Ur increases further. This reflects the desynchronization branch observed in Khalak and Williamson's (1996) experiment.

Although there is good overall agreement with the experimental measurements, it can be observed from Figure 6.4 that the change in amplitude of motion appears earlier, in the low Ur region, and the maximum A* does not match the actual experiment. However, the agreement with Pan et al's simulation can be shown . The sharp decrease in amplitude of motion seen in the Ur range from 11 – 12, is captured well.

The SST KW simulations show a reasonably good agreement with Pan et al's simulations results, however, the upper branch is not captured well. A maximum amplitude recorded with the value of 0.65D.

6.2.3.2. Oscillation frequency ratio

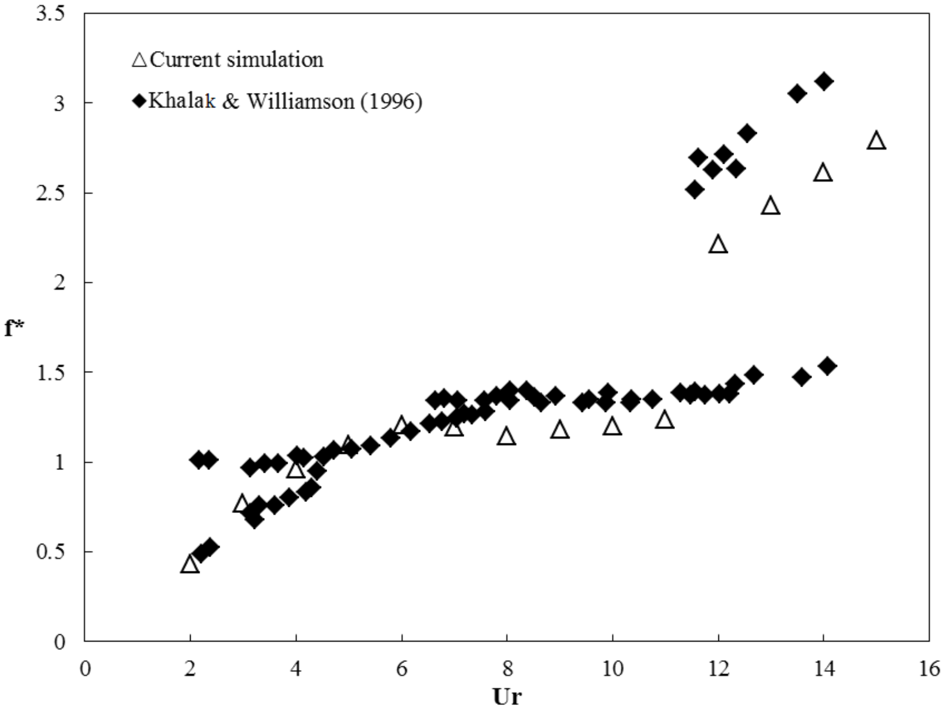

Figure 6.5. Frequency ratio in different reduced velocity using SKW models

The frequency ratio $f^* = f_o/f_n$ is plotted as a function of Ur in Figure 6.5. For $2 \leq U_r \leq 4$, the frequency ratio is relatively low, below 1. At reduced velocity Ur = 2, the frequency ratio f^* is as small as 0.5 and gradually increases with increasing reduced velocity. In the range 2 < Ur < 5, the ratio increases with increasing reduced velocity. For 5 < Ur < 12, frequency ratio stabilizes around 1.15 to 1.25 and the curve shows a nearly flat slope. At reduced velocity of approximately 12, the frequency ratio jumps to 2.2. This sudden increase happens in parallel with the rapid drop in the oscillation amplitude and illustrates the end of the synchronization range. The frequency ratio reaches values of 3 when Ur = 15. In general, the frequency ratio in Figure 6.5 shows a very good agreement with experimental trends.

6.2.3.3. Drag and lift coefficients.

The changes in drag and lift coefficients at different reduced velocities are shown in Figure 6.6, together with the motion amplitude. The mean drag coefficient value jumps from approximately 1.5 to more than 2 when the reduced velocity increases towards the "locked–in" area (Figures 6.6 a,b,c). As can be observed from figure 6.6 (b,c), at Ur = 5 and 8, the drag coefficient oscillates with very large amplitude and when Ur = 12, in the desynchronization branch, the drag decreases dramatically, with mean C_d about 1.1 and oscillating with very low amplitude. Similar observations were made by Pan et al. (2007) based on their numerical simulations.

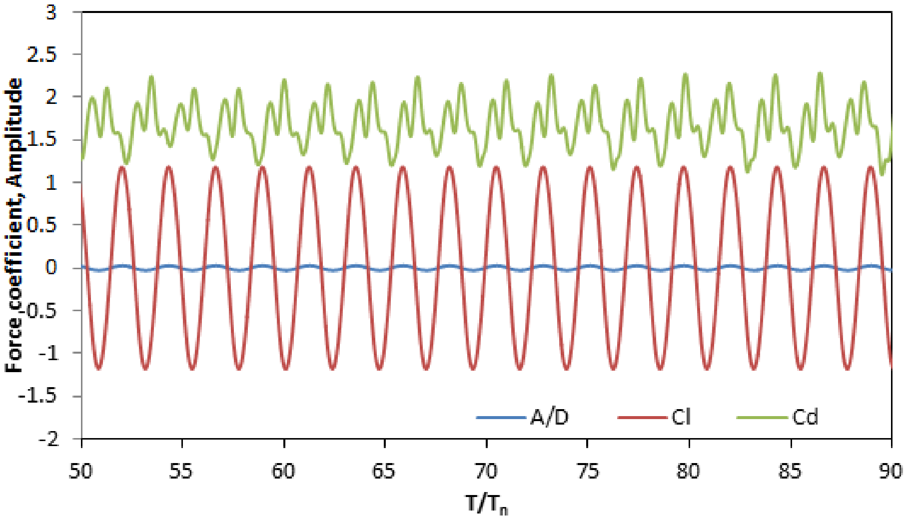

(a)

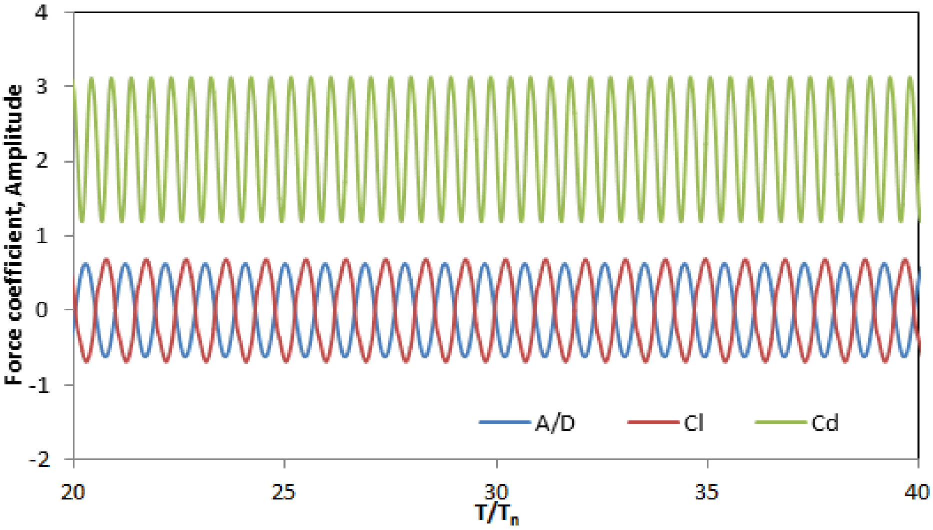

(b)

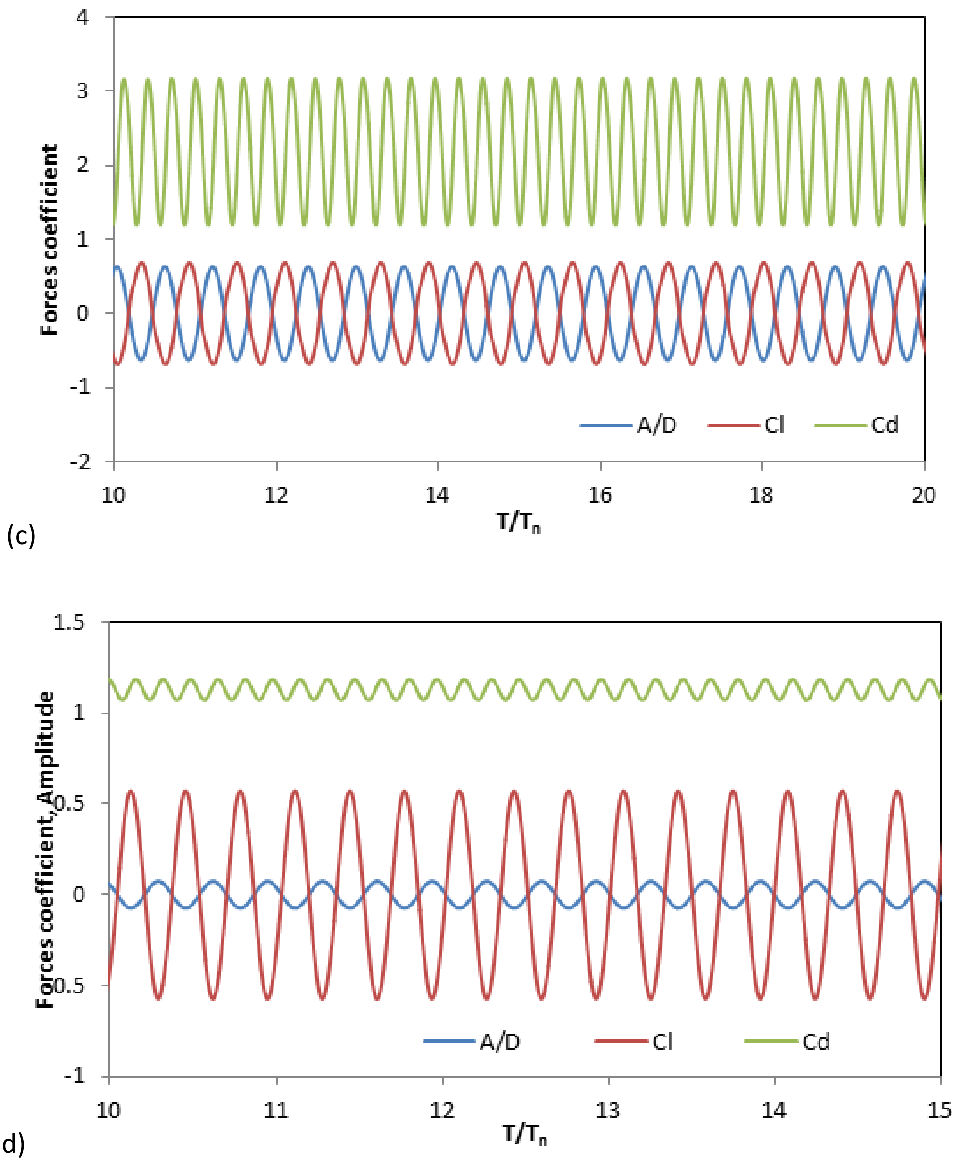

Figure 6.6. Forces and displacement time histories at different reduced velocity (a) Ur = 2,(b) Ur = 5, (c) Ur = 8, (d) Ur = 12

The lift coefficient reduces with increasing Ur, as can be observed in Figure 6.6. At low Ur values, the amplitude of the lift coefficient is more than 1, and it reduces when Ur increases with a value between 0.5 – 0.6 for $5 < Ur < 12$.

6.2.3.4. Effect of mass ratio

In addition to aforementioned work, the effect of mass ratio is investigated in the range $1.2 \leq m^* \leq 2.8$, as it is one of the most effective factors. In those simulations, damping coefficient was kept the same.

A reduction of mass ratio extends the locked-in region. For example, for m^* = 1.2, the cylinder still oscillates with an amplitude of 0.5D when Ur reaches 15. When m^* = 2.8, the locked-in region is shorter. As can be observed from Figure 6.7, the locked-in region stops at Ur = 8. This issue has also been mentioned in Govardhan and Wiliamson (2000).

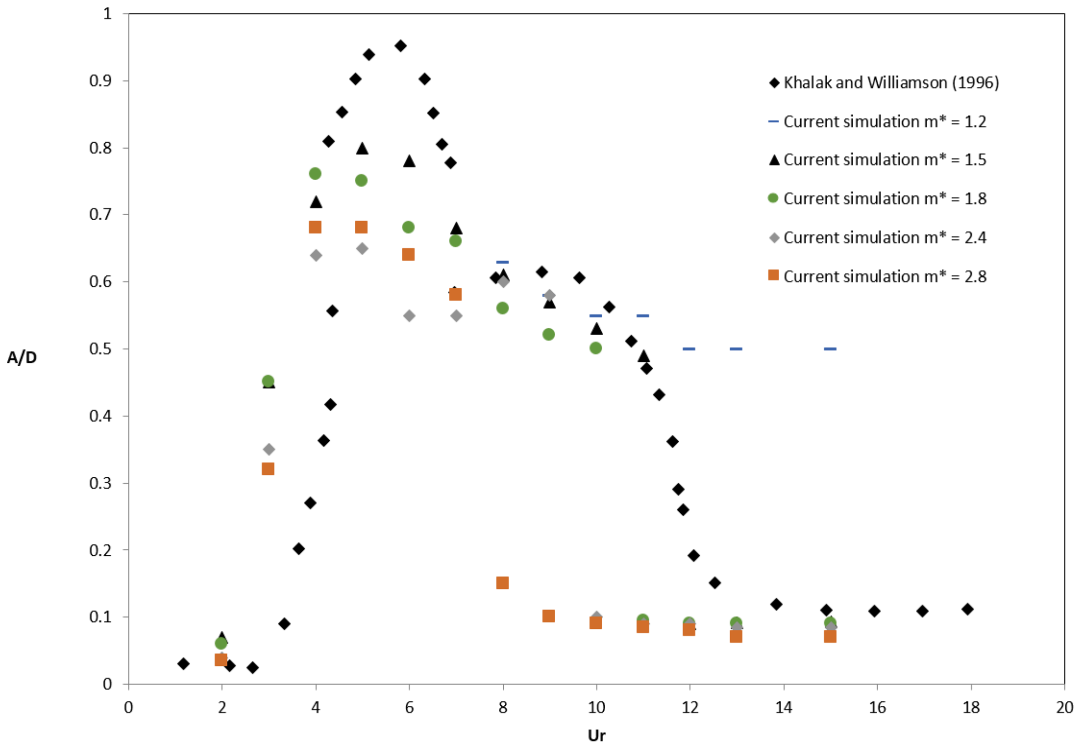

Figure 6.7. Effect of mass ratio

6.3. Vortex induced vibration with 2 dof

In this part, the rigid cylinder is undergoing VIV in both crossflow and inline direction (with 2 degree of freedom, or 2 dof) is investigated. The cylinder here is elastically mounted with spring-damper system, following equation 3.27, however in this case, this equation is applied to both inline and crossflow directions. The simulations are carried out for subcritical fixed Reynold number of 10,000 using SKW turbulence model and comparison are made with 1 dof results.

The 2 dof experimental results showed that, the vibration of the cylinder can reach maximum displacement of 1.6D. Such a large displacement may lead to large distortion in the adjacent meshing area around the cylinder and even break down. So that, in this 2 dof system, the bigger domain is used, with the same philosophies for 1 dof system, as seen in Figure 6.8.

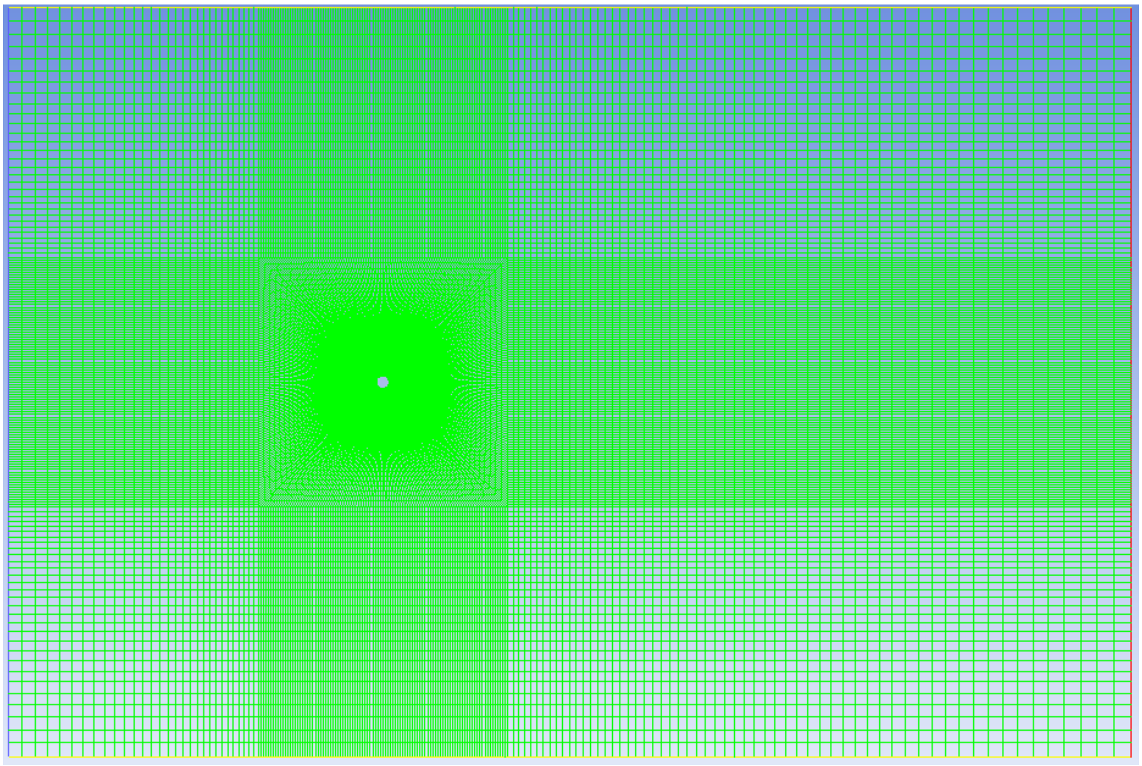

Figure 6.8. Computational domain for cylinder in 2 dof simulation

The computational domain was extended to 30D x 60D with total 60400 cells. With this domain, the cylinder is allowed to vibrate in both directions with the maximum amplitude of 5D. The boundary conditions, number of division around cylinder and y^+value are kept exactly the same. The test for fixed cylinder case produced the similar value of $C_d \approx 1.2$ & $C_l \approx 0.7$ compared to the previous case in Chapter 4 (Appendix D1).

The values of mass, damping, spring stiffness and natural frequencies are equal in both inline and crossflow directions as in the previous section. In typical 2 dof VIV, the following equations describe the relationship between inline and crossflow motion

$$y = A_y \sin(2\pi f_{ost-y} t) \qquad (6.4)$$

$$x = A_x \sin(2\pi f_{ost-x} t + \theta)$$

where A_x and A_y are inline and crossflow displacement amplitude respectively, θ is the phase angle between the inline and crossflow motions and f_{ost-x}, f_{ost-y} present frequencies in x, y direction. The relationship between the phase angle and trajectory of motion is summarised in Figure 6.9, where the phase angle decides the shape of the motion trajectory and the direction of motion is typically anti-clockwise (Jauvtis and Williamson, 2004).

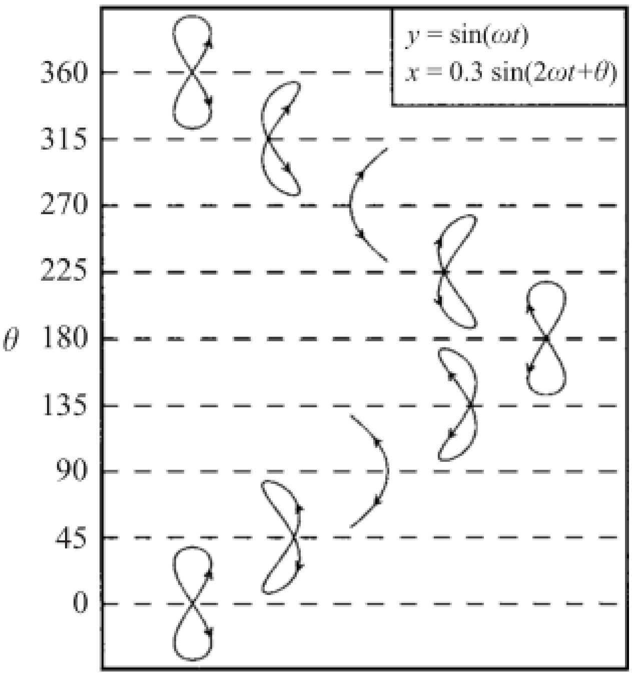

Figure 6.9: A sketch of 2 dof trajectory for a circular cylinder from (Jauvtis and Williamson, 2004).

The benchmark 2 dof VIV measurements of Jauvtis and Williamson (2004) will be selected to validate the data. Jauvtis and Williamson carried out these experiment in a water tunnel where the mass ratio (m^*) ranged from 1.5 to 25.0. The oscillating mass is defined as mass plus added mass, and their combined mass damping $(m^* + m_d C_a)\zeta$ ranged from 0.001 to 0.1, where C_a is ideal added mass coefficient $C_a = 1$. The Reynolds number ranged from 1000 to 15000 with a corresponding reduced velocity from 2 to 12. In this simulation, Jauvtis and Williamson (2004)'s measurement at $m^* = 2.6$ are selected for comparison.

6.3.1. Numerical method

In the previous section, SDOF was used to simulate the cylinder in VIV. However, SDOF Macros limit the cylinder to oscillate with 1 dof in one direction only. With the aim of further extension to more than 1 dof in each direction, a new UDF is developed based on the Finite difference method (FDM) (Appendix C.2).

Starting with the equation of motion (3.27): $m\ddot{y} + c\dot{y} + k\mathrm{y} = F_y(t)$ the displacement, velocity and acceleration and cylinder velocity can be achieved using FDM based on the values of cylinder position in three neighbouring time steps, $i-1, i, i+1$ namely:

$$\ddot{y} = \frac{y_{i+1} - 2y_i + y_{i-1}}{dt^2} \tag{6.5}$$

$$\dot{y} = \frac{y_{i+1} - y_{i-1}}{2dt} \tag{6.6}$$

When these are back substituted in equation 3.27, we obtain:

$$m\frac{y_{i+1} - 2y_i + y_{i-1}}{dt^2} + c\frac{y_{i+1} - y_{i-1}}{2dt} + ky_i = F_y \tag{6.7}$$

Solving for y_{i+1}, we obtain

$$y_{i+1} = \left\{\frac{1}{\frac{m}{dt^2} + \frac{c}{2dt}}\right\}\left[F_y + y_{i-1}\left(\frac{c}{2dt} - \frac{m}{dt^2}\right) + y_i\left(\frac{2m}{dt^2} - k\right)\right] \tag{6.8}$$

Equation 6.8 is a recurrence formula, which permits the user to calculate the displacement in the time domain. Value of y_{i+1} are calculated based on values of force F_y produced by ANSYS Fluent and previous time step values of displacements y_{i-1} and y_i. The velocity $\dot{y_i}$, at time step i is updated in ANSYS Fluent. This new velocity is used to calculate the displacement of the cylinder in the next time step, using Fluent defined Macro: DEFINE_CG_MOTION. This equation was applied to solve the 1 dof case for verification, showing that the results produced by FDM are the same with SDOF (Appendix E)

6.3.2. Simulation setup

Reynolds number is 10,000 for validation, as for Re < 22,000, it is not an influential factor. The frequencies of the system were changed to obtain the required Ur value. The properties of the system used are shown in Table 6.4:

Table 6.4: 2 dof simulation properties

Mass ratio	m^*	2.6
Damping ratio	ζ	0.005417
Mass damping	$m^*\zeta$	0.014
System frequency	f_n	0.012175 - 0.07305
Reduced velocity	Ur	2 - 12

The simulations are undertaken in the range of reduced velocities from 2 to 12 with the properties similar to Jauvtis and Williamson's experiment (see Table 6.4). The additional equation of motion is applied in inline direction, enabling the cylinder to move in x-direction.

6.3.3. Results

6.3.3.1. Response characteristics

Figure 6.10 shows the dimensionless motion amplitudes of the cylinder in the inline and crossflow direction at Ur = 5. The time history can be divided into two periods, transient and unsteady oscillation periods. The amplitude of motion of the cylinder A_x/D and A_y/D will be calculated based on the data on oscillation region. When the motions are not in harmonic form, the nondimensional amplitude of oscillation A_x/D and A_y/D will be calculated by $\sqrt{2}$ time standard deviation.

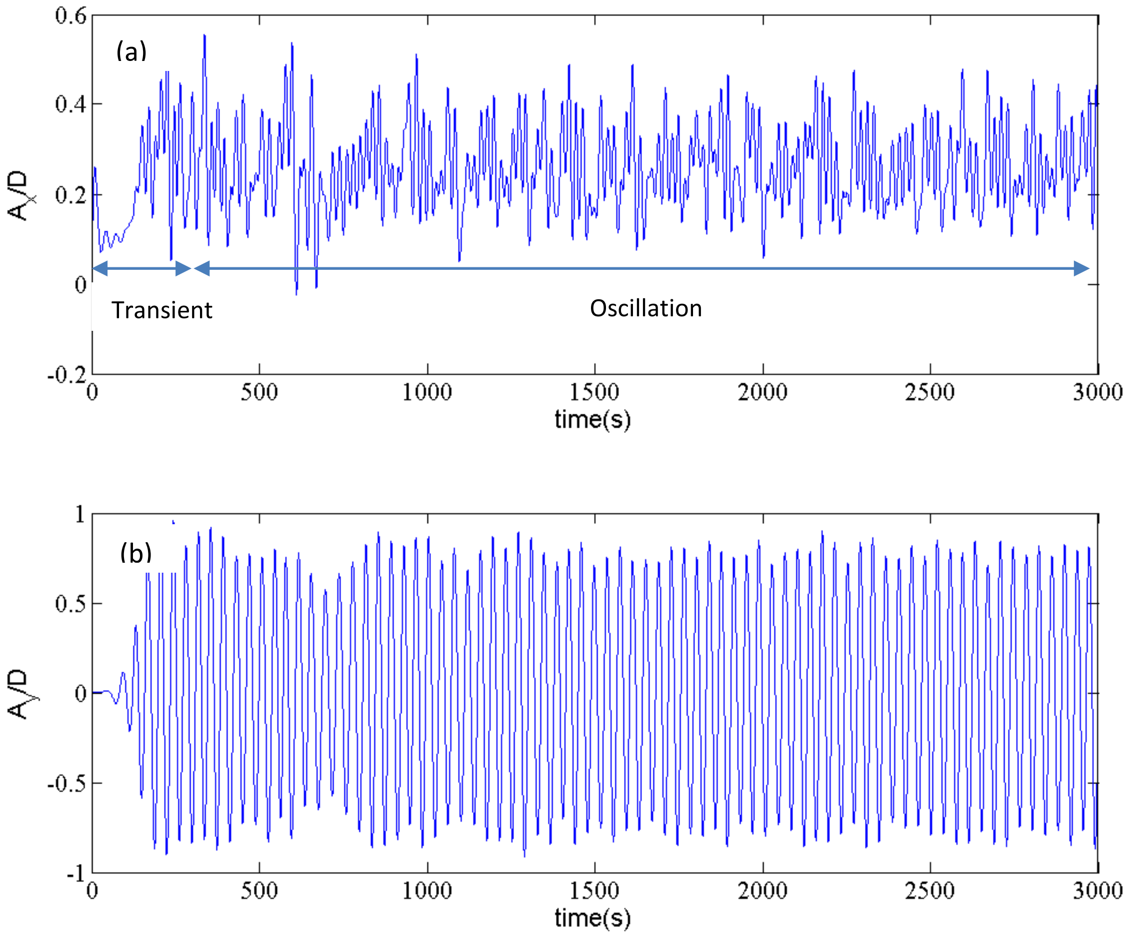

Figure 6.10. Vibration time histories of inline A_x/D in (a) and crossflow A_y/D in (b) at $Ur = 5$

However, at Ur = 8, the motion is more complicated. The time history now contains four distinct time histories of differing characteristics. In particular, transient high amplitude changes to high amplitude oscillation prior to low amplitude transient follow by low amplitude of oscillation.

The amplitudes of inline oscillation of the cylinder will be calculated based on intervals designated oscillation 1 and 2 in Figure 6.11 (a). The crossflow oscillations are determined similarly.

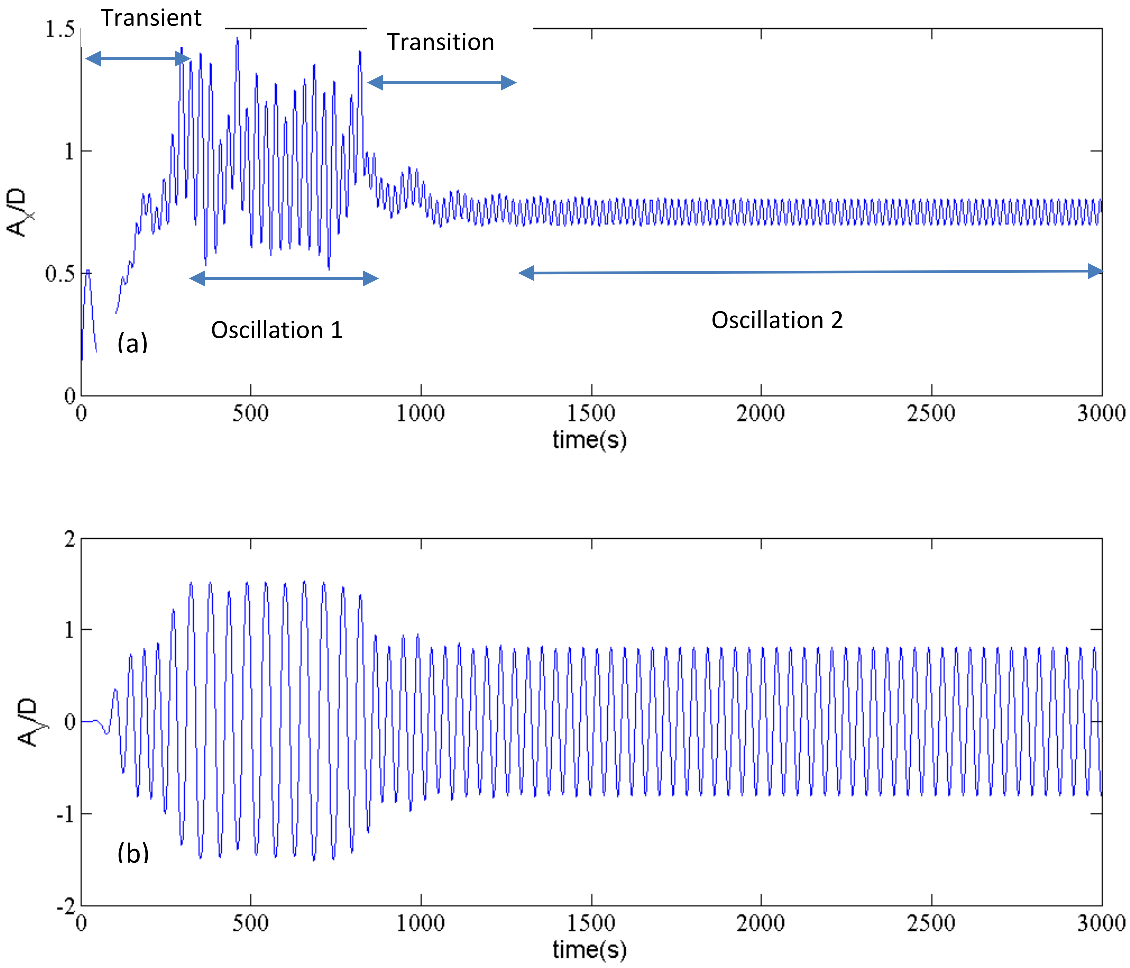

Figure 6.11. Times history of inline (a) and crossflow (b) vibration at $Ur = 8$

Figure 6.12 shows the dimensionless motion amplitudes of the cylinder in X and Y directions over a range of reduced velocities. As can be observed from this figure, VIV with 2 dof results in much higher amplitudes of motion, A_y/D = 1.5 at $U_r = 8$. This is almost 60% higher compared to 1 dof cylinder in crossflow VIV experimental peak amplitudes and almost double compared to 1 dof simulation. In general, the results agree well with Jauvis and Williamsons' (2004) results for the whole range of reduced velocities. The three different branches including initial branch (I), super upper branch (SU) and lower branch (L) can be observed.

At low reduced velocities range (Ur < 4), the influence of 2 dof is not significant, as the inline vibration is very small. The motion of the cylinder in the crossflow direction is similar to that of the 1 dof case of Khalak and Williamson's experiment. For Ur > 4, the sharp jump can be seen. However, for the 2 dof system the jump is less sharp than the 1 dof, but results in much higher amplitudes where the super upper branch appears. The peak amplitude of 1 dof system was observed at $Ur \approx 6$ whilst for 2 the dof system, the peak amplitude continues increasing, reaching A_y/D = 1.5 at Ur = 8. In the range of Ur from 7.5 to 8, there is a transition area where two oscillating amplitudes in both X and Y direction can be seen. In this range, the oscillating amplitude of the cylinder changes from super-upper branch to lower branch, also observed by Jauvtis and Williamson (2004) in the same reduced velocity range.

The lower branch also exhibits the same response as in the 1 dof case of Khalak and Williamson (1996)'s experiment where the amplitude of motion $A_y/D \approx 0.7$, is about 25% higher compared with a 1 dof system. However, the same trend can be recognised and the synchronisation range stops at $Ur \approx 13$. In general, the 2 dof crossflow amplitude shows much higher values compared with the 1 dof system, and the maximum amplitude is approximately double, as seen in Figure 6.12.

For the oscillation in the inline (x) direction, the current simulation also agrees well with the experiments. The important transition area is observed at $7.5 \leq Ur \leq 8.25$ with the peak amplitude of motion recorded $A_x \approx 0.35$D. At the lower and desynchronization region, the motion in x direction is minimal, less than 0.06D.

One problem with the current simulation is the first A_x peak at $Ur \approx 3$ is insignificant, unlike experimental observation. However, the trends are similar and predicted A_x/D is approximately 50% of that by Jauvtis and Williamson. In general, the current simulation agrees very well with the experimental results in terms of amplitude of motion over a range reduced velocities at Re = 10,000.

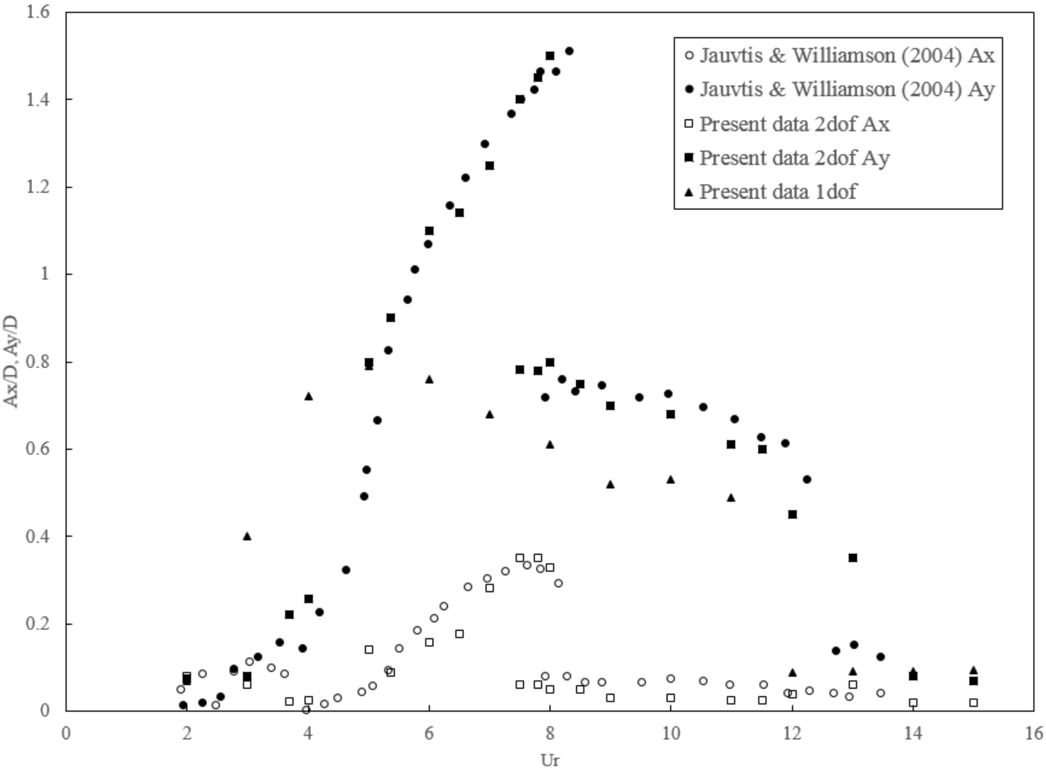

Figure 6.12. Response amplitude of the system in 2 dof for low mass damping ratio ($m^* = 2.6$) compare with Jauvtis & Williamson's experiment in 2 dof and previous simulation in 1 dof.

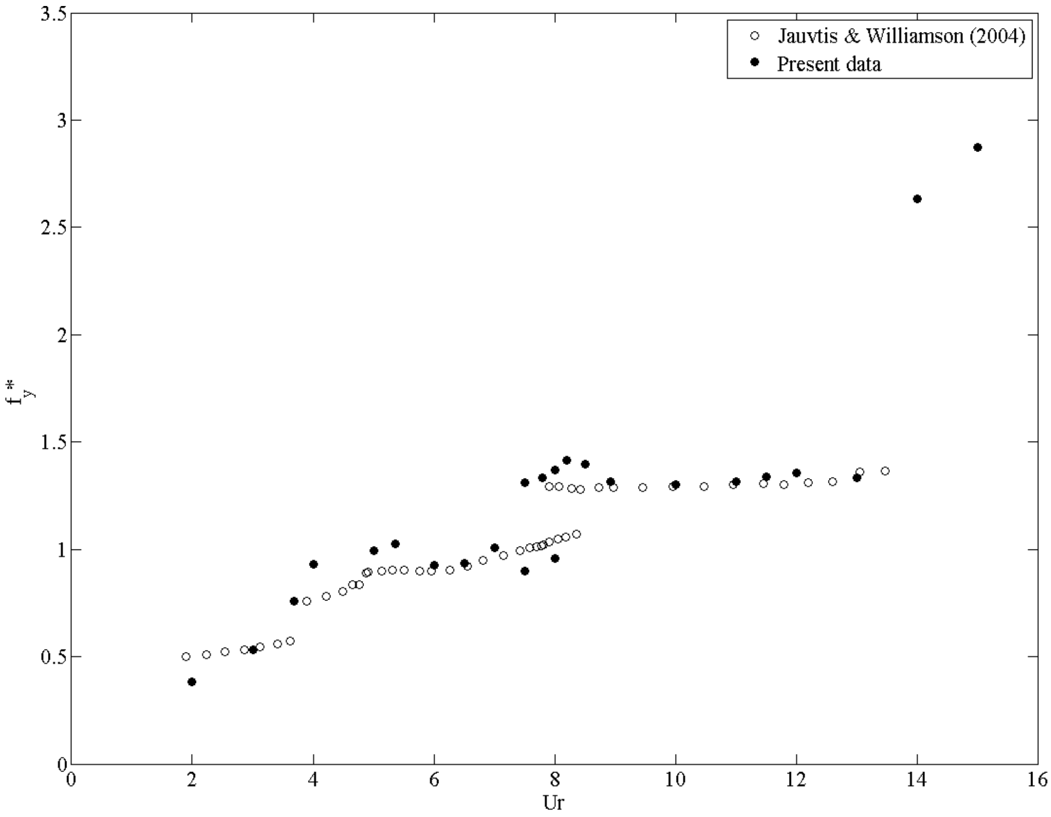

Figure 6.13. Crossflow frequency ratio of 2 dof system ($m^* = 2.6$) compared with Jauvtis & Williamson's experiments

Figure 6.13 shows the frequency ratio in crossflow direction $f_y^* = f_v/f_n$ where f_v is vortex shedding frequency and f_n is the natural frequency of the system. The data is compared to Jauvtis and Williamson's experiment. The current prediction shows reasonably good agreement with the experimental results. For the initial branch, f_y^* < 0.5 at Ur < 3. When the jump appears, where the cylinder is moving with much higher A_y amplitude, the $f_y^* \approx 1$ for 4 $\leq Ur \leq$ 8, which reflects the super-upper branch. At the transition area, 2 frequencies can be observed, where the lower frequency corresponding to $f_y^* \approx$ 1 and the other one to $f_y^* \approx$ 1.25. At the end of the super-upper branch reaching the lower branch, the frequency ratio is moving to 1.25, and maintains nearly the same value until the end of lock-in.

At the desynchronization area, a sharp jump is observed, with f_y^* > 2.5 and continues increasing with increasing Ur. This reflects a similar trend for 1 dof elastic mounted cylinder both numerically and experimentally. However, for the 2 dof case, there are no experimental values for Ur>14.

6.3.3.2. Motion trajectory

In oder to characterise the sytem dynamics, the motion tranjectories are plotted in Figure 6.14. The comparision to the measurement of Jauvtis and Williamson show similar shapes compared to the current simution, as well as direction. At very low reduced velocity, Ur = 2, the motion inline is larger although very small amplitudes of motion in both direction. For $Ur \leq 6$, the motion appears in 8 shape, with the moving direction is clockwise at the top but anti-clocksiwse in the bottom and amplitude of motion in crossflow is getting larger compare to inline direction. For $7 < Ur < 8$, the motion appears in a C shape due to strong inline motion in super upper branch. At higher reduced velocity, the other 8 shape was recognised, although, the inline motion is reasonably small. In lower branch, coresponding to $Ur > 9$, the motion trajectory returns to 8 shape, but the crossflow motion is dominant.

In the present simulation, it should be noted that the cylinder is displaced from its original position to a new downstream equilibrium position. This phenomenon is a result of constant drag force applied on the cylinder, namely an offset. However, this displacement does not change the oscillating characteristics of the system.

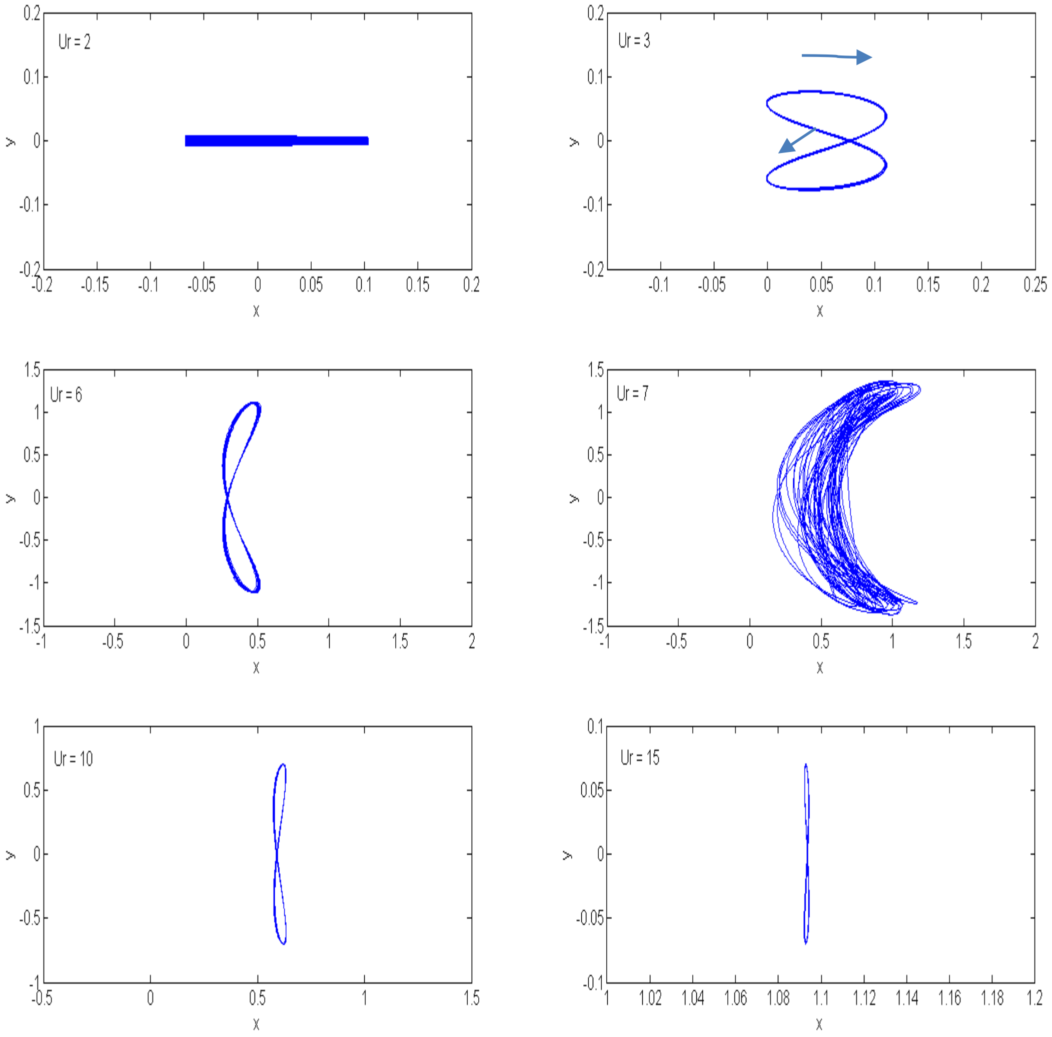

Figure 6.14. X, Y trajectory shapes at different reduced velocity.

6.3.3.3. Drag and lift coefficients

The drag and lift coefficient history is presented in Figure 6.15. At Ur = 2, C_d oscillated with very high amplitude whist C_l oscillation is minimal and the mean $C_d \approx 1$. This explains why the inline is bigger than crossflow motion at very low reduced velocities.

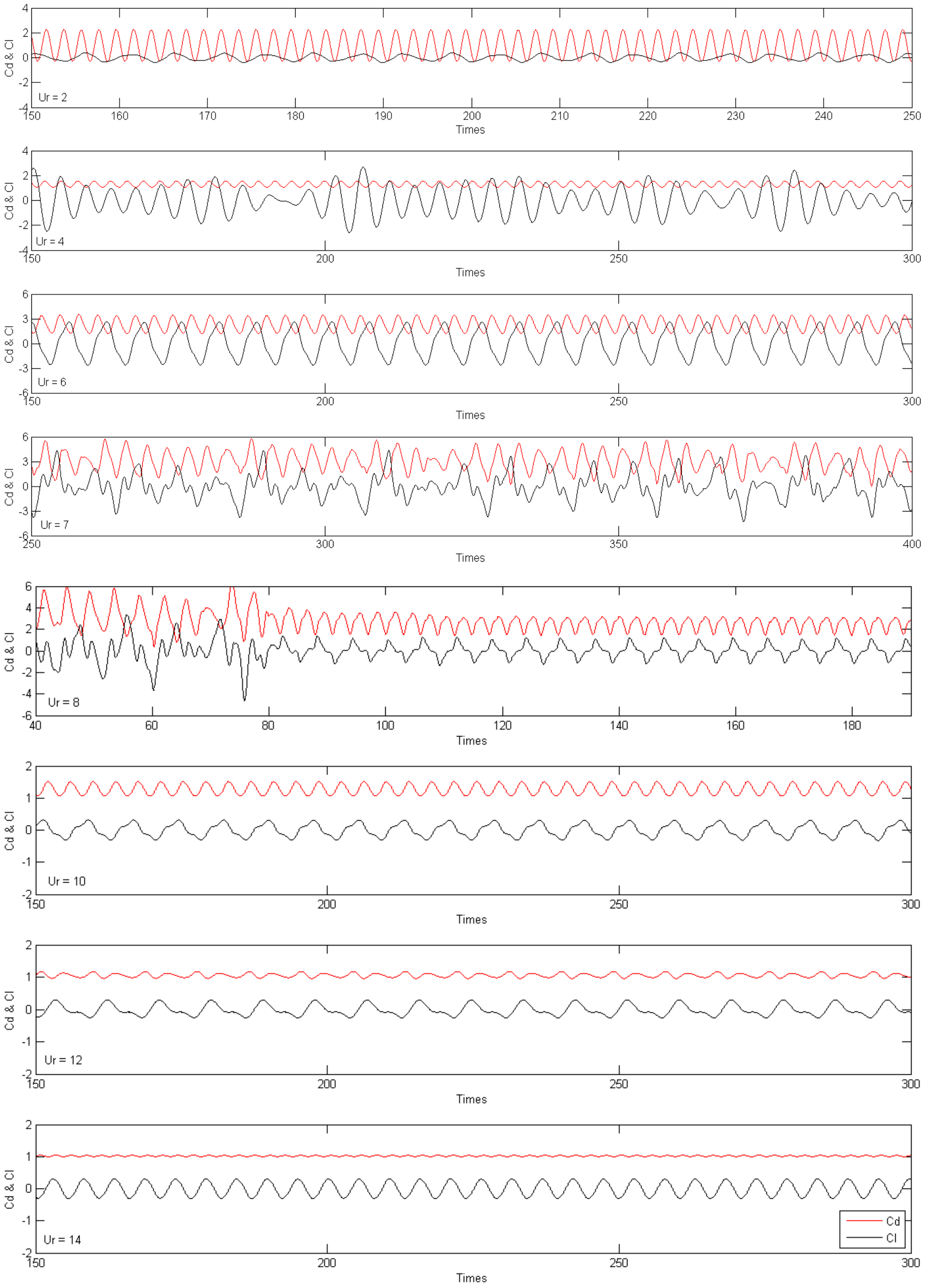

Figure 6.15: Time history of lift and drag coefficient

As Ur increases, the values of lift and drag both dramatically increase, until the transition area is approached. The maximum mean C_d > 2 with a big oscillating amplitude and C_l amplitude reach approximately 2.5. At the transition area, the "jump" down for both drag and lift coefficients can be observed, with the mean C_d reduced to 2 and C_l amplitude is approximately 1.2. At this transition area, two frequencies and two peak amplitudes can be observed and the lower frequency indicates the start of the lower branch. When Ur > 8, the drag and lift amplitude is much lower compared with the previous branch. Mean C_d reduced from 2 to 1.2 at Ur=10 and 1.05 at Ur =12 and the C_l amplitude is also reduced to less than 0.3. At this range, the oscillating lift is quite small compared to the upper branch, reflecting low amplitude of motion in X direction. Nevertheless, this lift still moves the cylinder A_y/D about 0.7, which is a little higher compared to 1 dof system. At Ur = 14, in the desynchronization branch, the drag oscillation is very small with mean C_d = 1 and the lift coefficient amplitude still nearly the same compared to that of Ur = 12.

6.3.3.4. Vortex pattern

The vortex formation in the wake of an oscillating cylinder is associated with the amplitude ratio A* and the reduced frequency velocity, as suggested by Williamson and Roshko (1988). For the 1 dof system, the response would be intermittently switching between the initial and lower branches on the "upper branch", as observed in experiments and in LES/DNS simulations. Therefore, the resulting vortex shedding formation in the wake would be mixed with the 2S and 2P mode.

However for the 2 dof system in Jauvtis and Williamson experiments, in addition to 2S and 2P vortex patterns, a new vortex pattern is identified. The current simulation is able to capture the vortex patterns for 2S, 2P and 2T at different reduced velocities as shown in Figure 6.16.

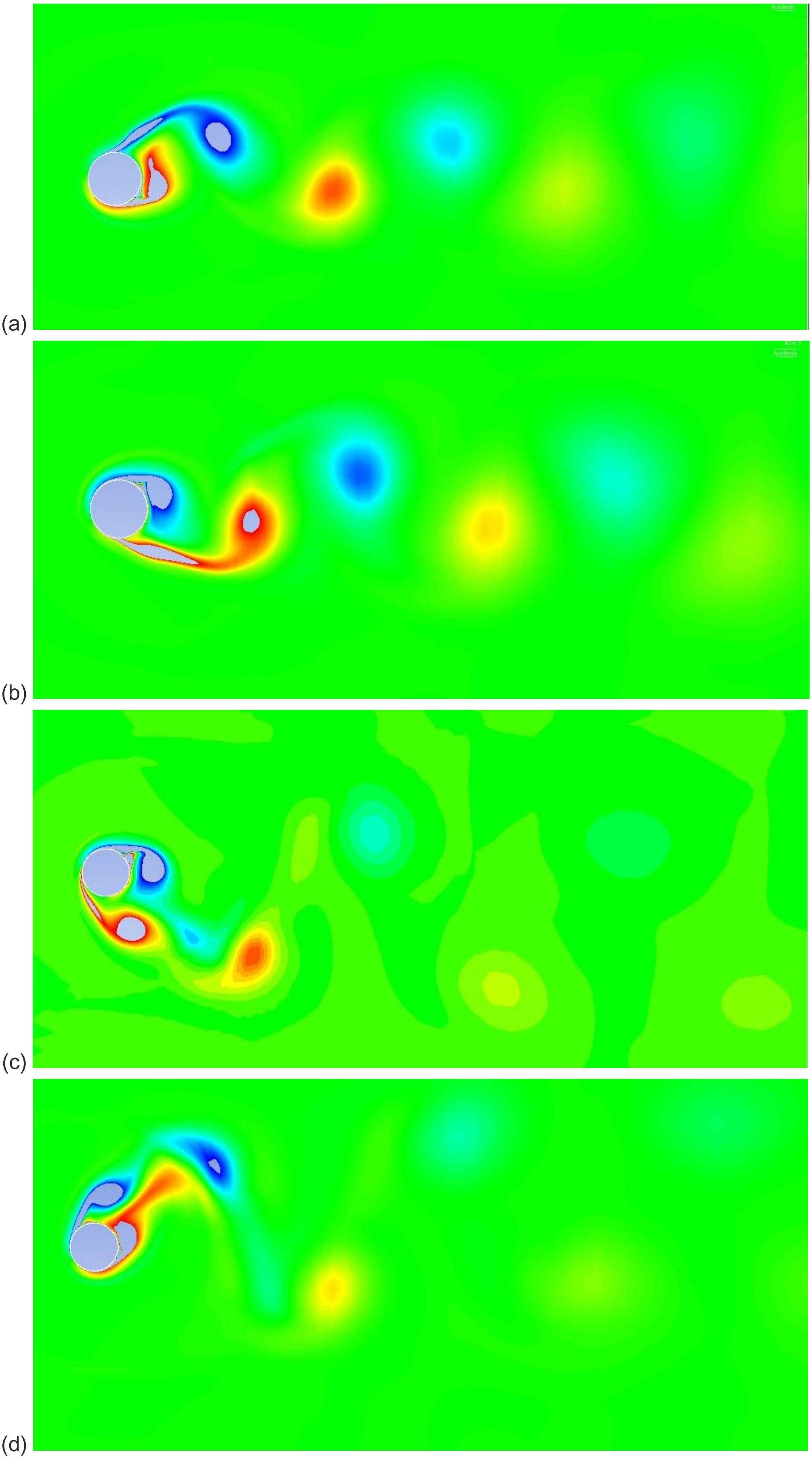
(a)
(b)
(c)
(d)

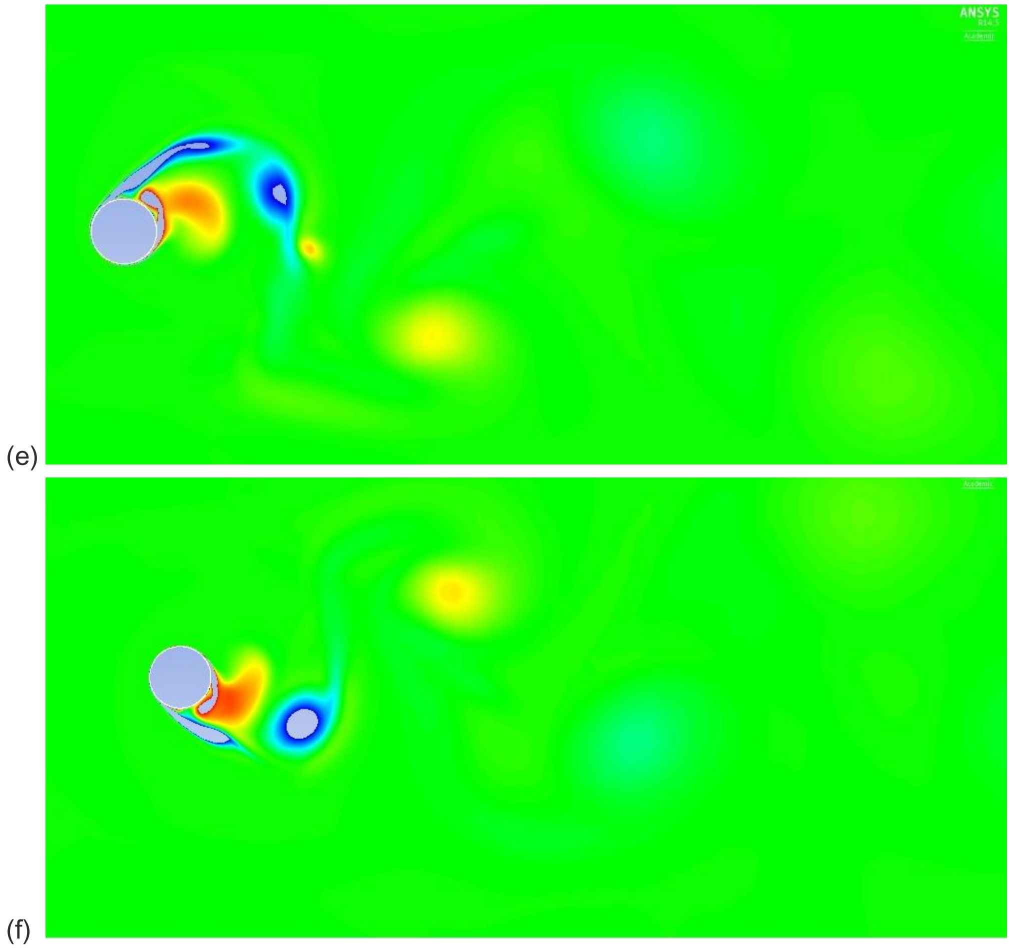

Figure 6.16 Vorticity around the cylinder (a,b) 2S at Ur = 3.69 , (c,d) 2P at Ur =6, (e,f) 2T at Ur =8

The vortex pattern is formed with 2S mode at the initial branch where Ur = 3.69. When Ur increases, similar to the 1 dof case of Govardhan and Williamson (2000), 2P mode is observed in the upper branch, when A/D < 1.4. The next pattern changes from 2S to 2P, as seem for Ur = 6. At the peak of super-upper branch when A_y/D > 1.4, the 2T model is observed. In this range, the vortices are formed in triple formation including S+P (Figure 6.16.e,f)

6.4. Conclusion

For the 1 dof system, a good overall agreement with experimental measurements is obtained for the freely oscillating cylinder in cross-flow, for a system with low mass damping value. It should be noted that as the random disturbance is erased by the Reynolds averaging procedure, RANS simulation results are statistically stable. Although the simulations did not capture the maximum oscillation amplitude value in the upper branch, they did capture the behaviour over the range of reduced velocities, including the lock-in regime and the desynchronization. The dramatic increase in amplitude of oscillation is shown along with a frequency ratio that is close to unity (lock-in), followed by a drop in amplitude of oscillation and jump in the frequency ratio (desynchronization).

For the 2 dof system, the simulation results show very good agreement with the benchmark experiments of Jauvtis and Williamson (2004). The coupling between inline and crossflow motions can increase the amplitude of motion by 60% compared with crossflow vibration only experimental results and near double compare with simulation. Furthermore, at the supper upper branch $A/D >$ 1.4, the 2T vortex shedding pattern can be observed. At low Ur area, the maximum crossflow amplitude is not affected by the inline motion.

The mean drag acting on the cylinder results in an offset, whereby the cylinder is pushed downstream before oscillating. For a single cylinder oscillation case this does not affect the results as the focus is on amplitude of vibration.

Current studies in this chapter were undertaken with 2D RANS turbulence model, showing reasonably good agreement with experimental measurement and other simulations. The SKW turbulence model has worked well for both stationary and oscillating cylinders. This provides confidence in the models used and open the way for further calculations with more complex elastic supports, especially downstream of a stationary cylinder in Chapter 7, 8 and 9.

Chapter 7 : Vortex and Wake Induced Vibration in a downstream cylinder.

7.1 Introduction

In this chapter, numerical CFD simulations are applied to a rigid cylinder undergoing oscillation in the wake of an upstream cylinder. Two cases are investigated, namely (i) 1 direction (crossflow only) and (ii) 2 directions (inline and crossflow). The downstream cylinder is located at a centre-to-centre spacing L = 5D from the upstream cylinder. The dynamic meshing scheme for the single cylinder with 2 dof of the previous chapter was used. In this case, the downstream cylinder undergoes not only Vortex Induced Vibrations but also Wake Induced Vibrations. The large amplitude of motion due to WIV is due to the vorticity in the gap region and the question of whether the upstream cylinder is stationary or free to move can be disregarded in cases with gap separations L > 5D (Huera-Huarte and Gharib, 2011b).

Simulations are carried out at sub-critical Reynolds number of 22,000 in order to investigate the effects of reduced velocity on the dynamic behaviour of the downstream cylinder. In this case, a higher Re is used due to the comparison for two stationary cylinders in tandem and availability of validation data. In addition to crossflow vibration (1 dof), the coupling effect of inline and crossflow vibration (1+1 dof) for cylinders in a tandem arrangement is also studied.

In the current simulation, low mass-damping ratio $m^{*}\zeta$ is applied. The values of spring stiffness, mass, damping and natural frequency are equal in both directions. The numerical prediction results are validated with experimental results by Assi et al. (2010) for m^{*} =2.6, $m^{*}\zeta$ = 0.018; Re < 25,000 and Chaplin and Batten (2014) for m^{*} =0.87, $m^{*}\zeta$ = 0.025, Re < 58,000. As mentioned in the preceding chapter, amplitudes of VIV are primarily related to the value of reduced velocity as well $m^{*}\zeta$ values. Therefore, the studies in this chapter are also carried out over a range of reduced velocities to predict the dynamic responses and transition areas (in 1 dof and 1+1(2) dof) of the downstream cylinder.

Figure 7.1. Configuration of (a) 1 dof (b) 1+1 dof elastically mounted system

To begin with, CFD predictions are obtained for the system shown in Figure 7.1 (a). The mass ratio was chosen equal to Chaplin and Batten's (2014) experiment and the centre to centre separation is 5D. The results of the simulations will also be compared with the benchmark experiment by Assi et al (2010) even though the system properties are different.

In literature, in the most cited experiments, the downstream cylinder is limited to only crossflow oscillation. Thus, in the second part, investigations explores the downstream cylinder oscillation in both directions using the 1+1 dof elastically mounted system shown in Figure 7.1b. The 1+1 dof system results are also compared with the 1 dof system at the Reynolds number of 22,000. The properties of the system are summarised in Table 7.1. Those parameters are applied similarly for elastically mounted system in both inline and crossflow direction:

Table 7.1. Downstream cylinder for 1 dof and 1+1 dof systems properties

Reynolds number	Re	22,000
Turbulence model	uRANS	Standard $k-\omega$
Mass ratio	m^*	0.87
Damping ratio	ζ	0.02873
Mass damping ratio	$m^*\zeta$	0.025

7.2. Numerical simulation setup

The two cylinders are placed in a 40D x 70D rectangular domain. The centre of the fixed upstream cylinder is located at 20D from the inlet boundary. The downstream cylinder is located at a distance of 45D from the outlet. In this arrangement, both cylinders are of the same diameter of D and the Reynolds number was kept constant at 22,000 . Figure 7.2 shows the computational domain for the test cases. The downstream cylinder circumference is divided into 420 cells and 100 cells were placed along the side of the surrounding rectangular area. The upstream stationary cylinder circumference is divided into 200 cells and 60 cells were placed along the side of surrounding square area. The mesh was coarsened outside in order to reduce computational cost. The current mesh is based on the features of the grids used for the two stationary cylinders in the tandem case in Chapter 4, applied to the upstream cylinder and the single oscillating cylinder in Chapter 6, applied to the downstream cylinder area. As mentioned in the literature, compared with a single cylinder in VIV cases, the downstream cylinder in VIV experiences much higher amplitude of motion, without any limitation in some cases (Chaplin and Batten, 2014).

In CFD simulation, the large displacement of the downstream cylinder may lead to a reduction of the mesh quality and even the mesh breakdown, as aforementioned in chapter 6. In order to avoid these issues due to high distortion, the mesh refinement around the downstream cylinder applies to a larger region compared with those of two fixed cylinders in tandem. This ensures that the downstream cylinder is able to oscillate up to 9D in inline and 5D in crossflow directions. A uniform flow in the horizontal direction is applied at the inlet boundary, the pressure outlet boundary is applied at the outlet of the domain. The upper and lower sides of the domain are treated as symmetry conditions. The mesh comprises 69200 cells, with 69839 nodes. The convergence test showed that mesh dependency is negligible (Appendix D2). The current model, for both cylinders fixed, produces similar lift and drag forces similar to two fixed cylinders in tandem at 5 L/D (Chapter 4.3)

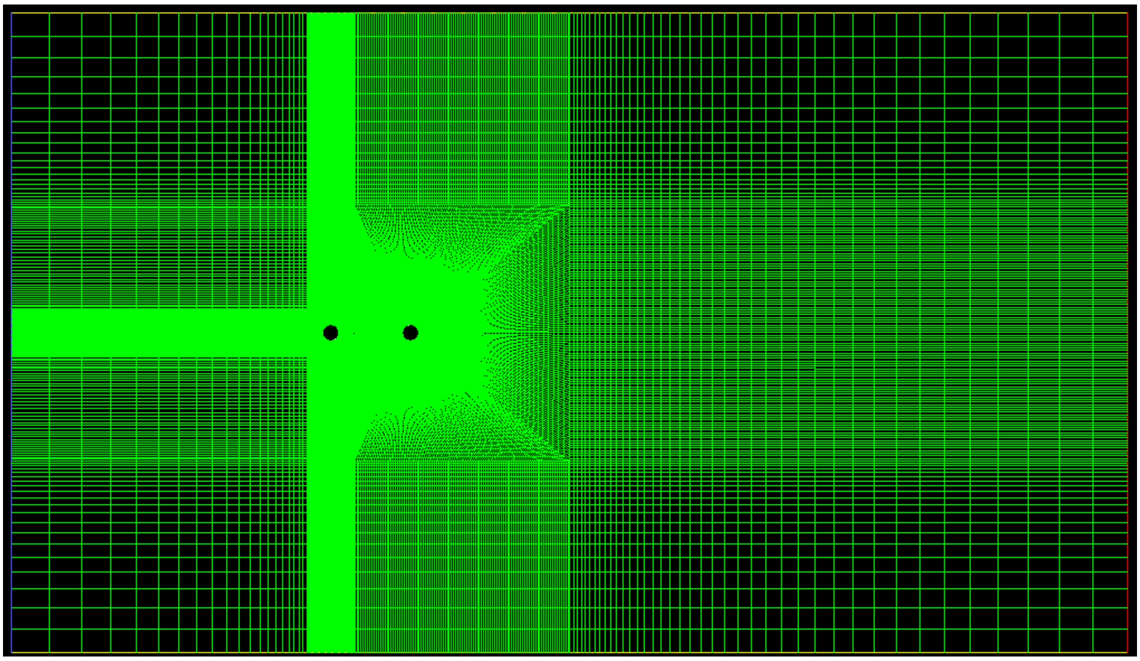

Figure 7.2: Computational domain for two cylinders in tandem at L/D = 5

To preserve the y^+ value around the cylinder, the diffusion parameter is used with value of 1, which is suggested by ANSYS Fluent for high deformation mesh cases. The application of the diffusion parameter keeps the area of 2D around the body unchanged; thus, the near wall distance and the mesh around the cylinder is preserved to obtain convergence value for the fluid forces around the cylinder. The numerical method in 6.3.1 is used for the downstream cylinder both for 1 dof and 1+1 dof system.

7.3. Downstream cylinder with 1 dof

Initially, the simulation results of a downstream cylinder attached to an elastically mounted system including spring and damper, is able to move in the crossflow (y) direction (1 dof), as shown in Figure 7.1(a).

Time history of the cylinder's crossflow vibration at Ur = 4 and 8 are presented in Figure 7.3.

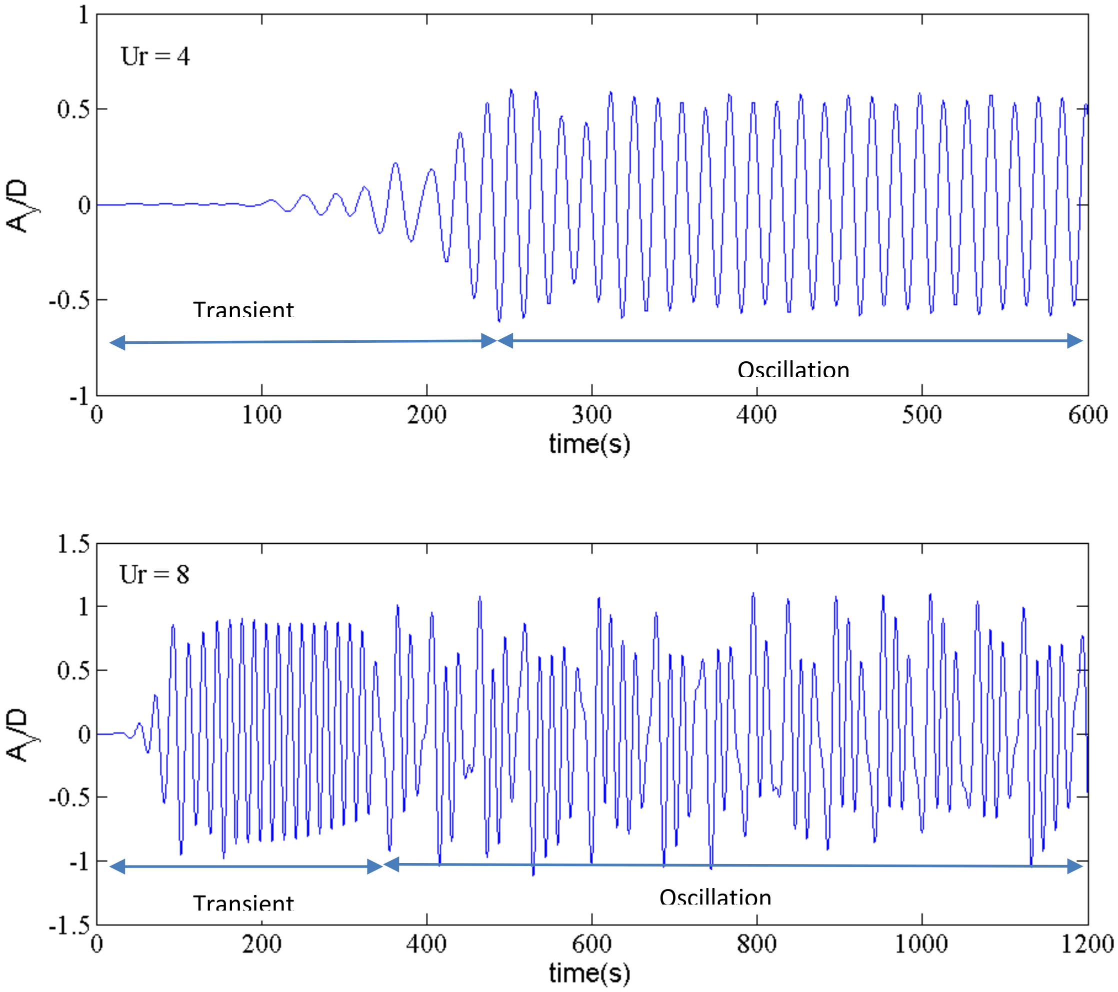

Figure 7.3. Motion of the cylinder time history at Ur = 4 and Ur = 8

Similar to a single cylinder in VIV, the illustrated time history can be divided into a transient and a period of almost steady and unsteady oscillation in the A_y for U_r= 4 & 8 respectively. At Ur = 4, the transient period is longer with almost 200s of transient, following by sinusoid oscillation period. However, at Ur = 8, the oscillation period is not so steady. To determine the oscillation amplitude, the transient periods are ignored and only the oscillatory period of data shown in Figure 7.3 will be used.

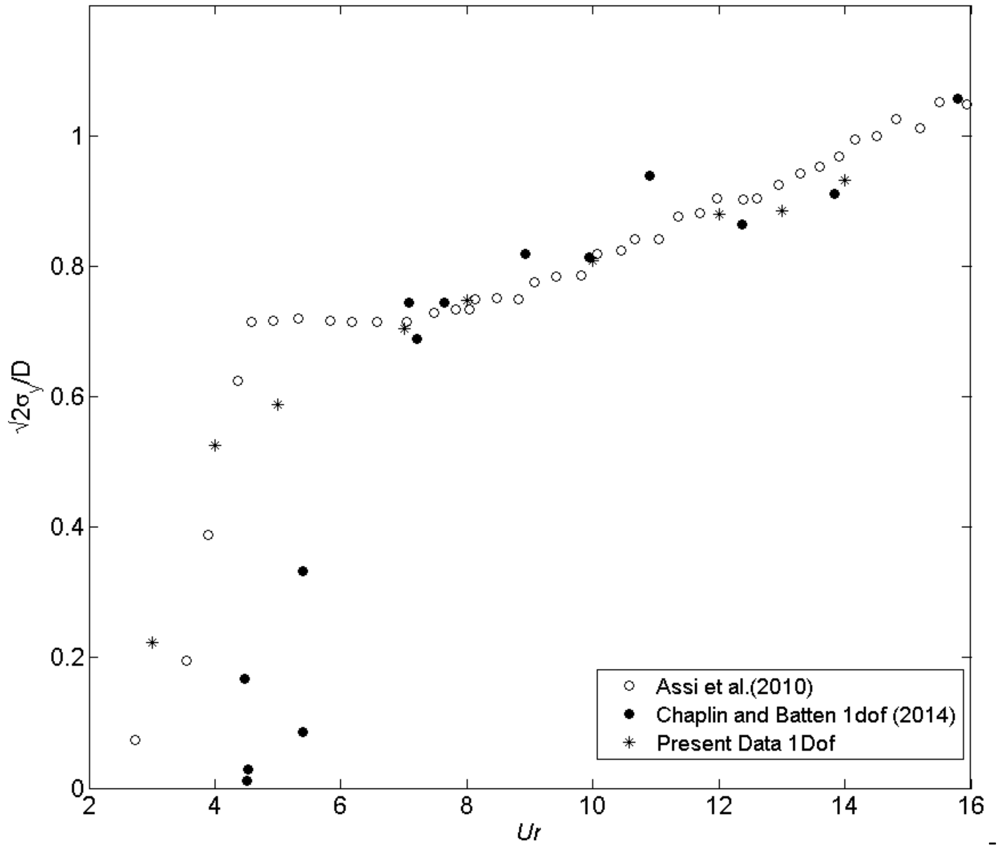

Figure 7.4. Cross flow amplitude of downstream cylinder at L/D = 5, 1 dof

Figure 7.4 compares the present results, with experimental measurement in form of $\sqrt{2}$ times the standard deviation of the displacement. The general agreement is reasonably good, and reflects the main trends of crossflow amplitude of motion of the downstream cylinder, particularly when Ur > 7. The transition area is observed, that agrees with Assi et al's experiment with the "jump" appearing when Ur increases from 3 to 5. However, in Chaplin and Batten's experiments, the jump occurs at higher Ur. This can be explained due to the much higher level of turbulence used in Chaplin and Batten's experiment, approximately 5% compared to Assi et al's experiment (<1%). In numerical simulations, modelling high level of turbulence is still a challenge. Even for a single cylinder with 2 dof VIV, the experiments of Chaplin and Batten recorded later transition compared to Jauvtis and Williamson (2004) due to their higher level of turbulence. For $5 < Ur < 7$, the amplitude of motion in the simulation was approximately 20% smaller compared to the experimental values. There is a gradual increase in amplitude of motion when Ur > 7. Overall, a good agreement could be observed.

The displacement of the cylinder at higher turbulence intensity $I = 5\%$ is showed in Figure 7.5 to compare with the previous data at $I = 1.4\%$. The higher turbulence intensity value does not change the gradient of standard deviation at low $U_r$behaviour is similar to lower turbulent intensity case, although the motion amplitudes over a range of Ur are higher. This behaviour is as expected, as increasing turbulence intensity will create the stronger forces acting on the body.

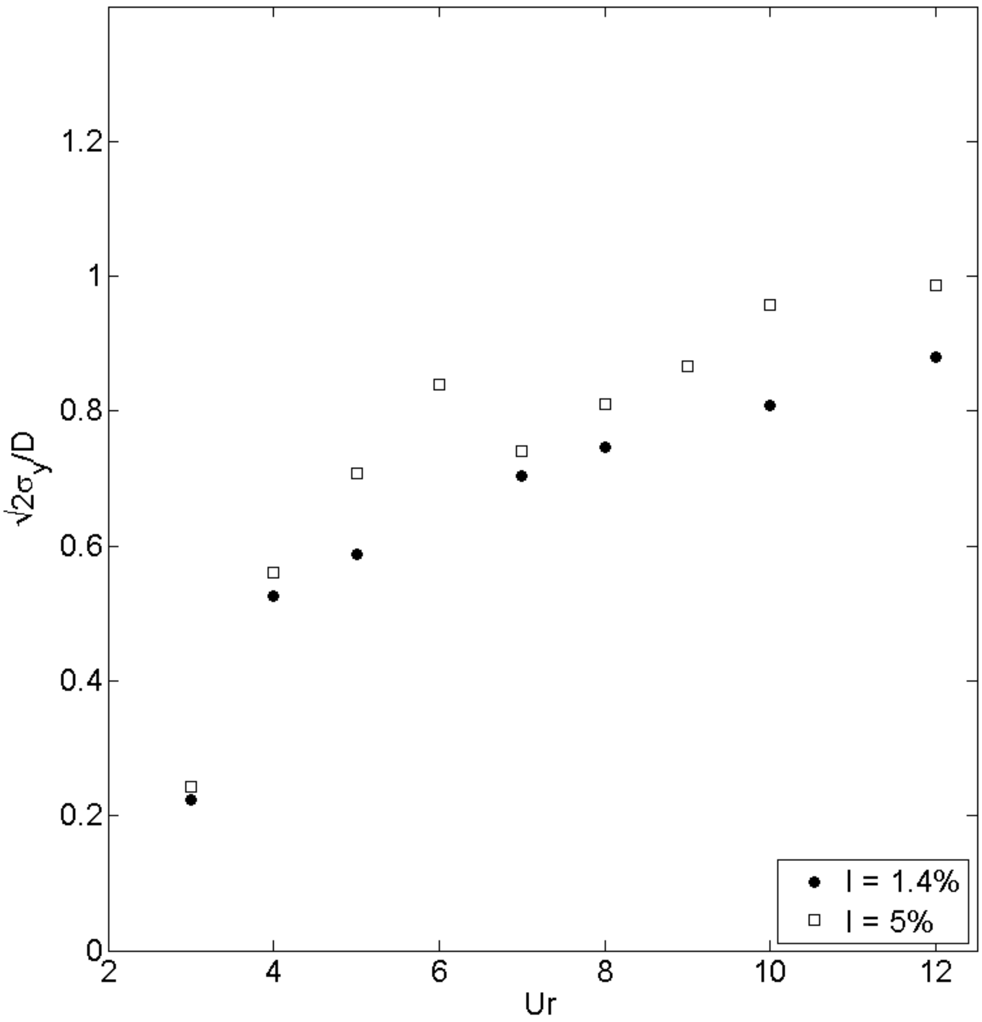

Figure 7.5. Effect of turbulence intensity.

Figure 7.6 shows the spectral response of the cylinder in the frequency domain plotted again the frequency ratio $f^* = f_o/f_n$. There is only a single peak for the spectrum for Ur = 4 at a Strouhal number close to 0.2 and f^* is approximately 0.9. As in Chapter 6, the cylinder response at this reduced velocity is dominated by vortex excitation and only a single frequency can be recognised. However, when Ur = 13, corresponding to desynchronization region for single cylinder VIV case, the wake-induced vibration with lower frequencies take over. The highest peak appears at $f^* = 3$, which agrees with the single cylinder VIV case as can be seen in Figure 7.6b whilst another lower frequency appears at f^* around 1.5. It can be seen that new frequencies due to vortices emanating from the upstream cylinder continue to drive the cylinder oscillations with high amplitudes of vibration, instead of low vibration amplitude as in the case of a single cylinder on elastic mounts.

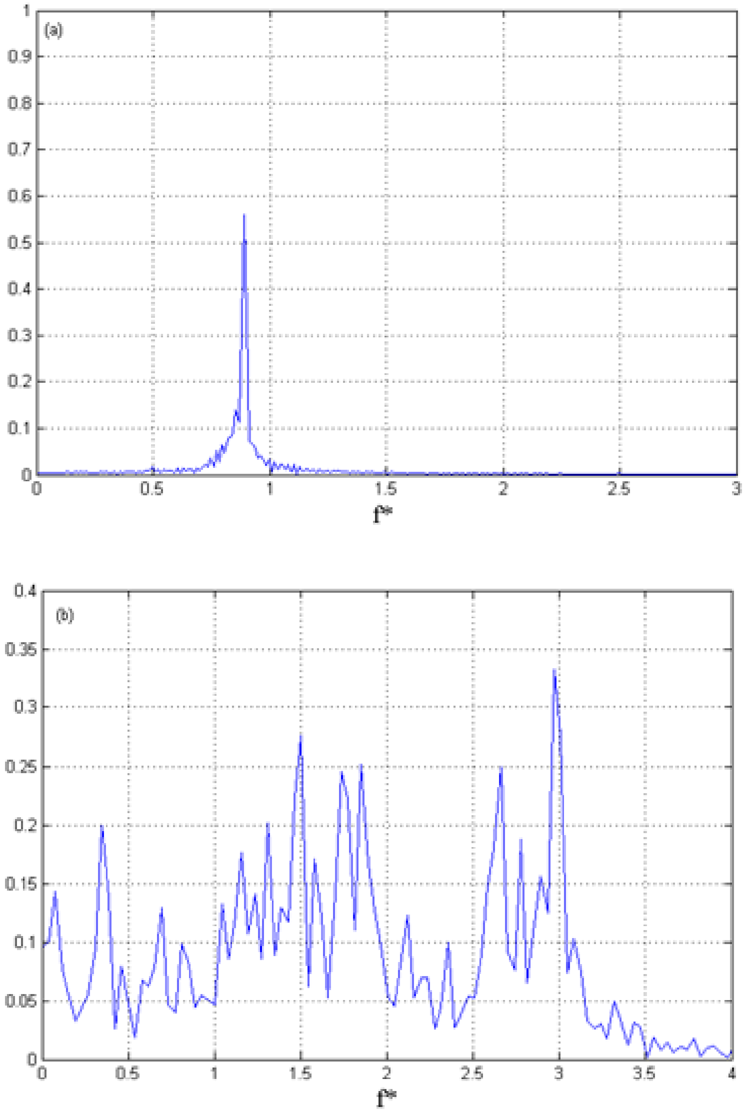

Figure 7.6. Spectra of downstream cylinder response with 1 dof (a) Ur = 4 (b) Ur = 13

The drag and lift coefficients dramatically changed in the critical area, where the amplitude of motion also changes. Figure 7.7 shows time history of lift and drag coefficients for 4 different reduced velocities Ur = 3, 4, 5 and 7. Lift and drag coefficients change the amplitude motion in a manner to the VIV case. Compared to the fixed cylinder cases, the lift coefficient is much higher even for very low amplitudes of motion where C_l = 2.15. This can be compared with $C_l \approx 1.1$ for fixed cylinder cases at the same Reynolds number, whilst the drag coefficient has similar values. Increasing Ur resulted in dramatic changes to the lift coefficient, reduced form C_l = 2.9 (Ur = 4) to C_l = 1.27 (Ur = 5) to C_l = 0.54 (Ur = 7). Further increases in Ur do not show further dramatic changes to lift and drag forces, reflecting the slow change in amplitude of motion of the downstream cylinder.

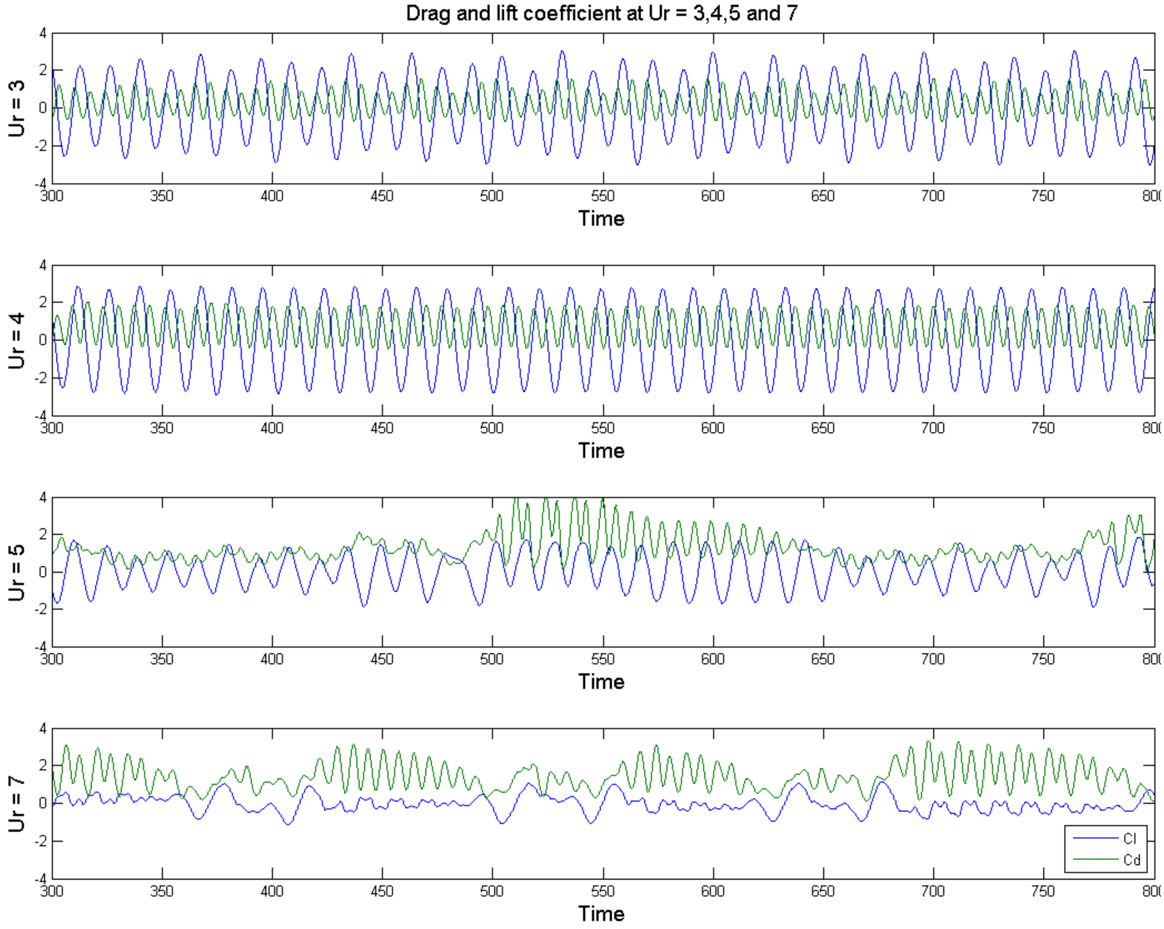

Figure 7.7. Time history of lift and drag of the downstream cylinder, over a range of Ur

On the upstream cylinder, the drag and lift coefficient remains the same for all cases, which shows its independent behaviour when $L/D \geq 5$ as can be seen in Figure 7.8. The mean $C_d \approx 1.2$ while the rms $C_l \approx 0.8$, which agree well with Ljungkrona et al's experiment for fixed cylinder in tandem at the same Reynolds number.

In general, this initial set of simulations for the downstream cylinder in 1 dof VIV + WIV show a good agreement with the published experimental results of Assi et al (2010) and Chaplin and Batten (2014). The results provide the confidence to continue investigations with 1+1 dof system using the same methodology.

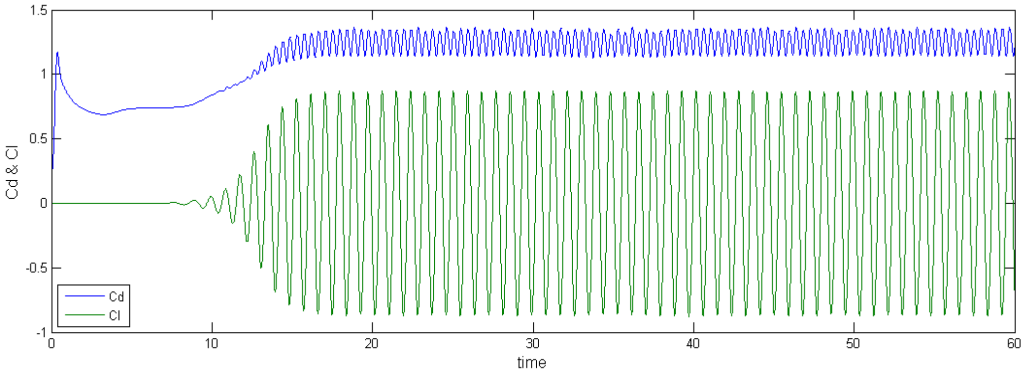

Figure 7.8. Time history of lift and drag of the upstream cylinder

7.4. Downstream cylinder with 1+1 dof

Following the good agreement of cylinders in tandem case with 1 dof, the new set of simulations of the downstream cylinder with 1+1 dof (crossflow + inline) is carried out. In the present case, the upstream cylinder is kept stationary and the downstream cylinder is located at a spacing L=5D. The benchmark experiments of Vortex and Wake induced vibrations in a tandem arrangement with far wake interface carried out by Huera-Huarte and Gharib (2011b), in addition to Chaplin and Batten (2014) and Assi et al. (2010). However, in all of these experiments, the cylinder's dynamic responses are available only in the crossflow direction although the cylinder used was able to vibrate in both directions.

The VIV research on an isolated single cylinder showed that crossflow vibration dominated while the inline vibration is reasonably small, peaking at an amplitude less than 0.4D compared with a maximum of 1.6D in crossflow vibration. In the present research, the relationship between inline and crossflow motion in the wake will be explored.

One challenge when simulating the downstream cylinder in the wake of upstream one is that the downstream cylinder will be displaced in the horizontal direction to a new equilibrium position, which is different to the expected centre-to-centre separation. At a new equilibrium position, the cylinder will start oscillating around this point. That causes a new problem that another L/D distance will be investigated instead of expecting L/D = 5 distance. The offset issues also appeared in 2 dof single cylinder test cases, however, for single cylinder scenarios, the offset does not affect the results as well as the nature of the testing system. This is also not a big problem when carried out by experiment, because experimental setup can always limit the displacement of the downstream cylinder in the inline direction. However, in simulation, the pre-oscillating displacement of the downstream cylinder is reasonably big due to large mean drag force acting on the downstream cylinder. The simulation results showed that for a downstream cylinder with 1+1 dof, the inline displacement is a big concern.

Simulations by ANSYS Fluent showed that the inline offset of the downstream cylinder is due to the drag force acting on the research body. Theoretically, drag force on the cylinder can be divided in to two components: mean drag component (F_{mean}) and fluctuating drag component ($F_{fluctuating}$). The fluctuating component will contribute to the vibration of the cylinder while F_{mean} will create the offset of the cylinder in downstream direction.

The aim of this current simulation in this chapter is to determine the vibration of the cylinder at L/D = 5, not at the new offset distance. To remove the offset of the system, the value equal to the mean drag force will be subtracted from the drag forces calculated by Fluent and only remaining fluctuating drag force is applied to Equation 6.8 to calculate the new position of the cylinder, defined as:

$$F_{fluctuating\ applied} = F_{drag} - F_{mean} \tag{7.1}$$

By removing the mean drag, the offset can be limited and the downstream cylinder is allowed to vibrate at the expected L/D ratio. The results of 1+1 dof downstream cylinder in WIV and VIV are presented in this section including response characteristics, wake mode, lift and drag forces history and motion trajectories.

7.4.1. Response characteristic

Figure 7.9 shows the dynamic response of the downstream cylinder at the separation of L = 5D. As can be seen, higher amplitude of motion is recorded. In addition, the jump in amplitude of motion appears at a lower Ur compared to Chaplin and Batten's experiment, however, it follows Assi et al's (2010) trend, due to similar turbulence used, as explained in the previous section. Present simulation results also followed the trend of Huera-Huarte and Gharib (2011b)'s experiments predicted in 1+1 dof, but amplitudes are higher. This can be explained by the mass ratio used by Huera-Huarte and Gharib was double $m^* = 1.8$ compared with m^* = 0.87 in the current simulation, while the damping is almost the same $\zeta \approx 0.0287$. This follows the trends shown in Figure 6.7 for increasing m^*, albeit for a single cylinder with 1 dof system.

At the low reduced velocity region $Ur < 5$, the difference between inline and crossflow motions is quite small, and the amplitudes are similar to 1 dof system in crossflow direction only. However, when Ur increases, Ur > 7, the amplitude of the motion in crossflow direction is reaching a higher value. At Ur = 8, 1 dof system amplitude was 0.8D, whilst 1+1 dof system records 0.96D, approximately 20% higher. But when Ur > 10, the difference recorded is almost 40% higher compared with the 1 dof case. Again, an increase in reduced velocity also increases the amplitude of motion, as observed previously, and when Ur > 10, WIV is dominant and VIV is in the desynchronization region.

The inline motion is also larger compared to the isolated cylinder in 1+1 dof VIV. The peak amplitude in the downstream cylinder reached 1D amplitude compared to the peak value of 0.4D in the single cylinder case. For Ur < 5, the inline vibration is reasonably small, approximately 0.2D. However, a further increase in Ur results in much higher amplitudes of motion. There is a dramatic jump at the range 9 < Ur < 10 where Ax/D nearly doubles. Similar to the crossflow motion, the inline amplitude also shows an uptrend without limitation. At Ur = 14, the inline motion is comparable to the crossflow vibration amplitude in 1 dof system.

The frequency ratio ($f^* = f_o/f_n$) is plotted in Figure 7.9b. It can be seen that the results follow well Huera-Huarte and Gharib (2011b) experiments for a downstream cylinder with 1+1 dof. The downstream cylinder frequency is “locked-in” at reduced velocity range 5 < Ur < 10 where f^* is around 1. The trend is maintained until Ur = 10 where VIV is still dominating, which was also the case for the single cylinder in 2 dof. However, contrary to the 2 dof single cylinder case, where the amplitude of motion reduced at the end of the locked-in region (Ur >11), in the present tandem case, the amplitude of motion continues to increase. This is due to WIV when the reduced velocities are outside the expected classical lock-in VIV region. The existence of vorticity in the gap region between the cylinders creates the WIV resulting in the downstream cylinder continuing to oscillate with large amplitudes outside the desynchronization VIV region.

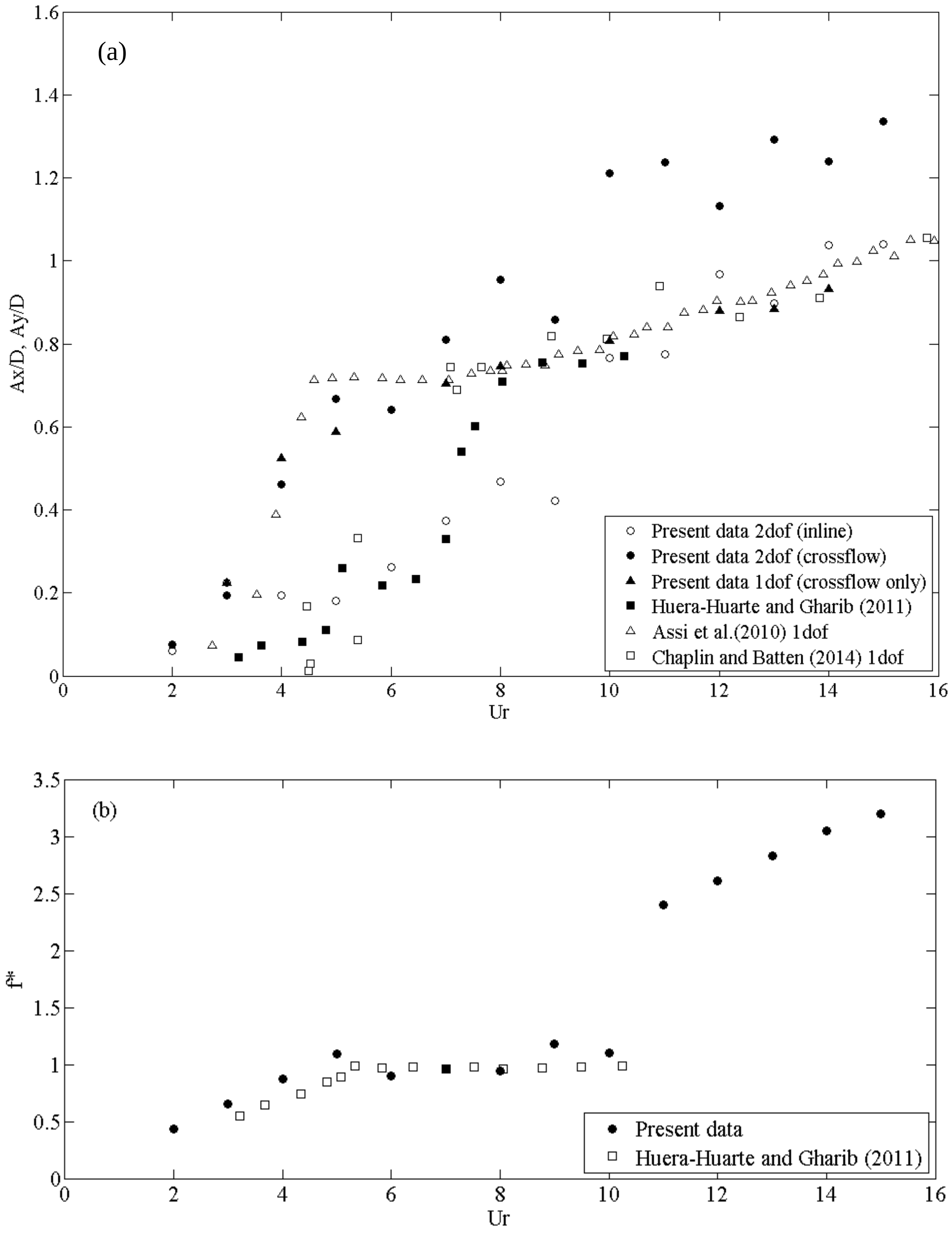

Figure 7.9. Dynamic response of the downstream cylinder in the wake of a stationary one at 5L/D (a) Amplitude of motion (b) 1+1 dof crossflow frequency ratio

7.4.2. Drag and lift coefficient

Considering the drag and lift coefficients, the upstream cylinder's force coefficients are very similar to the stand-alone fixed cylinder. The presence of the downstream cylinder at L/D = 5 showed very little effects on the upstream cylinder, as shown in Figure 7.10 at $Ur = 4$ and 8. It can be observed that the lift and drag coefficients are almost the same for the upstream cylinder for the two different reduced velocities and they also agree with the lift and drag coefficients of a stationary cylinder at the same Reynolds number, where ${C_d}_{mean} = 1.2$ and ${C_l}_{amplitude} = 1.05$.

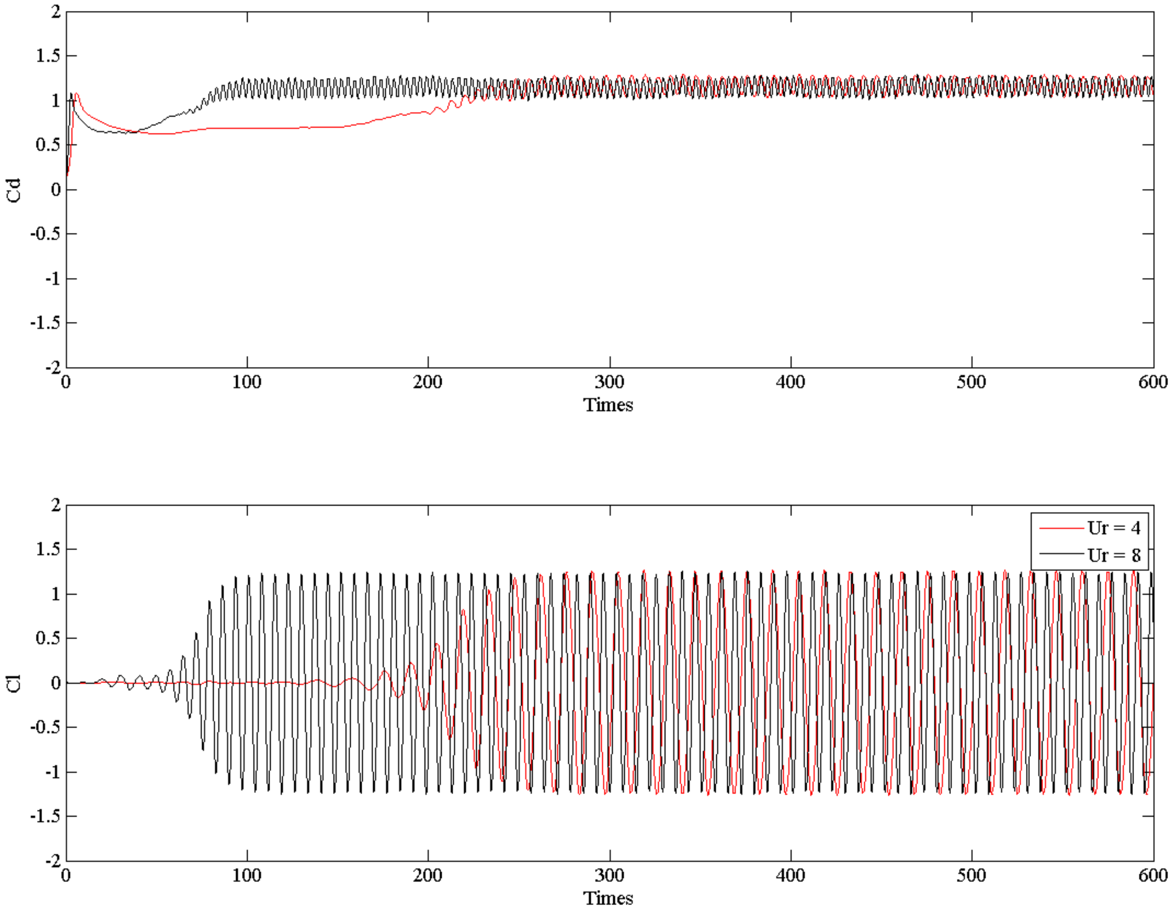

Figure 7.10. Time history of C_d & C_l for the upstream cylinder at Ur = 4 and 8.

However, for the downstream cylinder, C_d and C_l are not similar at difference Ur, which reflects the amplitude of motion of the downstream cylinder, as shown in Figure 7.11.

The lift coefficient starts with high amplitude when the oscillation amplitudes are small at the low reduced velocity Ur = 2, with a value C_l = 1.95. As reduced velocity increases, the value of lift decreases steadily. At the end of the locked-in region, C_l = 0.56, which is much lower compared with the low reduced velocity case. However, the amplitude of motion is much higher, 1.2D at Ur = 11 compare with 0.4D at Ur = 0.4.

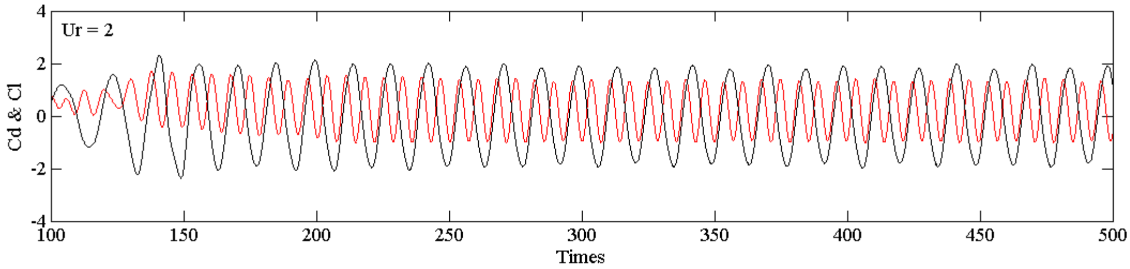

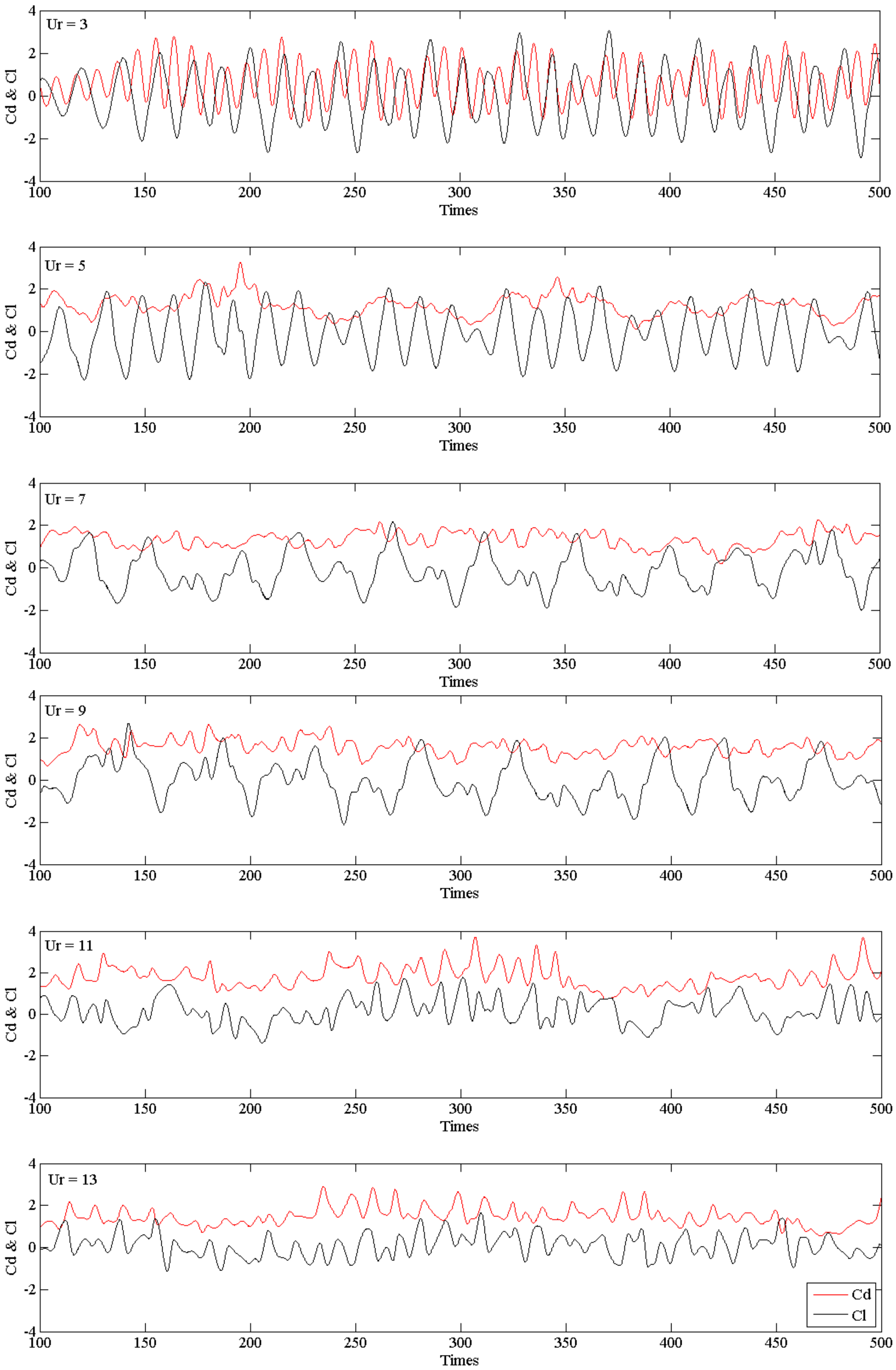

Figure 7.11. Time history of drag and lift coefficients for the downstream cylinder at Ur = 2, 3, 5, 7, 9, 11, 13

The drag coefficient shows high amplitudes of oscillation even at low reduced velocities, with a fluctuating amplitude of 0.8. However, the amplitude of motion is reasonably small, in the order of 0.2D. A higher reduced velocities, the amplitude of fluctuating drag force is smaller, even though a higher amplitude of inline oscillation is experienced. This trend is similar to the desynchronization of a single cylinder in 2 dof.

7.4.3. Motion trajectories

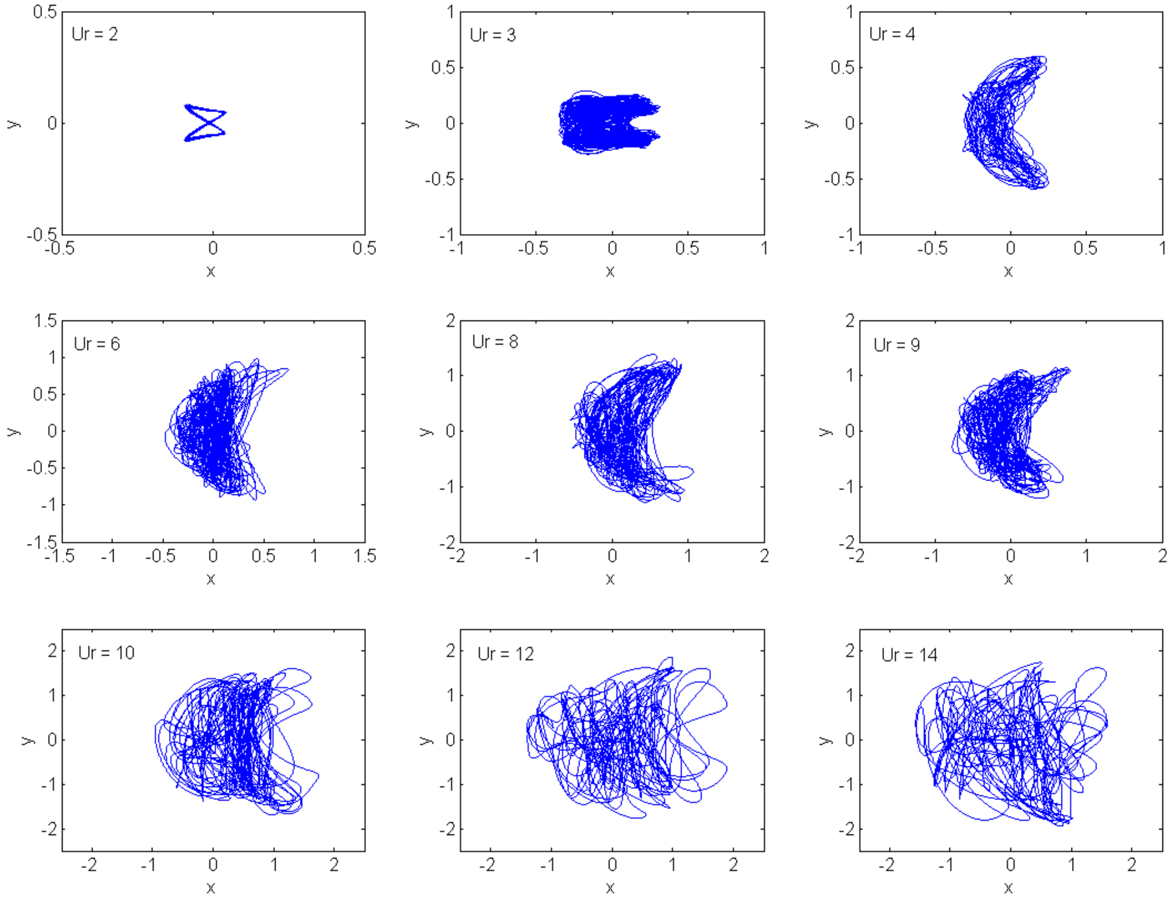

Figure 7.12. X-Y response of the downstream cylinder at spacing 5L/D

In order to further characterise the system dynamics, the motion trajectories of the downstream cylinder in tandem at L/D = 5 are shown in Figure 7.12. The trajectories correspond to approximately 40 cycles of motion. At $Ur < 10$, the C-shape trajectory are dominant. This is similar to the trajectory shapes at super-upper peak for the single cylinder in 2 dof, due to high oscillating amplitude in the x-direction, see Figure 6.12. At high-reduced velocities, $Ur > 11$, where the WIV is dominant, the downstream cylinder displays a disorganised response, where no particular shape can be discerned. This type of disorganised response of the downstream cylinder was also reported by Mittal and Kurma (2004) for simulation at Reynolds number of 1000 and higher mass ratio.

7.4.4. Vortex patterns

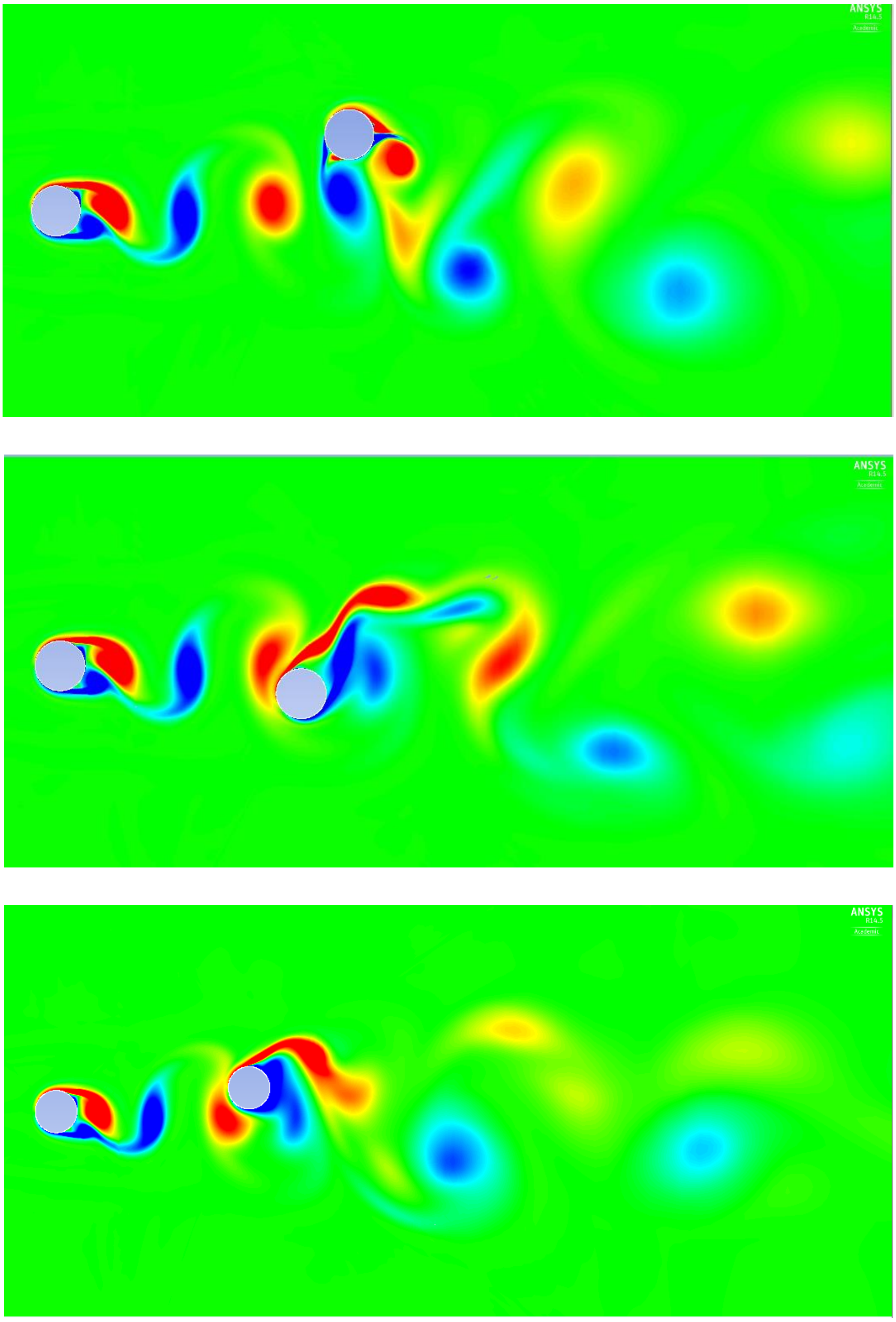

Figure 7.13. Vorticity contours of cylinders in a tandem arrangement in different positions at Ur=9

The fixed upstream cylinder sheds vortices in 2S model with the mean drag coefficient of 1.1 and $C_{l_{rms}}$ = 0.7, see Figure 4.26. Due to large amplitudes of motion in both directions, the downstream cylinder shows vortex shedding in 2T mode Figure 7.13 for Ur = 9. This agrees with the 2T vortex mode introduced for the single cylinder with 2 dof VIV at the super upper branch when the cylinder trajectory shape is C type.

7.5. Conclusion

The test cases in this section focused on the response dynamics of 1 dof and 1+1 dof elastic mounted downstream cylinders VIV for L/D =5, Re = 22,000. The amplitude of motion, frequency ratios, motion trajectories, vortex patterns and lift & drag coefficients were investigated for a range of reduced velocities at low mass-damping ratio $m^{*}\zeta$ = 0.025. In general, the investigated amplitude of transverse (crossflow) motion agrees well with the experimental results.

Similar to the single cylinder in 2 dof, the coupling of the x + y motions increases the amplitude of motion, approximately 40% higher compared with crossflow vibration only, reaching an A_y amplitude approximately 1.4D when Ur > 15. At Ur > 7 the 2T vortex shedding pattern can be observed at the downstream cylinder. However, the biggest difference compared to the isolated single cylinder case is the dramatic increase of the inline amplitude of motion, up to 1D for Ur = 15, while the single cylinder is only 0.4D.

The issue of the offset has been resolved by removing the mean drag component when calculating the inline vibrations, so separation distance is maintained at L/D = 5. The motion trajectories follow a C shape for Ur < 10 but confusing patterns for higher reduced velocities.

The current simulations in this chapter made use of elastic supports, resulting in 1 dof in each direction. To further research on FIV, a new system with more than 1 dof in each direction will be introduced.

Chapter 8 : A downstream cylinder with multi-degree of freedom vibration.

8.1. Preamble

In this chapter, flow induced vibration of the downstream cylinder is investigated with more than 1 dof in each direction. The novel system with 4 dof, shown in Figure 8.1(b), introduced by Chaplin and Batten (2014), is used for validation. The intermediate mass m_1 is attached to an elastic system, enabling vibrations with 2 dof in each direction. The system properties, based on Chaplin and Batten's experiments, are summarised in Table 8.1. The ratio between the high- and low- natural frequencies of the system, r=f_{n2}/f_{n1} is chosen as 10.3. This relatively large separation between natural frequencies was selected in Chaplin and Batten's experiment in the hope of capturing some features of response in two widely separated modes simultaneously. Effective mass m_2 was defined based on mass ratio $m^*$of the downstream cylinder plus its added mass. The value of the intermediate mass m_1 is determined using m_2 and r. The spring stiffness values are obtained from Table 8.1, where $\omega_2 = 2\pi f n_2$. The damping of the system was defined by a simulated free decay test to meet the value of 2% used in the experiment (Appendix F). The steady inflow velocity ranged from 0.3456 to 2.42 m/s, corresponding to Reynolds numbers between 4,700 and 33,000. The simulations were carried out for 200,000 time-step to achieve 80 vortex-shedding cycles.

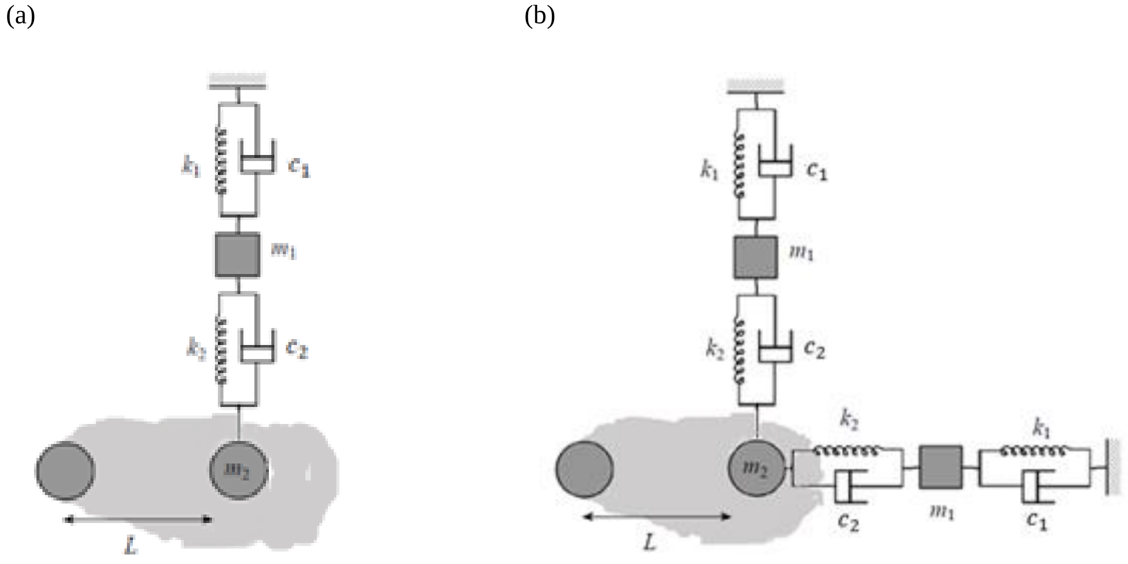

Figure 8.1. The concept of an elastic system for (a) two and (b) four degrees of freedom

Table 8.1 System properties for 2 dof and 4 dof systems

Mass ratio (m*)	2.38
Mass damping ratio	0.069
Reynolds number	< 30000
First natural frequency f_{n1}	0.084 Hz
Second natural frequency f_{n2}	0.864 Hz
Frequency ratio r	10.3
Cylinder mass	m_2
Intermediate mass	$m_1 = m_2 \left(\frac{1+r^2}{1-r^2}\right)^2$
Spring stiffness	$k_1 = 2m_2\omega_2^2 \frac{1+r^2}{(1-r^2)^2}$ $k_2 = m_2\omega_2^2 \frac{1+r^2}{2r^2}$
Damper	c_1, c_2

In Chaplin and Batten (2014) experiment, the cylinders were used with 76mm in diameter and 2.4m long between 190mm diameter endplates. They were mounted horizontally across the mid-section of the channel, and the mean elevation of the elastically-mounted downstream cylinder was 726mm (or 9.6D where D is the diameter of the cylinder) beneath the water surface. In-line and cross-flow separations between the cylinders were adjusted by moving the upstream cylinder to different fixed positions on its submerged support framework. The Reynolds numbers used were higher, up to 58,000 which is higher than current values of 33,000. Although the diameter of cylinders are not the same and carried out in 2D, however, the current simulated exactly others non-dimensional parameters used in Chaplin and Batten's experiment.

8.2. Verification of multi-degree of freedom UDF

To couple the fluid structure problem, the new User Defined Function (UDF) was written to calculate the motion of the cylinder based on FDM, using central different forms (CDM). One of the challenges is to verify that the UDF works properly. For the 1 dof system, there are validation data and the operation of the UDF was verified against the Six degree of freedom option produced by ANSYS Fluent. However, for the 2 dof system in each direction, checking the UDF operation is a challenge as the code can not be debugged by C platform.

To verify the UDF, initially, the multidegree of freedom solver code was programed on a C platform to calculate the displacement of the cylinder using FDM. In this test, the sinusoidal force was applied to drive the system instead of the fluid force calculated by ANSYS Fluent. The amplitude of motion of the current 2 dof UDF is obtained from a range different frequencies and compared with the analysis of 2 dof system in forced vibration by Rao (1990). The current code produces a very good agreement with Rao (1990) data, as showed in Figure 8.2.

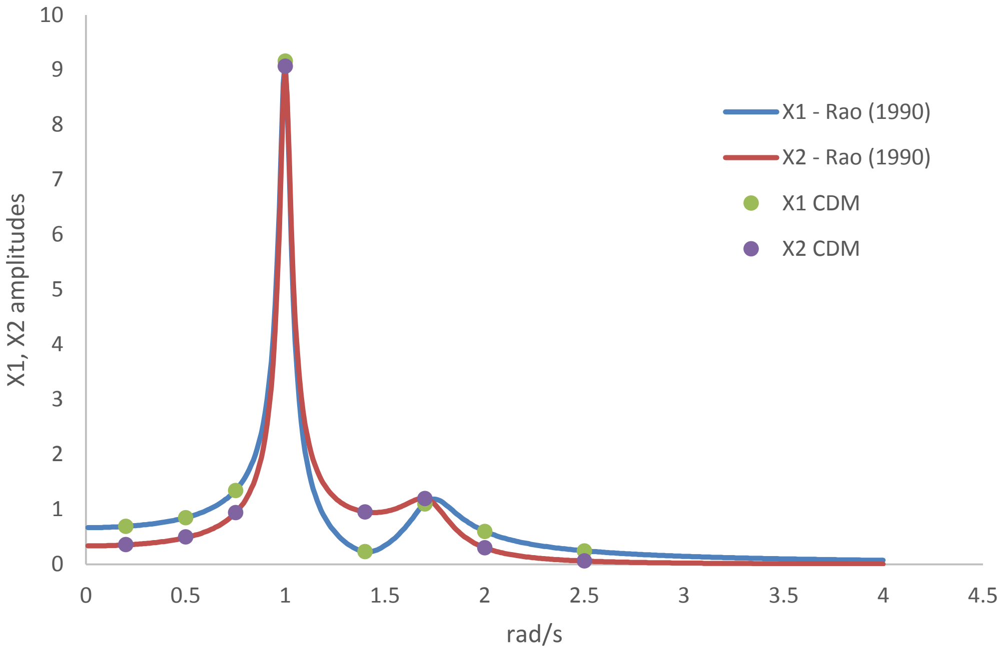

Figure 8.2. Amplitude of motion of 2 dof system in forced vibration analysis

Subsequently, the UDF based on the C code was complied with ANSYS Fluent. In this case, the sinusoidal forces are substituted by the fluid force calculated from ANSYS Fluent. The force vector $\vec{F} = \begin{pmatrix} F_1 \\ F_2 \end{pmatrix}$ is applied where $F_1 = 0$ and F_2 is the fluid force from Fluent. However, the 2 dof UDF needs to be verified to ascertain that it works properly within Fluent.

As there was no data to compare a 2 dof system in VIV, the validation was carried out based on reducing the intermediate mass m_1, (m_1 << m_2) in the 2 dof system. The spring stiffness and damping properties were selected from:

$$\frac{1}{k_{eq}} = \frac{1}{k_1} + \frac{1}{k_2} \tag{8.1a}$$

$$\frac{1}{c_{eq}} = \frac{1}{c_1} + \frac{1}{c_2} \tag{8.1b}$$

To ensure the 2 dof system behaves like 1 dof system. In these equations, k_{eq} and c_{eq} are equivalent stiffness and damping of the 1 dof system. The mass of the equivalent system is equal to m_2 as m_1 is negligible.

8.2.1. Comparison between 1 dof and 2 dof (≡1 dof) system

The verification is on the single cylinder with 2 dof in crossflow direction only for a range of reduced velocity from 3 to 12. The following system properties were used: m_1 = 0.1 kg, m_2 = 10.838 kg, k_1 = 6.2 N/m, k_2 = 4.1 N/m, c_1 = c_2 =3.412 Ns/m. The comparator 1 dof downstream cylinder case was run using $k = k_{eq}$ and $c = c_{eq}$ and $m = m_2$.

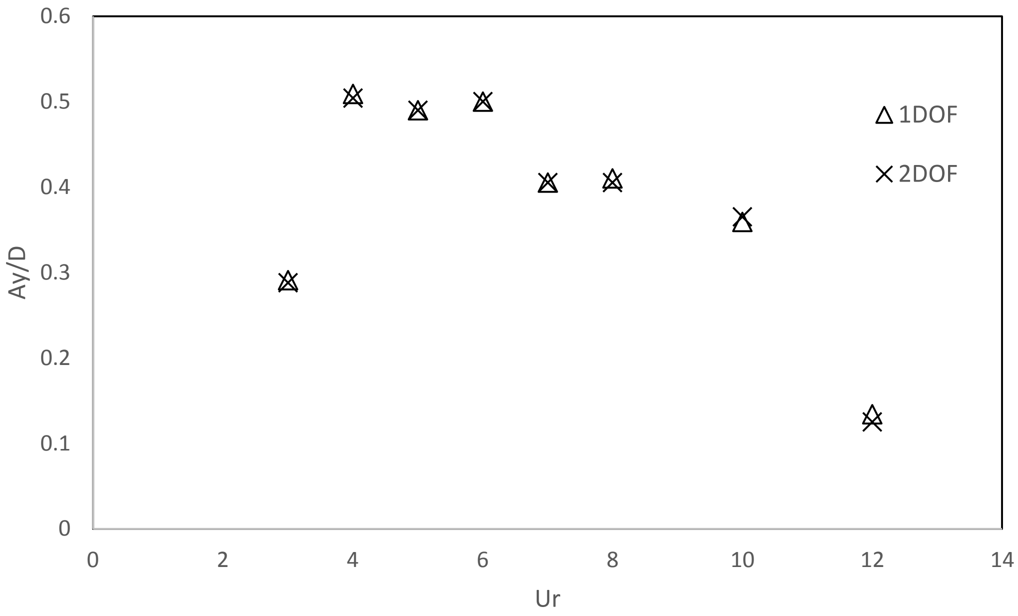

Figure 8.3. Comparison of amplitudes of motion between 1 dof and 2 dof (≡1 dof) single cylinder.

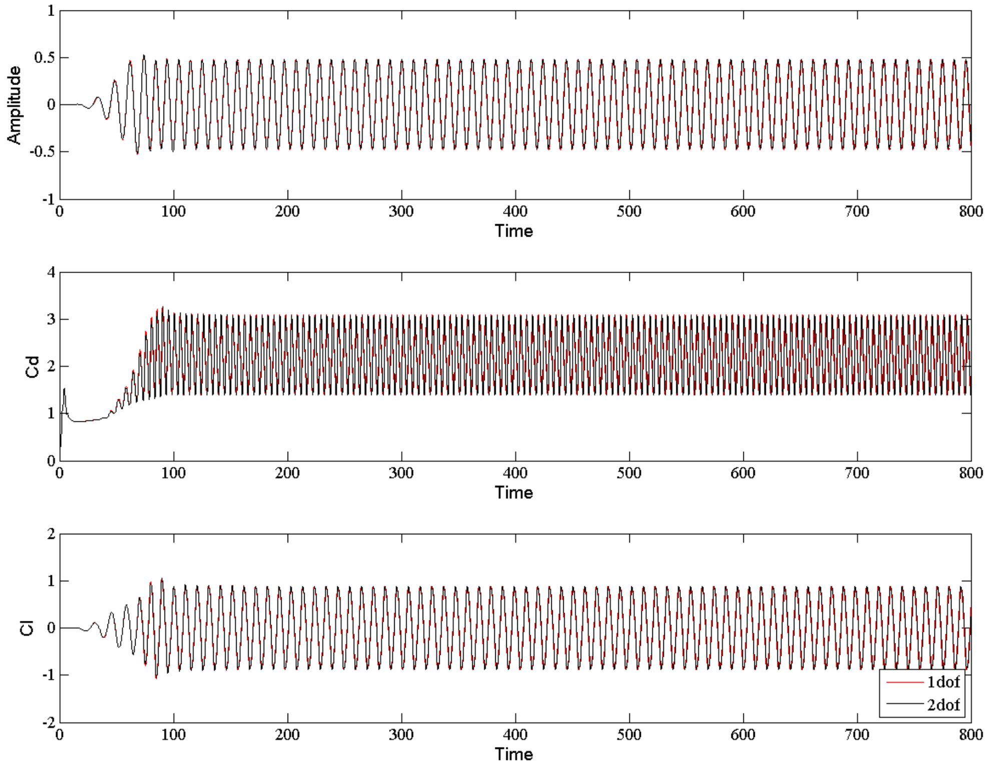

Figure 8.4. Comparison of amplitude, lift and drag coefficients between 1 dof and 2 dof at Ur = 6

Figure 8.3 shows that the amplitude of motions obtained using 1 dof and 2 dof formulations are almost the same for the whole range of reduced velocities. In more detail, the amplitude of motion, lift and drag coefficient time history as shown in Figure 8.4 at Ur = 6 shows excellent agreement. Thus, there is confidence that the new UDF (Appendix C.3) produces an accurate result for 2 dof elastically support system in one direction.

8.2.2. Comparison between 2 dof and 4 dof (≡2 dof) systems

An additional verification to confirm the suitable working of the UDF code was carried out for the 4 dof system (2 + 2 in each direction) velocity range from 3 to 10, using the same system properties in 8.2.1. Figure 8.5 shows the behaviour of the single cylinder when using 4 dof system compared with the equivalent 2 dof system. The agreement is very good overall in both inline and crossflow oscillation amplitudes. Differences are observed at Ur = 10. This is the transition area, where the cylinder changes to the desynchronization branch; hence the results show more sensitivity in terms of vibration amplitude.

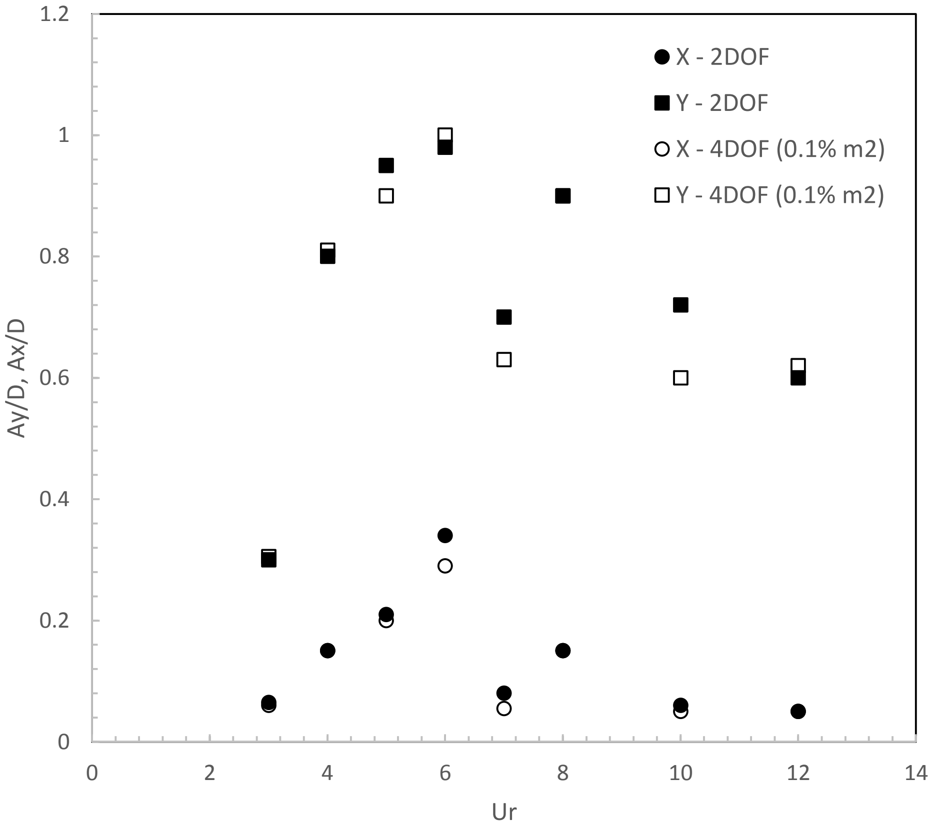

Figure 8.5. Comparison amplitudes of motion between 2 dof and 4 dof code

Based on these verifications, it is concluded that the developed UDF is reliable and will used for the cylinder in multi-degree of freedom configuration, including 2 dof (crossflow only) or 4 dof (inline + crossflow).

8.3. Numerical simulation setup

The simulation setup is similar to Chapter 7 with the upstream cylinder kept stationary and the downstream cylinder undergoing 2 dof and 4 dof oscillations using the new verified UDF. The same grid which used in Chapter 7, which obtained a good numerical simulation data were used in the present study, with 69200 quadrilateral cells is used in a 40 x 70D domain. The MDM with smoothing – diffusion with diffusion parameter of 1 and SKW turbulence model is used.

The simulation was carried out with the Reynolds number up to 33,000. Table 8.2 shows the properties of the system, value of m_2 is defined based on mass ratio and k_1, k_2 and m_1 are defined as seen in Table 8.2.

Table 8.2. 2 dof system properties

Cylinder diameter (m)	D	0.2
Fluid density (kg/m^3)	ρ	1.225
Dynamic viscosity $(kg/(ms))$	μ	$1.79x10^{-5}$
mass ratio	m^*	0.87
displacement mass(kg)	m_d	0.038485
mass $m_2(kg)$	m_2	0.033482
intermediate mass $m_1(kg)$	m_1	0.034768
spring stiffness 1(N/m)	k_1	0.019136
spring stiffness 1(N/m)	k_2	0.498009
omega 1(rad/s)	ω_1	0.527788
omega 2(rad/s)	ω_2	5.428672
damping coefficient	ζ	0.029
damping	c_1, c_2	0.001554

8.4. A downstream cylinder with 2 dof (2+0) in the crossflow direction

Figure 8.6 shows the crossflow amplitude in form of $\sqrt{2}\sigma_y$/D, where σ_y is the standard deviation. In this Figure, 2 dof and 4 dof system predictions are compared with Chaplin and Batten's (2014) 4 dof experiment. The reduced velocity is based on the higher natural frequency of the system. For the 2 dof system, the maximum displacement of the cylinder is around 0.8D for almost the whole range of reduced velocities with a “jump” appearing at reduced velocity values from 3 to 5. The 2 dof predictions follow Chaplin and Batten’s trend for 4 dof but with a lower amplitude of motion. This can be explained as the coupling between inline and crossflow directions can dramatically increase the amplitudes of motion. The simulation of a single cylinder with 2 dof of Williamson and Jauvtis (2004) showed the coupling in 2 directions motion can increase the maximum amplitude of motion due to VIV up to 60%.

The 4 dof simulation show considerably good agreement with Chaplin and Batten’s 4 dof experiment, but about 15% higher. The jump is captured correctly, and the trend is good. However, at $Ur \approx 5$, the numerical simulation over-predicts, with high peak amplitude of 1.2D compared with 0.9D from Chaplin and Batten’s experiment and the “jump” is shaper. At higher reduced velocities, $Ur > 8$, there is a small reduction in amplitude of motion until $Ur \approx 10$. When $Ur > 10$, there is a steady increase with Ur was observed due to WIV. That also can observed in Chaplin and Batten’s experiment where a decrease in amplitude of motion is record at $Ur \approx 10.5$. More detail analysis on the 4 dof system will be carried out in Section 8.5.

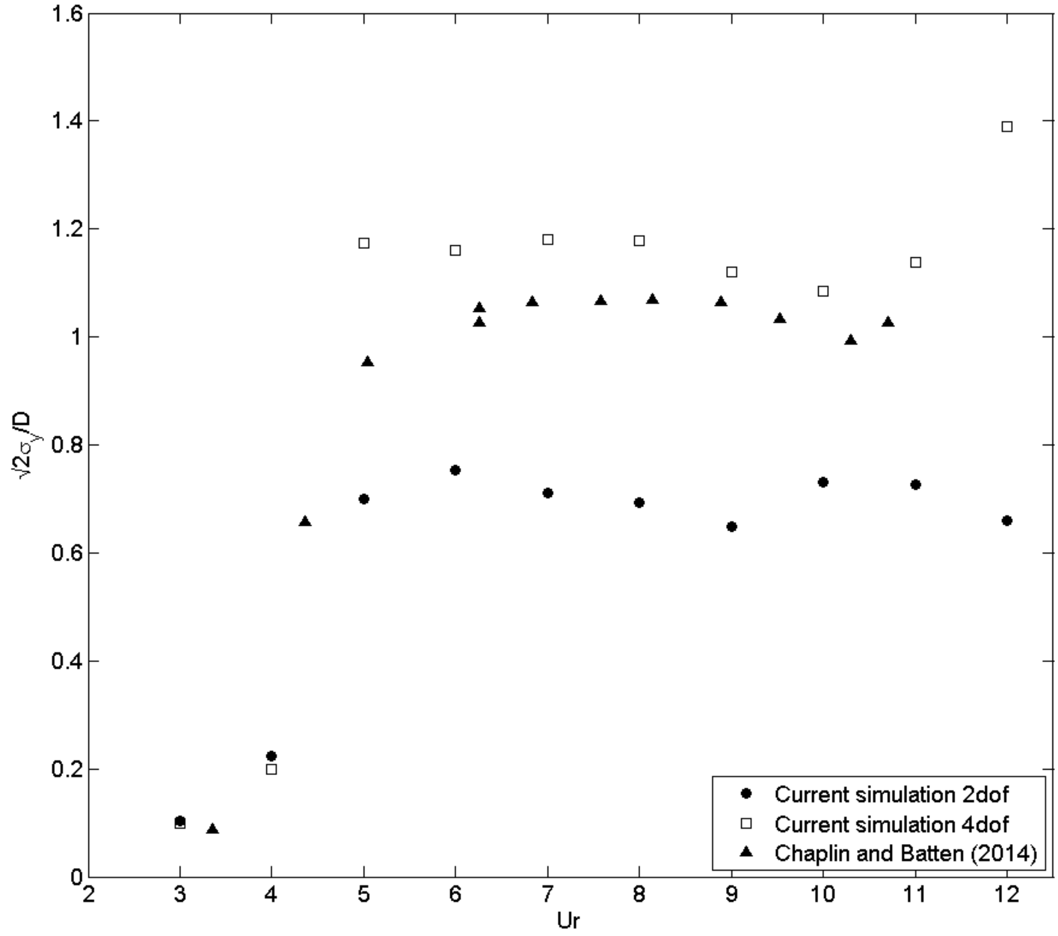

Figure 8.6. Downstream cylinder at L/D = 5, multi degree of freedom

The time history of the crossflow displacement can be split into two main components, corresponding predominantly to wake and vortex induced oscillation by applying low-pass and high-pass filters in Matlab, respectively. Typical results in two frequencies are shown in Figure 8.7 for some reduced velocity e.g. Ur = 5, Ur = 7 and Ur = 12.

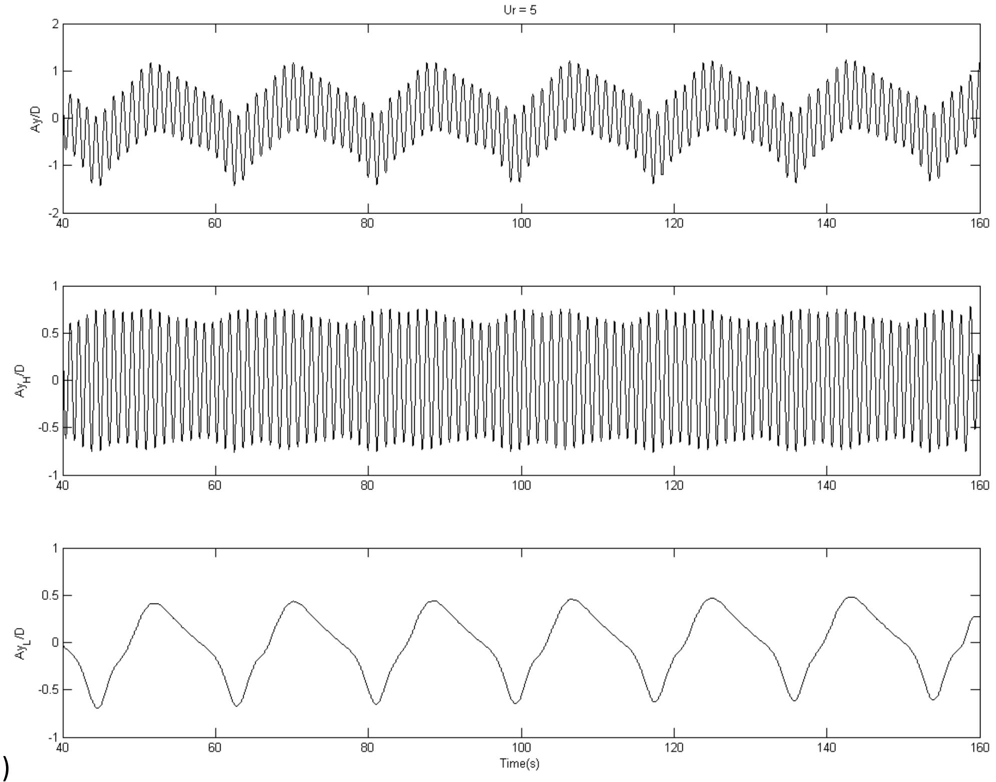

(a)

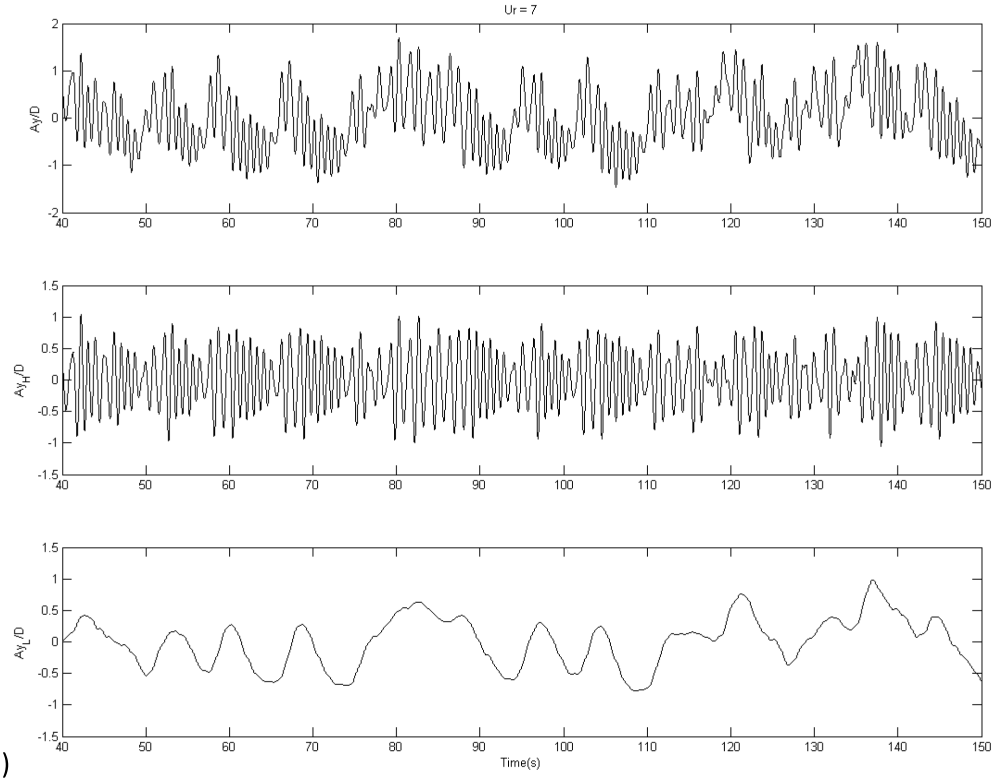

(b)

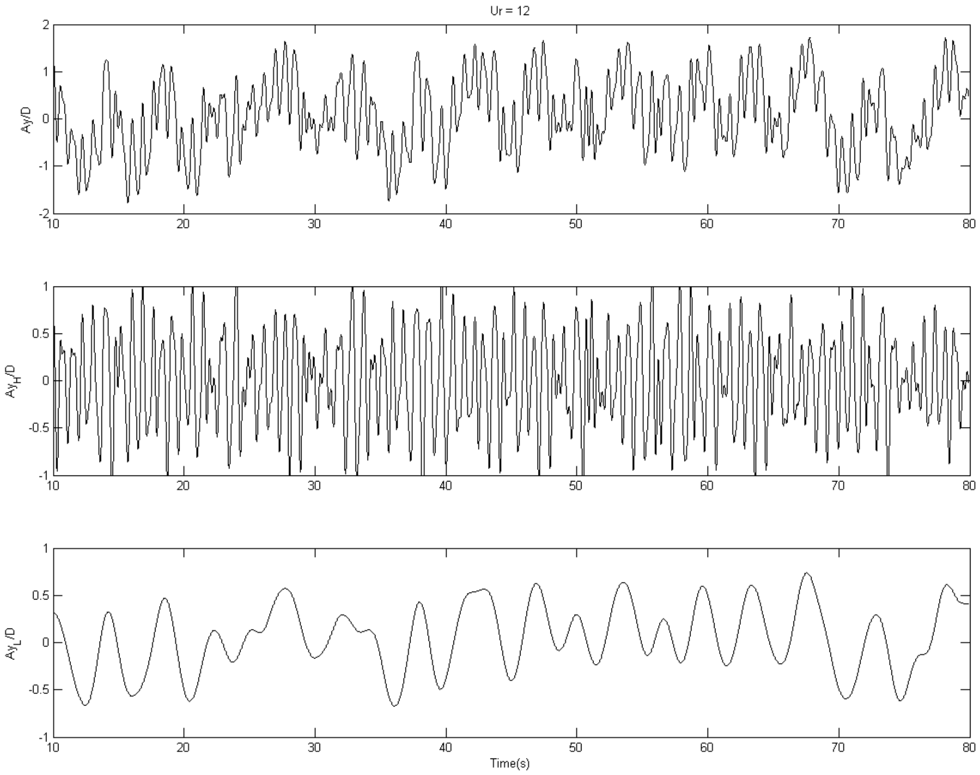

(c)

Figure 8.7. Time series of the downstream cylinder displacement with 2 dof system. Subscripts L and H denote the low and high frequency parts of the displacement that can be associated with wake – and vortex induced vibration. (a) Ur = 5, (b) Ur = 7 (c) Ur = 12

Two main frequencies can be observed these time histories. For Ur = 5, 7 and 12, the wake induced vibrations have dominant frequencies of 0.06, 0.13 and 0.2 Hz, respectively, that do not match the first natural frequency f_{n1} (0.084 Hz). Chaplin and Batten also noted this issue at the low frequency vibration. The vortex induced vibrations are at frequencies of 0.86, 1.3, 1.2 at Ur 5, 7, 12 that give the frequency ratio of 14.3, 10 and 6 respectively. It is, thus, noted that only at $Ur = 7$ the preset frequency ratio is satisfied. The amplitude of wake-induced vibration is comparable to the large amplitude vortex-induced vibration, as can be seen in Figure 8.7.

Figure 8.8 shows the power spectra density of the downstream cylinder displacement versus non-dimensional frequency $f^* = f/f_{n2}$, with f being the vibration frequency. The increase in reduced velocity increase the frequencies of the system, where f^*reaches to 2.8 at Ur = 12.

As can be observed from Figure 8.8, for all three cases, two or more peaks can be recognised based on the two natural frequencies of the system. Although some spectra contained multiple frequencies, two or more dominant frequencies can be identified. For Ur= 5, only two frequencies can be discerned, corresponding tof^*= 1 as the 1st primary frequency, denoted the response of the cylinder in VIV and $f^* = 0.06$ denoting WIV of the downstream cylinder, as seen in Figure 8.8a. At higher reduced velocities, when Ur > 7, more than two peaks can be recognised. In addition to wake frequency (f_w) and vortex frequency (f_v) there is another peak at $f_v - f_w$ and $2f_v - f_w$ corresponding to interaction between the two primary frequencies f_v and f_w. The high peak appear at $2f_v - f_w$ (Figure 8.8c) at f^* = 2.7 for Ur = 12 and f^* = 3 for Ur = 13 shows the strong coupling between the wake and vortex frequencies at high reduced velocities. In Figure 8.8c,d, three dominant peaks can be seen.

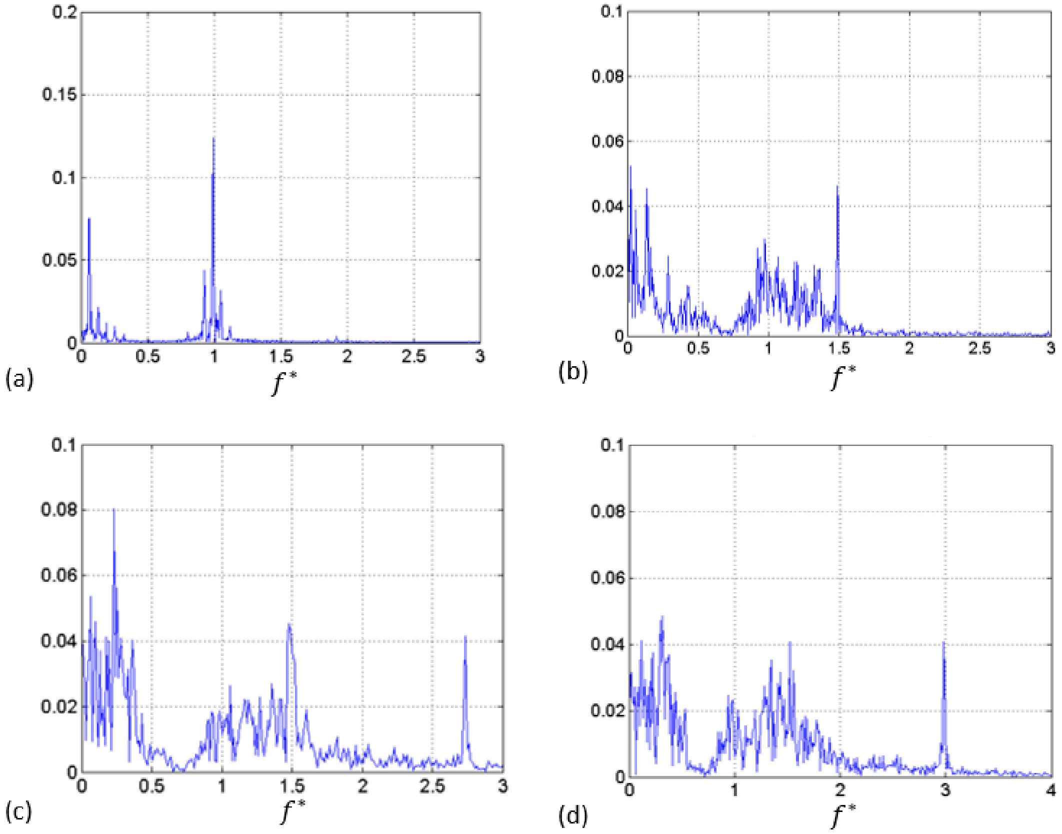

Figure 8.8. Spectra of crossflow response of the downstream cylinder at (a) Ur = 5, (b) Ur = 7, (c) Ur = 12, (d) Ur = 13

Variation of drag and lift coefficients with Ur are shown in Figure 8.9 along with dimensionless crossflow amplitude of motion (Ay/D). The drag coefficient were divided by mean and fluctuating component while the lift coefficient was calculated by r.m.s values time $\sqrt{2}$. The$\sqrt{2}$ r.m.s lift coefficients do not change much when Ur > 6, with the C_l value in the range of 0.64 – 0.8. The variation of amplitude of motion nearly follows the trend of the lift coefficient, and the highest amplitude of motion can be recorded at Ur = 10, where Ay/D = 0.8 with the lift coefficient of 0.84. However, there are big jumps at the range of 4 < Ur < 6. The first jump appears when 3<Ur<4, when the lift coefficient dramatically increases, from 0.82 to almost 1.95. However, in this range, the amplitude of motion stays low, approximately 0.26D. As the reduced velocity is outside of the locked-in region, even a very strong lift does note result in large vibration. Surprisingly, when Ur = 5, there is a dramatic drop in C_l with its value dropping down to approximate 0.4. In this reduced velocity, even reasonably small lift force is able to produce large amplitude of motion.

When at Ur > 5, there is a dramatic change in lift force, from C_l = 0.4 for Ur = 5 reaching, C_l = 0.78 for Ur = 6. However, from this point , the change in lift force does not result in a dramatic effect on the amplitude of motion and the cylinder moves with an amplitude of around 0.75D.

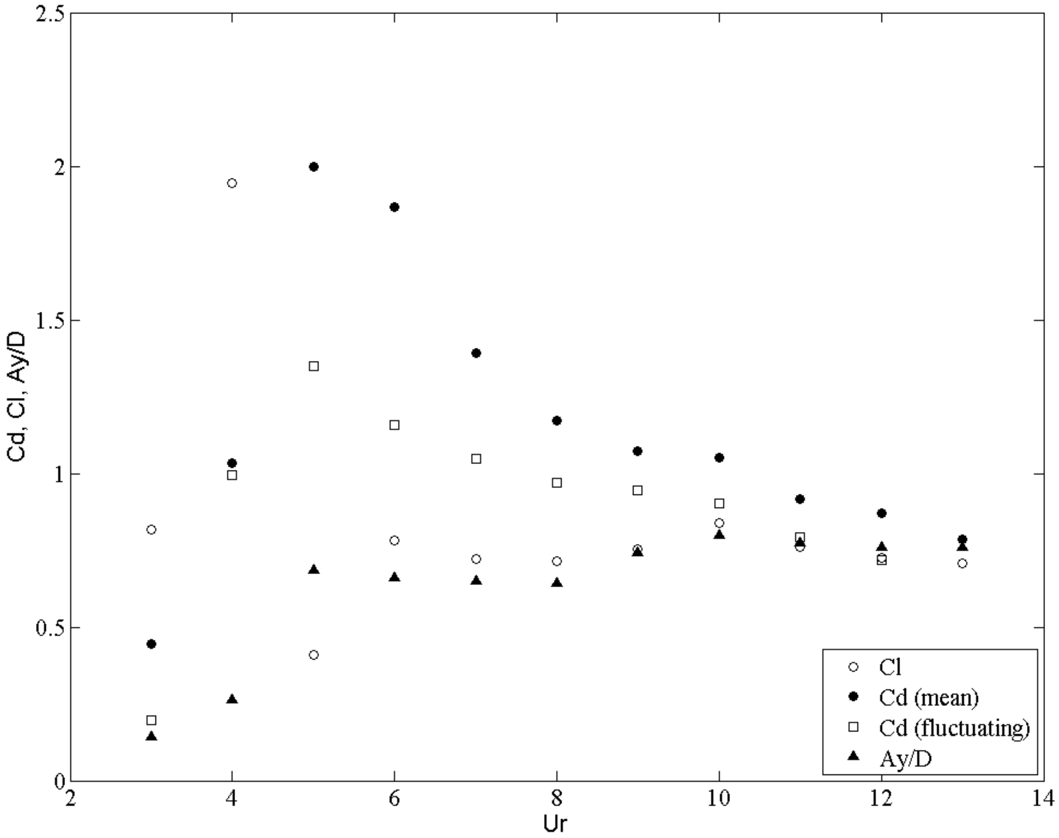

Figure 8.9. Mean & fluctuating drag, fluctuating lift and amplitude of motion (Ay/D) in a range of reduced velocity $Ur = U/f_{n2}D$

This 2 dof system is limited to the crossflow direction, hence mean drag force appears to be a less influential. However, a dramatic change can be observed in mean drag coefficient in Figure 8.9. At very low reduced velocity, the mean drag C_d is approximately 0.45. This is roughly similar to the experimental and simulated C_d for a fixed cylinder in tandem case ($C_d \approx 0.4$). However, when the cylinder starts moving, the drag coefficient changes, reaching a peak value of $C_d = 2$ at Ur = 5. Further increases in Ur gradually reduce the drag on the cylinder, but it is still almost double compared to the stationary cylinder case.

The fluctuating drag (√2 time standard deviation) also shows even higher values compared with fluctuating lift, peaking at approximately 1.4 at Ur = 5. It can be noted that, if the inline vibration is included, the amplitude will be considerable, potentially higher than crossflow vibration in some point.

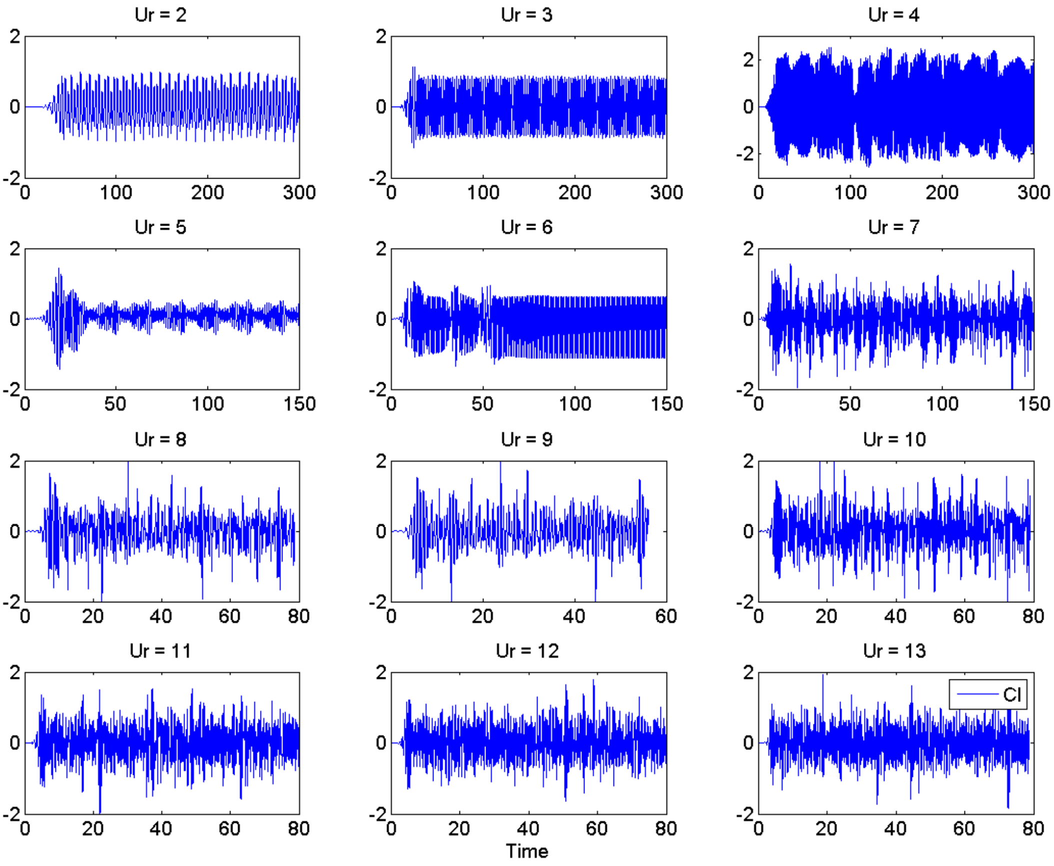

Figure 8.10: Time history of lift coefficient of the downstream cylinder in 2 dof crossflow oscillation

The time history of lift coefficient shows that most dramatic changes happen when $Ur < 10$. At Ur = 5, a transition can be seen, as the lift coefficient changes from high into low amplitude. When $Ur > 10$, there are very minor changes in C_l as seen in Figure 8.10

The upstream cylinder, similar to previous cases behaves independently of downstream cylinder at L/D = 5. The drag and rms lift coefficient on the upstream cylinder is 1.2 and 0.7 respectively, as seen in Figure 8.11, which behave similar to the fixed single cylinder in cross flow (Chapter 6).

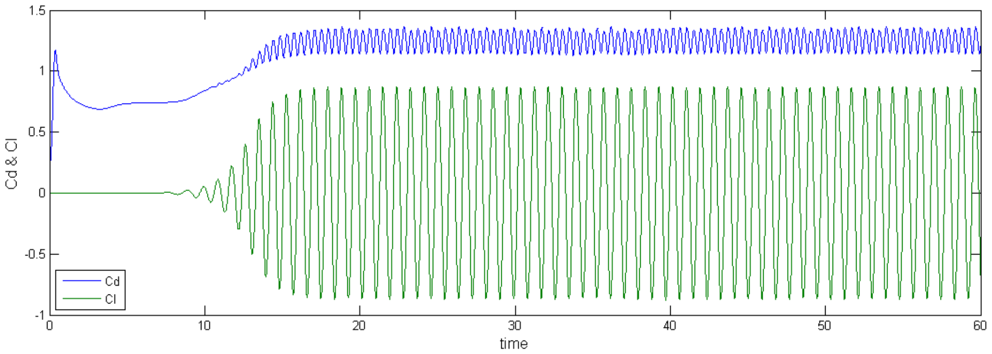

Figure 8.11. Time history of lift and drag coefficients for the upstream cylinder, 2 dof system

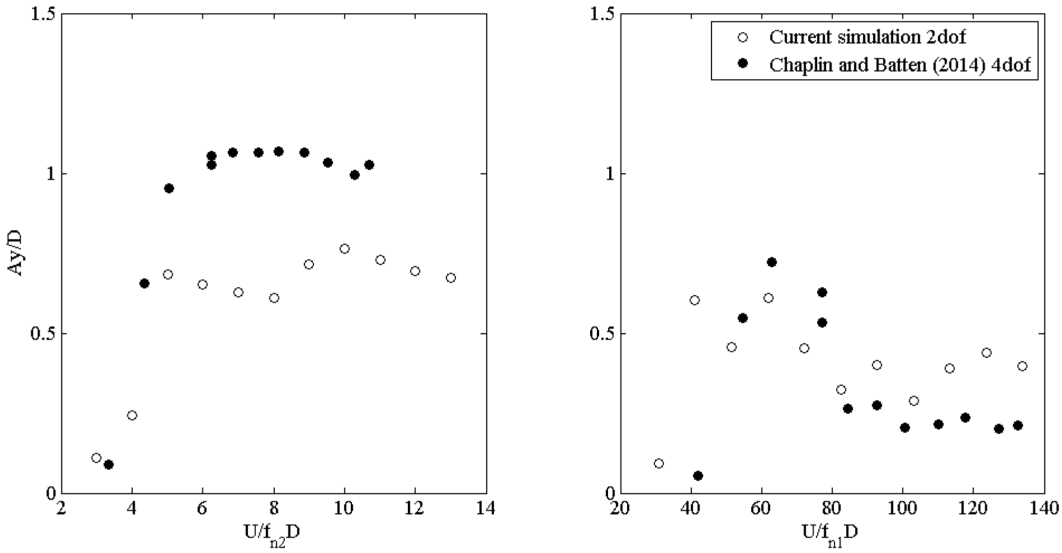

Figure 8.12. Amplitude of high (left) and low (right) frequency components of displacement (2 dof) compare with Chaplin and Batten (4 dof).

The low and high frequency components of the crossflow motion are shown in Figure 8.12 and compared with Chaplin and Batten's data for the downstream cylinder 4 dof. High and low frequency components were separated with a cut-off frequency of $f^* = 0.8Hz$. As observed in Figure 8.8, at $0.7 < f^* < 0.9$, the amplitude spectrum is very small, so the filtering point at $f^* = 0.8$ was chosen.

The high frequency components follow the trends well, but with lower amplitudes, approximately 40%, in most of the range $6 \leq Ur \leq 11$. The low frequency component is quite comparable in terms of amplitude of vibration. An alternative reduced velocity base on low frequencies components $Ur_{low} = U/f_{n_1}D$ reaching up to 140. The trend follows Chaplin and Batten's data at $U/f_{n_1}D$ up to 100, where the peak value is 0.6D at $U/f_{n_1}D$ = 60. When Ur_{low} > 100, the low frequency components still maintain high values, and at Ur_{low} ≈ 130, the amplitude of motion is 0.35D. A major disagreement occurs at Ur_{low} ≈ 41.3 where the amplitude of predicted low frequency motion is quite large. Furthermore, the transition area appears at lower Ur_{low} in the simulation compared to experiments, due to lower level of turbulence applied in the current simulations, as mentioned before.

8.5. A downstream cylinder with 4 dof

In this section, the downstream cylinder with 4 dof is investigated as shown in Figure 8.1(b) (2 dof inline +2 dof crossflow direction). The numerical setups and initial conditions are the same as the 2 dof in this chapter.

As mentioned in Chapter 7, one significant problem when using CDF to simulate inline vibrations of the downstream cylinder is the offset, in which the cylinder is displaced in the inline direction until equilibrium is obtained. Due to the mean drag force, the downstream cylinder is displaced by a large distance before the oscillations due to the fluctuating drag component commence. This issue can be overcome in the experiment by adjust the top tension force and the spring stiffness of the system. The large offsets experienced with the 2 dof inline system are because

- The 2 dof system is much more flexible compared to the 1 dof system, and
- The downstream cylinder mean drag force is much higher compared with the fixed cylinder case.

To counteract the offset, the process applied in chapter 7, based on equation 7.1, can be used, namely.

$$F_{fluctuating} = F_{fluid,x} - F_{mean}$$

However, in the 4 dof system, with 2 dof inline vibration, it was very hard to determine the mean drag force of the cylinder. When the cylinder is displaced, the drag coefficient is changing and the value of fluctuating component is very large compared to previous simulations. If F_{mean} is not large enough, then the cylinder offset may be more than 8D, which is unacceptable. This can not happen with the experiment as the whole structure setup will prevent any large offset.

A sensitivity test had been carried out to select the appropriate F_{mean} value to subtract defined by $F_{mean} = 0.5C_d\rho U^2 D$, with varying value of drag coefficient C_d in the range from 0.4 to 2.1, depending on different reduced velocities. The detail of mean drag force coefficient used are summarised in Table 8.3. There are two steps in applying F_{mean}

1. At the beginning of the simulation, the low drag force, referring to low drag coefficient $C_{d_{low}}$, applied as a negative force to the system is done to avoid the strong downstream. This step is unnecessary for the case with 1 dof in each direction in previous chapter as that system is stiffer and less sensitive to variations; hence only step 2 is required. However, the 2 dof inline system is much more flexible. Subtracting to the mean drag component from the drag force from beginning of the simulation can lead to excessive reverse displacement with possibility, the two cylinders crashing. The low drag force coefficient is smaller than 0.8 (Table 8.3), which is much lower compared with the mean drag force calculated, but it's importance in reducing the large offset and reaching equilibrium condition before applying higher drag force equal to mean drag.

2. In the second step, when the cylinder has reached equilibrium, the higher drag force is applied, which is equal to the mean drag force of the oscillating cylinder. The values for a range of reduced velocities are summarised in Table 8.3 for Cd_{high}. The mean drag force was removed and only expected fluctuating components of drag force will take place. The transition point to switch from

$C_{d_{low}}$ to $C_{d_{high}}$ is 1D, determined in a sensitivity test. In addition, due to high oscillating amplitude in both directions, the under relaxation factor for pressure was reduced to 0.9.

Table 8.3: Summary of applied drag coefficient

Ur	Cd_{low}	Cd_{high}
3	0.415	
4	0.5	
5	0.6	1.9
6	0.8	2.1
7	0.7	2.1
8	0.6	1.9
9	0.6	1.5
10	0.6	1.3
12	0.6	1.9

Unlike the 2 dof (1+1) system, where the cylinder can be maintained at the correct position L/D ≈ 5, for the 4 dof (2+2) system, the cylinder cannot be kept at L/D = 5. Due to applying the switch condition at distance 1D, the cylinder will displace to a distance more than L/D ≈ 6 before oscillating.

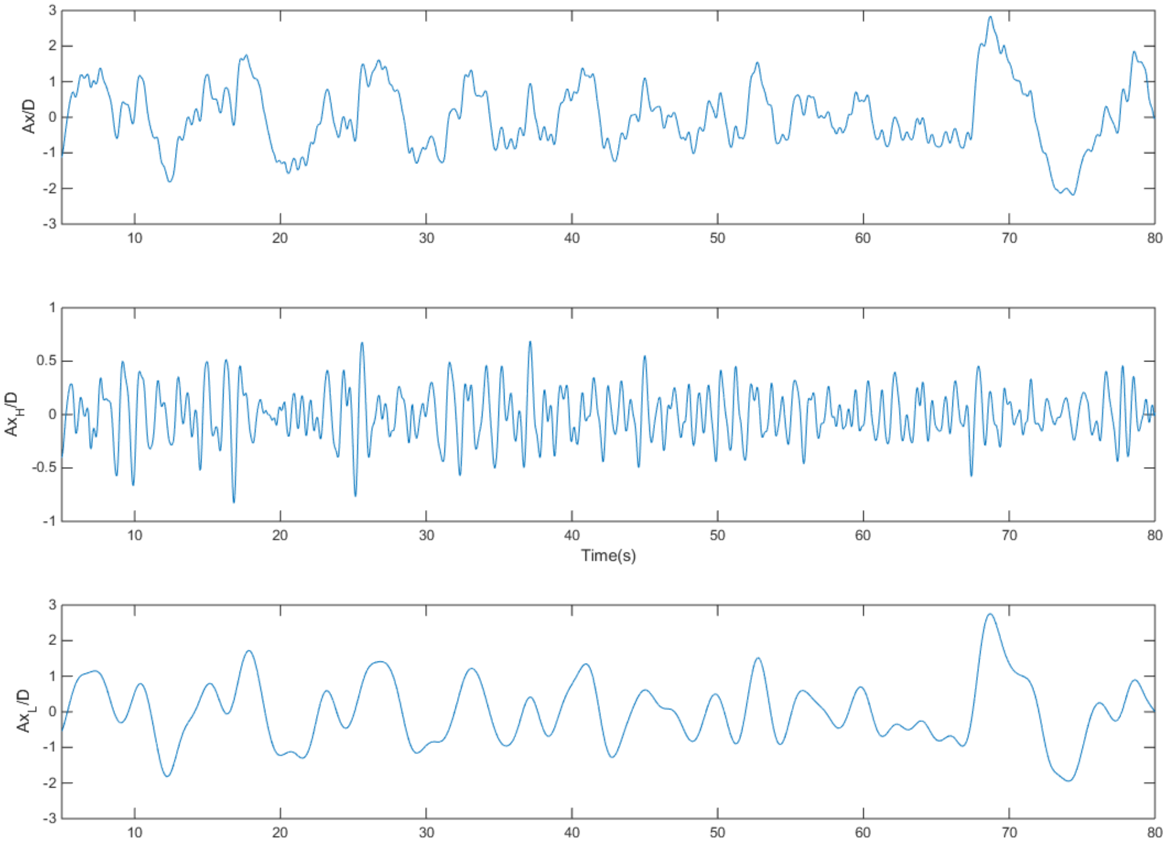

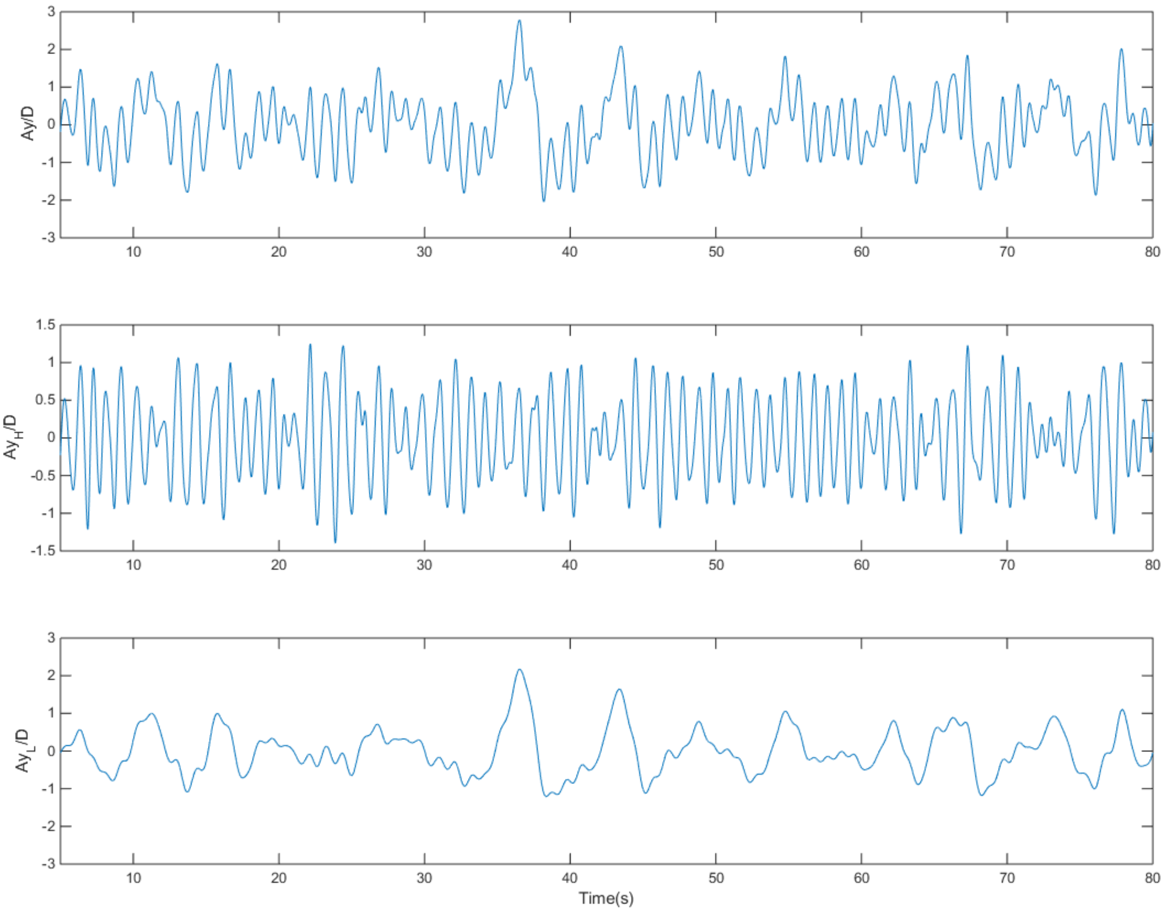

Figure 8.13. Time series of the downstream cylinder displacement with 4 dof system at Ur = 8.

The motion of the downstream cylinder can be analysed into high (HF) and low frequency (LF) components from the original vibration signal, as seen in Figure 8.13, e.g. at Ur = 8. The high amplitude components show more harmonic motion with lower amplitudes while the LF components are higher with the maximum amplitude are more than double in the crossflow and fourth time in the inline direction. Similar to Chapter 7.4, the amplitude A_x and A_y are determined by standard deviation time $\sqrt{2}$.

The high and low frequency components over a range of reduced velocity are shown in Figure 8.14 & 8.15 respectively. The data is compared to Chaplin and Batten's 4 dof experiments for L/D = 5 & 10 and previous results for the 2 dof system in crossflow direction only.

For the crossflow direction (Figure 8.14b), the HF amplitude of motions have smaller values compared to Chaplin and Batten's experiences. The trend follows well with the experiments, where two main transition areas can be observed. At the initial branch, the current simulations follow Chaplin and Batten (2014) for L/D = 5. The sharp increase in amplitude of motion occurs at the reduced velocity $Ur = U/f_{n2}D$ range from 3.5 – 6. The amplitude in that range is about 10%

smaller, but follows the experimental trend very well. The second turning point appears at a reduced velocity range of 10 – 10.5 with the HF amplitude beginning to increase after continuous reduction in the reduced velocity range of 6 -10. The gradual decrease in this range is similar to experiences at L/D = 10. This difference occurred in Chaplin and Batten's experiment, where the cylinder was fixed exactly at L/D = 5 and L/D = 10. Hence the vibration of the cylinder at high frequencies has a mixture of characteristic from the L/D = 5 and L/D 10 experiments. Comparing with 2 dof system in crossflow direction only, the coupling between inline and crossflow vibrations increase the HF amplitude of motion by about 20%. However, at reduced velocities in the range 9 < Ur < 10, the end of the synchronisation region, the amplitudes are quite similar. When Ur > 11, the HF amplitudes of the 4 dof system are approximately 20% greater.

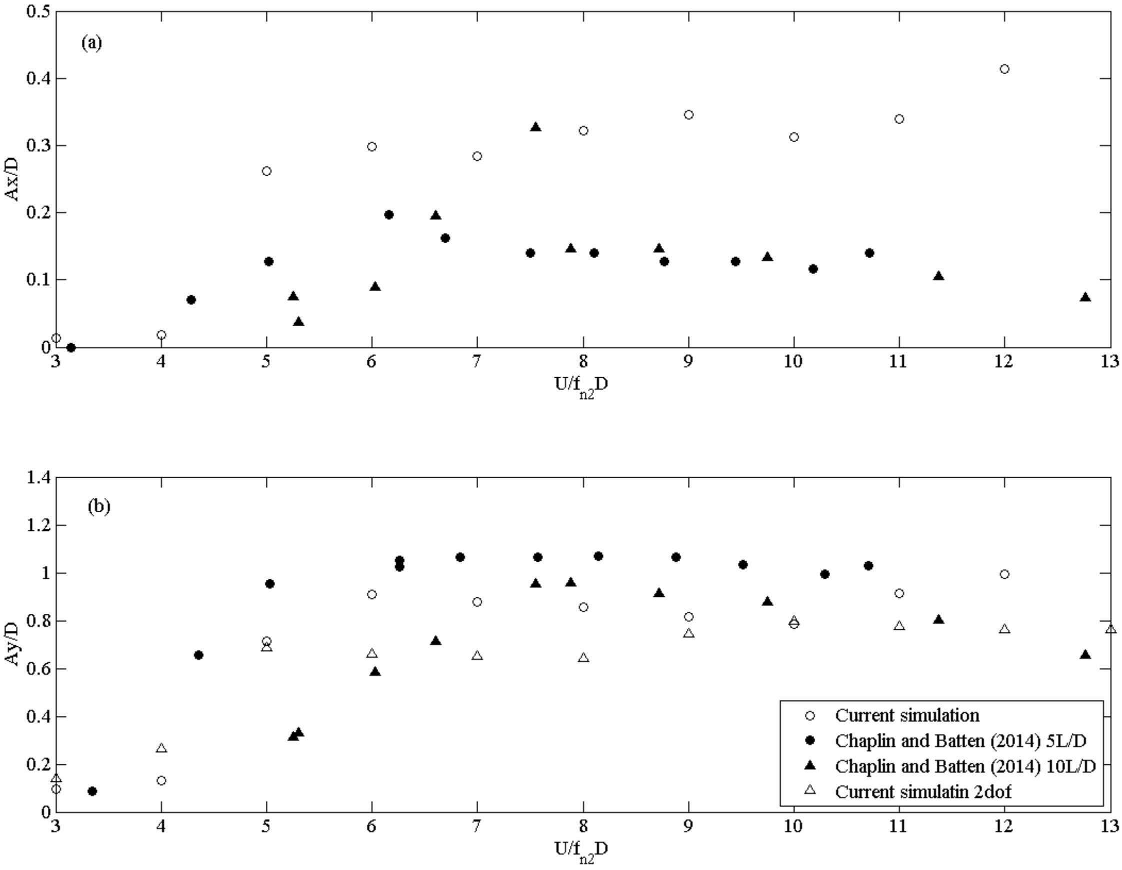

Figure 8.14. High frequency components of the response of the cylinder (a) inline motion, (b) crossflow motion

However, the predicted inline amplitude is much higher than in Chaplin and Batten's experiments, as seen in Figure 8.14(a). Although the trend is similar, the amplitude of motion in the inline direction is approximately 0.35 D compared to that of the experiments which is lower than 0.2D. The dramatic change occurs at 4 < Ur < 5, when the amplitude of motion changes from approximately 0.025D at Ur = 4 to 0.28D at Ur =5. When Ur > 11, the amplitude of motion increases to approximately 0.4D. The simulation results are reasonably high, along the line of the simulation VIV case in Chapter 7.

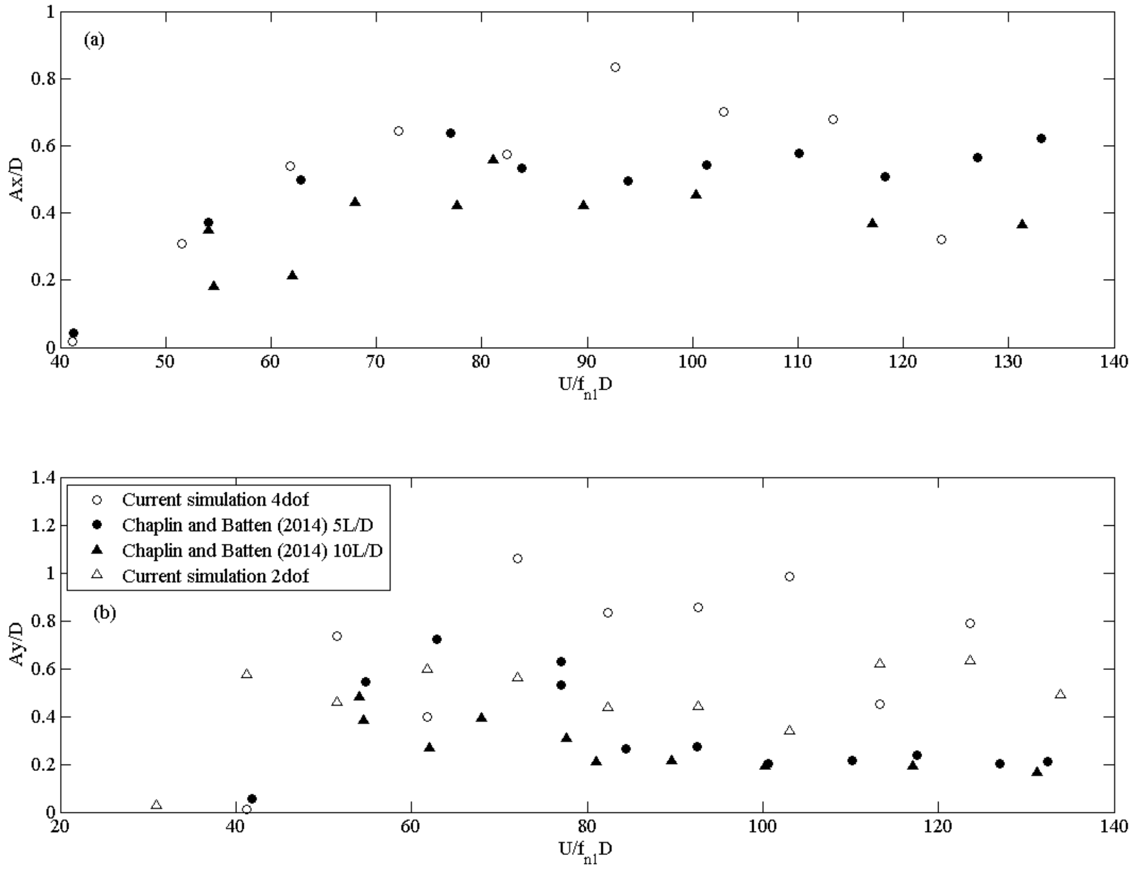

Figure 8.15. Low frequency components of the response of the cylinder (a) inline motion, (b) crossflow motion

For the low frequency components, the amplitudes of motion are shown against reduced velocity based on the low-frequencies component of the system $Ur_{low} = U/f_{n1}D$. In general, the amplitude of motion is reasonably high, as seen in Figure 8.15. Simulation with 2 dof (crossflow) system showed that the low frequency vibration amplitudes can reach up to more than 0.7D and the coupling between inline and crossflow oscillation further increases the low frequency amplitudes in crossflow, reaching 1.1D at $U/f_{n1}D$ approximately 70.

The LF inline amplitude shows a similar trend with Chaplin and Batten’s experiment. However, the peak amplitude is about 30 % higher. The amplitude of motion increases with increasing reduced velocity, as can be seen in Figure 8.15a, up to Ur = 80. The LF amplitude of motion are of the order of 0.7D in when $U/f_{n1}D$ > 70 showing 20% difference compared to the experimental values. The peak amplitude recorded at $U/f_{n1}D$ = 92 and is 0.8 A/D

The LF crossflow motion amplitudes are, in general, higher compared to the experimental results. The transition area can be observed at 40 < $U/f_{n1}D$ < 60 where the sharp change in amplitude occurs. In this transition area, VIV is dominant and the cylinder vibration moved into the “locked in regime”, also present in Chaplin and Batten’s experiments. The peak amplitude is record when 60 < $U/f_{n1}D$ < 90 with the value of 1.1D. This value is approximately 40% higher compared to the experiment by Chaplin and Batten.

When $U/f_{n1}D$ > 80, the LF amplitude of crossflow motion, is much higher compared with the experiments. However, this trend was also observed in 2 dof transverse vibrations, where the low frequency amplitude of vibration is also higher than in the experiments (see Figure 8.12). The coupling between inline and crossflow vibration increases the amplitude of motion by approximately 50%.

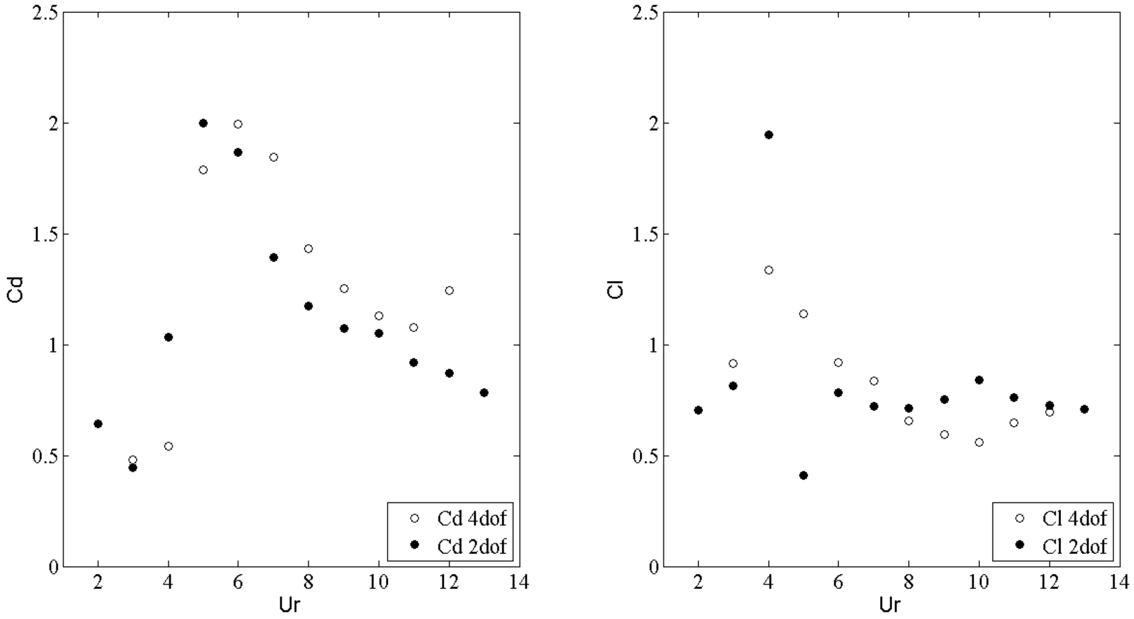

Figure 8.16: Comparison of the drag (right) and lift (left) coefficients between 4 dof and 2 dof systems

The lift and drag coefficients are shown in Figure 8.16, comparing mean drag coefficient (Cd) and lift amplitude between 4 dof system and 2 dof system. The drag coefficient shows the similar behaviour between both systems. The peak mean drag is about 2 and the drag coefficient reduces after reaching the peak. However, the transition region appears at a smaller Ur in 2 dof (at Ur = 5) compared with 4 dof (Ur =6). Differences are observed at $Ur > 10$, where the drag shows opposite trends. Thus, it may be concluded that, the drag coefficient is not affected by coupling between inline and crossflow vibrations.

The amplitude of lift coefficient shows some similar trends. However, the lift for the 4 dof system is smaller than the 2 dof system overall. The transition area occurs at Ur = 4 where the “locked-in” regime starts. The lift coefficients change by approximately 50%, when Ur increases from 3 to 4. At

8.5 < Ur < 10, the amplitudes of motion are similar for both system, but the lift coefficients in this range show some differences.

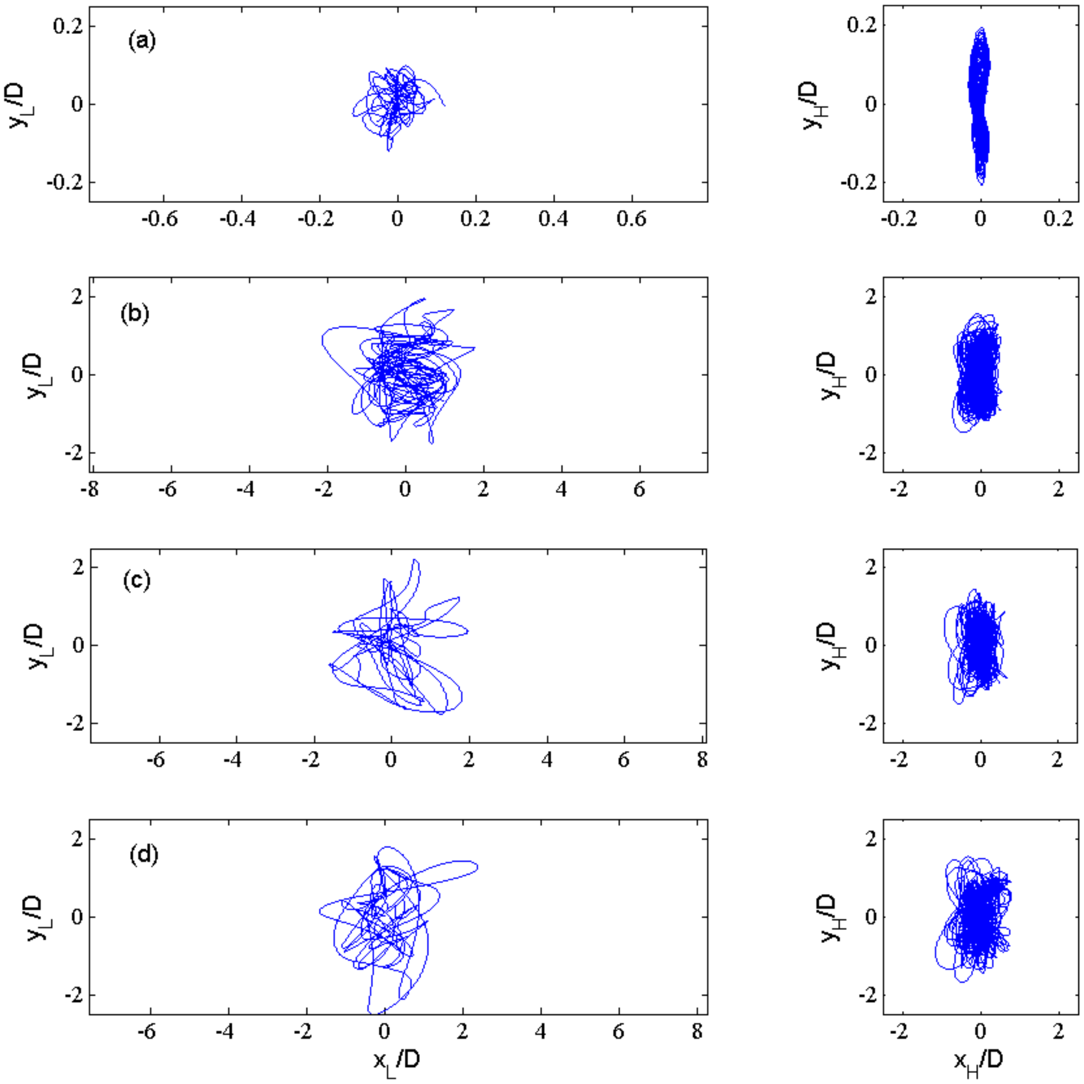

Figure 8.17. Trajectories of high (H) and low (L) frequency components of the downstream cylinder for L = 5D at (a) $U/f_{n2}D$ = 4, $U/f_{n1}D$ = 41, (b) 7 ; 72.1, (c) 10; 103, (d) 12; 124

Trajectories of the low and high frequency motion components are shown in Figure 8.17. In general, no obvious shapes can be discerned, except at $U/f_{n2}D$ = 4, where a figure of eight motion can be seen. For larger reduced velocities, the trajectories are chaotic for both high and low frequency components. The low frequency motions, exceeding 2D in some cases, show that the effect of wake- induced vibration is significant for the downstream cylinder vibration and inline vibrations can be larger than crossflow ones as in Figure 8.17(b,c,d). As the duration of the experiments usually exceeds 40 vortex-shedding cycles of low frequency motion, the present simulation really needs longer runs. However, to meet the excepted number of 40, at least 400 motion cycles based on high frequency are required (based on f_{n2}/f_{n1} = 10.3). This is a big challenge as simulations of more than 200,000 time steps have been run for each cases to achieve 80 vortex-shedding cycles. To increase this fivefold to 1,000,000 time steps is not very realistic, even with 2D modelling.

8.6. Conclusion

In this chapter, the interaction between two cylinders in a tandem arrangement in the unsteady flow has been carried out to provide results of simultaneous vortex- and wake- induced vibration. In the wake of the upstream stationary cylinder, the downstream cylinder was elastically mounted with 2 dof in each directions (4 dof in total). The ratio between high and low natural frequencies is about 10.3:1, and the reduced velocity based on the lower natural frequency exceed 130.

The simulation in 2 dof (crossflow) showed the amplitude of motion is approximately 30% smaller compared to the system with coupling inline and crossflow vibration. Two main frequencies of vibration based on wake- and vortex- induced vibrations can be discerned and additional frequencies due to interaction between f_v and f_w also appear at high reduced velocity ($U/f_{n2}D$). The predicted amplitudes for the 4 dof (2+2) system, show reasonably good agreement in terms of high frequency components compared with the experiments results. However, in terms of low frequency amplitude components, both inline and transverse motion amplitude are, in general higher than experiments, especially transverse motion. This was also observed for the 2 dof (crossflow) system.

The lift and drag coefficients do not show any significant differences between 2 dof and 4 dof systems, having similar peaks and trends. However, the lift and drag coefficients appear to be less influential since the amplitudes of motion are larger in the 4 dof system compared to the 2 dof.

Motion trajectories show no obvious shape, and the motion of the downstream cylinder is reasonably chaotic. However, at low frequencies, the figure of 8 shape can be clearly seen, similar to the single cylinder case with 2 dof. The amplitude of motion due to wake-induced vibration is dominant compared to HF vibration due to vortex-induced vibration, especially for high reduced velocity values. To find out more on low frequencies trajectories, longer runs are necessary.

The differences observed between experimental and numerical results due to two main reasons:

- In Chaplin and Batten’s experiments, quite high level of turbulence, about 5% were used. This is not feasible for current simulation models, where high turbulence simulation of free stream is still a challenge. All current mathematical model, such as RANS, LES, DES although they produce good predictions for VIV, the free stream flow is quite smooth for most cases, with very low level of turbulence (typically < 1%). Where good agreement was shown with experiments, those experiments were all carried out at very low levels of turbulence.

- The current simulation was carried out using 2D modelling. 3D effects have been shown to influence VIV and WIV simulation (Saltara et al., 2011). However, with currently used mesh and number of time steps the computational cost required for 3D simulation is not feasible.

Although relatively few experimental, as well as numerical data were available to compare the predicted effects of simultaneous wake and vortex induced vibrations, the current simulations showed that wake induced vibration and the inline vibrations are quite crucial factors, which will affect the design of risers. The simulations also suggest that the presence of higher modes of motion in more than 1 dof may significantly influence features of fluid structure interaction.

Chapter 9 : A downstream cylinder with multi-degrees of freedom in staggered arrangement.

9.1. Preamble

In this chapter, two cylinders in staggered arrangements are investigated. In this case, the downstream cylinder is again supported as a 2 dof (crossflow) or 4 dof (2+2) system, located at the same center– to – center separation (L = 5D), but with an offset B = D in crossflow direction as indicated in Figure 9.1.

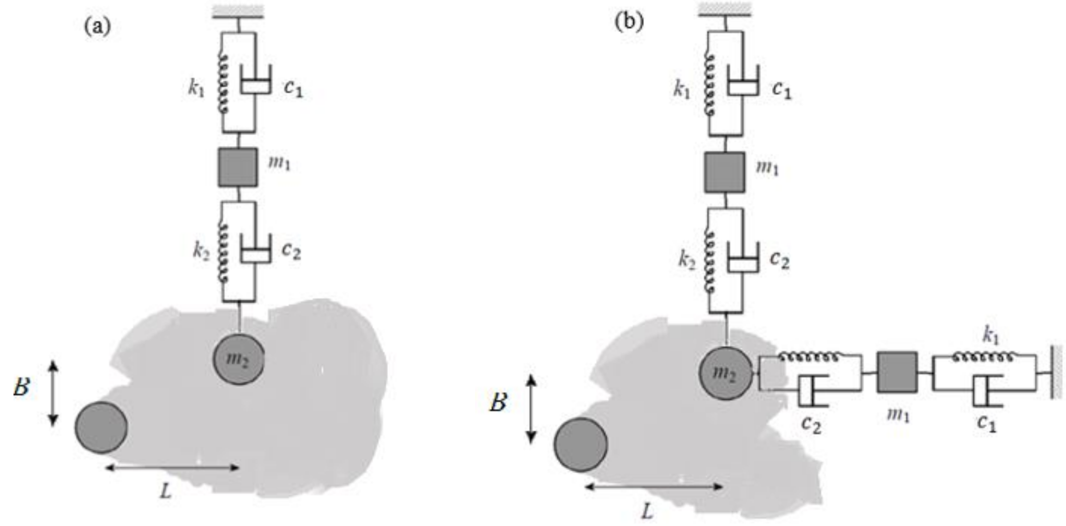

Figure 9.1. Schematic sketch of cylinder in staggered arrangements (a) 2 dof (b) 4 dof (Chaplin and Batten, 2014)

In these simulations, as in Chapters 7 and 8, the upstream cylinder is stationary. The downstream cylinder is mounted on an elastic system comprising springs, masses, dampers as shown in Figure 9.1. The mass ratio is the same as chapter 8, and the properties of the system are defined as per Table 8.1 in both inline and transverse directions.

A 40D x 70D rectangular domain is used, albeit with 71200 cells. This is larger than the 69200 cell mesh in Chapter 7 and 8 due to the extended refinement zone for the staggered arrangement, as shown in Figure 9.2, which is slightly bigger compared with the tandem case. The mesh is also designed to accommodate a dynamic mesh scheme, which allows movement of up to 5D in crossflow direction and 9D in the downstream direction. As in the previous chapter, the dynamic mesh scheme, smoothing – diffusion was used and the diffusion parameter was set to 1.5 to maintain the mesh quality around the cylinder, hence the y+ value is kept at approximately 1.

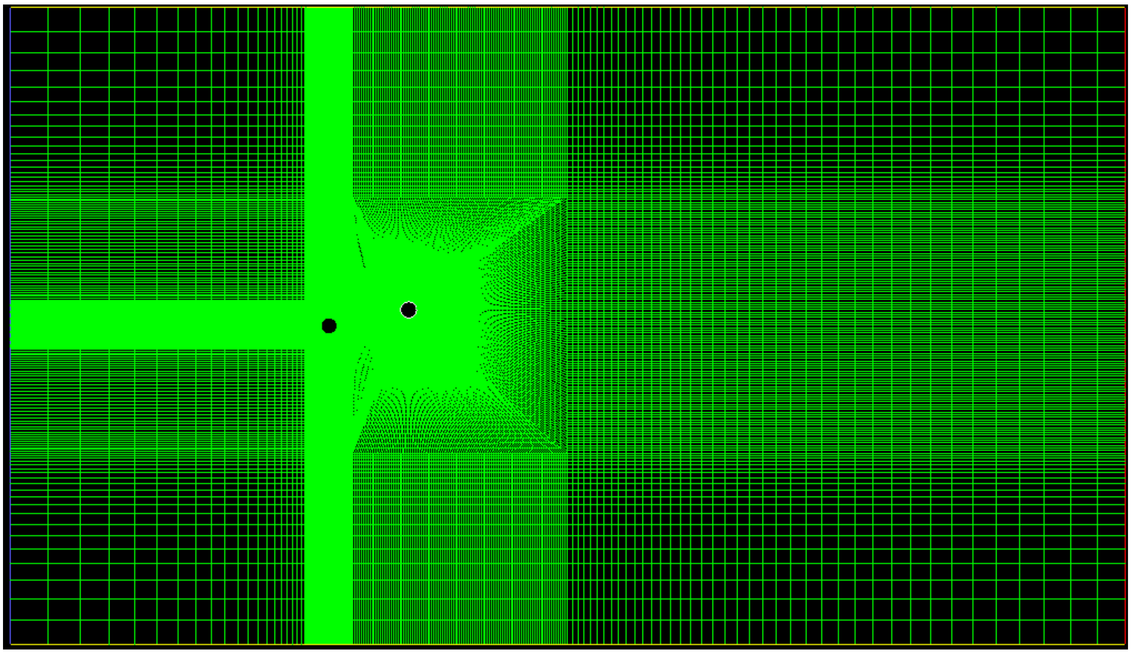

Figure 9.2. Computation domain for staggered arrangement (B=D, L=5D)

The initial displacement and velocity of both cylinder in crossflow and inline directions are assumed to be zero as per previous cases in chapters 7 and 8. The velocity was changed to reach the expected reduced velocity based on the highest natural frequency of the system. Accordingly the Reynolds number reaches 33,000 with $U/f_{n2}D$ = 14.

In this case, the simulations were carried out for two cases,

(1) the downstream cylinder is elastically mounted on a 2 dof system in crossflow direction only (2 + 0) and there is no vibration in the inline direction (Figure 9.1a).

(2) the downstream cylinder is elastically mounted on a 4 dof system (2+2), where the inline motion is also included to investigate the coupling effects between inline and transverse directions (Figure 9.1b).

9.2. A downstream cylinder in staggered arrangement - 2 dof system

In this section, simulation are undertaken for the case shown in Figure 9.1a, with the downstream cylinder is elastically supported by a 2 dof system in crossflow direction only.

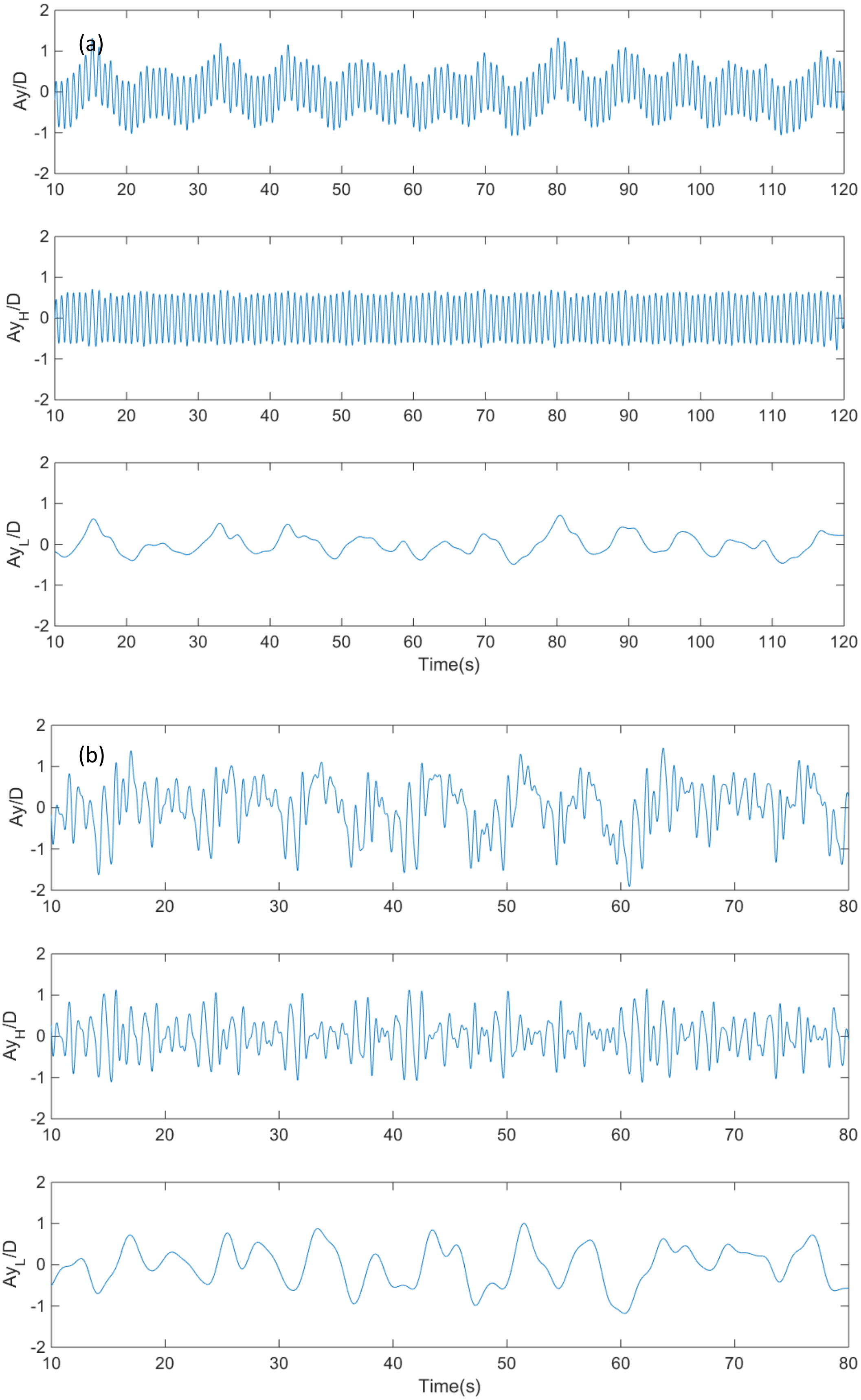

Figure 9.3. Time series of the downstream cylinder displacement with 2 dof system in staggered arrangement B = D, (a) Ur = 6, (b) Ur = 9.

Similar in a tandem arrangement cases, the time history of the displacement can be split into two main components, which is showed in Figure 9.3. Two main frequencies can be seen by separating the main signal. The cut-off frequency used for this purpose was one half of the cylinder higher natural frequency f_{n_2}. The amplitude by wake-induced vibration is comparable with high frequency component by VIV (Figure 9.3)

The crossflow amplitude of vibration of the downstream cylinder in a staggered arrangement over a range of reduced velocities is examined, as shown in Figure 9.4, and compared to Chaplin and Batten's experiments with 4 dof, the same offset B = D.

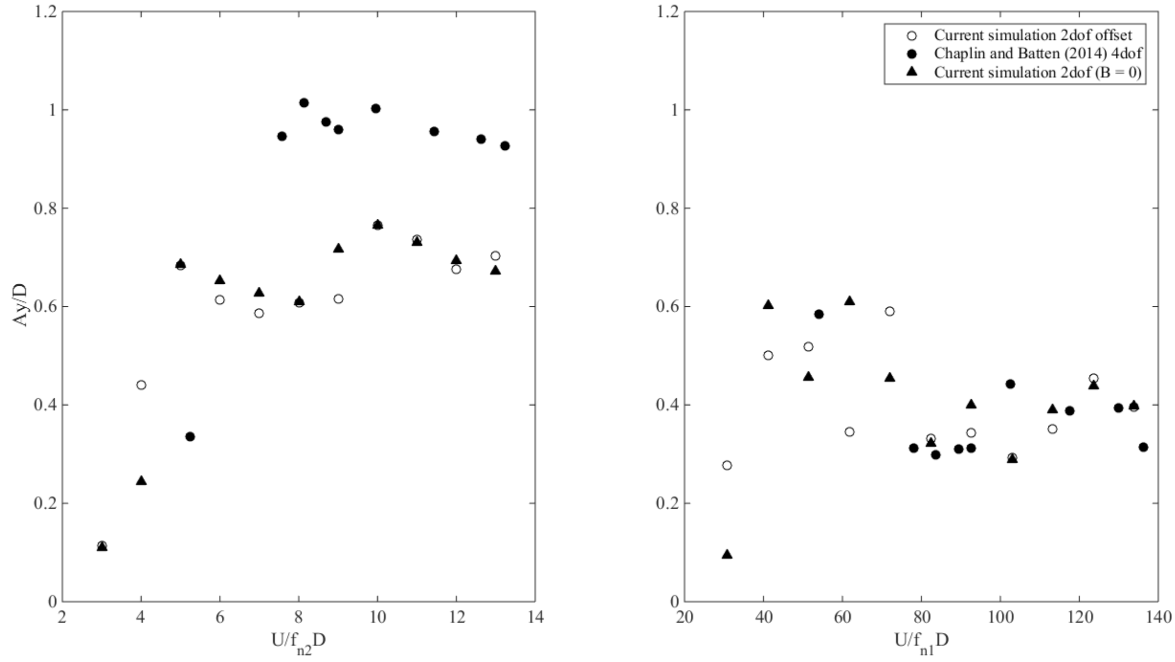

Figure 9.4 (a) Amplitude of high (left) and (b) low (right) frequency components of crossflow displacement L = 5D, B = D and L = 5D, B = 0, 2 dof system compared with Chaplin and Batten's experiment (4 dof)

Compared to Chaplin and Batten's experiments in 4 dof, the current staggered arrangement predictions have smaller amplitudes of motion for HF components. The peak amplitude recorded was approximately 0.8D at $U/f_{n_2}D$ = 10, which is 20% smaller compared to the experiments. The transition appears when Ur increases from 3 to 5 and there is a sevenfold increase in the motion, from 0.1D to approximately 0.7D. At $U/f_{n_2}D$ = 3, there is good agreement with the experiment probably because at this reduced velocity, the inline vibration is not significant. The transverse amplitude of vibration is reduced slightly when the reduced velocity increases. At the other transition point of $U/f_{n_2}D$ = 9, the amplitude of motion increases by approximately 30%, from 0.6D to 0.8D. The comparison with previous 2 dof system in tandem (crossflow only, chapter 8.5) shows these are very similar for the HF amplitude except the different at low reduced velocity range

($U/f_{n_2}D$ = 4), where the amplitude of motion due to the staggered arrangement is nearly doubled. It can be observed that the offset in vertical direction with B = D does not have a strong effect on the high frequency vibration of the system.

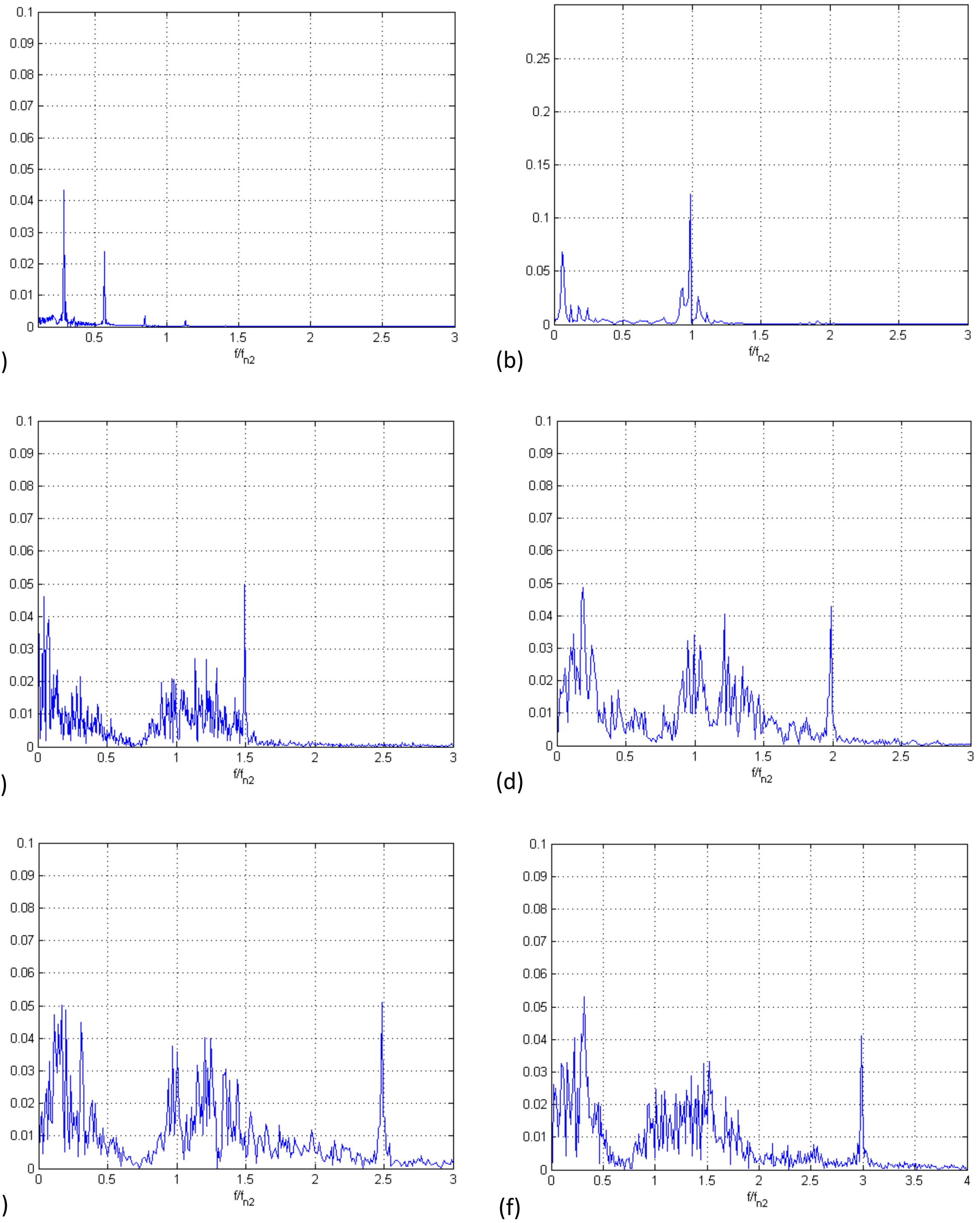

(a) (b) (c) (d) (e) (f)

Figure 9.5. Spectra of response of downstream cylinder with 2 dof at L = 5D, B = D for (a) Ur = 3, (b) 5, (c) 7, (d) 9, (e) 11, (f) 13

The LF amplitude of motion shows better agreement with Chaplin and Batten's experiment as can be seen from Figure 9.4b. However, in some cases, for example at $U/f_{n_1}D$ = 103, the amplitude of motion in the experiment is 50% higher, 0.3D compared with 0.45D. In general, the coupling between 2-direction vibration and 1-direction in crossflow direction does not have a strong effect on low frequencies amplitude, as was observed in Chapter 8.

Spectra of response amplitudes of the downstream cylinder are shown in Figure 9.5 as functions of reduced velocities based on the HF of the system $Ur = U/f_{n_2}D$. At low reduced velocity Ur < 5, only two peaks are recorded the ratio of 3 (Ur = 3) and 10 (Ur = 5) between HF and LF peaks. At higher reduced velocity, more peaks appears as shown in Figure 9.5 (c,d,e,f). In those figures, two main frequencies appear, relating to WIV (f_w) and VIV (f_v). However, another strong peak in the wake of downstream cylinder, approximately $2f_v$ show the 2 dof system can result in vibration with more than 2 frequencies and make the system more complicated to control. The very high peak at a frequency of $2f_v$ may be caused because of the interaction between two main frequencies and resulting much higher amplitudes. In general, compared with the spectra of crossflow response in the tandem case (Figure 8.8), the current results are very similar.

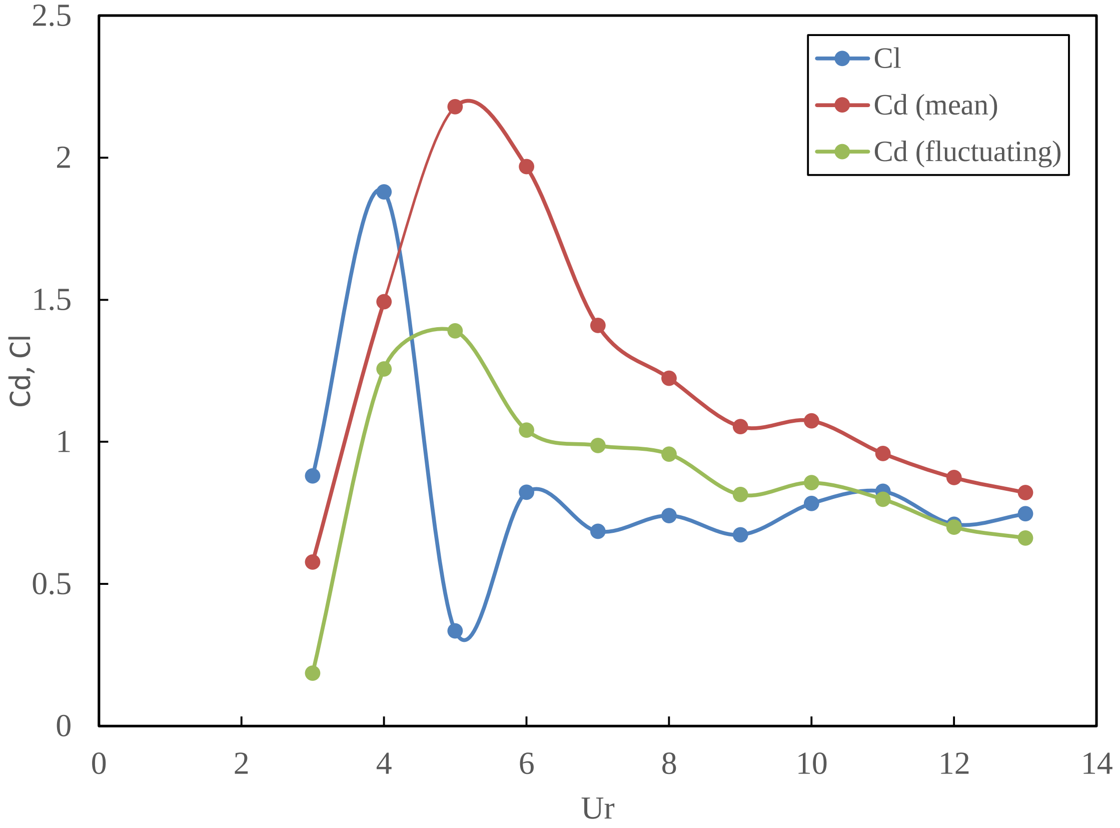

Figure 9.6. Lift and drag coefficient of downstream cylinder with 2 dof (crossflow) in a staggered arrangement

Figure 9.6 shows the variation of drag and lift coefficients in the significant range of reduced velocities. The lift coefficient was calculated in terms of √2 times the standard deviation. The drag coefficient was split into 2 components, namely, mean drag coefficient and fluctuating drag coefficient. It can be obviously seen that the fluctuating drag coefficient is reasonably high compared with previous 1 dof in one direction in the tandem arrangement case, e.g. Figure 7.11, when the fluctuating drag is quite small compared to lift coefficient. At low reduced velocities, the transition appears at $3 < Ur < 5$, when the mean drag coefficient increases from 0.2 to exceed 2, peaking at $Ur \approx 5$ (C_d = 2.2). The mean drag coefficient is reduced quite sharply, when $5 \leq Ur \leq 9$ from 2.2 to 1.1. In the final branch, the drag coefficient reduces gradually with the increase of reduced velocity, and at Ur =13, C_d = 0.82. The fluctuating component shows a similar trend in the range $3 < Ur < 7$ where the peak at Ur = 6. The amplitude of fluctuating drag also decreases with increasing reduced velocity.

The transition in lift coefficient appears at lower Ur, when the lift increases from 0.54 at Ur = 2 to about 1.9 at Ur = 4, followed by a dramatic fall, when the lift coefficient reduces to less than 0.4. When Ur > 7, the lift coefficient is lying in the range of 0.75 and does not show any large changes with increasing of Ur. This also reflects the vibration of the cylinder in this range of Ur

The interesting point to note in this analysis is that the fluctuating drag coefficient is quite high, exceeding the value of fluctuating lift for almost the whole Ur range except when Ur < 4 and and Ur =13. For fixed cylinder cases in the tandem case, the mean drag coefficient is $Cd(mean)$ = 0.715 with the fluctuating drag coefficient $C_{d_{flactuating}}$ = 0.35 whilst when the cylinder is moving the fluctuating drag coefficient can be 2 - 3 times bigger. The mean components at high reduced velocities is also 20% bigger compare with the fixed case. That shows potentially, the inline vibration if the cylinder is allowed to move in the inline direction will be remarkable, and should not be ignored.

The time history of drag and lift coefficients is showed in Figure 9.7 for lift coefficient and Figure 9.8 for drag coefficient. It can be noted that the lift and drag time history is quite similar, at Ur > 7. At low Ur regime, the drag coefficient time history change from high at Ur = 4 to low oscillating amplitude at Ur = 5. The lift coefficient time history at low Ur = 4 behaviours similar to stationary cylinder in tandem, with $C_l \approx$ 0.5. The dramatic change occur when Ur change from 4 to 5, corresponding the amplitude of motion was nearly double, from 0.4D at Ur = 4 to approximately 0.7D at Ur = 5. In general, the time history shows the non-harmonic vibration in both lift and drag for almost Ur, just except, $Ur = 3, 5$ and 6.

Compared with the time history of Figure 8.10, the trend of lift is very similar. At $Ur < 6$, the amplitude and oscillation is also almost the same, especially, at $Ur = 5$, the lift coefficient changes from high to very low amplitude, as seen in Figure 9.7. That also explains why the amplitude of crossflow motion between 2 dof (staggered) and 2 dof (tandem) is very similar.

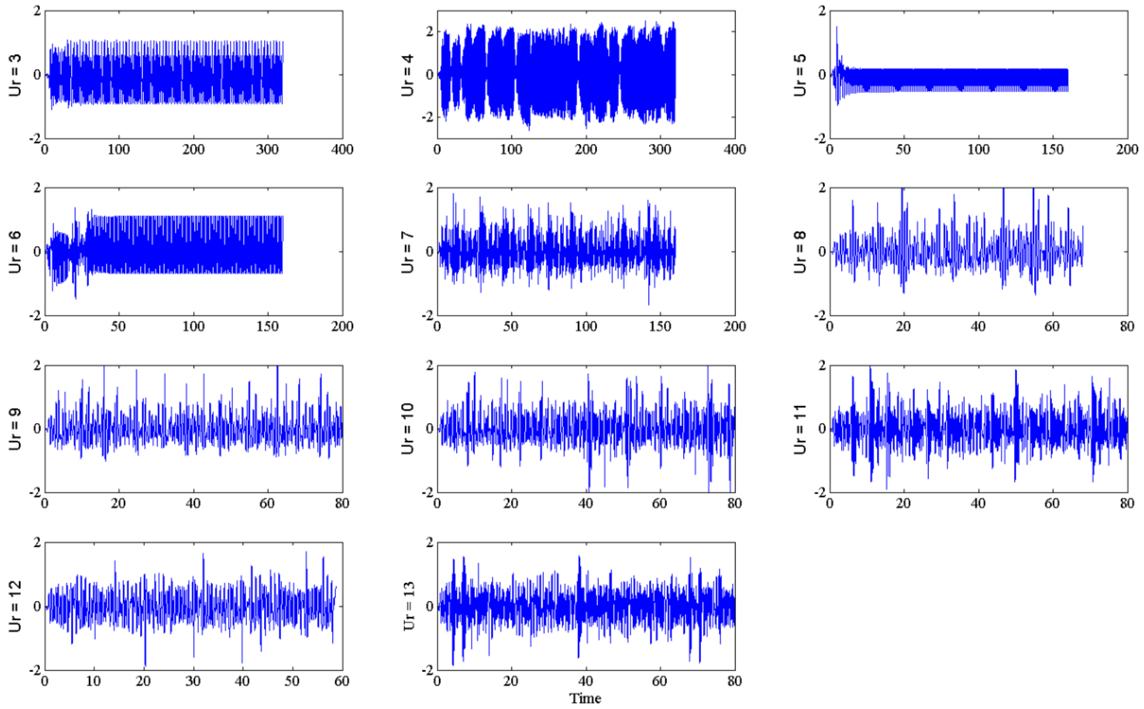

Figure 9.7. Lift coefficient time history in $3 \leq Ur \leq 13$ region

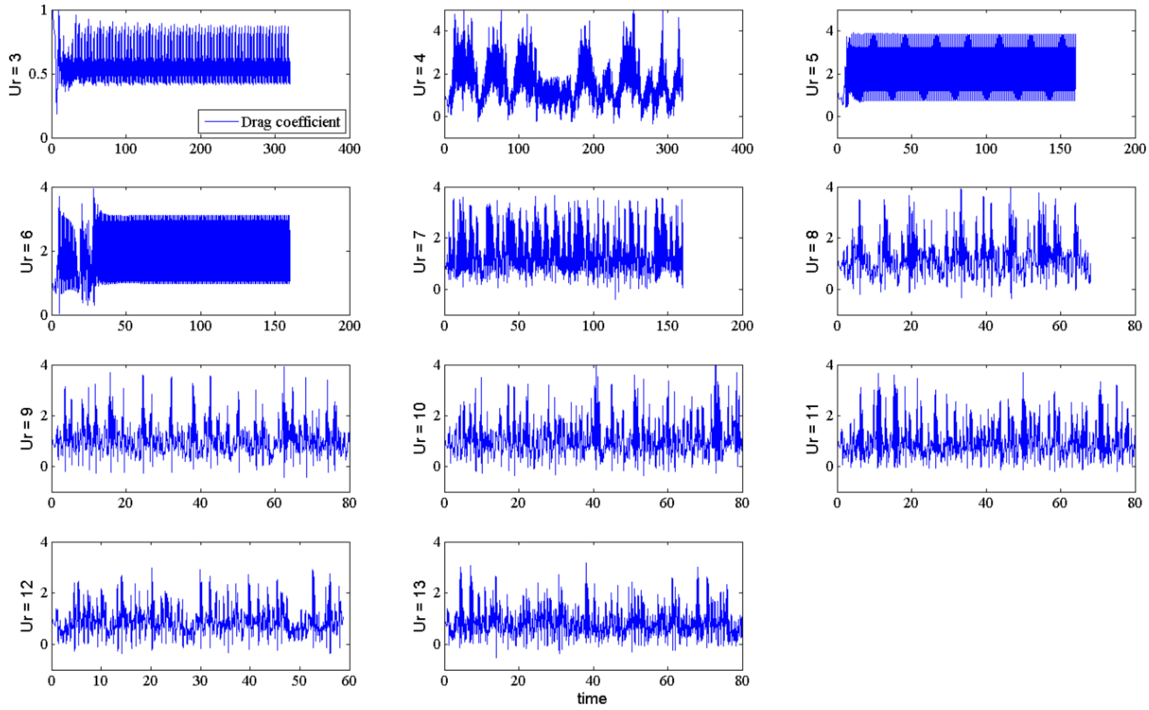

Figure 9.8. Drag coefficient time history in $3 \leq Ur \leq 13$ region

The dominant VIV frequencies of current offset simulation B=D are shown in figure 9.9a and are very close to those from Jauvtis & Williamson (2004) for a single cylinder with two degrees of freedom, and agree well with Chaplin and Batten's experiment. It can be noted that the influence of offset is not great in the vibration of VIV frequency of the 2 dof staggered system, as can be seen in Figure 9.9(a). The ratio between the two main frequencies (f_v/f_w) is shown in Figure 9.9b, which also agree with Chaplin and Batten's (2014) experiment. At some reduced velocity, e.g, Ur = 5 and 7, the ratio between the two frequencies is similar to that of the pre-defined frequencies ratio of the system. However, with increasing reduced velocity, this ratio decreases, to approximately 5, that also is presented in Chaplin and Batten's experiment. This difference may be caused by the interaction between two main frequencies of the system where a high peak could be observed at higher frequencies ($f_v/f_{n_2} > 2.5$).

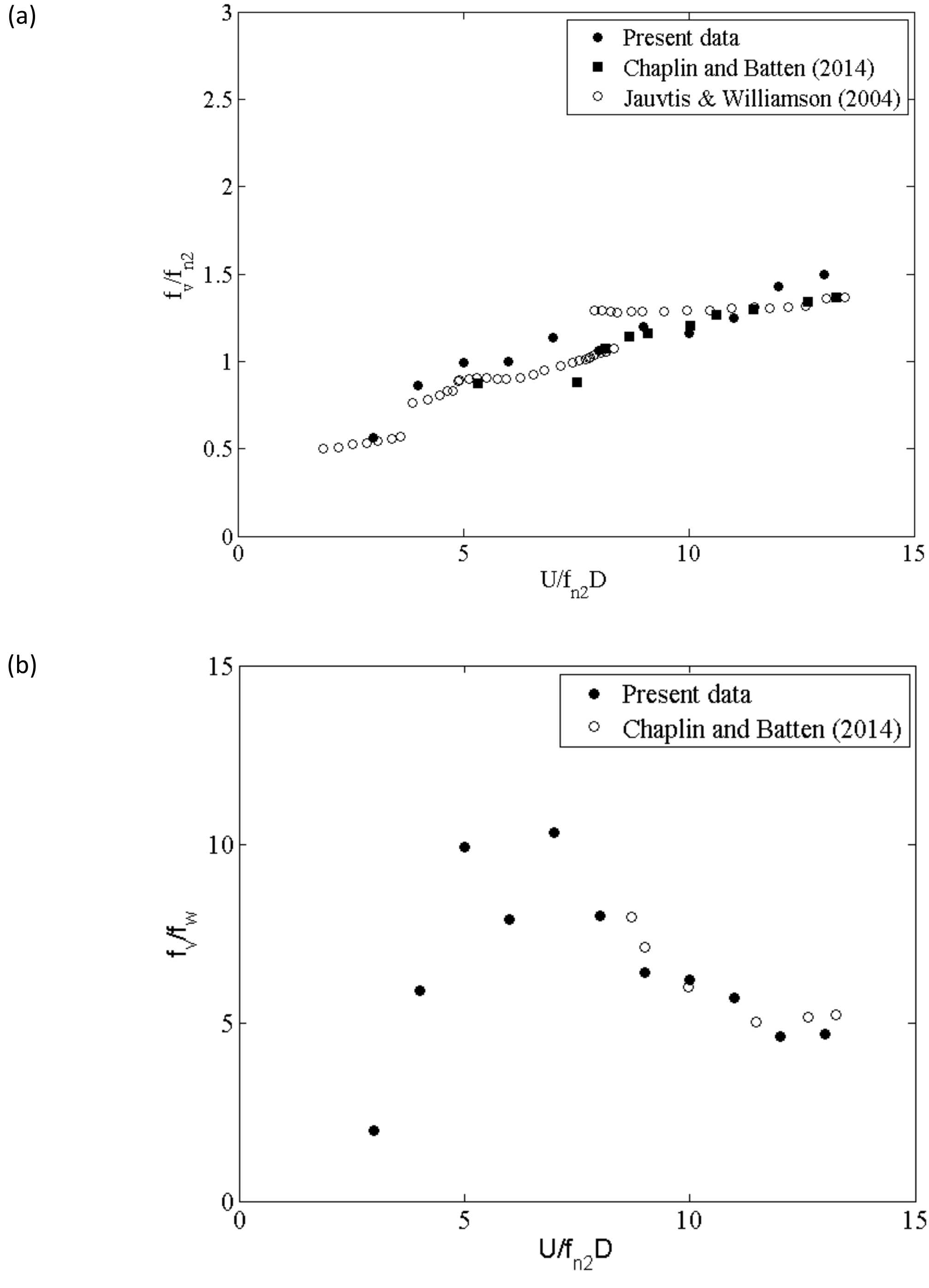

Figure 9.9. Variation of frequency ratio with reduced velocity in crossflow VIV response(a) as a proportion of the dominant frequency, (b) as a proportion of the dominant frequency in the inline WIV response

9.3. A downstream cylinder in a staggered arrangement with 4 dof

In this section, two cylinders in a staggered arrangement, where the upstream one is stationary and the downstream is on an elastic 4 dof (2+2) system is numerically investigated. The sketch of the system is presented in Figure 9.1 (b), and the system properties as per chapter 8.

In the tandem case, the strong displacement of the cylinder is a big issue, whereby the mesh is distorted significantly, leading to mesh failure and change in the nature of the system. Instead of remaining in the area of interest with L = 5D, the downstream cylinder could be displaced to distances of 10D or more. These problems have already been mentioned in Section 8.5 and arise from the strong drag force in the wake of the upstream cylinder. The drag coefficient is high both in terms of mean drag and fluctuating drag.

Thus, the sensitivity test was carried out to select the appropriate mean drag component, and this component will be subtracted from the drag force allowing only the fluctuating component to remain and used when updating displacement of the cylinder. As in section 8.5, this is applied in two stages (1) using Cd_{low} and (2) using Cd_{high} and the intermittency occurs at the switch point. The input data will be summary in Table 9.1

Table 9.1. Summary of applied drag coefficient for staggered case L/D=5, B/D=1

Ur	Switch (L/D)	Cd_{low}	Cd_{high}
3		0.75	
4	1	0.95	1.5
5	1	0.9	1.7
6	1	0.9	2.1
7	1	0.9	2.1
8	1	1.0	1.9
9	1	1.0	1.5
10	1	1.0	1.9
11	1	1.0	1.9
12	1	1.0	1.5

In the staggered arrangement cases, the low drag coefficient (Cd_{low}) shows much higher values compared with the tandem arrangement with zero offset as the mean drag coefficient in the staggered arrangement case is higher, even when considering crossflow vibration only. Hence the equivalent force components to be subtracted have a value of Cd = 0.9 - 1.0 for $C_{d_{low}}$ and up to 2.1 for $C_{d_{high}}$. The under relaxation factor for pressure is reduced to 0.9 to maintain the stability of the simulation. The cylinder is stabilized when displaced by 1 – 2 D and oscillating. Hence, the actual center-to center distance between the two cylinders is more than 6D.

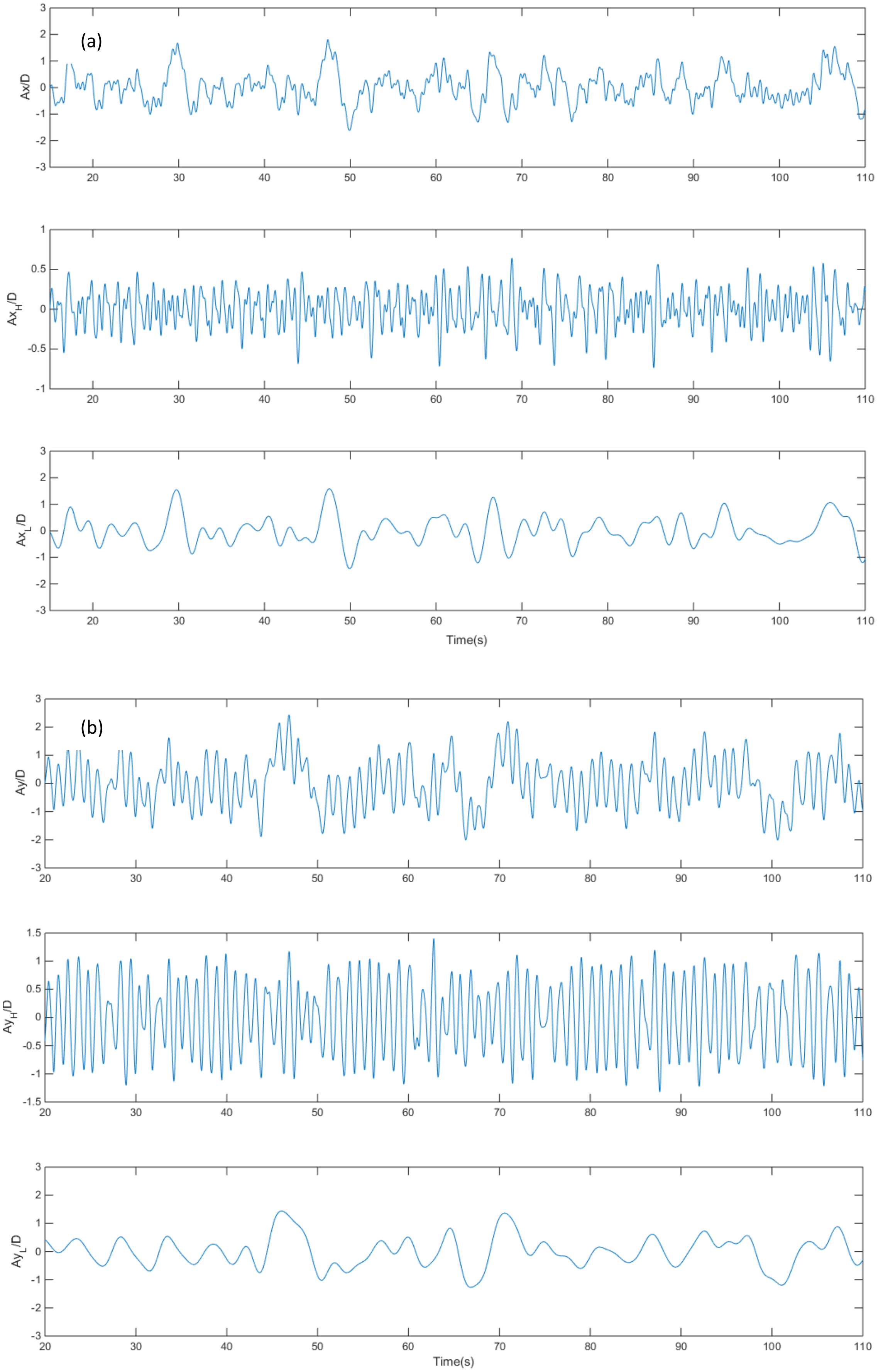

Figure 9.10. Time series of the downstream cylinder displacement in tandem (B = D) with 4 dof system at Ur = 7 (a) inline, (b) crossflow.

Time series of the downstream cylinder in tandem are showed in Figure 9.10 at Ur = 7 where the amplitude A_x and A_y are determined by standard deviation time $\sqrt{2}$. The cut-off frequency used also one half of the cylinder higher frequency, as mention in section 9.2.

The amplitude of motions of the downstream cylinder are presented in Figure 9.11 and 9.12 for the high and flow frequencies components, respectively. The vibration time histories of cylinder were filtered into two components, high and low frequencies components of inline and transverse motion.

The high frequency components of cylinder response are shown in Figure 9.11 against reduced velocity based on the high natural frequency in the range $3 < U/f_{n2}D < 13$. The results are compared with Chaplin and Batten's experiment in the same staggered arrangement. The data from section in 9.2 for a 2 dof system is also included in this comparison. The amplitude of crossflow motion shows a similar transition region where the amplitude of motion increases sharply with increasing reduced velocity. The peak amplitude at Ur ≈ 8 of approximately 1D agrees well with the experiment. When Ur > 10, a declining trend is observed in both simulation and experiment. However, when Ur > 9, the amplitude of motion for current simulation is generally smaller than in Chaplin and Batten's (2014) experiment, e.g the simulation result is approximately 0.65D compare with 0.95D in the experiment.

Compared with the 2 dof system, the coupling between inline and crossflow motions increases with the amplitude of motion. The peak amplitude predicted in 4 dof simulations is 1D, which is 25% than the 2 dof predictions (0.79D). In the range 6 < Ur < 8, the differences can be up to 60%. However, the simulation results show at 9 < Ur < 11, the differences are not large, and at Ur = 10, the amplitude of motion is almost the same. Hence, at the VIV transition area, from "locked-in" to "desynchronization", the predictions show very small differences due to coupling.

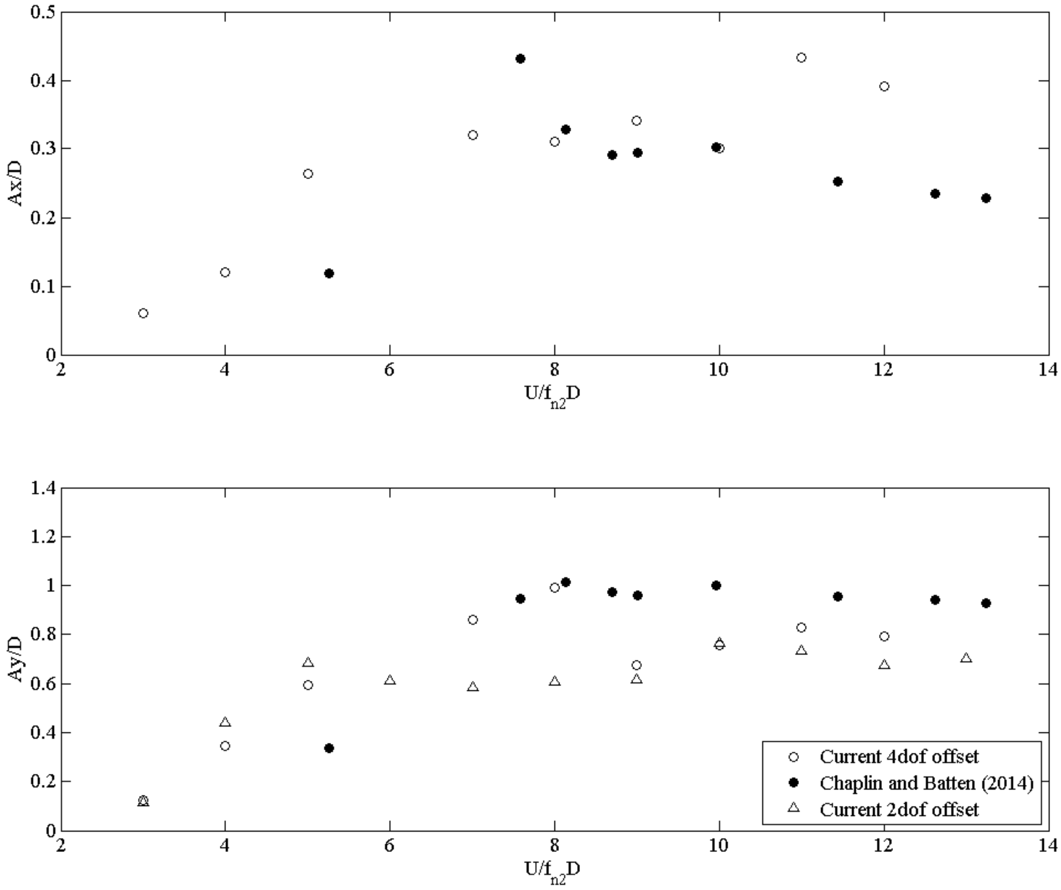

Figure 9.11. High frequency response components of the downstream cylinder (a) inline motion, (b) transverse motion of downstream cylinder in staggered arrangement L=5D, B=D.

The high frequency vibration of the downstream cylinder in the inline direction, in Figure 9.11a, shows agreement with experiments for peak amplitude of motion, of approximately 0.45D. The same increasing trend in the amplitudes can be observed when Ur increases to 7, although the increase is much sharper in the experiment. Good agreement can be seen for 8 < Ur < 10. However, when Ur > 11 the predicted amplitudes are higher than in Chaplin and Batten's experimental results. In general, the simulation results show increasing inline amplitude of motion, peaking at Ur = 11. This shows some disagreement with the experiment, but as per observations of the case with zero offset (see Figure 8.14a) where the inline vibration is increasing with increasing Ur.

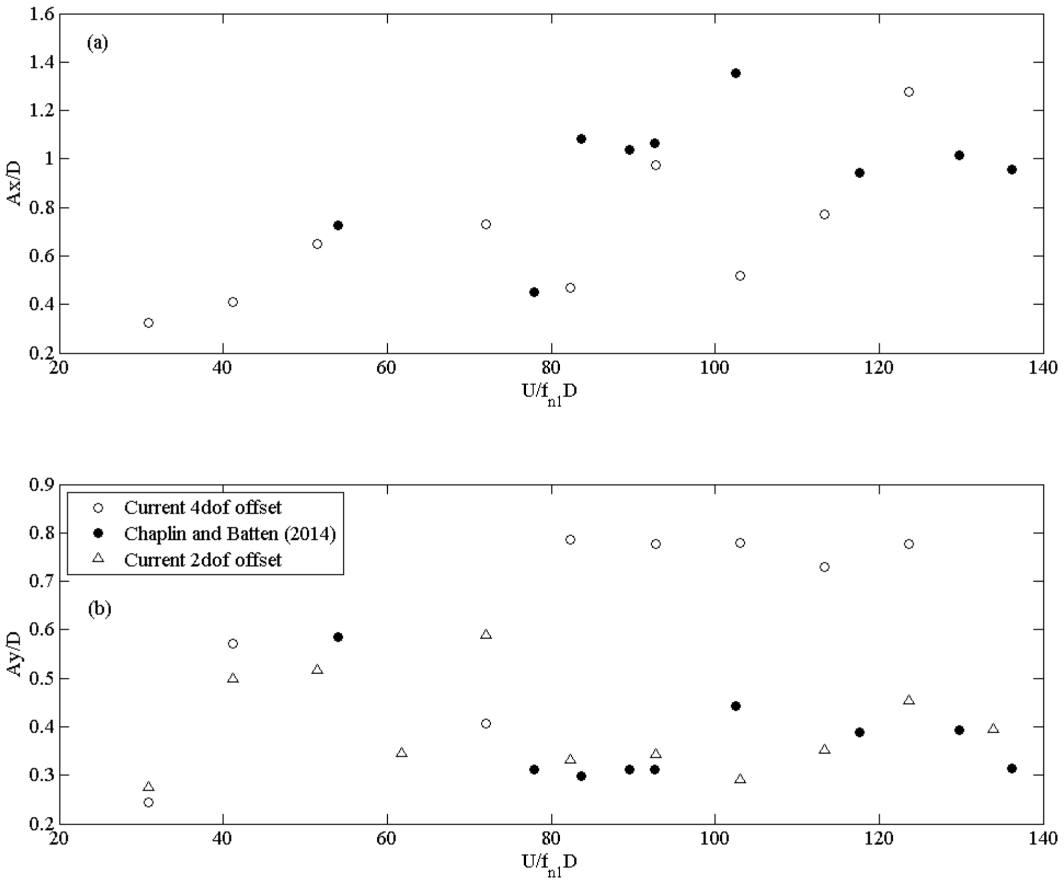

Figure 9.12. Low frequency components response of the cylinder (a) inline motion, (b) crossflow motion of downstream cylinder in staggered arrangement L = 5D, B = D.

The downstream cylinder response in LF components are shown in Figure 9.12. The amplitude of motion is plotted against the reduced velocity based on the low natural frequency of the system, $U/f_{n1}D$, exceeding 130. In the crossflow direction amplitude, agreement can be seen for $U/f_{n1}D$ < 80. However for$U/f_{n1}D$ > 80, there is no agreement with the amplitude of motion, approximately 0.8D, compare with 0.45D recorded in the experiment. Comparing the 2 dof and 4 dof system, the latter has much higher crossflow amplitude of vibration which was also observed in chapter 8, Figure 8.15(b). This can be due to 3D effects in the experiments, not captured in the 2D simulation.

The LF inline vibration shows better, but patchy agreement in the whole range of reduced velocity. There is reasonably good agreement at the reduce velocity $U/f_{n1}D$ < 100. Differences are observed at the $U/f_{n1}D$ = 103 where Chaplin and Batten's experiment shows higher amplitudes of motion (1.4D) compared with 0.6D from the simulation. The maximum amplitude of motion, due to LF components is similar in both simulation and experiments of the order of 1.4D.

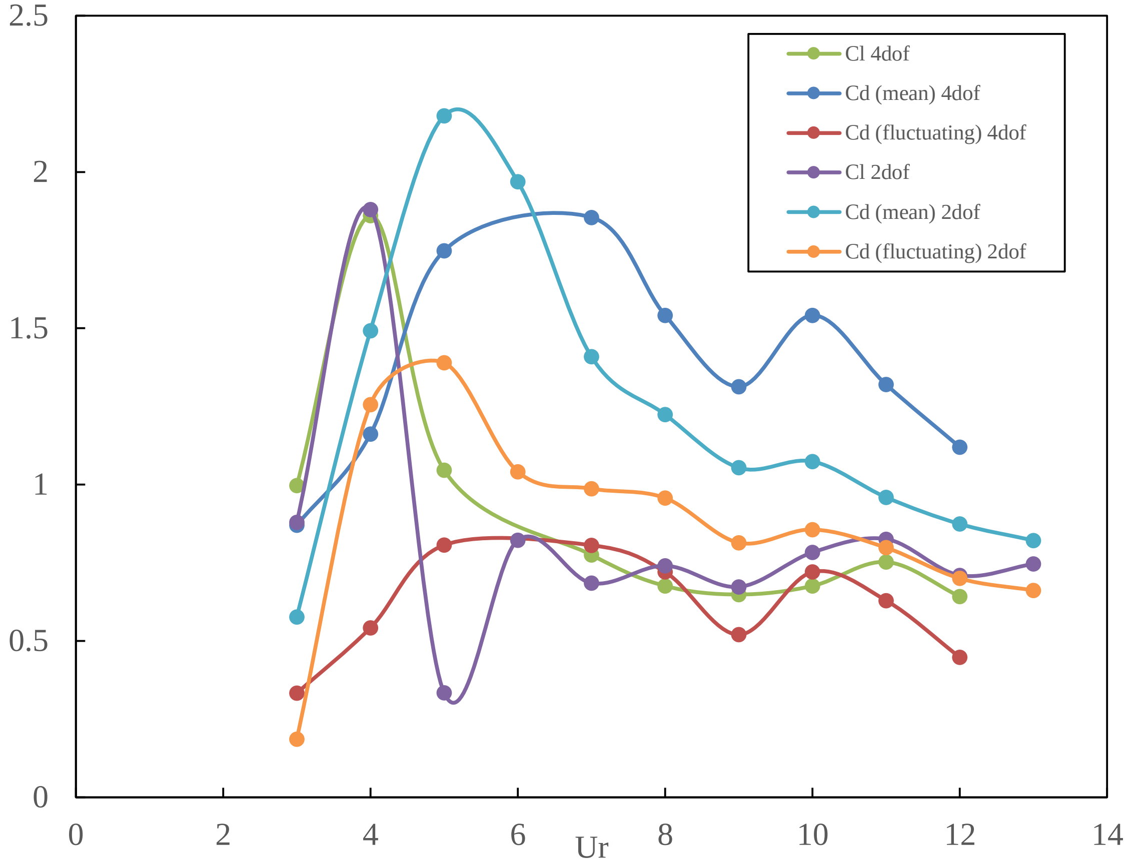

Figure 9.13. Drag and lift coefficients in a range of reduced velocity.

Variations of drag coefficient and lift coefficient with reduced velocity are shown in Figure 9.13. The lift coefficient is calculated in form of $\sqrt{2}$ times the standard deviation while the drag coefficient is separated in two components: mean drag coefficient and fluctuating drag coefficient, the latter is calculated in the form of $\sqrt{2}$ times the standard deviation.

The lift coefficient in the 4 dof system is similar to that of the 2 dof system, the only main difference is seen at Ur = 5. It should be noted that, at Ur = 5, the difference in amplitude of crossflow motion for both high and low frequency components is not significant.

The fluctuating drag coefficient of the 4 dof system is generally smaller compared to that of the 2 dof system. The biggest differences are seen at Ur = 4 and 5, with the drag fluctuating drag of the 4 dof is approximately twice that of the 2 dof system. This shows that the vibration of the cylinder influences greatly the drag coefficient. On the other hand, the mean drag of the 2 dof system is larger that that of the 4 dof system only up to $Ur \approx 6$. For $Ur > 6$, the mean drag of the 4 dof system is larger. The time history of drag and lift coefficient are also included in Figure 9.14 and 9.15 for $3 \leq Ur \leq 12$.

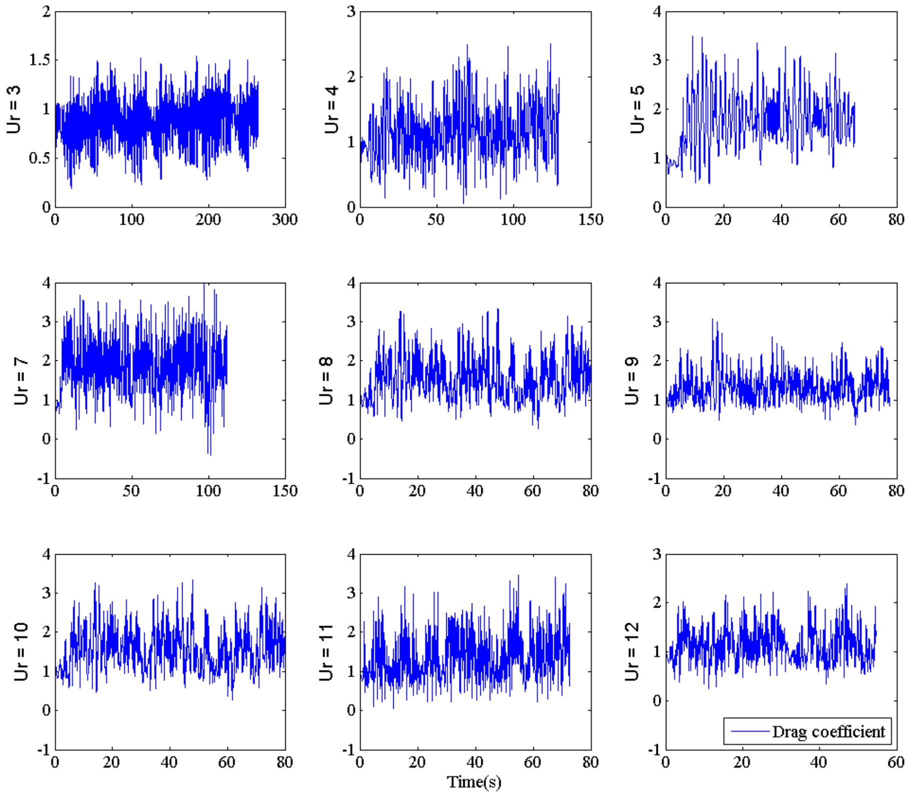

Figure 9.14. Time history of drag coefficient at downstream cylinder in staggered arrangement (L = 5D, B =D) over a range of reduced velocities.

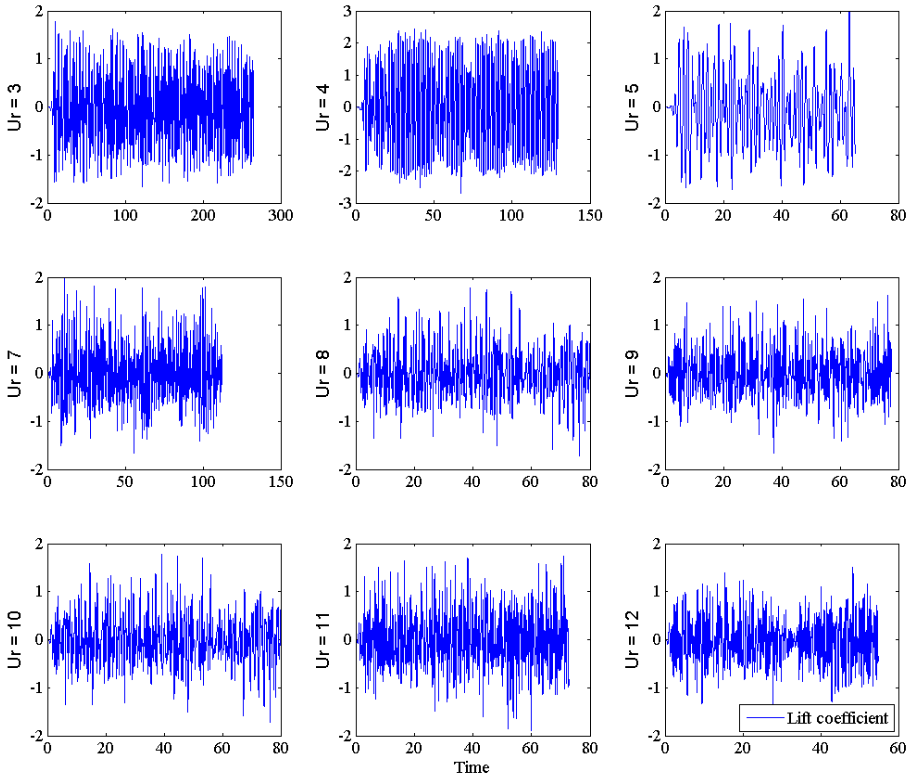

Figure 9.15 Time history of lift coefficient at downstream cylinder in staggered arrangement (L = 5D, B =D) over a range of reduced velocities.

It should be noted that the lift and drag time history is not in the harmonic form, and the amplitude of vibration again time is very random. The amplitude of fluctuation in drag coefficients is bigger than lift coefficient for almost whole range, except low reduced velocity region Ur <5. In addition, a low frequency with high amplitude could be observed when $Ur > 8$ in drag coefficient time history, corresponding to high amplitude of motion in inline motion.

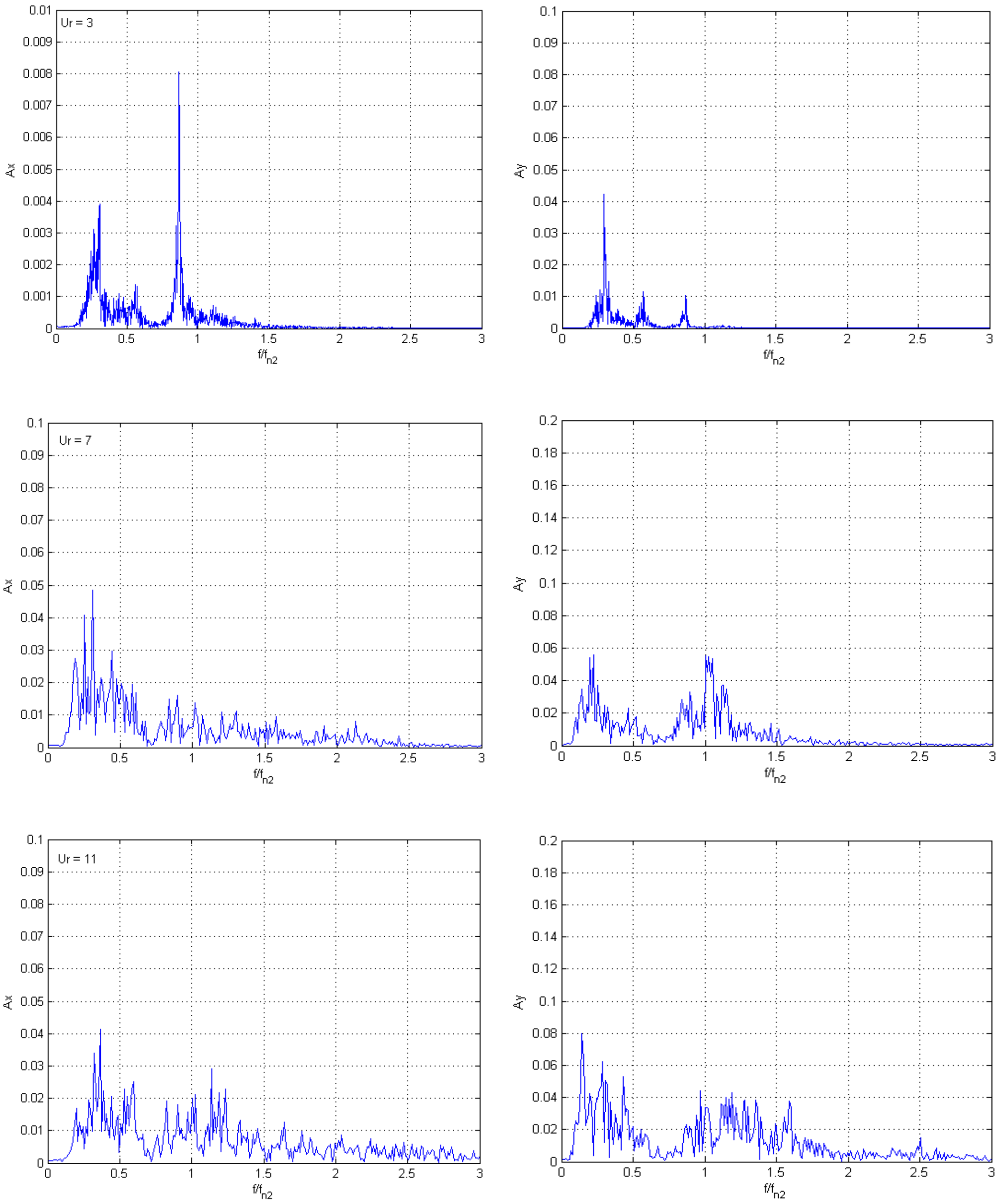

Figure 9.16. Response spectra of the downstream cylinder with 4 dof, L/D = 5, B/D =1 at Ur = 3, 7 and 11. The left hand side is for inline vibration and right hand side is transverse vibration

Response spectra of the downstream cylinder are shown in Figure 9.16 for reduced velocity of 3, 7 and 11. Several peaks can be identified where the dominant WIV frequency is about 1/6 to 1/4 of the dominant vortex induced vibration frequency (Figure 9.17b).

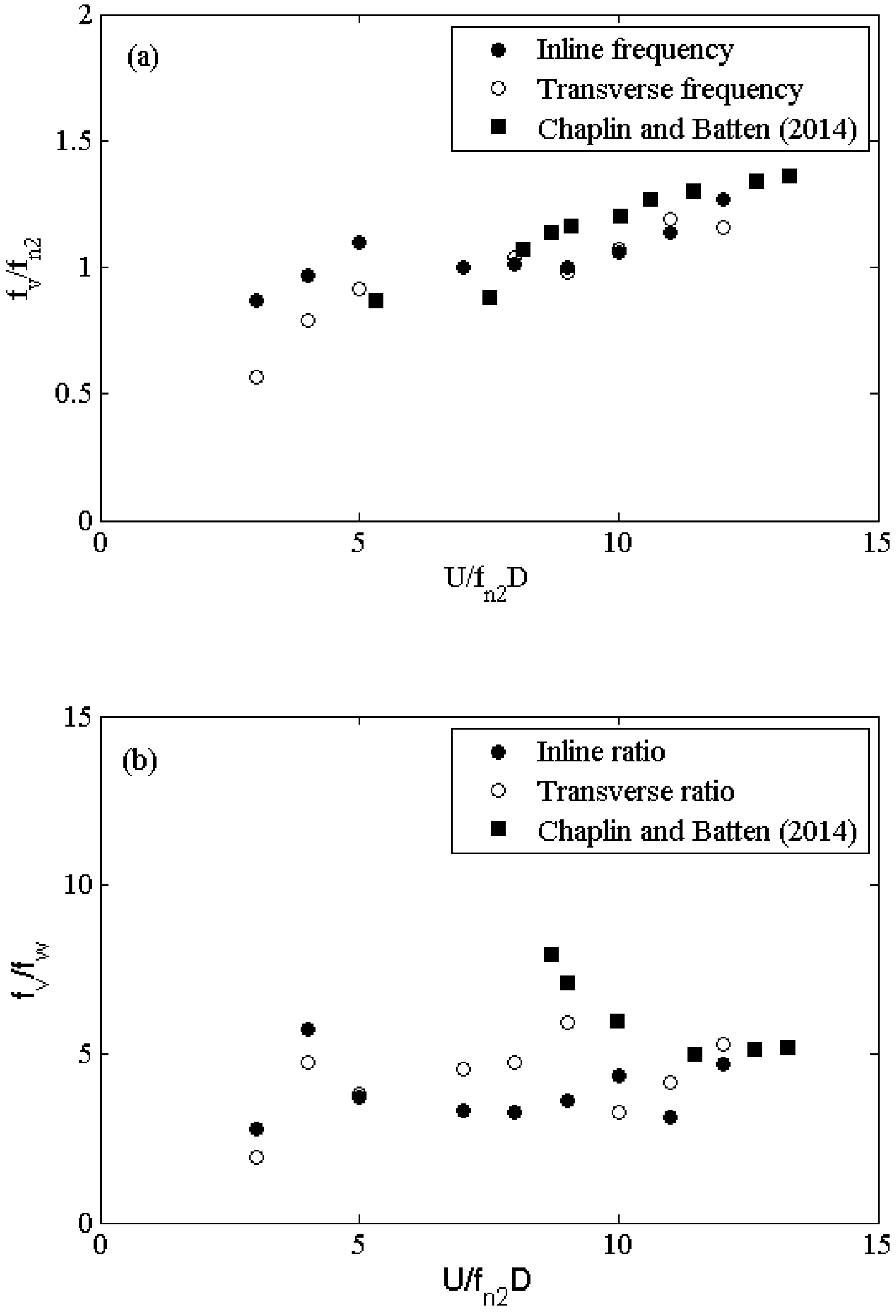

Figure 9.17 Variation of the frequency ratio for inline and crossflow response (a) as a proportion of dominant high frequency f_{n2}(b) as a proportion of the dominant frequency in-inline WIV response f_w.

The frequency ratio f/f_{n2} shows good agreement with the experiment in crossflow motion. The inline motion, also similar frequency ratio with the crossflow as seen in Figure 9.17 (a). Although the current predictions are smaller in value, the general trend is captured correctly with approximately less than 10% difference. Inline frequency ratio is higher value compared to the crossflow frequency ratio, especially at low Ur range (Ur < 5), when the cylinder starts moving into the “locked-in” regime, which is approximately 15% higher. When $Ur > 6$, the dominant vortex frequencies in both inline and crossflow direction are very similar.

Considering the variation of f_v/f_w , the inline frequency ratio has, in general, lower values, compared to the crossflow frequency ratio. The ratio is also smaller than the one obtained in the experiment except at high reduced velocities area, where ratio of 5 can observed.

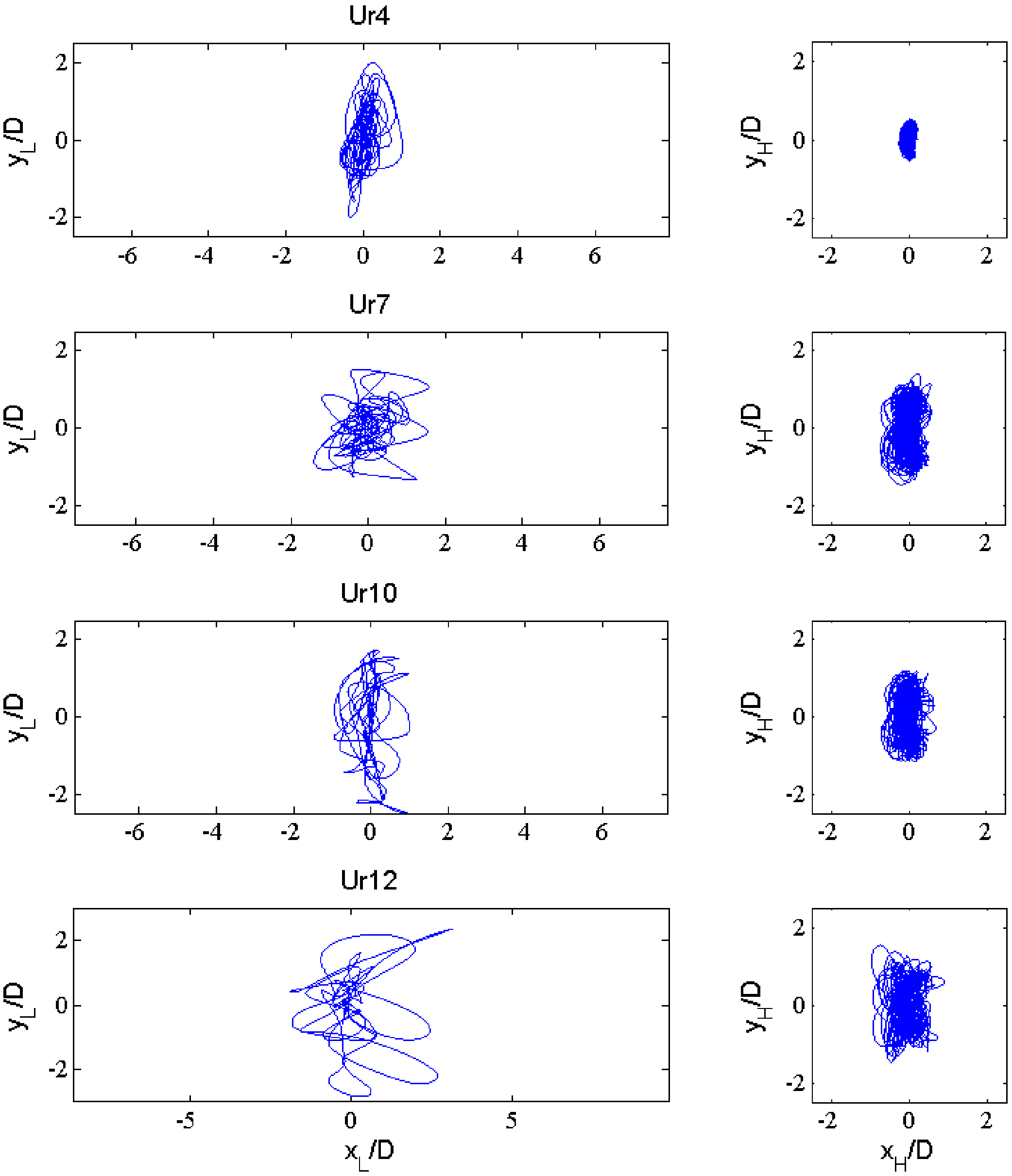

Figure 9.18. Trajectories of high (H) and low (L) frequency components of the downstream cylinder in staggered arrangement L = 5D, B = D at (a) $U/f_{n2}D$ = 4, $U/f_{n1}D$ = 41, (b) 7 ; 72.1, (c) 10; 103, (d) 12; 124

Trajectories of the low and high frequency part of the motion for the downstream cylinder in staggered arrangement (L/D = 5, B/D = 1) are plotted separately in Figure 9.18. For the low frequency components, no obvious trajectory shapes can be recognised. However, at $U/f_{n2}D$ = 7 and 10, an underlying figure of eight shape motion can be recognised and at $U/f_{n2}D$ = 8, the motion is more chaotic.

The low frequency motions appear to be random, and the motion at low frequencies can exceed 2D in some cases showing in the influence of coupling between inline and crossflow motions due to WIV and its combination with VIV. However, as explained in chapter 8, more vortex shedding cycles are required as well as more investigation on WIV trajectories.

9.4. Conclusion

In this chapter, simulations of two cylinders in a staggered arrangement (L=5D, B=D) were numerically carried out to provide results of simultaneous vortex- and wake- induced vibration. The downstream cylinder is elastically mounted with 2 dof in one or both directions whilst the upstream cylinder is stationary. Again, the reduced velocity based on the low natural frequency exceeds 130.

For the 2 dof system, the simulation results are very similar to those of a tandem arrangement in terms of the high frequency crossflow vibration. Low frequency components of the offset case show some differences. However, in general the trend and amplitude of vibration range are similar. The novel 2 dof system shows there are multiple frequencies in the oscillation of the downstream cylinder.

For the 4 dof system, the coupling of inline and crossflow also significantly increase the amplitude of motion, especially the LF components. The staggered arrangement simulation also shows higher inline vibrating amplitude in LF components, with almost double value, peaking at approximately 1.4D. The HF components show similarities in trend and values with the experimental results. The ratio between vortex and wake frequencies is approximately half of the system frequency ratio.

Similar to single cylinder case, the motion of the downstream cylinder changes the drag in both mean and fluctuating components up to 25%. The motion trajectories show in figure of eight shape motion in high frequency components while chaotic mode could be recognised in WIV trajectories.

Although the simulation cannot show very good agreement, the current CFD methods and motion can capture some essential characteristic of FIV such as amplitude, frequency of vibration and the trajectories of the cylinder. The 3D model could improve the current data with more expensive computational turbulence model e.g. LES. However, with current computer capability, it is still a challenge.

Chapter 10 : Conclusions

A series of numerical simulations is carried out in this thesis, by which Vortex Induced Vibration (VIV), Wake Induced Vibration (WIV) and its simultaneous effects were addressed for a circular cylinder. A numerical approach, Computational Fluid Dynamics (CFD), has been used for predictions using 2D Reynolds Averaged Navier Stokes (RANS) method. The best working ranges as well as limitations are identified. The studies have covered:

- The flow around a stationary cylinder and two stationary cylinders in a tandem arrangement.
- A forced oscillating cylinder.
- VIV of a single cylinder at Reynolds number 10,000 modelled as 1 dof and 2 dof systems.
- Vortex and wake induced vibration of the downstream cylinder in a tandem arrangement at the separation L = 5D modelled as 1 dof, 1+1 dof (1 dof crossflow +1 dof inline), 2 dof (crossflow only) and 4 dof (2 dof crossflow + 2 dof inline) systems.
- WIV and VIV of the downstream cylinder in a staggered arrangement at the separation B = D, L = 5D modelled as 2 dof (crossflow) and 4 dof system.

In addition to the concluding remarks in each chapter, a closure of the present work is presented herein. The items below will summarise all findings in this thesis followed by suggestions for future research.

10.1. Summary of Findings

10.1.1. CFD in VIV research

The applications of CFD techniques in modelling flow around cylinders has demonstrated continuous success in past decades. With the development of mathematical models and computational resources, CFD results become more and more feasible for investigating Flow Induced Vibration (FIV) problems, especially VIV and WIV. Today, as VIV problems involved more complex structures or flows, the need for modelling has become more important due to limitations of experiments and the need to provide reasonably good results at low cost.

Studies on flow around fixed circular cylinders were carried out at the subcritical Reynolds number range from 10 to 22,000 and focus on two particular Reynolds numbers 3900 and 10000 (for single cylinder) and 22000 (for two cylinders in a tandem arrangement). Different grid resolutions and turbulence models were tested in the early stage of the thesis. The pros and cons of different turbulence models were identified and analysed and the standard $k-\omega$ model has shown good agreement compared to benchmarks in term of lift and drag coefficients, Strouhal number and pressure distributions. The free stream turbulence dependence of the $k-\omega$ model has been addressed using appropriate input turbulence parameters (I,β) from sensitivity tests and is appropriate for VIV research. The moving dynamic mesh and Finite Difference Method (FDM) methods are used to tackle cylinder vibration problems, which are investigated throughout this thesis. The Fluid Structure Interaction (FSI) coupling problems are solved by application of User Defined Functions.

The present 2D simulations show a reasonably good performance for VIV prediction. It was found that the force coefficients, response amplitudes, vortex patterns and motion frequencies for a single cylinder VIV generally agree well with experimental results for a cylinder with low mass-damping. On the three branches of vibration identified in Chapter 6, the maximum amplitude in the upper branch is approximately 20% lower compared to experimental results.

However, the VIV results using a 2 dof model show very good agreement with the benchmarks. The interesting feature is that the super-upper branch can be captured, even with very modest computational cost using 2D RANS. The coupling in X-Y motion can increase the maximum amplitude to nearly double of the 1 dof model and the 2T vortex shedding pattern could be observed in the region of maximum amplitude.

Another interesting finding related to a 2 dof single cylinder VIV simulation is that the transition region can be observed. At $8 \leq Ur \leq 9$, the cylinder oscillates with two different amplitudes, starting with high amplitude of motion and changing to low amplitude at one reduced velocity. The transition region in lift and drag coefficients can also be recognised. A few different motion trajectories including a figure of eight shape, C shape can be observed in a range of reduced velocities.

The availability of computational resources remains an important factor in deciding the quality of VIV simulations. This is important when a high number of vortex shedding cycles is required and for high Reynolds numbers. Increases in Reynolds number require a much denser grid with a smaller first cell height. This significantly increases the computational cost. Due to the needs of current research, this simulations reported have focused on Re range smaller than 33,000.

10.1.2. A downstream cylinder in VIV and WIV response analysis

Based on the investigation undertaken in this thesis, the following points were noted:

- The WIV amplitude increases with the increasing reduced velocity as well as Reynolds number without any limitation. The increase in mass damping $m^*\zeta$ could not reduce this trend.
- Coupling between motions in 2-direction (4 dof model) could increase the crossflow amplitude of motion, up to twice of 1-direction (crossflow) motion only. This trend appears in both studies on a 1+1 dof downstream cylinder in a tandem arrangement and a 2 (1+1) dof single cylinder.
- The inline vibration of the downstream cylinder in the wake of the upstream one is much larger (up to 1D) compared to a single cylinder case (approximately 0.4D). Instead of three branches of vibration amplitude, the downstream cylinder using 1+1 dof system presented only one transition area where the amplitude of the motion increased dramatically at low reduced velocities ($Ur \approx 5$).
- The downstream cylinder WIV and VIV are in harmonic form at low reduced velocities, where the inline motion is reasonably small. The C-shape motion trajectories can be observed, similar to a single cylinder case. However, VIV and WIV responses become non-harmonic at higher reduced velocities, e.g. Ur >10 showing chaotic motion. As VIV and WIV responses become non-harmonic, calculations of force coefficients were not based on the harmonic assumption, widely applied in the literature.
- The upstream cylinder at L/D = 5 acts like an isolated single cylinder that is not affected by the motion of the downstream cylinder
- Even with a simplified setup with low computational cost, the 2D simulation shows its use in research on 2 dof VIV and the effects of VIV and WIV on the downstream cylinder. They have produced similar dynamic responses with benchmarks at the sub-critical Re with low $m^*\zeta$, able to capture high amplitude of motion in tandem arrangements, motion trajectories and vortex shedding patterns.

10.1.3. Cylinder with 2 dof elastic support in each direction

In addition to 1 dof elastic support system used in the literature, a novel numerical simulation on 2 dof (Y direction) and 4 dof (X and Y directions) elastic support was carried out using 2D simulation to study simultaneous vortex- and wake- induced vibrations. Two arrangement were modelled, namely tandem and staggered. The following observations can be made:

For cylinders in a tandem arrangement:

- The system is able to move in more than two dominant frequencies, in which the low frequencies relate to WIV while high frequencies relate to VIV. The WIV in the present research resulted in a large vibration amplitude that is comparable with VIV. Combination of WIV and VIV could increase the maximum amplitude more than 2D.

- The coupling effect in two directions motion increases the peak amplitude up to 30% compared to the system limited in crossflow direction only. The simulations show reasonably good agreement in term of high frequency (HF) components. Compared to the experimental results, the amplitude in the inline direction is over-estimated. This trend is also recorded for 1 dof – 1 direction system, where the inline vibration is reasonably high.
- The motion is non-harmonic and no clear motion trajectories could be discerned. The downstream cylinder was moving in disorganised manner.
- The lift and drag coefficients do not show any significant changes even when the cylinder is moving in 1 or 2 directions at the separation more than L = 5D.

For the downstream cylinder in a staggered arrangement

- The dynamic response of the downstream cylinder in 2 dof system (crossflow direction) is very similar to a tandem arrangement case, at low mass damping ratio. The coupling between inline and crossflow motion (4 dof) also increases the amplitude of motion up to 30% for the high frequency component and almost double for low frequency (LF) in the crossflow direction. The inline motion is remarkably high, exceeding crossflow amplitudes at some reduced velocities. The low frequency inline amplitude of motion for a staggered arrangement is up to 1.5D.
- No particular motion trajectories were recorded; however, in the HF component, a figure of eight shape motion can be seen at some reduced velocities. To find out more about LF motion trajectories of the cylinder, more vortex shedding cycles would be required.

In both cases, the frequency ratio between f_w and f_v did not match the pre-defined ratio of 10.3. The study showed the ratio was about 5. f_v was recorded at expected frequencies ratio, around 1 – 1.5, however f_w is typically at a higher value compared to low natural frequency. Nevertheless, the experiment also showed higher value in f_w.

Some differences between the experiments and the current simulation were due to differences in high level of turbulence. High turbulence simulation at free stream is still a challenge for mathematical models for RANS, LES, DES, although good results in VIV simulation were achieved with low levels of turbulence. The 3D effects also influence VIV and WIV simulation results. However, with the current model and the number of time steps and computational cost required 3D simulation is not feasible.

10.2. Future considerations

So far, the studies in this thesis were at the sub-critical Reynolds numbers < 35000. The main difficulty for high Reynolds number simulations is the lack of numerical or experimental benchmark studies. Actually, most data available on VIV response are limited to lower area of sub-critical regime, approximately 23,000. The research at higher Reynolds numbers should be carried out to investigate the dynamic behaviour of cylinders.

The current novel simulations are carried out using 2D modelling, due to limitation of computational cost and high number of vortex shedding cycles required. Although 2D simulations have shown a reasonably good agreement for investigating VIV and simultaneous WIV and VIV, 3D simulation (LES, DNS) could be used further advances development in computational resources. The simulation have to “scarify” the 3D effect to balance the present computational resources; however, that could improve the accuracy of the results with the application of more expensive 3D computational source.

In addition, the fully 3D FSI between ANSYS Fluent and Transient System, an ANSYS FEM model, can be carried out to simulate marine riser VIV and the downstream cylinder VIV and WIV, to obtain riser deflections by simultaneous VIV and WIV will be defined.

The effect of offset could be explored with a different B/D ratio, from B = 1.5D up to B = 5D. In the current simulation, only an offset B = D was investigated due to the time constraint of the research, however, it would be interesting if the multi-degree of freedom system can be applied over a range of different offset.

Finally, if CFD can provide the answers to VIV problems for the cylinder in VIV and downstream cylinder in a tandem arrangement and a staggered arrangement at L = 5D, it will be very interesting to explore the capability of CFD in simulating FIV for a closer separations, especially at drag “critical” range L = 3.25D . In addition, the cylinders in circular and square configurations can be studied out to explore the effect of FIV on a series of cylinders. FIV of tubes inside the tube bundle adds further complexity to CFD and is another interesting area to consider for further research.

Appendices

Appendix A Velocity used to achieve different Reynolds number

Table 10.1. Velocity in different Reynolds number

D (m)	Density (kg/m^3)	Viscosity (kg/ms)	Reynolds number	Velocity (m/s)
1	1.225	1.79E-05	150	0.002192
1	1.225	1.79E-05	200	0.002922
1	1.225	1.79E-05	400	0.005845
1	1.225	1.79E-05	700	0.010229
1	1.225	1.79E-05	1000	0.014612
1	1.225	1.79E-05	3900	0.056988
1	1.225	1.79E-05	10000	0.146122
1	1.225	1.79E-05	20000	0.292245

Appendix B Forced oscillation UDF at non-dimensional frequency of 0.18

```
#include "udf.h"

static real v_prev = 0.0;

FILE *fout;

DEFINE_CG_MOTION(osc_sinusoidal,dt,vel,omega,time,dtime)
{

  Thread *t;
  Domain *d = Get_Domain(1); /*pointer to the domain*/
  real x_cg[3], force[3], moment[3]; /*Position, force, moment*/
  real f = 0.0263; /*Defined frequency*/
  real amp = 0.3; /*Defined amplitude*/

  int i;

  t = DT_THREAD(dt);
  for(i=0;i<3;i++)
    x_cg[i]=DT_CG(dt)[i];

  Compute_Force_And_Moment(d, t, x_cg, force, moment, TRUE);

  vel[0] = 0.0;
  vel[1] = 2.*M_PI*amp*f*cos(2.*M_PI*f*time); /*Equation of motion via velocity*/

  fout = fopen("results.txt", "a"); /*open file*/
  /*Write data into file*/
  fprintf(fout, "%g %g \n", time, DT_CG(dt)[1]);
  fclose(fout);

}
```

Appendix C User Defined Functions

The code below is used to solving the cylinder’s equation model. The code communicates with ANSYS Fluent in order to implement flow-excited vibrations. Some of values was changed to meet the expected reduced velocity and input parameters.

C.1 SDOF UDF for 1dof system with $m^* = 2.4$

```
#include "udf.h"
#include "dynamesh_tools.h"
#include "unsteady.h"

FILE *fout; /*Write the output file*/
static real v_prev; /*Velocity in previous time step*/

DEFINE_SDOF_PROPERTIES(stage, prop, dt, time, dtime)
{
  Thread *t;
  Domain *d = Get_Domain(1);
  real x_cg[3], force[3],moment[3];
  real cg; /*Centre of gravity position*/
  real vel; /*Cylinder velocity*/
  real Fy; /*Lift force*/
  real mass = 2.31; /*Cylinder mass*/
  real fn = 0.02922; /*System frequency*/
  real wn = 2*M_PI*fn; /*System angular velocity*/
  real z = 0.005417; /*Damping coefficient*/
  real k = mass*wn*wn; /*System stiffness*/
  real c = 2*mass*wn*z; /*System damping*/

  /*get the thread pointer for which this motion is defined */
  t = DT_THREAD(dt);

      prop[SDOF_MASS] = 2.31; /*system mass of the 6 dof*/

      /*limit 5 dofs from 6 dof Macro*/
      prop[SDOF_ZERO_TRANS_X] = TRUE;
      prop[SDOF_ZERO_TRANS_Z] = TRUE;
      prop[SDOF_ZERO_ROT_X] = TRUE;
      prop[SDOF_ZERO_ROT_Y] = TRUE;
      prop[SDOF_ZERO_ROT_Z] = TRUE;

      cg = DT_CG(dt)[1];
      vel = DT_VEL_CG(dt)[1];

      prop[SDOF_LOAD_F_Y] = -k*cg - vel*c;

      fout = fopen("results.txt", "a"); /*Open file*/

      /*Write data into file*/
      fprintf(fout, "%g %g %g \n", time, DT_CG(dt)[1], DT_VEL_CG(dt)[1]);
      fclose(fout);

      }
```

C.2 FDM UDF for a single cylinder with the 2dof system at Ur = 6

```
#include "udf.h"
#include "stdio.h"
#include "stdlib.h"
#include "sg_mem.h"
#include "dynamesh_tools.h"
#include "unsteady.h"

#define mass 2.31
#define md 0.962
#define fn 0.02435
#define z 0.005417
#define ZONE_ID1 10

static real v_prev1, v_prev0;
static int i;
static real Fx, Fy;
static real wn,k,c,dv;

FILE *fout, *fout1;

DEFINE_ON_DEMAND(vel)
{
  Thread *t;
  Dynamic_Thread *dt;
  Domain *d = Get_Domain(1);

  real vel[3], x_cg[3], force[3], moment[3];
  real time, dtime;
  real X[100000];
  real Y[100000];
  wn = 2*M_PI*fn;
  k = (mass+md)*wn*wn;
  c = 2*(mass+md)*wn*z;
  t = Lookup_Thread(d, ZONE_ID1);

  Compute_Force_And_Moment(d, t, x_cg, force, moment, TRUE);
  Fx = force[0]; /* force[0] in x direction*/
  Fy = force[1];

  /* compute the updating position*/

  i = N_TIME;  /* set i = time step number*/

  X[0]=0; X[1]=0;

  dtime = CURRENT_TIMESTEP; /*Set dtime = timestep*/
  time = CURRENT_TIME; /*time = current time*/

  X[i+1] = (Fy - X[i-1]*(mass/(dtime*dtime) - c/(2*dtime)) - X[i]*(-
2*mass/(dtime*dtime) + k))/(mass/(dtime*dtime) + c/(2*dtime)); /* calculate position
by FDM in Y direction*/
  Y[i+1] = (Fx - Y[i-1]*(mass/(dtime*dtime) - c/(2*dtime)) - Y[i]*(-
2*mass/(dtime*dtime) + k))/(mass/(dtime*dtime) + c/(2*dtime)); /* calculate position
by FDM in X direction*/

  v_prev1=(X[i+1]-X[i])/dtime; /*inline velocity*/
  v_prev0=(Y[i+1]-Y[i])/dtime; /*crossflow velocity*/

}
```

```
/* Update velocity using CG_MOTION Macro*/

DEFINE_CG_MOTION(cylinder, dt, vel, omega, time, dtime)
{
  vel[1] = v_prev1; /*update crossflow velocity*/
  vel[0] = v_prev0; /*update inline velocity*/
  fout = fopen("results.txt", "a");
  fprintf(fout, "%g %g %g \n", time, DT_CG(dt)[1], DT_CG(dt)[0]);
  fclose(fout);
}
```

C.3 FDM UDF for a downstream cylinder with the 4dof system at Ur = 6

```
#include "udf.h"
#include "stdio.h"
#include "stdlib.h"
#include "sg_mem.h"
#include "dynamesh_tools.h"
#include "unsteady.h"

#define mr 0.87
#define md 0.03848451 /*add mass*/
#define m1 0.034768045 /*intermediate mass*/
#define m2 0.033481524 /*cylinder mass*/
#define k1 0.019135886 /*spring stiffness 1*/
#define k2 0.498008676 /*spring stiffness 2*/
#define k3 0
#define c3 0
#define f1 0.084 /*natural frequency 1*/
#define f2 0.864 /*natural frequency 2*/
#define z 0.029 /*damping ratio*/
#define w1 0.5278
#define w2 5.428
#define c1 0.0015542092 /*damping 1*/
#define c2 0.0015542092 /*damping 2*/
#define ZONE_ID1 9

static real v_prev, v_prev_x; /*previous time step velocity*/
static int i;
static real Fx, Fy; /*Lift and drag force*/
static real dv; /*velocity change*/

FILE *fout, *fout1;

DEFINE_ON_DEMAND(vel)
{
  Thread *t;
  Dynamic_Thread *dt;
  Domain *d = Get_Domain(1);

  real vel[3], x_cg[3], force[3], moment[3];
  real time, dtime, detA, a;
  real X1[300000], X2[300000], A1, B1;
  real X1x[300000], X2x[300000], Ax1, Bx1;

  real mass[2][2] = { { m1, 0},
                       { 0, m2 }}; /*mass matrix*/
  real damping[2][2] = { { c1+c2, -c2},
                       { -c2, c2+c3 }}; /*damping matrix*/
  real stiff[2][2] = { { k1+k2, -k2},
                       { -k2, k2+k3 }}; /*stiffness matrix*/
  real A[2][2],B[2][2],C[2][2];

  int m, n;
  dtime = CURRENT_TIMESTEP; /*Set dtime = timestep*/
  time = CURRENT_TIME; /*time = current time*/

  for ( m = 0 ; m < 2 ; m++ )
      for ( n = 0 ; n < 2 ; n++ )
         A[m][n] = (1/(dtime*dtime))*mass[m][n] + (1/(2*dtime))*damping[m][n];
  for ( m = 0 ; m < 2 ; m++ )
      for ( n = 0 ; n < 2 ; n++ )
         B[m][n] = stiff[m][n] - (2/(dtime*dtime))*mass[m][n];
  for ( m = 0 ; m < 2 ; m++ )
```

```
      for ( n = 0 ; n < 2 ; n++ )
         C[m][n] = (1/(dtime*dtime))*mass[m][n] - (1/(2*dtime))*damping[m][n];

  detA = A[0][0]*A[1][1] - A[0][1]*A[1][0];

  t = Lookup_Thread(d, ZONE_ID1); /*Look up the dynamic zone*/

  i = N_TIME;

  Compute_Force_And_Moment(d, t, x_cg, force, moment, TRUE);

  if (X2x[i] > 0.1) {a = 0.250195599;}
     else {a = 0.105345516;}

  Fx = force[0] - a; /* force[0] in x direction*/

  Fy = force[1]; /* force[1] in y direction*/

  /* compute the updating position*/

    /* set i = time step number*/

  X1[0]=0; X1[1]=0; X2[0]=0; X2[1]=0;

       A1 = (-(B[0][0]*X1[i]+B[0][1]*X2[i])-(C[0][0]*X1[i-1]+C[0][1]*X2[i-1])); /*
A1 Value*/
       B1 = (-(B[1][0]*X1[i]+B[1][1]*X2[i])-(C[1][0]*X1[i-1]+C[1][1]*X2[i-1]));/* B1
Value*/

       X1[i+1] = (1/detA)*((-(B[0][0]*X1[i]+B[0][1]*X2[i])-(C[0][0]*X1[i-
1]+C[0][1]*X2[i-1]))*A[1][1] - (Fy + (-(B[1][0]*X1[i]+B[1][1]*X2[i])-(C[1][0]*X1[i-
1]+C[1][1]*X2[i-1])))*A[0][1]);  /* calculate X1_i+1*/
       X2[i+1] = (1/detA)*(-(-(B[0][0]*X1[i]+B[0][1]*X2[i])-(C[0][0]*X1[i-
1]+C[0][1]*X2[i-1]))*A[1][0] + (Fy + (-(B[1][0]*X1[i]+B[1][1]*X2[i])-(C[1][0]*X1[i-
1]+C[1][1]*X2[i-1])))*A[0][0]); /* calculate X2_i+1*/

        X1x[i+1] = (1/detA)*((-(B[0][0]*X1x[i]+B[0][1]*X2x[i])-(C[0][0]*X1x[i-
1]+C[0][1]*X2x[i-1]))*A[1][1] - (Fx + (-(B[1][0]*X1x[i]+B[1][1]*X2x[i])-
(C[1][0]*X1x[i-1]+C[1][1]*X2x[i-1])))*A[0][1]);  /* calculate X1x_i+1*/
       X2x[i+1] = (1/detA)*(-(-(B[0][0]*X1x[i]+B[0][1]*X2x[i])-(C[0][0]*X1x[i-
1]+C[0][1]*X2x[i-1]))*A[1][0] + (Fx + (-(B[1][0]*X1x[i]+B[1][1]*X2x[i])-
(C[1][0]*X1x[i-1]+C[1][1]*X2x[i-1])))*A[0][0]); /* calculate X2x_i+1*/

  v_prev=(X2[i+1]-X2[i])/dtime;
  v_prev_x=(X2x[i+1]-X2x[i])/dtime;


  fout1 = fopen("demand.txt", "a");
  fprintf(fout1, "%g %g %g\n", time, X2[i], X2x[i]);
  fclose(fout1);

}

/*update centre of gravity position*/
DEFINE_CG_MOTION(cylinder, dt, vel, omega, time, dtime)
{
  vel[1] = v_prev;
  vel[0] = v_prev_x;
  fout = fopen("results.txt", "a");
  fprintf(fout, "%g %g %g \n", time, DT_CG(dt)[1], DT_CG(dt)[0]);
  fclose(fout);
}
```

Appendix D Meshes Validation

D.1 Comparison C_d and C_l produced by the old mesh and the new mesh (for 2 dof) for a single stationary cylinder.

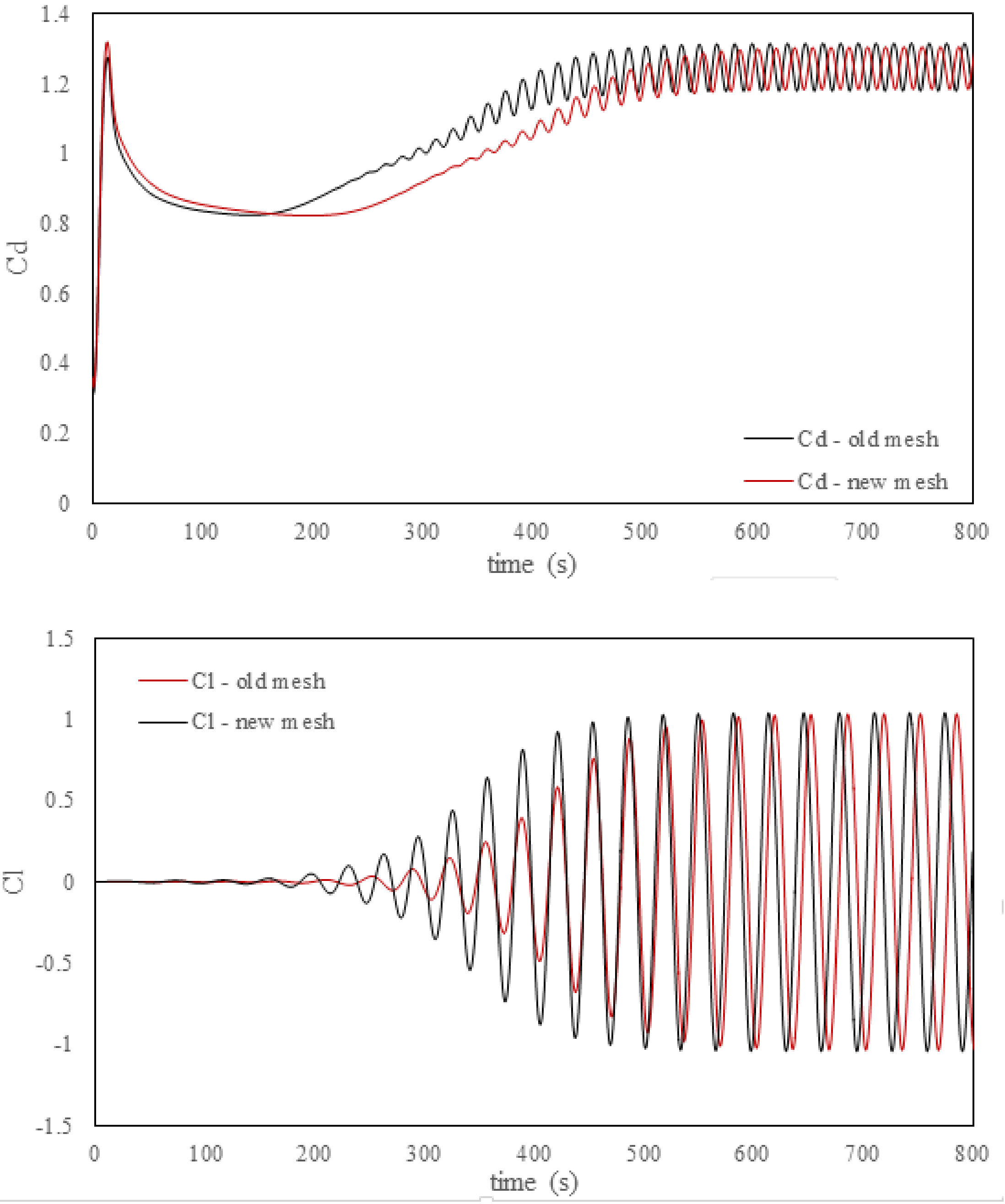

Figure 10.1. Comparisons in C_d and C_l between old grid and new grid for a single cylinder case.

D.2 Comparison C_d and C_l produced by the old mesh and the new mesh for cylinders in a tandem arrangement.

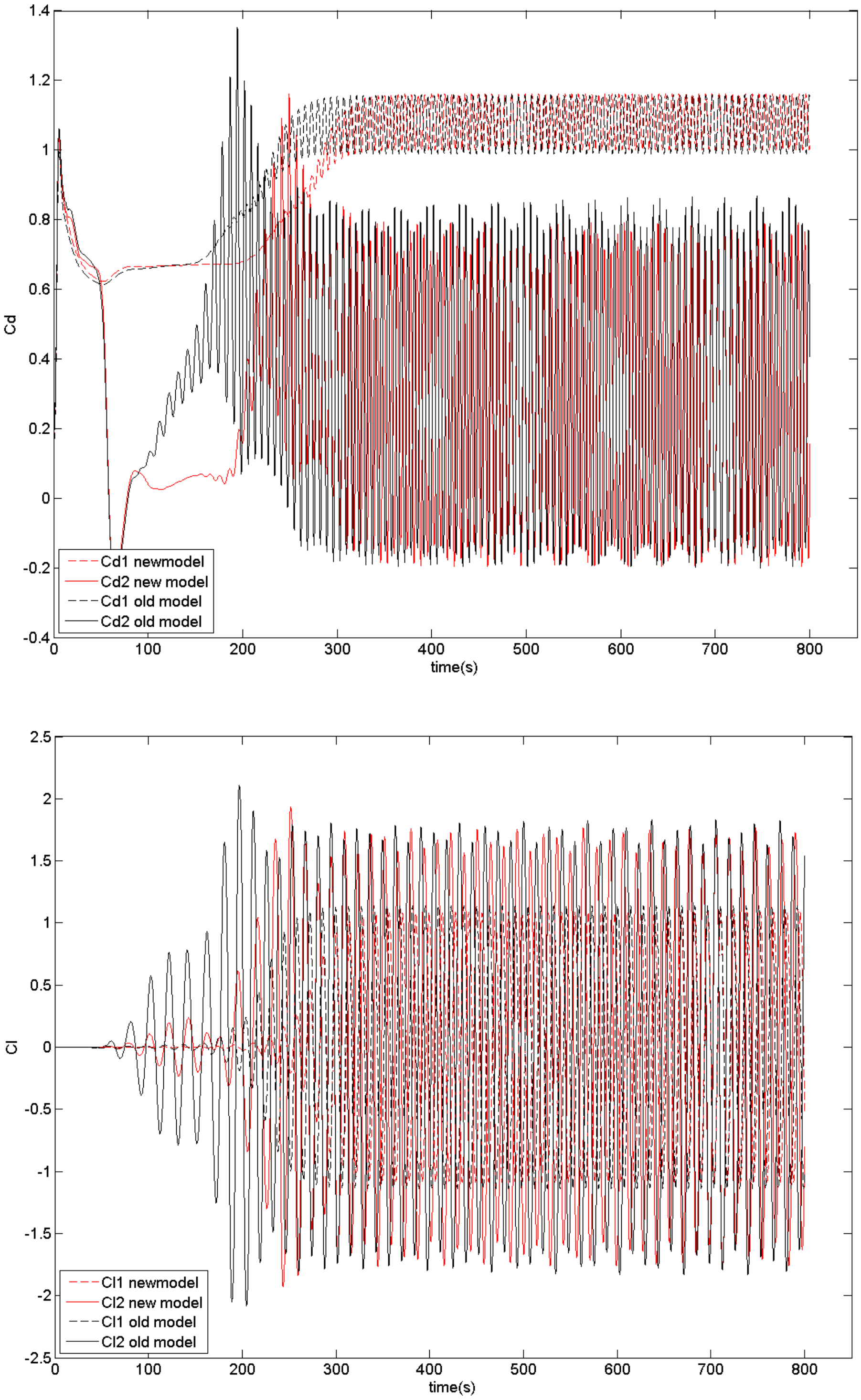

Figure 10.2: Comparison between old and new model in lift and drag coefficients.

Appendix E Compare the output of FDM and SDOF

To validate the accuracy of the FDM method, comparisons between FDM and SDOF methods were compared based on:

- Lift coefficient
- Drag coefficient
- Amplitude of motion due to VIV

The FDM was conducted with good agreement compare with previous SDOF method. As we can see from below graph, the lift, drag and amplitude of motion produced at Ur = 5 was nearly the same.

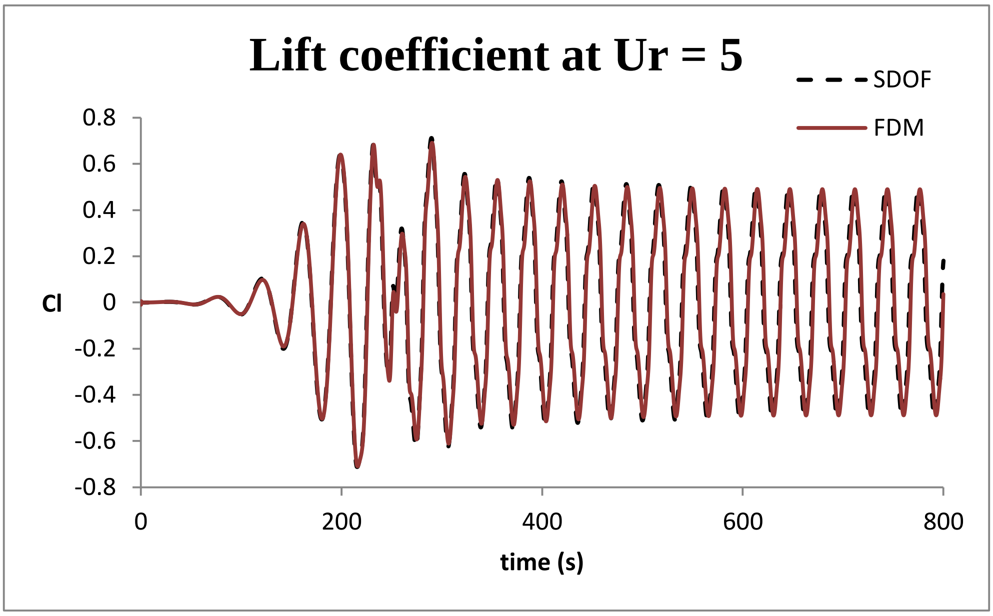

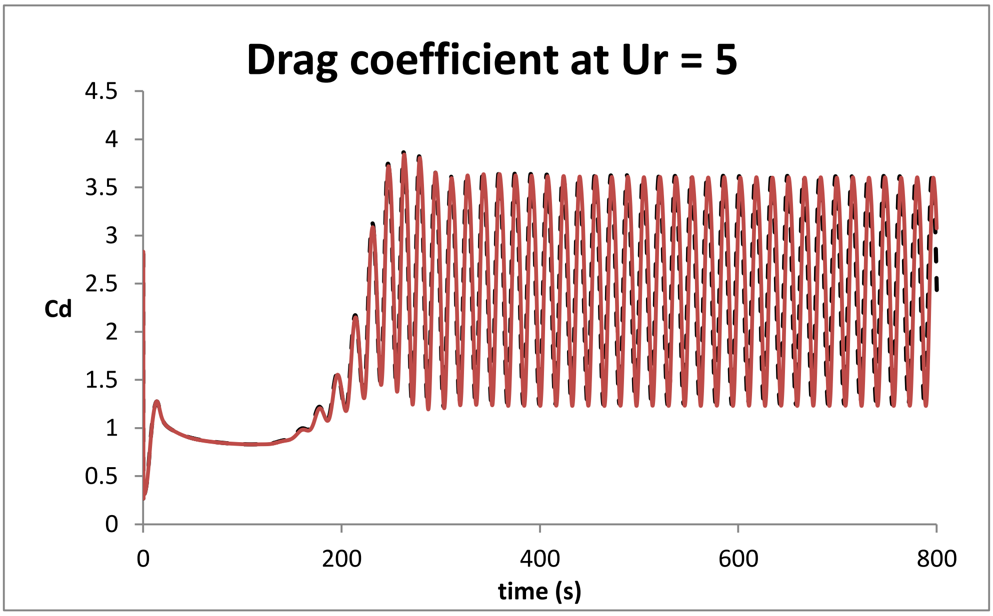

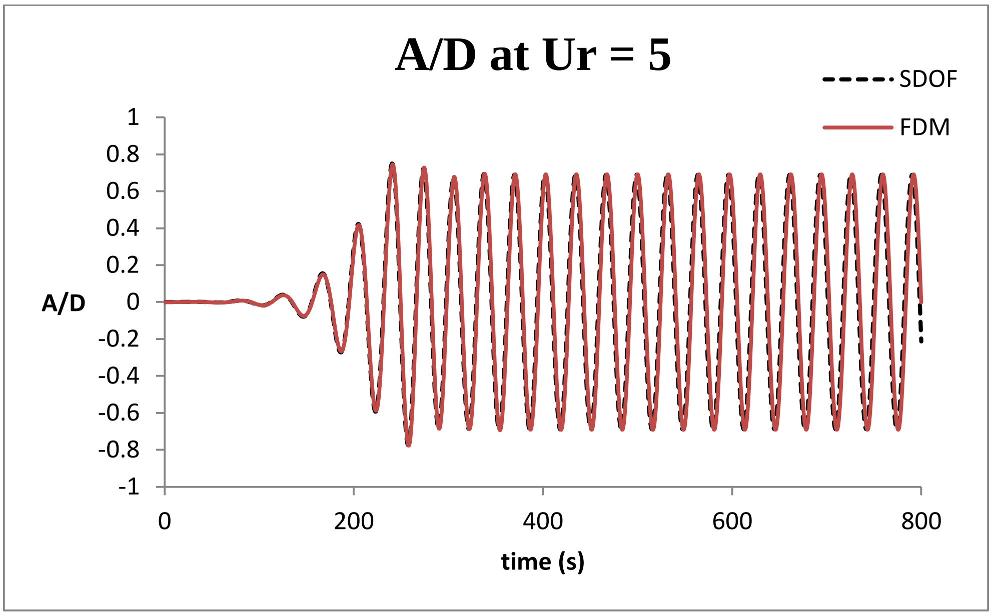

Figure 10.3. Comparison between lift, drag coefficient and amplitude of motion produced by SDOF and FDM

To ensure the FDM code could produce good results for a Ur range, the simulation had been carried out on single cylinder VIV with $3 \leq Ur \leq 16$, and compare to SDOF results using exactly similar setup. The results show good agreement of two methods with $m^* = 2.4$, at the same $m^*\zeta$ ratio.

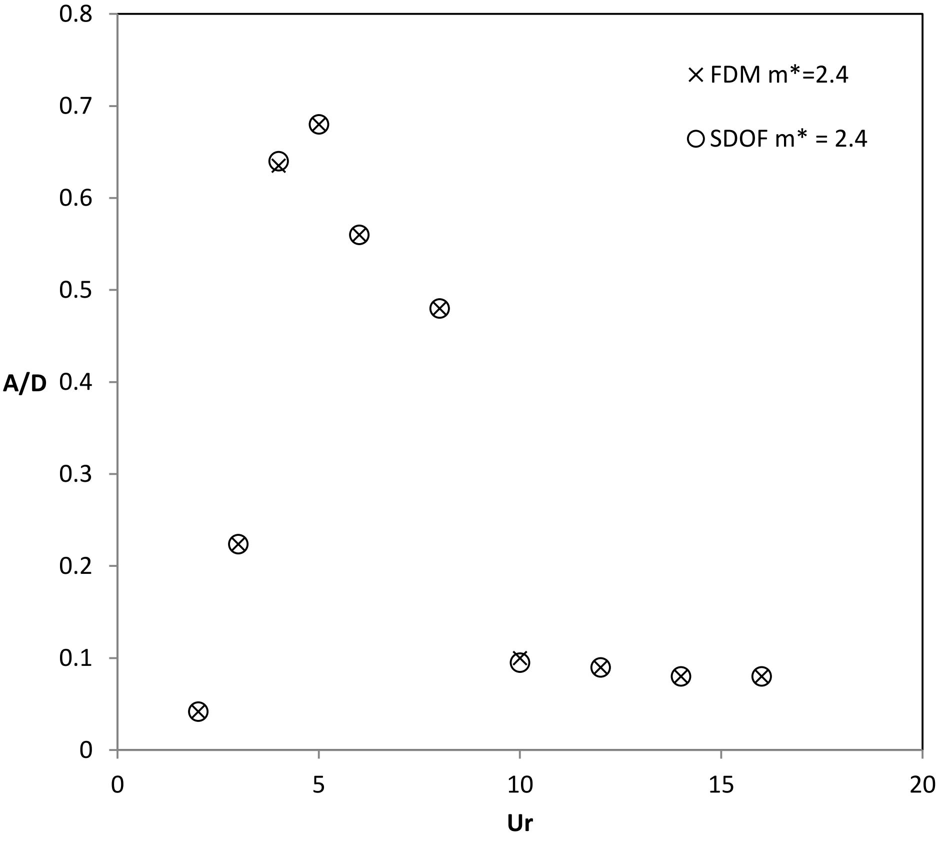

Figure 10.4. Amplitude of motion in a range of Ur produced by FDM and SDOF at $m^* = 2.4$

Appendix F The Free Decay test

To determine the damping for the 2 dof system, the free decay test was carried out. The test was programmed using C code. The 2 dof system was driven by a forced oscillation initially and free oscillating after approximately 260 s. The properties of the testing system are used from Table 8.3 in Chapter 8.3, with $c_1 = c_2 = 0.001554$.

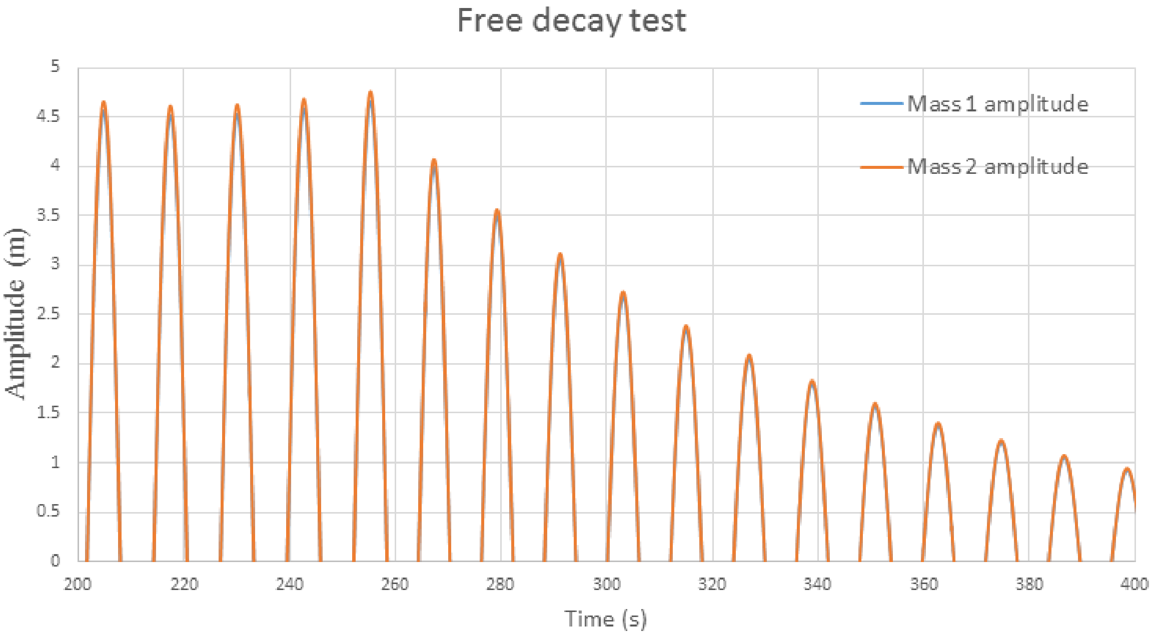

Figure 10.5. Free decay test for the 2 dof system.

From Figure 10.5, for two success amplitude at 280 and 292s, the oscillating of mass 2 was x_1 =3.6 and $x_2 = 3$ respectively.

The amplitude reduction factor (ARF) $\ln(\frac{x_1}{x_2})$ can be defined as:

$$\ln\left(\frac{x_1}{x_2}\right) = \ln\left(\frac{3.6}{3}\right) = 0.1823$$

The damping coefficient of the system can be defined as (Dunn, 2015):

$$\zeta = \frac{ARF}{\sqrt{4\pi^2 + ARF^2}} = 0.029$$

With the damping values $c_1 = c_2 = 0.001544$, the system produced the same damping coefficient with the experimental result in the free decay test. Hence, values of damping $c_1 = c_2 = 0.001544$ will be used for the 2 dof system.

List of References

ACHENBACH, E. & HEINECKE, E. 1981. On vortex shedding from smooth and rough cylinders in the range of Reynolds numbers 6×103 to 5×106. *Journal of Fluid Mechanics*, 239-251.

AL-JAMAL, H. & DALTON, C. 2004. Vortex induced vibrations using Large Eddy Simulation at a moderate Reynolds number. *Journal of Fluids and Structures,* 19, 73-92.

ANDERSON, J. D. 1995. *Computational Fluid Dynamics, The basics with applications*, McGraw-Hill.

ANSYS 2011. Ansys Fluent Manual, release 14.0.

ASSI, G. R. S., BEARMAN, P. W. & MENEGHINI, J. R. 2010. On the wake-induced vibration of tandem circular cylinders: the vortex interaction excitation mechanism. *Journal of Fluid Mechanics,* 661, 365-401.

BAKKER, A. 2012. *The Colorful Fluid Mixing Gallery* [Online].

BARANYI, L., HUYNH, K. & MUREITHI, N. 2010. *Dynamics of flow around a cylinder oscillating in-line for low Reynolds numbers,* New York, Amer Soc Mechanical Engineers.

BARANYI, L., SZABO, S., BOLLO, B. & BORDAS, R. 2009. Analysis of low Reynolds number flow around a heated circular cylinder. *Journal of Mechanical Science and Technology,* 23, 1829-1834.

BARTH, T. J. & JESPERSEN, D. 1989. The design and application of upwind schemes on unstructured meshes. *Technical Report AIAA-89-0366,* AIAA 27th Aerospace Sciences Meeting, Reno, Nevada.

BEARMAN, P. W. 1984. Vortex Shedding from Oscillating Bluff Bodies. *Annual Review of Fluid Mechanics,* 16, 195-222.

BEARMAN, P. W. & WADCOCK, A. J. 1973. The interaction between a pair of circular cylinders normal to a stream. *Journal of Fluid Mechanics,* 61, 499-511.

BEARMAN, P. W. & ZDRAVKOVICH, M.M 1978. Flow around a circular cylinder near a plane boundary. *Journal of Fluid Mechanics,* 89.

BISHOP, R. E. D. & HASSAN, A. Y. 1963. The Lift and Drag Forces on a Circular Cylinder in a Flowing Fluid. *Proc. R. Soc.Lond. A 277:51-75*.

BLEVINS, R. D. 2001. *Flow induced vibration,* New York, Van Nostrand Reinhold Co.

BREDBERG, J. 2000. On the Wall Boundary Condition for Turbulence Models. Goteborg, Sweden: Department of Thermo and Fluid Dynamics, Chalmers University of Technology.

BREUER, M. 1998. Large eddy simulation of the subcritical flow past a circular cylinder: numerical and modeling aspects. *International Journal for Numerical Methods in Fluids,* 28, 1281-1302.

BYRD, R. C., DONALD J. MILLER & WIESE, S. M. 2014. Cost Estimating for Offshore Oil & Gas Facility Decommissioning. *AACE International technical paper*.

CARBERRY, J., SHERIDAN, J. & ROCKWELL, D. 2005. Controlled oscillations of a cylinder: forces and wake modes. *Journal of Fluid Mechanics,* 538, 31-69.

CATALANO, P., WANG, M., IACCARINO, G. & MOIN, P. 2003. Numerical simulation of the flow around a circular cylinder at high Reynolds numbers. *International Journal of Heat and Fluid Flow,* 24, 463-469.

CHAPLIN, J. R. & BATTEN, W. M. J. 2014. Simultaneous Wake- and Vortex-Induced Vibrations of a Cylinder With Two Degrees of Freedom in Each Direction *Journal of offshore mechanics and arctic engineering - Transaction to Asme,* 136.

CHAPLIN, J. R., BEARMAN, P. W., HUERA HUARTE, F. J. & PATTENDEN, R. J. 2005. Laboratory measurements of vortex-induced vibrations of a vertical tension riser in a stepped current. *Journal of Fluids and Structures,* 21**,** 3-24.

CHEN, C. F. & BALLENGE, D. B. 1971. Vortex shedding from circular cylinder in an oscillating freestream. *Aiaa Journal,* 9**,** 340-&.

CHEN, H.-C., CHEN, C.-R. & S.MERCIER, R. 2006. CFD Simulation of Riser VIV.

CONSTANTINIDES, Y. & OAKLEY, O. H. 2006. Numerical prediction of bare and straked cylinder VIV. *25th International Conference on Offshore Mechanics and Arctic Engineering.*

CONSULTANTS, W. A. 2006. Best practice guildlines for marine applications of computational fluid dynamics. Imperial College of Science & Technology.

COURANT, R. 1943. Variational methods for the solution of problems of equilibrium and vibrations. *Bulletin of the American Mathematical Society,* 49**,** 1-23.

COURANT, R., FRIEDRICHS, K. & LEWY, H. 1928. Über die partiellen Differenzengleichungen der mathematischen Physik. *Mathematische Annalen* 100**,** 32-74.

CUI, Z., ZHAO, M. & TENG, B. 2014. Vortex-induced vibration of two elastically coupled cylinders in side-by-side arrangement. *Journal of Fluids and Structures,* 44**,** 270-291.

DEHKORDI, B. G., MOGHADDAM, H. S. & JAFARI, H. H. 2011. Numerical simulation of flow over two circular cylinders in tandem arrangement. *Journal of Hydrodynamics, Ser. B,* 23**,** 114-126.

DERAKHSHANDEH, J. F., ARJOMANDI, M., DALLY, B. & CAZZOLATO, B. 2014. The effect of arrangement of two circular cylinders on the maximum efficiency of Vortex-Induced Vibration power using a Scale-Adaptive Simulation model. *Journal of Fluids and Structures,* 49**,** 654-666.

DONG, S. & KARNIADAKIS, G. E. 2005. DNS of flow past a stationary and oscillating cylinder at Re = 10000. *Journal of Fluids and Structures,* 20**,** 519-531.

DUNN, D. J. 2015. *Damped Vibration* [Online].

ELMILIGUI, A., ABDOL-HAMID, K. S., MASSEY, S. J. & PAO, S. P. 2010. Numerical Study of Flow Past Circular Cylinder Using Hybrid Turbulence Formulations. *Journal of Aircraft,* 47**,** 434-440.

FANG, Y. Y. & HAN, Z. L. 2011. Numerical experimental research on the hydrodynamic performance of flow around a three dimensional circular cylinder. *In:* ZHOU, X. J. (ed.) *Advances in Civil Engineering, Pts 1-4.* Stafa-Zurich: Trans Tech Publications Ltd.

FENG , C. C. 1968. The measurement of vortex induced effects in flow past a stationary and oscillating circular and D-section cylinders. University of British Columbia: Victoria , British Columbia , Canada.

FERGIZER, J. H. & PERIC, M. 1997. *Computational Methods for Fluid Dynamics,* Berlin, Germany, Springer.

FUJARRA, A. L. C., MENEGHINI, J.R., FRANCISS, R., FRANZINI, G.R.,KORKISCHKO, I. 2007. Experimental Investigation of Vortex-Induced Vibration on an Inclined Circular Cylinder. *ASME Conference Proceedings.*

GERMAIN, G., GAURIER, B., LE BOULLUEC, M., FONTAINE, E. & CAPUL, J. 2006. Vortex and Wake Effects on Closely Spaced Marine Risers. *ASME Conference Proceedings.* ASME.

GERMANO, M., PIOMELLI, U., MOIN, P. & CABOT, W. H. 1991. A dynamic sub-grid scale eddy viscosity model. *Physics of Fluids***,** 1760-1765.

GOPALKRISHNAN, R. 1993. *Vortex-induced forces on oscillating bluff cylinders.* PhD, Massachusetts Institute of Technology.

GOVARDHAN, R. & WILIAMSON, C. H. K. 2000. Modes of vortex formation and frequency response of a freely vibrating cylinder. *Journal of Fluid Mechanics,* 420**,** 85-130.

GOVARDHAN, R. N. & WILLIAMSON, C. 2006. Defining the 'modified Griffin plot' in vortex-induced vibration: revealing the effect of Reynolds number using controlled damping. *Journal of Fluid Mechanics,* 561**,** 147-180.

GRID-ARENDAL 2014. Worldwide progression of water depth capabilities for offshore drilling and production (as of March 2011).

GUILMINEAU, E. & QUEUTEY, P. 2004. Numerical simulation of vortex-induced vibration of a circular cylinder with low mass-damping in a turbulent flow. *Journal of Fluids and Structures,* 19**,** 449-466.

HUERA-HUARTE, F. J. & GHARIB, M. 2011a. Flow-induced vibrations of a side-by-side arrangement of two flexible circular cylinders. *Journal of Fluids and Structures,* 27**,** 354-366.

HUERA-HUARTE, F. J. & GHARIB, M. 2011b. Vortex- and wake-induced vibrations of a tandem arrangement of two flexible circular cylinders with far wake interference. *Journal of Fluids and Structures,* 27**,** 824-828.

IGARASHI, T. 1984. Characteristics of the flow around two circular cylinders arranged in tandem 2nd report: unique phenomenon at small spacing. *Bulletin of JSME,* 27**,** 2380–2387.

JAISWAL, V. & VANDIVER, J. K. 2007. VIV response prediction for long risers with variable damping. *In:* OMAE2007-29353 (ed.) *Proc. 26th Int. Conf. on Offshore Mechanics and Arctic Engineering.* San Diego, USA.

JAUVTIS, N. & WILLIAMSON, C. H. K. 2004. The effect of two degrees of freedom on vortex-induced vibration at low mass and damping. *Journal of Fluid Mechanics,* 509**,** 23-62.

JESTER, W. & KALLINDERIS, Y. 2003. Numerical study of incompressible flow about fixed cylinder pairs. *Journal of Fluids and Structures,* 17, 561-577.

KARIM, M. M., RAHMAN, M. M. & ALIM, M. A. 2008. Numerical computation of viscous drag for axisymmetric underwater vehicles. *Jurnal Mekanikal,* 26**,** 9-21.

KEEFE, R. T. 1961. An investigation of the fluctuating forces acting on a stationary circular cylinder in a subsonic stream, and of the associated sound field. *Univeristy of Toronto Institute for Aerospace Studies (UTIAS).76.*

KHALAK, A. & WILLIAMSON, C. H. K. 1996. Dynamics of a Hydroelastic cylinder with very low mass and damping. *Journal of Fluids and Structures,* 10**,** 455-472.

KHALAK, A. & WILLIAMSON, C. H. K. 1997. FLUID FORCES AND DYNAMICS OF A HYDROELASTIC STRUCTURE WITH VERY LOW MASS AND DAMPING. *Journal of Fluids and Structures,* 11**,** 973-982.

KIM, S., WILSON, P. A. & CHEN, Z.-M. 2014. Numerical simulation of force and wake models of an oscillating cylinder. *Journal of Fluids and Structures,* 44.

KING, R. & JOHNS, D. J. 1976. Wake interaction experiments with two flexible circular cylinders in flowing water. *Journal of Sound and Vibration,* 45, 259-283.

KIRKGOZ, M. S., ONER, A. A. & AKOZ, M. S. 2009. Numerical modeling of interaction of a current with a circular cylinder near a rigid bed. *Advances in Engineering Software,* 40**,** 1191-1199.

KITAGAWA, T. & OHTA, H. 2008. Numerical investigation on flow around circular cylinders in tandem arrangement at a subcritical Reynolds number. *Journal of Fluids and Structures,* 24**,** 680-699.

KIYA, M., TAMURA, H., ARIE, M 1980. Vortex shedding from a circular cylinder in moderate Reynolds number shear flow. *Journal of Fluid Mechanics,* 101**,** 721-735.

LEE, L., ALLEN, D. W. & D.L., H. 2006. Vortex-Induced Vibration Tests of Two Faired Cylinders in Tandem at Prototype Reynolds Numbers. *ASME Conference Proceedings.*

LESOINNE, M. & FARHAT, C. 1996. Geometric conservation laws for flow problems with moving boundaries and deformable meshes, and their impact on aeroelastic computations. *Computer Methods in Applied Mechanics and Engineering,* 134**,** 71-90.

LIENHARD, J. H. 1966. *Synopsis of Lift, Drag, and Vortex Frequency Data for Rigid Circular Cylinders,* Washington State Universitu, Technical Extension Service.

LINH, T. T. N. 2012. 9 months reports. University of Southampton.

LJUNGKRONA, L., NORBERG, C. & SUNDÉN, B. 1991. Free-stream turbulence and tube spacing effects on surface pressure fluctuations for two tubes in an in-line arrangement. *Journal of Fluids and Structures,* 5**,** 701-727.

LOURENCO, L. M. & SHIH, C. 1993. Characteristics of the Plane Turbulent Near Wake of a Circular Cylinder. A Particle Image Velocimetry Study. . *Private Communication.* .

MA, Q. W. & PATEL, M. H. 2001. On the non-linear forces acting on a floating spar platform in ocean waves. *Applied Ocean Research,* 23**,** 29-40.

MENEGHINI, J. R., SALTARA, F., SIQUEIRA, C. L. R. & FERRARI JR, J. A. 2001. NUMERICAL SIMULATION OF FLOW INTERFERENCE BETWEEN TWO CIRCULAR CYLINDERS IN TANDEM AND SIDE-BY-SIDE ARRANGEMENTS. *Journal of Fluids and Structures,* 15**,** 327-350.

MENTER, F. R. 1994. Two-Equation Eddy-Viscosity Turbulence Models for Engineering Applications. *AIAA Journal,* 32**,** 1598–1605.

MITTAL, S. & KURMA, V. 2004. Vortex induced vibrations of a pair of cylinders at Reynolds number 1000. *International Journal of Computational Fluid Dynamics,* 18**,** 601-614.

MORIYA, M., SAKAMOTO, H., KIYA, M. & ARIE, M. 1983. Fluctuating pressures and forces on two circular cylinders in tandem arrangement. *Transactions of the JSME* 49**,** 1364–1374 (in Japanese).

NAUDASCHER, E. 1987. Flow-Induced Streamwise Vibrations of Structures. *Journal of Fluids and Structures,* 1**,** 265-298.

NAVROSE & MITTAL, S. 2013. Free vibrations of a cylinder: 3-D computations at Re=1000. *Journal of Fluids and Structures,* 41**,** 109-118.

NISHIKAWA, T., YAMADE, Y., SAKUMA, M. & KATO, C. 2013. Fully Resolved Large Eddy Simulation as an Alternative to Towing Tank Tests – 32 Billion Cells Computation on K Computer *16th Numerical Towing Tank Symposium* Mülheim/Germany

NORBERG, C. Pressure distributions around a circular cylinder in cross-flow. Proceedings of the symposium on bluff body wakes and vortex-induced vibrations (BBVIV3) 2002 Port Arthur, Queensland (Australia).

OHYA, Y., OKAJIMA, A. & HAYASHI, M. 1988. Wake interference and vortex shedding. *Encyclopedia of Fluid Mechanics, Aerodynamics and Compressible Flow.* Gulf Publishing Company.

OKAJIMA, A. & SUGITANI, K. 1984. Flow around a circular cylinder immersed in a wake of an identical cylinder. *Transactions of the JSME,* 50**,** 2531-2538 (in Japanese).

ONGOREN, A., ROCKWELL, D. 1988. Flow structure from an oscillating cylinder. *Journal of Fluid Mechanics,* 191.

ORSZAG, S. A. 1970. Analytical Theories of Turbulence. *Journal of Fluid Mechanics,* 41**,** 363–386.

OZONO, S., ODA, J., YOSHIDA, Y. & WAKASUGI, Y. 2001. Critical nature of the base pressure of the upstream circular cylinder in two staggered ones in cross-flow. *Theoretical and Applied Mechanics,* 50**,** 335–340.

PAN, Z. Y., CUI, W. C. & MIAO, Q. M. 2007. Numerical simulation of vortex-induced vibration of a circular cylinder at low mass-damping using RANS code. *Journal of Fluids and Structures,* 23**,** 23-37.

PINTO, A., BROGLIA, R., D., M. A., CAMPANA, E. F. & ROCCO, P. 2006. Numerical Investigation of the Unsteady Flow at High Reynolds Number Over a Marine Riser With Helical Strakes. *ASME Conference Proceedings.*

PLACZEK, A., SIGRIST, J.-F. & HAMDOUNI, A. 2009. Numerical simulation of an oscillating cylinder in a cross-flow at low Reynolds number: Forced and free oscillations. *Computers & Fluids,* 38**,** 80-100.

POPE, S. B. 2000. *Turbulent Flows*. Cambridge University Press, Cambridge, UK.

RAO, S. S. 1990. *Mechanical vibrations, 2nd Edition*.

RICHARDSON, L. F. 1911. The approximate arithmetical solution by finite differences of physical problems involving differential equations, with an application to the stresses in a masonry dam. *Phil. Trans. Royal Soc., London,* 210**,** 307-357.

ROSHKO, A. 1955. On the wake and drag of bluff bodies. *Journal of aerosol science,* 22.

RZENTKOWSKI, G. 1990. *Current Induced Vibration in Multi-tube Marine Riser.*

SALTARA, F., D'AGOSTINI NETO, A. & LOPEZ, J. I. H. 2011. 3D CFD Simulation of Vortex-induced Vibration of Cylinder. *International Journal of Offshore and Polar Engineering,* Volume 21, Number 3.

SARPKAYA, T. 1978. Fluid forces on oscillating cylinders. *American Society of Civil Engineers, Waterway, Port, Coastal and Ocean Division,* 104**,** p. 275-290.

SARPKAYA, T. 2004. A critical review of the intrinsic nature of vortex-induced vibrations. *Journal of Fluids and Structures,* 19**,** 389-447.

SAXENA, A. 2008. *Guidelines for Specification of Turbulence at Inflow Boundaries* [Online]. ESI CFD.

SCANLAN, R. & BILLAH, K. 1991. Resonance, Tacoma Narrows Bridge Failure, and Undergraduate Physics Textbooks. *American Journal of Physics,* 59**,** 118 - 124.

SCHLICHTING, H. T. & KESTIN, J. 1979. *Boundary-layer theory*, McGraw-Hill (New York).

SCHMITT, F. G. 2007. About Boussinesq's turbulent viscosity hypothesis: historical remarks and a direct evaluation of its validity. *Comptes Rendus Mécanique,* 335**,** 617-627.

SHAO, J. & ZHANG, C. 2007. *Numerical studies of flow past two side-by-side circular cylinders,* Beijing, Tsinghua University Press.

SHIH CHIEH LO, HOFFMANN, K. A. & DIETIKER, J.-F. 2005. Numerical Investigation of High Reynolds Number Flows over Square and Circular Cylinders. *Journal of Thermophysics and Heat Transfer,* 19**,** 72-80.

SHUR, M., SPALART, P. R., SQUIRES, K. D., STRELETS, M. & TRAVIN, A. 2005. Three Dimensionality in Reynolds-Averaged Navier–Stokes Solutions Around Two-Dimensional Geometries. *AIAA Journal,* 43.

SPALART, P. R. 1997. Comments on the feasibility of LES for wing and on a hybrid RANS/LES approach. *1st ASOSR CONFERENCE on DNS/LES.* Texas, USA.

SRIVILAIRIT, T. & MANUEL, L. 2007. Vortex-induced vibration and coincident current velocity profiles for a deepwater drilling riser. *In:* OMAE2007-29596 (ed.) *Proc. 26th Int. Conf. on Offshore Mechanics and Arctic Engineering.* San Diego, USA.

STEPHEN, W., HILDE, O., S., V., M, B., K. & ALAIN, D. 2011. Variational multiscale large-eddy simulations of the flow past a circular cylinder: Reynolds number effects. *Computers & Fluids,* 47**,** 44-50.

SUN, T. F., GU, Z. F., HE, D. X. & ZHANG, L. L. 1992. Fluctuating pressure on two circular cylinders at high Reynolds numbers. *Journal of Wind Engineering and Industrial Aerodynamics,* 41-44, 577-588.

TECHET, A. H. 2005. Vortex Induced Vibrations.

TENNEKES, H. & LUMLEY, J. L. 1972. A First Course in Turbulence. Massachusetts, USA: The MIT Press.

TUTAR, M. & HOLDO, A. E. 2000. Large Eddy Simulation of a Smooth Circular Cylinder Oscillating Normal to a Uniform Flow. *Journal of Fluids Engineering,* 122**,** 694-702.

VANDIVER, J. K. 1987. The Relationship between In-Line and Cross-Flow Vortex-Induced Vibration in Cylinder. *Journal of Fluids and Structures,* 1**,** 381-399.

VANDIVER, J. K., MARCOLLO, H., S., S. & JHINGRAN, V. 2005. High Mode Number Vortex-Induced Vibration Field Experiments. *Offshore Technology Conference*

VERSTEEG, H. K. & MALALASEKERA, W. 1995. *An Introduction to Computational Fluid Dynamics: The finite Volume Method*. Longman, Harlow UK.

VICKERY, B. J., WATKINS, R.D.,. Flow-induced vibration of cylindrical structures. First Australian Conference, 1962. University of Western Australia, 213–241.

WANG, X. Q., SO, R. M. C., XIE, W. C. & ZHU, J. 2008. Free-stream turbulence effects on vortex-induced vibration of two side-by-side elastic cylinders. *Journal of Fluids and Structures,* 24**,** 664-679.

WIESELBERGER, C. 1921. Neuere feststellungen uber die Gestze des Fl ¨ ussigkeits- und Luftwider-¨stands. *Phys. Z,* 22**,** 321–328.

WILCOX, D. C. 1988. Re-assessment of the scale-determining equation for advanced turbulence models. *AIAA Journal,* 26**,** 1299-1310.

WILLIAMSON, C. H. K. & GOVARDHAN, R. 2004. Vortex induced vibrations. *Annual Review of Fluid Mechanics,* 36**,** 413-455.

WILLIAMSON, C. H. K. & JAUVTIS, N. 2004. A high-amplitude 2T mode of vortex-induced vibration for a light body in XY motion. *European Journal of Mechanics - B/Fluids,* 23**,** 107-114.

WILLIAMSON, C. H. K. & ROSHKO, A. 1988. Vortex formation in the wake of an oscillating cylinder. *Journal of Fluids and Structures,* 2**,** 355-381.

WILSON, J. F. & TINSLEY, J. C. 1989. Vortex Load Reduction: Experiments in Optimal Helical Strake Geometry for Rigid Cylinders. *Journal of Energy Resources Technology,* 111**,** 72-76.

WILSON, J. F., TINSLEY, J. C 1989. Vortex Load Reduction: Experiments in Optimal Helical Strake Geometry for Rigid Cylinders. *Journal of Energy Resources Technology,* 111**,** 72-76.

ZDRAVKOVICH, M. M. 1985. Flow induced oscillations of two interfering circular cylinders. *Journal of Sound and Vibration,* 101**,** 511-521.

ZDRAVKOVICH, M. M. 1987. The effects of interference between circular cylinders in cross flow. *Journal of Fluids and Structures,* 1**,** 239-261.

ZDRAVKOVICH, M. M. 1997. *Flow around circular cylinders: A comprehensive guide through flow phenomena, experiments, applications, mathematical models, and computer simulations,* Oxford University Press

ZDRAVKOVICH, M. M. & MEDEIROS, E. B. 1991. Effect of damping on interference-induced oscillations of two identical circular cylinders. *Journal of Wind Engineering and Industrial Aerodynamics,* 38**,** 197-211.

ZDRAVKOVICH, M. M. & PRIDDEN, D. L. 1977. Interference between two circular cylinders; Series of unexpected discontinuities. *Journal of Wind Engineering and Industrial Aerodynamics,* 2**,** 255-270.

ZHANG, H. & MELBOURNE, W. H. 1992. Interference between two circular cylinders in tandem in turbulent flow. *Journal of Wind Engineering and Industrial Aerodynamics,* 41-44, 589-600.

ZHAO, M. & CHENG, L. 2012. Numerical simulation of vortex-induced vibration of four circular cylinders in a square configuration. *Journal of Fluids and Structures,* 31**,** 125-140.

ZHAO, M., CHENG, L., TENG, B. & DONG, G. 2007. Hydrodynamic forces on dual cylinders of different diameters in steady currents. *Journal of Fluids and Structures,* 23**,** 59-83.

ZIENKIEWICZ, O. C., TAYLOR, R. L. & NITHIARASU, P. 2014. The Finite Element Method for Fluid Dynamics. *The Finite Element Method for Fluid Dynamics (Seventh Edition).* Oxford: Butterworth-Heinemann.